THÈSE

En vue de l'obtention du

DOCTORAT DE L'UNIVERSITÉ DE TOULOUSE

Délivré par l'Université Toulouse 3 - Paul Sabatier

Cotutelle internationale : Université Cadi Ayyad Marrakech

Présentée et soutenue par

Bouchra AIT HSSAINE
Le 16 juillet 2019

Spatialisation des flux d'énergie et d'eau: combinaison de la modélisation des échanges de surface-atmosphère et de la télédétection optique, thermique et micro-ondes.

Ecole doctorale : **SDU2E Sciences de l'Univers, de l'Environnement et de l'Espace**

Spécialité : **Surfaces et interfaces continentales, Hydrologie**

Unité de recherche :

CESBIO - Centre d'Etudes Spatiales de la Biosphère

Thèse dirigée par

Olivier MERLIN et Said KHABBA

Jury

Mme Zohra LILI CHABAANE, Rapporteure

M. Kamal LABBASSI, Rapporteur

M. Ahmed BAHLAOUI, Examinateur

M. El Khadir LAKHAL, Examinateur

M. Olivier MERLIN, Directeur de these

M. Said KHABBA, Co-directeur de thèse

TABLE OF CONTENTS

Abstract ..... **iv**

Résumé ..... **v**

Remerciement ..... **i**

Résumé étendu ..... **i**

TABLES ..... **xii**

FIGURES ..... **xiii**

Chapter.I. Introduction and state of art **1**

I.1. General context 2

I.2. In-situ measurements of Evapotranspiration 8

I.3. Modeling approaches of Evapotranspiration 10

I.3.1. Empirical models 11

I.3.2. Mechanistic models 11

I.3.3. Surface Energy Balance (SEB) models 13

I.4. Remote sensing of Evapotranspiration 16

I.4.1. Models based on vegetation index 16

I.4.2. Models based on Land Surface Temperature 17

I.4.3. Models based on Surface soil moisture 18

I.5. Objectives 21

Chapter.II. Modeling approaches : Description and implementation **24**

II.1. Introduction 25

II.2. TSEB Model Description and Implementation 25

II.2.1. Algorithm for solving the energy balance and the equation system 28

II.2.2. Calibration procedure 29

II.3. TSEB-SM Model Description and Implementation 30

II.3.1. Algorithm for solving the energy balance and the equation system 30

II.3.2. Calibration procedure 32

II.4. Aggregation scheme 35

II.5. Disaggregation model of SM data 37

II.6. Conclusion 39

Chapter.III. Sites and data used **40**

III.1. Introduction 41
III.2. Sites and in-situ data description 41
III.2.1. Watershed of Tensift el Haouz 41
III.2.2. Wankama basin (Niger) 48
III.2.3. Spatial data 52
III.3. Conclusion 54
Chapter.IV. Validation of TSEB model over sparse and heterogeneous vegetation in Sahel region (Niger) 55
IV.1. Introduction 56
IV.2. Results and discussion 57
IV.2.1. Experimental data analysis 57
IV.2.2. Results of multi-Scale surfaces fluxes 61
IV.3. Summury and Conclusions 72
Chapter.V. Improving TSEB model by integrating sm data (TSEB-SM): a feasibility study using in-situ data (LST, fcand SM) 75
V.1. Introduction 76
V.2. TSEB-SM Model Description and Implementation 77
V.3. Retrieving (a_{rss}, b_{rss}) and α_{PT} parameters 77
V.3.1. Calibration first step 77
V.3.2. Calibration 2nd step 78
V.3.3. Calibration 3th step 80
V.4. Results 82
V.4.1. Interpretation of α_{PT} variabilities 82
V.4.2. Surface fluxes 84
V.5. Summary and Conclusions 88
Chapter.VI. Remote sensing application of TSEB-SM (combining DisPATCh SM and MODIS LST data for mapping ET at 1 km resolution 90
VI.1. Introduction 91
VI.2. TSEB-SM Model improvements 91
VI.3. Accuracy of Remote Sensing data 92
VI.4. Retrieving (a_{rss}, b_{rss}) parameters 97
VI.5. α_{PT} variablities 98
VI.5.1. Using in-situ data 98
VI.5.2. Using satellite data 99

VI.5.3. Interpretation of α_{PT} variabilities 100
VI.6. Surface fluxes 101
VI.6.1. Using in-situ data 102
VI.6.2. Using satellite data 105
VI.7. Summary and Conclusions 109
Chapter.VII. Conclusion and perspectives 110
References 117

Abstract

A precise estimate of evapotranspiration (ET) at the landscape scale remains a priority to understand land-atmosphere-interactions, especially over semi-arid lands. Regarding data availability over large areas and at multiple scales, remote sensing observations provide very relevant information to feed ET models. Commonly, there are three main variables, derived from remote sensing, that can be used to determine the spatial distribution of ET: the surface (0-5 cm) soil moisture (SM) derived from microwave data, the land surface temperature (LST) derived from thermal infrared radiances and vegetation indices (or fractional vegetation cover f_c) derived from visible/near infrared reflectances. However, very few studies have attempted to combine all three variables within a single ET model. In this context, the main objective of this thesis is to improve the estimation of ET by combining multi-resolution optical / microwave remote sensing and surface-atmosphere exchange modelling.

In the first part, the thermal-based two-source energy balance (TSEB) model based on LST, f_c and the Priestley Taylor (PT) coefficient (α_{PT}) relating ET to the net radiation is tested over an heterogeneous watershed in Niamey, Niger (Wankama catchment). The model predictions of area-averaged latent (LE) and sensible (H) heat fluxes are compared to data acquired by a Large Aperture Scintillometer (LAS) set up over a transect about 3.2 km-long and spanning three vegetation types (millet, fallow and degraded shrubs). The results obtained for H and LE are relevant. However, an overestimation of simulated fluxes is recorded at the end of the season. This is mainly due to the fixed maximum value for α_{PT} (generally set to 1.26).
In the second part, a new model named TSEB-SM derived from the TSEB formalism is developed by using, in addition to LST and f_c data, the near-surface SM as an extra constraint on soil evaporation. An innovative calibration procedure is proposed to retrieve three key parameters: the Priestley Taylor coefficient (α_{PT}) and the parameters (a_{rss} and, b_{rss}) of a soil resistance formulation. In practice, a_{rss} and b_{rss} are retrieved at the seasonal time scale from SM and LST data with f_c lower than a given threshold $f_{c,thres}$($f_{c,thres}$ is set to 0.5), while α_{PT} is retrieved at the daily time scale from SM and LST data for $f_c > f_{c,thres}$. TSEB-SM model is tested over 1 flood- and 2 drip-irrigated wheat fields using in situ data collected during two field experiments in 2002‑2003 and 2016‑2017 in the Tensift watershed, central Morocco. The coupling of the soil resistance formulation with the TSEB formalism improves the estimation of soil evaporation, and consequently, improves the partitioning of ET. Analysis of the retrieved time series indicates that the daily α_{PT} mainly follows the phenology of winter wheat crop with a maximum value coincident with the full development of green biomass and a minimum value reached at harvest.
Finally, TSEB-SM is applied in real-life using 1 km resolution MODIS LST and f_c data and the 1 km resolution SM data disaggregated from SMOS (Soil Moisture and Ocean Salinity) observations by using a disaggregation algorithm (DisPATCh). The approach is validated during a four-year period (2014-2018) over a rainfed wheat field in the Tensift basin, central Morocco. The field was seeded for the 2014-2015 (S1), 2016-2017 (S2) and 2017-2018 (S3) agricultural season, while it remained under bare soil conditions during the 2015-2016 (B1) wheat seasons. The constraint applied on the soil evaporation by using the SM derived from SMOS data is one of the main controlling factors of the evaporative fraction, which helps determine with more accuracy the LE/H partitioning. Moreover, the retrieved α_{PT} increases after rainfall events, suggesting a relationship with the soil water availability in the root zone.

Keywords: TSEB, TSEB-SM, DisPATCh, Evapotranspiration, Priestley Taylor coefficient, soil resistance

Résumé

Une estimation précise de l'évapotranspiration (ET) à grand échelle est une priorité pour comprendre les interactions sol-atmosphère, particulièrement dans les zones semi-arides. La télédétection fournit des informations très pertinentes à grande échelle pour alimenter les modèles d'ET. Généralement, trois variables dérivées de la télédétection sont utilisées pour déterminer la distribution spatiale de l'ET : l'humidité du sol en surface (SM) dérivée des données micro-ondes, la température de surface (LST) dérivée des données infrarouges thermiques et les indices de végétation (ou fraction de couvert f_c,) issus des réflectances visible/proche infrarouge . Cependant, très peu d'études ont tenté de combiner les trois variables dans un même modèle ET. Dans ce contexte, l'objectif principal de cette thèse est d'améliorer l'estimation de l'ET en combinant la modélisation par télédétection optique /micro-ondes à multiples résolutions et la modélisation des échanges surface-atmosphère.

Dans la première partie, le modèle de bilan d'énergie à double source (TSEB) basé sur les données de LST, f_c et le coefficient de Priestley Taylor (α_{PT}) qui relie l'ET au le rayonnement net est testé sur une zone hétérogène à Niamey, Niger (Wankama). Les prédictions du modèle en terme de flux de chaleur latente (LE) et sensible (H) sont comparées aux données acquises par un scintillomètre à grande ouverture (LAS) installé sur un transect d'environ 3,2 km couvrant trois types de végétation (mil, savane et jachère). Les résultats obtenus pour H et LE sont pertinents. Cependant, une surestimation des flux simulés à la fin de la saison est remarquée. Ce qui est principalement due à la valeur de α_{PT} (fixé généralement à 1,26).

Dans la 2ème partie, un nouveau modèle appelé TSEB-SM dérivé du formalisme TSEB a été développé en utilisant, en plus des données LST et f_c, les données de SM comme une contrainte supplémentaire sur l'évaporation du sol. Une calibration innovante est proposée pour extraire trois paramètres clés : le coefficient de Priestley Taylor (α_{PT}) et les paramètres (a_{rss} and, b_{rss}) de la résistance du sol. En pratique, a_{rss} et b_{rss} sont extraits à l'échelle saisonnière à partir des données SM et LST avec f_c inférieur à un seuil donné $f_{c,thres}$($f_{c,thres}$ = 0.5), tandis que α_{PT} est inversé à la échelle journalière à partir des données SM et LST pour $f_c > f_{c,thres}$. Le modèle TSEB-SM est testé sur une parcelle de blé inondée et 2 parcelles de blé irriguées en goutte-à-goutte en utilisant les données in-situ collectées lors de deux expériences expérimentales en 2002-2003 et en 2016-2017 dans le bassin versant du Tensift. L'insertion de la résistance du sol dans le modèle TSEB améliore l'estimation de l'évaporation du sol et, par conséquent, améliore la partition de l'ET. L'analyse de la série temporelle indique que α_{PT} suit principalement la phénologie de la culture de blé, avec une valeur maximale correspondant au développement complet de la biomasse verte et une valeur minimale atteinte à la récolte.

Finalement, TSEB-SM est appliqué à l'état réel en utilisant les données MODIS LST et f_c à 1 km de résolution et les données SM issu de satellite SMOS (Soil Moisture and Ocean Salinity) désagrégées à l'aide d'un algorithme de désagrégation (DisPATCh) à 1 km de résolution. L'approche est validée sur une période de quatre ans (2014-2018) sur une parcelle de blé pluvial dans le bassin du Tensift, au Maroc. La parcelle a été semée pour la saison agricole 2014-2015 (S1), 2016-2017 (S2) et 2017-2018 (S3), alors qu'elle n'était pas labouré (sol nu) pendant la saison 2015-2016 (B1). La contrainte appliquée sur l'évaporation du sol en utilisant le SM dérivé des données SMOS est l'un des principaux facteurs de contrôle de la fraction évaporative, ce qui permet de déterminer avec plus de précision la partition LE / H.

De plus, α_{PT} inversé augmente après les événements pluvieux, suggérant un lien avec la disponibilité en eau du sol dans la zone racinaire.

Mots clés : TSEB, TSEB-SM, DisPATCh, Evapotranspiration, coefficient de Priestley Taylor, résistance du so

Remerciement

Une thèse, bien entendu pour certaines personnes, est une chance de plaisir et de joie, de liberté académique pour travailler sur terrain et assister à des conférences, et une opportunité pour parcourir et découvrir le monde. Pour d'autres, c'est une source infinie de misère, d'insécurité, de disputes, de dépression et d'échec. Or, j'ai un point de vue légèrement différent après avoir travaillé trois ans et demi sur cette thèse. Un doctorat est une alternance de ces deux cas extrêmes. Une grande satisfaction qui me procure quand les résultats sont achevés et surtout quand un papier est accepté, suivi de d'une période de détresse au cas contraire. Ma vie de thèse a été comme une balance déséquilibrée au cours de ces dernières années. Autrement, je ne peux pas nier que j'étais très chanceuse de travailler au sein d'une équipe passionnée par la recherche, qui m'a ouvert la porte de découvrir ce domaine de la recherche et de créer de nombreux contacts. Cette période de doctorat aura été probablement l'un des plus beaux chapitres de ma vie. Cependant, j'espère aussi que ce n'est que le début et j'ai hâte de voir où les pistes m'emmèneront ensuite.

C'est avec une certaine émotion et beaucoup de sincérité que je voudrais exprimer ma profonde gratitude envers toutes les personnes qui ont soutenu et contribué de près ou de loin à la réalisation de cette thèse

Je souhaite remercier en premier lieu mes directeurs de thèse, Mr Olivier Merlin, Mr Said Khabba de m'avoir encadré, orienté, aidé et conseillé. Je suis également reconnaissante pour le temps qu'ils m'ont accordé, leurs qualités pédagogiques et scientifiques, ainsi que leurs franchises. Ils ont su être disponibles et à l'écoute à chaque moment décisif. J'en profite pour leurs adresser ma gratitude pour rendre mon expérience de doctorat productive et stimulante.

J'adresse de chaleureux remerciements à mon co-directeur de thèse, Jamal Ezzahar, qui m'a fait confiance dès mon arrivée. Merci pour votre écoute et votre efficacité qui m'ont permis de garder le cap et de ne jamais me décourager, vos grandes qualités humaines et scientifiques m'auront permis de mener à bien cette thèse.

J'exprime toute ma reconnaissance aux membres du jury pour avoir accepté d'évaluer mon travail de thèse. Je remercie Mme Zohra Lili Chabaane, Mr Kamal Labbassi et Mr El Khadir Lakhal d'avoir pris le temps de juger mon travail en tant que rapporteurs. Je remercie spécialement Mr El Khadir Lakhal d'avoir accepté de présider ma soutenance de thèse. Merci également à Mr Ahmed Bahlaoui et Mr Abdelghani Chehbouni d'avoir accepté d'examiner mon mémoire.

Je suis très reconnaissante envers Lionel Jarlan pour son implication dans ce travail de thèse. Merci pour tous tes conseils, tes suggestions et les discussions scientifiques qui m'ont guidé au cours de ces 3 ans et demi.

J'associe à ces remerciements Mr Salah Er-Raki et Mr Abderrahman lahrouni directeurs des laboratoires LMI TREMA et Laboratoire Modélisation Molécolaire et Ecophysiologie, non seulement pour m'avoir accueilli au sein du laboratoire mais aussi pour sa contribution à la réalisation de cette thèse

Je remercie également tous les thésards et les autres membres du laboratoire LMI-TREMA, notamment ceux avec qui j'ai eu l'occasion de travailler et les autres simplement pour les

bons moments partagés. Un merci spécial à Simohamed Kasbani et Adnane Chakir pour leur soutien au terrain et traitement des données.

Au nom de l'équipe LMI-TREMA, je tiens à remercier particulièrement l'agriculteur Mr Omar Rafi de nous avoir donné accès à ses champs à Chichaoua.

Je désire en outre remercier tous les membres de laboratoire CESBIO pour leur sympathie, leur amitié. J'ai eu beaucoup de plaisir à travailler avec eux. Le cadre de travail était idéal.

Merci à IsardSAT et LABferrer, pour ces merveilleux moments passés en votre compagnie, l'ambiance chaleureuse et la sympathie pendant mes séjours à Barcelone.

Je remercie le Programme ARTS Allocations de recherche pour une thèse au Sud pour m'avoir octroyé une bourse de recherche et a permis la réalisation de cette thèse en cotutelle entre l'UCAM et l'UPS. Merci aux projets PHC-Toubkal et REC H2020/Rise pour leurs soutiens financiers lors des stages et des séjours de formations à l'international.

J'adresse toute ma gratitude à tous mes ami(e)s et à toutes les personnes qui m'ont aidé dans la réalisation de ce travail. Merci Majida, Karima, Mariem, Asmaa, Nadia, Fatiha, Ibtissam, Hakima, Chaimae, Ftèm, Hanane, Fatimazohra, Bouchra, Mourad, Ismail, Jamal, Omar, Tarik, Zoubair, Charif, Houssine, Hatim, Yoann.

Je remercie de tout mon cœur, ma sœur Laila et son mari Mouhand et la petite Ghita, ma sœur Loubna et son mari Brahim et mes deux nièces Mariem et Simane, mon gros frère et mon père spirituel Hatim avec sa femme Samira et mes chouchous Aya Sohayb et Aahd, mon frère Brahim et son épouse Safaa et la belle nièce Loujayne, et enfin mon frère Khalil avec sa femme Sanaa et la petite copie à moi Rim.

Enfin, les mots les plus simples étant les plus forts, j'adresse toute mon affection à ma famille, et en particulier Maman et Papa, merci pour votre présence et votre soutien depuis toujours. Le symbole de la bonté par excellence, la source de tendresse et l'exemple du dévouement qui n'a pas cessé de m'encourager et de prier pour moi. Leur prière et leur bénédiction m'ont été d'un grand secours pour mener à bien mes études. Aucune dédicace ne saurait être assez éloquente pour exprimer ce que vous méritez pour tous les sacrifices que vous n'avez cessé de me donner depuis ma naissance, durant mon enfance et même à l'âge adulte.

A tous ceux que j'oublie ici et qui ont contribué de près ou de loin à l'élaboration de ce travail… qu'ils y trouvent l'expression de ma profonde gratitude.

Résumé étendu

1. Introduction

Le Maroc est l'un des 45 pays du monde les plus affectés par la pénurie d'eau ((Figure I.2, chapitre I). Cette situation est le résultat de la double pressions climatique (augmentation de la température, diminution et irrégularité spatio-temporelle de la précipitation …) et anthropique (extension des zones irriguées, intensification de la consommation d'eau par les secteurs touristique et domestique ….). Selon le rapport du World Ressources Institute, le niveau de stress hydrique au Maroc sera extrêmement élevé d'ici 2040. En effet, le Maroc atteindra une situation de stress hydrique extrême dans moins de 25 ans (Word Bank, 2017). L'agriculture, qui contribue à l'économie nationale entre 14 et 20% du PNB (Produit National Brut) en fonction des précipitations de l'année (Balaghi et al., 2012) et consomme environ 85% des ressources en eau mobilisées du pays (Jarlan et al., 2015), sera sans doute le secteur le plus touché par ce stress. Donc, la gestion des ressources hydriques deviendra ainsi un facteur limitant le développement du pays.

Dans ce contexte, une bonne gestion des ressources en eau est liée à la modélisation des flux hydrologiques, tels que l'infiltration des sols, le ruissellement et l'évapotranspiration (ET). ET est une composante cruciale du cycle de l'eau, particulièrement dans les zones semi-arides. À l'échelle du bassin versant, les pertes en eau par ET constituent généralement la partie la plus importante du bilan hydrique et peuvent être responsables de la dissipation de 60% de l'apport pluviométrique (Oudin, 2004). De plus, une estimation précise de l'ET détermine les besoins en eau des cultures, ce qui permet par la suite d'améliorer la gestion de l'eau d'irrigation (Allen et al., 1998). Une grande variété de modèles et de mesures de l'ET ont été rapportés dans la littérature (Allen et al., 2011; Olivera-Guerra et al., 2014; Subedi et Chávez, 2015). Cependant, l'estimation de l'ET sur des zones étendues comprenant différents biomes et climats est encore sujette à des incertitudes importantes (Ershadi et al., 2014; Pereira, 2004), bien que les principaux moteurs de l'ET, tels que la demande d'évaporation atmosphérique, le type de végétation, les stades de développement, les caractéristiques biophysiques de surface et la disponibilité en eau du sol (Federer et al., 2003) sont maintenant bien identifiés. Une difficulté majeure dans la modélisation de ce processus réside dans le manque de données d'entrée pertinentes disponibles aux échelles d'espace et de temps souhaitées (Allen et al., 2011; Pereira et al., 2015). La précision des estimations de l'ET à une échelle donnée

représente donc un compromis entre complexité et réalisme du modèle, qui est généralement liée au: i) nombre de paramètres de modèle et de variables de forçage et ii) la disponibilité des données qui diminue généralement avec l'étendue spatiale (Allen et al., 2011; Gharsallah et al., 2013). Quant à la disponibilité des données, les observations satellitaires sont en mesure de fournir des mesures intégrées à différentes échelles temporelles et spatiales et dans différentes bandes spectrales. La télédétection multi-spectrale fournit des outils puissants pour observer les surfaces continentales et les composants hydrologiques tels que l'humidité du sol (SM) à l'aide de satellites SMOS (Soil Moisture and Ocean Salinity, Kerr et al (2001)) et SMAP (Soil Active Passive Moisture, Entekhabi et al (2010)). La température de surface (LST) dérivée de satellite MODIS (Moderate-Resolution Imaging Spectroradiometer) fournit également des informations sur l'état thermique des surfaces et sur les variations temporelles des flux hydrologiques (Anderson, 1997) à l'interface surface-atmosphère à travers les bilans énergétique et hydrique (Anderson et al., 2008; Brunsell et al., 2011; Kustas et Anderson, 2009). En outre, l'indice de végétation normalisé (NDVI) et la fraction de végétation, qui sont des paramètres essentiels pour la modélisation de ET sur les couverts végétaux, peuvent être estimés à partir de données visibles proche-infrarouge fournies par MODIS. Généralement, ces observations (LST, SM, NDVI et f_c) de télédétection fournissent des informations très pertinentes pour l'alimentation des modèles ET. En effet, SM contrôle l'évaporation du sol, la transpiration des plantes et la partition des eaux de pluie en infiltration et ruissellement (Chanzy et Bruckler, 1993), f_c constitue une contrainte structurelle essentielle pour la partition de l'évaporation / transpiration (Allen et al., 2000) et LST représente une signature de l'énergie disponible et de l'ET (Norman et al., 1995). Pour cette raison, des efforts ont été faits pour intégrer ces données en tant qu'informations supplémentaires et complémentaires pour l'estimation de l'ET (Price, 1990).

Cependant, l'utilisation efficace des observations satellitaires pour des applications agricoles et hydrologiques présente plusieurs limites. En particulier, la représentativité spatiale de la mesure, qui joue un rôle majeur dans la précision de cette mesure. Dans ce contexte, plusieurs algorithmes ont été développés afin désagréger les données satellites. On cite par exemple l'outil DisPATCh (DISaggregation based on Physical and Theoretical Scale Change, Merlin et al. 2013, Malbeteau et al. 2016, Molero et al. 2016) qui permet de fournir des produits d'humidité avec une résolution d'1km comparable avec celle du MODIS.

2. **Objectifs et méthodologie de la thèse**

L'objectif essentiel de cette thèse est d'améliorer l'estimation de l'ET en combinant les observations satellitaires d'humidité du sol en surface (issue des données micro-ondes, SMOS) et de température de surface (issue des données optiques dont thermiques, MODIS). La stratégie proposée consiste à estimer un indice de stress hydrique de la végétation dérivée de la transpiration. Cette dernière sera estimée à haute résolution spatiale en développant les trois axes suivants: la désagrégation des données d'humidité du SMOS (axe 1); l'estimation de l'évaporation du sol (axe 2) et la partition de l'évapotranspiration entre l'évaporation du sol et la transpiration des plantes (axe 3).

a. *Désagrégation de données spatiales* :

Un algorithme de désagrégation des données d'humidité DisPATCh (Merlin et al. 2013, Malbeteau et al. 2016, Molero et al. 2016) a été utilisé. Ce modèle permet d'améliorer la résolution spatiale des données SMOS de plusieurs ordres de grandeur. La méthode se base sur le lien spatial entre l'humidité du sol en surface inversée des données micro-ondes et l'efficacité évaporative du sol déduit des données optiques à plus haute résolution spatiale. L'humidité désagrégée à haute résolution spatiale s'exprime comme un développement de Taylor d'un modèle d'efficacité évaporative du sol autour de l'humidité du sol observée à basse résolution (Section II.5 Chapitre II). La résolution en sortie de désagrégation est de 1 km avec les données MODIS (MODerate resolution Imaging Spectroradiometer). Le processeur C4DIS (Molero et al. 2016) est la version opérationnelle du prototype DisPATCh (Merlin et al. 2012 ; Merlin et al. 2013) appliqué aux données SMOS de niveau 3 (humidité CLF31A/D) et aux produits MODIS (température MOD11A1, MYD11A1 et NDVI MOD13Q2). Le processeur a été validé dans différentes régions en Espagne (Merlin et al. 2013), en Australie (Malbeteau et al. 2016, Molero et al. 2016) et aux Etats Unis (Molero et al. 2016). Dans le cadre de cette thèse, le processeur C4DIS a été appliqué à la tuile MODIS au Maroc afin de générer le produit d'humidité sur la période 2014-2018. Les SM désagrégées sont ensuite évaluées par les mesures in-situ des sites intensifs de l'observatoire Tensift (http://trema.ucam.ac.ma).

b. *Estimation de l'évaporation du sol:*

Les données d'humidité DisPATCh sont ensuite utilisées en entrée d'un modèle de l'évaporation du sol (section 3, chapitre II). Une revue complète et détaillée des méthodes pour estimer l'évaporation à partir des observations d'humidité du sol en surface est proposée par Mahfouf et al. (1991), Lee and Pielke (1992), Ye et al. (1993), Mihailovic et al. (1995),

Dekic et al. (1995) et Cahill et al. (1999). Bien que de nombreuses formulations ont été proposées depuis les années 1960, il n'existe toujours pas de consensus sur une meilleure façon de modéliser l'évaporation sur de grandes étendues (Desborough et al. 1996, Sakaguchi et al. 2009). Néanmoins, la revue bibliographique de ces modèles nous permet de tirer les enseignements suivants: 1) les formulations existantes diffèrent selon quatre aspects: les valeurs limites basse et haute de l'humidité, la non-linéarité de la relation entre évaporation et humidité, les données d'entrée nécessaires autres que l'humidité et la profondeur des mesures d'humidité (Merlin et al. 2011), 2) des expressions empiriques simples peuvent être plus précises et robustes que d'autres modèles à base physique (Dekic et al. 1995, Mihailovic et al. 1995), et 3) aucune de ces formulations n'a été évaluée dans ces conditions de sol et atmosphériques variées. Sur la base de ces résultats, un nouveau modèle développé par Merlin et al. (2016) a été utilisé pour estimer l'évaporation du sol (équation II.17, chapitre II).

c. *La partition de l'évapotranspiration entre l'évaporation du sol et la transpiration des plantes*:

Un nouveau modèle de bilan énergétique pour la partition d'évaporation / transpiration est développé pour intégrer simultanément les données de télédétection LST et SM. Pour construire ce modèle à partir d'une modélisation état de l'art de l'ET, en tenant en compte les caractéristiques suivantes: i) modélisation à partir de données LST, ii) utilisation d'une représentation à deux sources permettant une séparation explicite de l'évaporation du sol et de la transpiration des plantes, et iii) paramétrer les flux de surface avec un réseau de résistances, plus directement liés au SM que les modèles à efficacité d'évaporation.

Nous choisissons donc le modèle TSEB (Norman et al. 1995) car il satisfait ces trois critères. La transpiration dans le modèle TSEB est basée sur l'approche Priestley Taylor (PT). Le coefficient PT noté α_{PT} relie directement le flux de chaleur latente à l'énergie disponible en surface. En négligeant le terme de résistance aérodynamique inclus dans l'équation de Penman-Monteith (Monteith, 1965), la formulation du PT est relativement simple, nécessite moins de données d'entrée et s'est révélée remarquablement précise et robuste pour estimer l'ET potentielle dans un large éventail de conditions (Fisher et al., 2008). Il est donc bien adapté aux applications opérationnelles (McAneney et Itier, 1996) et à grande échelle (Anderson et al., 2008). Néanmoins, plusieurs études (Ait Hssaine et al., 2018a; Fisher et al., 2008; Jin et al., 2011; Yang et al., 2015) ont souligné que α_{PT} varie selon les types de surface et les conditions atmosphériques entre 0.5 et 2.0 avec une valeur moyenne estimée autour de

1,3 (Fisher et al., 2008; Jin et al., 2011; Yang et al., 2015). D'autres études (Gonzalez-dugo et al., 2009; Long et Singh, 2012 et Morillas et al., 2014) ont montré que l'approche PT peut surestimer l'ET du couvert, en particulier en cas de faible humidité du sol et / ou de faible couvert végétal, car elle n'inclut pas une réduction raisonnable de l'ET initiale dans des conditions de stress. Dans ce but, la modification du formalisme TSEB basé sur le PT (Kustas et al., 1999; Norman et al., 1995) a été étudiée en intégrant simultanément les données LST et SM (la version modifiée s'appelle TSEB-SM). Une procédure de calibration innovante a également été mise en œuvre pour inverser les principaux paramètres d'évaporation du sol (résistance du sol) et de transpiration des plantes (α_{PT}).

3. Modèles utilisés

a. Le modèle TSEB :

Le modèle TSEB calcule deux bilans d'énergie distincts pour le sol et la végétation, puis estime l'évaporation comme terme résiduel du bilan d'énergie. Deux variables dérivées d'instruments de télédétection sont des éléments clés de modèle TSEB: LST, qui est utilisée dans l'estimation des flux de chaleur sensible, et f_c, qui contrôle le partitionnement de l'énergie entre la végétation et le sol (Figure II.1, chapitre II). α_{PT} est l'un des paramètres les plus sensibles de TSEB, car il pilote le flux de chaleur latent de la végétation. La plupart des études menées avec TSEB ont utilisé sa valeur générique autour de 1.3.

b. Le modèle TSEB-SM :

Le modèle TSEB-SM est basé sur le formalisme original de TSEB, ce qui signifie que le bilan énergétique de la végétation est identique à celui de TSEB utilisant la formule PT, bien que l'évaporation du sol est estimée en fonction de SM en utilisant une résistance du sol développée par Sellers et al. (1992) (Figure II.2, chapitre II). L'utilisation de la formulation de résistance du sol est justifiée par le fait que ses paramètres principaux (a_{rss}, b_{rss}) peuvent être ajustés en fonction des caractéristiques de texture du sol (Merlin et al., 2016) ou en combinant les données de SM et de LST dans les conditions du sol nu ou partiellement couvert (Figure V.1, chapitre V et figure VI.4, chapitre VI). Les paramètres a_{rss} et b_{rss} sont déterminés en considérant que, lorsque f_c est inférieure à un seuil donné ($f_{c,thres}$), la dynamique de ET total est principalement contrôlée par la variation temporelle de l'évaporation du sol. Cela signifie que les deux paramètres de sol sont estimés lorsque le coefficient PT est réglé sur une valeur constante. Une fois que la résistance du sol a été calibrée, le coefficient PT est récupéré à

l'échelle journalière pour f_c supérieure à $f_{c,thres}$. En fait, une boucle itérative est exécutée sur les paramètres de sol et de végétation pour atteindre la convergence de tous les paramètres (Figure II.3, chapitre II). Les principales équations du modèle et de la procédure de calibration sont détaillées dans le chapitre II (pages 31-34).

4. **Sites et dispositifs expérimentaux associés**

Nos approches ont été testées sur deux bassins versants (Tensift (Maroc), Wankama (Niger)) situées dans des régions caractérisées par un climat semi-aride, et une variabilité spatiale et temporelle marquée de précipitations. Différentes données ont été utilisées en entrée pour alimenter les deux modèles (Chapitre II). En particulier, les deux entrées clés, LST et f_c, sont utilisées pour forcer le modèle TSEB. Alors que SM est utilisée comme contrainte supplémentaire de l'évaporation du sol dans le modèle TSEB-SM. Ces trois produits sont soit mesurés à l'échelle de la parcelle à l'aide des mesures in-situ, soit extraits d'images satellitaires thermique /optique et micro-ondes (Chapitre III). En plus de ces produits, les données météorologiques comprenant la température de l'air, le rayonnement solaire, l'humidité relative et la vitesse du vent sont également utilisées pour forcer TSEB et TSEB-SM. Le modèle TSEB classique a été testé entre 23 Juillet et 23 Octobre 2006 sur trois parcelles pluviales (mil, savane et jachère) dans le bassin de Wankama (Niger) (Chapitre IV). Des flux de chaleur sensible (H) et latente (LE) provenant des systèmes d'Eddy covariance (EC) et de scintillomètre ont été utilisés pour valider l'estimation du TSEB à l'échelle du patch et de la grille. Alors que le modèle TSEB-SM a été testé durant deux saisons agricoles 2002-2003 et 2016-2017 sur deux parcelles de blé irrigué en goutte à goutte (Chichaoua et R3) (Chapitre V) et durant quatre saisons 2014-2015, 2015-2016, 2016-2017 et 2017-2018 sur une parcelle de blé pluvial (Bour) (Chapitre VI) dans la plaine de Haouz du bassin versant du Tensift (centre du Maroc).

5. **Résultats**

a. Validation du TSEB classique :

Dans un premier temps, le chapitre « Les résultats de la validation du modèle TSEB sur une végétation éparse et hétérogène dans la région du Sahel (Niger) » vise à tester le modèle TSEB piloté par des observations MODIS (Moderate resolution Imaging Spectroradiometer) en conjonction avec un schéma d'agrégation spatiale. Le but est d'estimer les flux de chaleur sensible à la surface (H) et latente (LE) sur un trajet de 3 km couvrant trois cultures dominantes dans le bassin de Wankama (Mil, Jachère et la savane). Les données qui ont servi

à la validation de cette approche ont été collectées dans le cadre du projet AMMA. Chaque site a été équipé par des stations météorologiques et des systèmes d'Eddy Covariance ainsi qu'un scintillomètre à grande ouverture installé sur un trajet de 3 km afin de dériver les valeurs de H et LE moyens sur les trois champs. Premièrement, le modèle TSEB a été évalué à l'échelle du patch (Mil, Jachère et la Savane), et ensuite à l'échelle du grid qui est composé des trois champs, en utilisant les données in-situ (chaque 30 minutes), Météosat seconde génération (MSG) (3 km de résolution et à l'heure de passage MSG-SEVIRI) et MODIS (1 km de résolution et à l'heure de passage Terra et Aqua). En tenant compte de la complexité de chaque champ liée à la dispersion du couvert végétal, les résultats obtenus à l'échelle de la station pour H et LE sont pertinents, en particulier lors de l'utilisation de données in-situ. Quelques dispersions constatées sont principalement liées à la différence entre les footprints des systèmes de mesure, ainsi qu'à la valeur de α_{PT} fixée à 1,26 durant toute la saison. TSEB a été ensuite évalué à l'échelle de grid. En général, les flux prédits par TSEB en utilisant les données in-situ concordent bien avec les observations par scintillomètre avec un RMSE de l'ordre de 37 et 75 W / m^2 pour H et LE, respectivement. L'accord entre H et LE simulés par TSEB forcé par les données MSG et les observations du scintillomètre est très médiocre, (R = 0,39 et 0,2 pour H et LE, respectivement). Cette dispersion peut être attribuée au fort biais sur les LST de MSG SEVIRI lié à l'hétérogénéité du site. Ce qui souligne la nécessité de représenter l'hétérogénéité des sous-pixels. Ceci a été testé en dernière étape en utilisant les produits MODIS à 1 km comme entrée du modèle TSEB en conjonction avec trois schémas d'agrégation de complexité croissante (une moyenne simple des entrées à l'échelle de résolution MODIS, une moyenne simple sans tenant en compte l'étendue du footprint du scintillomètre, et une moyenne pondérée des entrées en tenant en compte la fonction du footprint du scintillomètre). Les valeurs de H et LE simulées par la 3ème méthode d'agrégation étaient plus précises que par les deux autres méthodes. Les valeurs des métriques statistiques obtenues sont R = 0,71, RMSE= 63 W/m^2 et MBE= -23 W / m^2 pour H et R = 0,82, RMSE = 88 W/m^2 et MBE = 45 W/m^2 pour LE.

b. Intégration des données in-situ de SM au modèle TSEB :

La deuxième partie de la thèse est dédiée à l'amélioration du modèle TSEB en intégrant les données SM (TSEB-SM) avec une étude de faisabilité utilisant des données in-situ (LST, f_c et SM) ». Pour ce but, un nouveau modèle de calcul de ET appelé TSEB-SM est dérivé du formalisme TSEB en représentant explicitement l'évaporation du sol par une équation basée sur la résistance du sol. Pour contraindre la partition évaporation / transpiration de TSEB-SM,

une approche de calibration innovante est également développée pour inverser les principaux paramètres d'évaporation du sol (résistance du sol, r_{ss}) et de transpiration des plantes (α_{PT}). En pratique, les paramètres de résistance du sol sont extraits à l'échelle saisonnière à partir des données SM et LST avec $f_c \leq f_{c,thres}$ (un seuil empirique permettant la séparation itérative des paramètres sol / végétation dans les estimations de ET), tandis que α_{PT} est récupéré à l'échelle journalière à partir des données SM et LST pour $f_c > f_{c,thres}$. Le modèle TSEB-SM a été testé sur une parcelle de blé irrigué en gravitaire (R3) et 2 parcelles de blé irrigué en goutte-à-goutte (Une parcelle (Référence) qui a été irriguée en fonction des besoins en eau des cultures estimés selon la méthode FAO tous les 3-4 jours, et une autre parcelle (contrôlée) qui a été subie plusieurs périodes de stress lorsque l'irrigation est délibérément coupée, Chichaoua) en utilisant des données in-situ recueillies lors de deux expériences réalisées en 2002-2003 (R3) et en 2016-2017 (Chichaoua). La convergence des trois paramètres (a_{rss}, b_{rss} et α_{PT}) est atteinte en 2 ou 3 itérations. Ce résultat confirme bien la robustesse d'appliquer la calibration selon un seuil de f_c. La paire (a_{rss}, b_{rss}) calibrée est respectivement (5.67, 1.40), (6.51, 3.82) et (9.47, 6.87) pour la parcelle de R3, et les deux de Chichaoua (contrôlée et référence). Les valeurs moyennes récupérées (7.2, 4.0) sont relativement proches de celles estimées par Sellers et al. (1992) (8.2, 4.3). La variabilité de a_{rss}et b_{rss} peut être expliquée par de nombreux facteurs tels que la texture du sol (Merlin et al., 2016) et les conditions météorologiques (Merlin et al., 2011). Néanmoins, les paramètres récupérés sont significativement différents pour les deux sites de Chichaoua (référence et contrôlé), alors qu'ils sont situés à environ 200 m l'un de l'autre et ont une texture du sol et des conditions météorologiques similaires. Cela peut être expliqué par la compensation entre a_{rss} et b_{rss} ce qui révèle la nature empirique de la formulation r_{ss} de Sellers et al. (1992). La valeur moyenne de α_{PT} est respectivement 0,81, 0,88 et 1,24 pour la parcelle R3, contrôlée et référence. Cette valeur est très proche de la valeur théorique α_{PT} pour la parcelle référence. Néanmoins, elle est nettement inférieure à la valeur par défaut pour la parcelle R3 et contrôlée. Cela peut être associé à des conditions de stress pouvant survenir pendant la phase de développement du blé. Une analyse de la variation journalière de α_{PT} indique que les valeurs inversées sur les deux parcelles de Chichaoua sont supérieures à celles inversées sur R3. Cela pourrait s'expliquer par la différence entre les pratiques agricoles de chaque parcelle (date de semis, épisodes d'irrigation, précipitations et fertilisation) ainsi que par les incertitudes concernant l'inversion de α_{PT}. Une fonction de lissage est utilisée pour supprimer toutes les valeurs aberrantes tout en gardant des tendances significatives à l'échelle

journalière. Les α_{PT} lissés varient de 0.03 à 1.22, 0,17 à 1.26 et 0.61 à 1,38 respectivement, pour la parcelle R3, contrôlée et référence. Les α_{PT} lissés sont ensuite normalisées entre une valeur minimale supposée (0) et une valeur maximale lissée. Les α_{PT} calibrés varient alors de 0 à 1.22, de 0 à 1.26 et de 0 à 1.38 respectivement pour la parcelle R3, contrôlée et référence. En conclusion, l'intégration de la résistance du sol dans le modèle TSEB améliore l'estimation de l'évaporation du sol et, par conséquent, améliore la partition de l'ET. La série temporelle récupérée indique que α_{PT} journalier suit la phénologie de la culture de blé d'hiver, avec une valeur maximale correspondant au développement maximal de la biomasse verte et une valeur minimale atteinte au moment de la récolte. Une analyse qualitative des variabilités de α_{PT} en relation avec l'humidité du sol à 5 cm et à une profondeur de 30 cm indique que α_{PT} ne peut pas être considéré comme une constante (Figure V.4, chapitre V). Des écarts importants par rapport à la valeur de 1,26 risquent de se produire pendant la saison agricole, en particulier en période sèche et de déficit en eau. En termes des flux turbulents H et LE, TSEB fournit des résultats satisfaisants pour le site R3, mais pas pour les deux autres sites de Chichaoua. La surestimation de LE par TSEB pendant la sénescence est associée à la valeur maximale fixée pour α_{PT} (égale à 1,26). Cette limitation identifiée dans le formalisme TSEB semble être en partie résolue par l'approche TSEB-SM avec une pente de la régression linéaire est beaucoup plus proche de 1 dans tous les cas. Le RMSE (pour les trois sites) entre l'ET simulée par TSEB-SM et les mesures d'EC est de 67 W/m^2 (erreur relative de 24%), contre 108 W/m^2 (erreur relative de 38%) pour la version originale de TSEB utilisant le paramétrage par défaut (α_{PT} = 1.26).

c. *Intégration des données SM-DisPATCh et des données MODIS (LST, f_c) pour l'estimation de l'ET à une résolution de 1 km :*

Le 3ème axe de la thèse « Combinaison de l'humidité du sol DisPATCh et des données MODIS (LST, f_c) pour cartographier l'ET à une résolution de 1 km » vise à évaluer la performance de TSEB-SM en conditions réelles en utilisant les LST et f_c MODIS à 1 km de résolution et les données SM SMOS désagrégées à 1 km de résolution à l'aide de DisPATCh. L'approche est appliquée sur un champ de blé pluvial dans le bassin du Tensift, pendant une période de quatre ans (2014-2018). La parcelle a été semée pour la saison agricole 2014-2015 (S1), 2016-2017 (S2) et 2017-2018 (S3), alors qu'elle n'était pas labourée pendant la saison de blé 2015-2016 (B1) (sol nu) à cause du retard de la pluie. Malgré la différence d'échelle entre les données MODIS / DisPATCh et les mesures in-situ, les paramètres (a_{rss}, b_{rss}) calculés tout au long de la période d'étude à l'aide des données satellitaires sont relativement proches

de ceux dérivés des mesures in situ. La deuxième étape de calibration consiste à inverser α_{PT} pour $f_c > f_{c,thres}$ à l'aide des données LST et SM. Les maximum α_{PT} journaliers calibrés sont respectivement 1,38, 1,25 et 0,87 pour S1, S2 et S3. Ces valeurs correspondent aux quantités totales de précipitations, qui étaient respectivement de 608, 214 et 421 mm / saison de blé pour S1, S2 et S3. En effet, S1 et S2 ont la même tendance de α_{PT} calibré à l'échelle journalière en comparaison avec le α_{PT} récupéré à l'aide des données in-situ, tandis que α_{PT} reste à une valeur constante (0.7) pendant toute la période d'étude S3 en raison de non disponibilité des produits MODIS pendant les jours nuageux. Comparé aux mesures d'EC, le modèle TSEB basé uniquement sur les données LST et f_c surestime de manière significative les flux de chaleur latente pour les quatre saisons. Les MBE globaux sont d'environ 119, 181, 94 et 128 W / m^2 pour respectivement S1, B1, S2 et S3. La surestimation de LE peut s'expliquer par le fait que PT est fixé à 1,26 pendant toute la saison agricole, même en conditions de stresse. Cela provoque des erreurs plus importantes sur l'estimation du LE, en particulier pendant la phase de croissance. Les erreurs sont réduites lors de l'utilisation de TSEB-SM. En fait, la contrainte sur la transpiration de la plante, lors de l'inversion de la série temporelle de α_{PT}, améliore les estimations de l'ET surtout en stade de croissance et en phase de sénescence, le biais important de LE est considérablement réduit. De plus, la contrainte sur l'évaporation du sol via les SM DisPATCh réduit clairement les valeurs de MBE pendant la période d'émergence ($f_c \leq f_{c,thres}$). Enfin, la contrainte appliquée aux flux de sortie TSEB-SM en utilisant l'énergie disponible dérivée de LST et la fraction évaporative dérivée de TSEB-SM (équation VI.1, chapitre VI) améliore les estimations de LE pour toute la période d'étude. Les MBE sont d'environ 39, 4, 7 et 62 W / m^2 pour respectivement S1, S2, S3 et B1. TSEB présente des erreurs systématiquement importantes sur l'estimation de H (Figure VI.10, chapitre VI), avec des valeurs de RMSE allant jusqu'à 98, 73, 56 et 66 W / m^2 pour respectivement S1, S2, S3 et B1. Le RMSE est amélioré avec l'utilisation de TSEB-SM, avec des valeurs d'environ 55, 41, 24 et 27 W / m^2 pour respectivement S1, S2, S3 et B1.

En perspectives de ce travail, on propose d'estimer l'humidité en zone racinaire à une haute résolution spatiale car elle représente un enjeu important pour le suivi des ressources. Elle permet à la fois de détecter les périodes de stress hydrique et d'anticiper le besoin en eau des cultures. Ceci nécessite une répartition appropriée de l'ET en transpiration et évaporation du sol. Des efforts supplémentaires doivent être déployés pour étudier la variabilité de α_{PT} à des échelles de temps journalières et plus fines et pour relier ses variations à des variables autres que la biomasse et la disponibilité de l'eau du sol.

TABLES

Table II. 1. Input data of DisPATCh chain **39**

Table III. 1. Characteristics of the instruments equipping EC station. **50**

Table IV. 1. Statistical metrics of the comparison between measured and estimated values of available energy and turbulent fluxes (H and LE) at patch and grid scale..... **65**

Table V. 1. Error statistics (RMSE, R^2 and MBE) between modeled and measured sensible and latent heat fluxes for the flood, controlled drip- and reference drip-irrigated fields, and for TSEB and TSEB-SM model, separately (R_n and G are forced to their measured value)..... **87**

Table V. 2. Error statistics (RMSE. R^2 and MBE) between modeled and measured net radiation, conductive flux, and sensible and latent heat fluxes for the flood, controlled drip- and reference drip-irrigated fields, and for TSEB and TSEB-SM model, separately. **88**

Table VI. 1. Validation results of DisPATCh SM and MODIS LST at Sidi Rahal site. **94**

Table VI. 2. Statistical results (RMSE, R^2 and MBE) between modeled and measured sensible and latent heat fluxes for S1, S2, B1 and S3, and for TSEB and TSEB-SM model, separately (R_n and G are forced to their measured value). **104**

Table VI. 3. Same as Table VI.2. but for simulated R_n and G **108**

FIGURES

Figure I. 1. Global world distribution of the water resource under different aspects "Source: www.consoglobe.com." **2**

Figure I. 2. Global water map. Source: World Resouces Institute **4**

Figure I. 3. Multi-sensor / multi-resolution remote sensing data for crop monitoring and agro-hydrological applications (from Malbéteau, (2016)) **7**

Figure II. 1. Schematic diagram of TSEB model **29**

Figure II. 2. Schematic diagram of TSEB-SM model **32**

Figure II. 3. Schematic diagram of the two-step calibration strategy of TSEB-SM model. **35**

Figure II. 4. Footprint of the LAS, calculated using the footprint model of Horst and Weil, superposed with a LST/MODIS image on DOY 273. ..... **37**

Figure III. 1. Geographical situation of the Tensift watershed, its hydrographic network as well as the limit of the Haouz plain. **42**

Figure III. 2. Location of the four study sites: (a) flood-irrigated wheat crop in the R3 zone (east of Marrakech), (b) rainfed wheat crop in Bour site (east of Marrakech) and (c) two (controlled and reference) drip-irrigated wheat crops near Chichaoua city (west of Marrakech) in the Tensift basin, central Morocco. (Flat area). **44**

Figure III. 3. Example of the digital processing procedure for photos taken in rainfed wheat field **46**

Figure III. 4. Photograph of (a) TDR (Time Domain Reflectometry) and (b) Theta Probe instruments **48**

Figure III. 5. (a) Map of the Wankama basin; (b) location of the three study sites (millet, fallow and (c) basin toposequence **49**

Figure III. 6. (a) An overview of theWankama basin and the experimental setup, locations of LAS (T and R stand for transmitter and receiver, respectively) and three EC systems are shown (millet, fallow and degraded shrubs sites). Photos (EC system (b) and scintillometer (c)) were taken by J. Ezzahar as part of the ACN project. **51**

Figure IV. 1. Time series of LAS latent and sensible heat fluxes (daily average between 9am and 5pm) **59**

Figure IV. 2. Scatterplot of MODIS Ts (a), and α (b) versus in-situ data (only Millet and Fallow sites are considered) **60**

Figure IV. 3. Scatterplot of MODIS versus MSG SEVIRI LST **61**

Figure IV. 4. Scatterplot of simulated versus observed AE,H and LE for the (left) Millet, (middle) Fallow and (right) Degraded shrubs, respectively, using in-situ data. **64**

Figure IV. 5. Scatterplot of simulated versus observed AE,H and LE for the (left) Millet, (middle) Fallow and (right) Degraded shrubs, respectively, using MODIS data. **67**

Figure IV. 6. Sensible (a) and latent (b) heat fluxes scatterplots between LAS measurements and TSEB prediction feeded by aggregated in-situ data (at 30min time). **68**

Figure IV. 7. Sensible and latent heat fluxes scatterplots of the comparison between the LAS grid scale measurements and TSEB predictions based on MSG SEVIRI products (at MSG-SEVIRI overpass time)..... **69**

Figure IV. 8. Sensible and latent heat fluxes scatterplots of the comparison between the LAS grid scale measurements and TSEB predictions based on MODIS products for a simple averaging (a,d), area weighted method (b,e) and footprint weighted method (c,f) (at MODIS overpass time). **70**

Figure IV. 9. Time series of the comparison between the LAS grid scale measurements ($\mathbf{H_{LAS}}$and $\mathbf{LE_{LAS}}$) and TSEB predictions based on MODIS products (H_{sim} and LE_{sim}) for footprint weighted method (at MODIS overpass time)..... **72**

Figure V. 1. Iterative values of a_{rss},(a), b_{rss} (b) and mean value of retrieved α_{PT} (c) for the flood-, controlled drip- and reference drip-irrigated wheat fields separately (calibration step 1)..... **78**

Figure V. 2. Time series of daily retrieved and smoothed α_{PT} for the (a) flood-, (b) controlled drip- and (c) reference drip-irrigated wheat fields, separately (calibration step 2). **80**

Figure V. 3. Time series of calibrated daily α_{PT}, superimposed with fc for the (a) flood-, (b) controlled drip- and (c) reference drip-irrigated wheat fields, separately. The red segments represent irrigations during the season. **82**

Figure V. 4. Time series of $\alpha_{PT,cal,daily}$ superimposed with 5-cm/30-cm soil moisture (SM) and vegetation water content (VWC) for: (a) flood-, (b) controlled drip- and (c) reference drip-irrigated fields, respectively. For the flood-irrigated wheat, VWC is unavailable..... **84**

Figure V. 5. Scatterplot of simulated versus observed LE for the (top) food-, (middle) controlled drip- and (bottom) reference drip-irrigated fields and for (left) TSEB-SM and (right) TSEB models, respectively. **86**

Figure V. 6. Scatterplot of simulated versus observed H for the (top) food-, (middle) controlled drip- and (bottom) reference drip-irrigated fields and for (right) TSEB and (left) TSEB-SM model, respectively..... **87**

Figure VI. 1. Scatter plots of MODIS versus in-situ LST at Sidi Rahal site for S1 (2014-2015), B1 (2015-2016), S2 (2016-2017) and S3 (2017-2018) agricultural seasons, separately, (red dashed line is the line(1:1)-black line is the regression line)..... **93**

Figure VI. 2. Scatter plots of the 1 km resolution DisPATCh versus in-situ SM at Sidi Rahal site for S1 (2014-2015), B1 (2015-2016), S2 (2016-2017) and S3 (2017-2018) agricultural seasons, separately. **96**

Figure VI. 3. NDVI image derived from Landsat data acquired on 17/04/2018. The experimental field and the overlaying 1 km resolution MODIS pixel are superimposed..... **96**

Figure VI. 4. log($\mathbf{r_{ss}}$) versus SM/ SM_{sat}(calibration step 1) using in-situ (a) and satellite (b) data. **98**

Figure VI. 5. Time series of daily retrieved and smoothed α_{PT} (calibration step 2-using in-situ data, and satellite data) collected during S1, S2 and S3. **100**

Figure VI. 6. Time series of calibrated daily α_{PT} (red-using in-situ data, green- using satellite data) superimposed with NDVI and the rainfall events during S1, S2 and S3, separately. **101**

Figure VI. 7. Scatterplot of simulated versus observed LE for (top) TSEB and (bottom) TSEB-SM models using in-situ data collected during S1, B1, S2 and S3, respectively. **103**

Figure VI. 8. Same as Fig VI.7 but for H fluxes. **104**

Figure VI. 9. Same as Fig VI.7 but for satellite data. **106**

Figure VI. 10. Same as Fig VI.8 but for H fluxes and satellite data. **107**

Chapter.I. Introduction and state of art

Chapter.I. Introduction and state of art 1
I.1. General context 2
I.2. In-situ measurements of Evapotranspiration 8
I.3. Modeling approaches of Evapotranspiration 10
I.3.1. Empirical models 11
I.3.2. Mechanistic models 11
I.3.3. Surface Energy Balance (SEB) models 13
I.4. Remote sensing of Evapotranspiration 16
I.4.1. Models based on vegetation index 16
I.4.2. Models based on Land Surface Temperature 17
I.4.3. Models based on Surface soil moisture 18
I.5. Objectives 21

I.1. General context

Water makes up about 71% of the Earth's surface, 97% of all the Earth's water is contained within the oceans as salt water, while the remaining 3% is freshwater (Figure I.1). Glaciers and ice caps cover about 70% of the world's freshwater. Unfortunately, most of these resources are located far from human habitation and are not readily accessible for human use. According to the United States Geological Survey (USGS), Groundwater is by far the most abundant and readily available source of freshwater, followed by lakes, reservoirs, rivers and wetlands. The groundwater represents over 90% of the world's readily available freshwater resource (Boswinkel, 2000). About 1.5 billion people depend upon groundwater for their drinking water supply (WRI, UNEP, UNDP, World Bank, 1998).

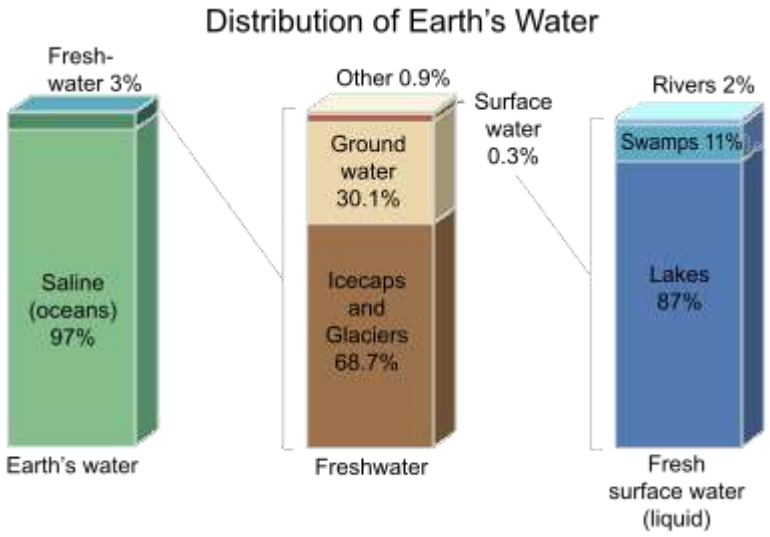

Figure I. 1. *Global world distribution of the water resource under different aspects "Source: www.consoglobe.com."*

According to the United Nations Environmental Program (UNEP, 2012), the human survival depends on clean water. "The achievement of all the Millennium Development Goals... hinges on the quality and quantity of available water as water plays a disproportionately powerful role through its impact on, among other things, food production and security, hygiene, sanitation and health and maintenance of ecosystem services."The water issue becomes a major concern for the majority of countries; especially because it covers a real complexity related to geopolitical, security, ecological, social and economical issues. As a result, the pressure on water resources is growing under the combined effects of anthropogenic pressure (population growth, urban development and the increase of water consumingby agriculture,

industry and tourism) and climate changes (temperature increases, precipitation decreases especially in southern mediterranean, increase of drought frequency …).

In most regions of the world, over 70 percent of freshwater is used for agriculture (FAO, 2011). By 2050, the global water demand of agriculture is estimated to increase by a further 19% due to irrigational needs. Countries in the southern Mediterranean have only 1% of the world's freshwater resources and gather more than half of the water-poor population (namely an average less than 1000 m^3 per year per capita). This area is characterized by a strong spatio-temporal variability in precipitation associated with a marked seasonality of evaporative demand, resulting in a period of high water deficit in summer (Bolle, 2003). In this region, crop irrigation consumes up to 80-90% of the mobilized water (FAO, 2015), which makes the relationship between water availability and agricultural production for a continuously growing population more critical (Vorosmarty et al., 2000). Mediterranean countries are already facing major problems of water stress, desertification, loss of biodiversity and extreme weather events such as floods and droughts. In particular, the Mediterranean area has been identified as a hot spot of climate change (Giorgi, 2006). According to the International Panel on Climate Change (IPCC, 2014) a rise of temperatures of 2 to 3° C is expected in the Mediterranean region by 2050, and 3 to 5 ° C by 2100. The increase of the length of dry spell (days) is expected (Schleussner et al., 2016) and the decrease in precipitation, especially in summer and with important regional differences (IPCC, 2013). The general increase in water scarcity as a consequence of climate change is enhanced by the increasing demand for irrigated agriculture to stabilize production and to maintain food security (Schwabe et al., 2013). The irrigation demands in the region are projected to increase between 4 and 18% by the end of the century (Cramer et al., 2018).

Morocco is one of the 45 countries, in the world, most affected by water shortage, according to World Resources Institute water scarcity map (Figure I.2), which reveals Morocco's critical situation (Plan Bleu, 2009). A difficult situation for the population and, among others, agriculture. The latter is by far the largest water user of all human activities; accounting for 85% of the country's mobilized water resources (Jarlan et al., 2015). Agriculture contributes to the national economy in the range 14-20 % of GNP depending on the rainfall of the year (Balaghi et al., 2012). According to the World Resources Institute report, Morocco will reach an extremely high level of water stress by 2040. Indeed, Morocco is expected to enter a situation of extreme water stress in less than 25 years (Word Bank, 2017). A shortage that

could be mainly explained by the fast expansion the irrigated areas and the intensification of water consumption by the touristic and domestic sectors.

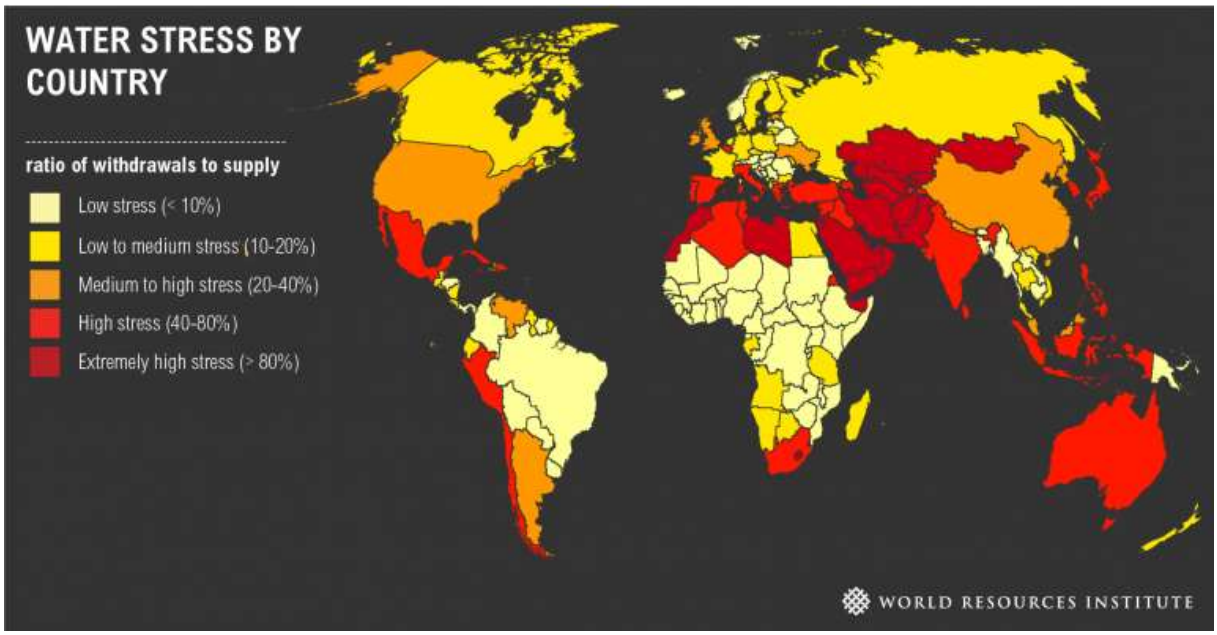

Figure I. 2. *Global water map. Source: World Resouces Institute*

Aware of the situation severity, significant efforts have been made since 1961 in term of water resources mobilization. Currently, Morocco has 135 dams with an overall storage capacity of about 17.5 billion m^3. To reinforce this infrastructure, Moroccan government plans to build about 59 large dams by 2030 (Loudyi et al., 2018). Several departments and agencies are also involved in the management of water resources, including: Basin Hydraulic Agencies (development and management of water resources between different uses ...), Regional Offices for Agricultural Development (development of irrigated perimeters, agricultural development, management of irrigation networks, and management of water resources for agriculture), ONEE-Water (production and management of drinking water). At the beginning of the 21st century, the Moroccan government launched the Green Moroccan program, to promote the economy and the development of water resources in agriculture, including:

• The National Irrigation Water Economics Program (PNEEI) with the objective of converting 550 000 ha to localized irrigation (2008-2020), increasing productivity and water valuation, and sustainable management of water resources;

• The Irrigation Extension Program (PEI), aimed at making public investment in water resource mobilization (dams), creating nearly 60 000 permanent jobs, increasing farmers' incomes.

Monitoring water resources is therefore strongly linked to the modeling of hydrological fluxes, such as soil infiltration, runoff and evapotranspiration. Evapotranspiration (ET) is a crucial component of the water cycle, especially in semi-arid areas where it strongly impacts the water resource management, drought monitoring, and climate (Littell et al., 2016; Molden et al., 2010). At the watershed scale, water losses by ET are generally the most important part of the water balance, and can be responsible for the dissipation of 60% of the rainfall contribution (Oudin, 2004). Furthermore, a precise estimate of ET determines the crop water requirements, which subsequently allow for optimizing water management practices and irrigation regimes (Allen et al., 1998). A large variety of ET models and measurements have been reported in the literature (Allen et al., 2011; Olivera-Guerra et al., 2014; Subedi and Chávez, 2015). However, ET estimation over extended areas including different biomes and climates is still subject to significant uncertainties (Ershadi et al., 2014; Pereira, 2004). Although the main drivers of ET, such as atmospheric evaporative demand, vegetation type, development stages and health, surface biophysical characteristics and soil water availability (Federer et al., 2003), are now well identified. One major difficulty in modeling this process lies in a lack of relevant inputs data available at the desired space and time scales (Allen et al., 2011; Pereira et al., 2015). The accuracy of ET estimates at a given scale thus currently represents a trade-off between model complexity and realism, which is usually related to: i) the number of model parameters and forcing variables and ii) the data availability that generally decreases with the spatial extent (Allen et al., 2011; Gharsallah et al., 2013). Regarding data availability, satellite observations are able to provide integrated measurements at different temporal and spatial scales and in different spectral bands. Multi-spectral remote sensing provides powerful tools for observing continental surfaces and hydrologic components such as soil moisture using SMOS satellites (Soil Moisture and Ocean Salinity, Kerr et al (2001)) and SMAP (Soil Active Passive Moisture Entekhabi et al (2010)). Surface temperature from the thermal infrared also provides information on the state of the surfaces and on the temporal variations of the hydrological fluxes (Anderson, 1997) at the surface-atmosphere interface through the energy balance and water balance (Anderson et al., 2008; Brunsell et al., 2011; Kustas and Anderson, 2009). Meteorological satellites, either geostationary (Geostationary Operational Environmental Satellites (GOES), Meteosat

satellites) or polar (Global Precipitation Measurement (GPM), Tropical Rainfall Measuring Mission (TRMM)) can detect precipitation and estimate their intensity (Hou et al., 2014; Huffman et al., 2007). In addition, a number of space programs aim to create a multi-spectral synergy. A recent example of this motivation is the Sentinel satellite constellation. Visible and near infrared (VIS-NIR, Sentinel 2), thermal infrared (TIR, Sentinel 3) and C-band microwave (Sentinel 1) data are available with unprecedented spatio-temporal resolution. These strategies are based on the development of a system of complementary observations in order to better characterize the continental surfaces. However, there are several limitations in the efficient use of remote sensing observations for agricultural and hydrological applications. Especially, the spatial representativeness of the measurement, which plays a major role in the accuracy of this measurement. Yu et al. (2017) validated MODIS LSTs using station observations from the River Basin in China. For all the observations, the bias of the MODIS LST range from -0.27 K to 2.39 K and the RMSE range from 3.32 K to 4.93 K. Serbin et al. (2013) found the MODIS LAI displayed larger seasonal variation compared to field measurement, with an RMSE of about 0.63 m^2/m^2 for a boreal forest landscape in northern Manitoba, Canada. Fensholt et al. (2004) reported that MODIS LAI is overestimated by approximately 2–15%. However, several factors plays crucial role in increasing or decreasing the errors between observations and MODIS products including the type of land cover, land topography, the reliability of the atmospheric correction method and the coarse resolution of the thermal band (1 km).

Spatial and temporal resolutions are of paramount importance to realistically integrate spatial observations into hydrological models, or even to model hydrological processes from satellite observations. The spatial resolution depends mainly on the sensitivity of the sensor to receive energy emitted by the surface. This sensitivity is strongly dependent on the wavelength domain and plays an important role since it determines the size of the region observed and the size of the objects that will be possible to characterize. For example, the radiometers have a coarse-scale resolution (about 40 km for SMOS and 50 km for AMSR-E) which is too wide to be directly integrated into agro-hydrological models, in contrary to measurements from the radar which have a finer resolution (about 10 m for Sentinel 1). The temporal resolution is the time required for the satellite to make a complete orbital cycle, ie to observe exactly the same scene again from the same point in space, it is related to the spatial resolution for a given wavelength domain because it depends on the orbit of the satellite. For example, in the thermal infrared, Landsat data have a spatial resolution of 100 m but a temporal resolution of

16 days whereas the MODIS data have a spatial resolution of 1 km but with a frequency of 1-2 days. Generally, spatial and temporal resolution must be chosen according to the objects observed and / or modelled (Figure I.3).

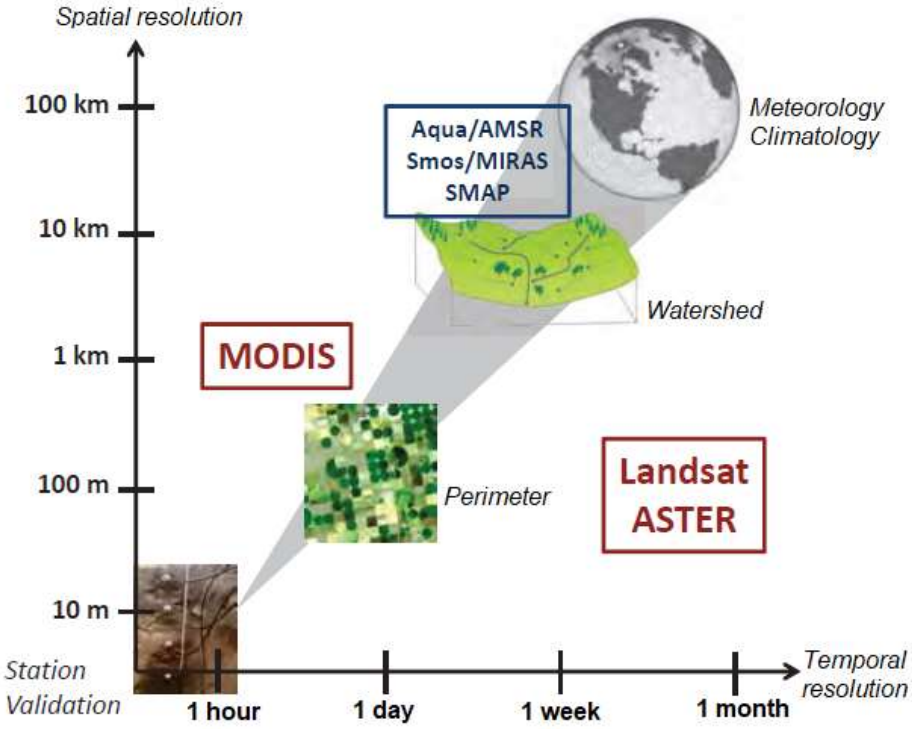

Figure I. 3. *Multi-sensor / multi-resolution remote sensing data for crop monitoring and agro-hydrological applications (from Malbéteau, (2016))*

Overall, remote sensing observations provide very relevant information to feed ET models such as vegetation indices (Normalized Difference Vegetation Index NDVI and vegetation fraction cover f_c, VIS-NIR), land surface temperature (LST, TIR) and near-surface soil moisture (SM, microwave). More specifically, SM is one of the main controlling factors of soil evaporation (Chanzy and Bruckler, 1993), vegetation cover fraction (f_c) provides an essential structural constraint on evaporation/ transpiration partitioning (Allen et al., 2000) and LST is a signature of available energy and ET (Norman et al., 1995). For this reason, efforts have been made to integrate those data as additional and complementary information on ET (Price, 1990).

Many measurement devices are used to develop, calibrate and test important ET process models. A bibliographic review of the main methods of ET measurement at the plot scale is describedin the following sub-section.

I.2. In-situ measurements of Evapotranspiration

a. Eddy covariance method

The Eddy correlation (EC) method is considered as a reference technic for several reasons (Allen et al., 2011): it allows a direct measurement of the latent and sensible heat flux densities within atmospheric boundary layers at field scale. It introduces no artefact on the system it is measuring, it is quasi-continuous and represents a relatively large upwind extent.Early examples of eddy instrumentation were described by Tanner. (1988) and Tanner et al. (1993). Since then, many advances in instrumentation have been made and this method is now widely used as described by Wilson et al. (2002), Baldocchi. (2003).

The EC method is based on the turbulent transport theory in the surface layer of the atmosphere. Indeed, the average vertical flux density ($\overline{F_x}$) of a magnitude X (e.g. temperature, water vapor or carbon dioxide) is proportional to the covariance of fluctuations between the vertical wind velocity and the concentration of that magnitude, at a specific point above the area of interest.

Turbulent fluxes (momentum, sensible heat, latent heat and gaseous concentration) can be expressed as the product of the fluctuations term of the vertical velocity and the fluctuations term of the magnitude considered. In particular, the sensible heat flux density H, is given by:

$$H \approx \rho c_p \overline{w'T'} \ (W.m^{-2}) \qquad (I.1)$$

The vertical flux density of water vapor called latent heat or evapotranspiration is defined by:

$$LE \approx \rho \overline{w'q'} (W.m^{-2}) \qquad (I.2)$$

In general, the eddy correlation method requires personnel who are well-trained in electronics, turbulent theory, and biophysics. Instrumentation is relatively fragile and expensive.The footprint of the EC system, depends on wind speed, but doesn't exceed 100 m (Ezzahar et al., 2007). It uses complex calculations, and utilizes many assumptions. It has proposing perspectives for the future use in various natural sciences (Allen et al., 2011).

b. Lysimetry method

The lysimeter is a device, generally a tank or container, to define the water movement across a soil boundary (Howell et al., 1991; Prueger et al., 1997; Young et al., 1997), and to quantify

actual evaporation from a bare soil or actual ET from a soil covered by vegetation (Kashyap and Panda, 2001; Parlange and Katul, 1992).

Lysimeters of varying designs, sizes, shapes, and measurement systems have been built over the years (Allen et al., 2011; Howell et al., 1991). Thechnically, there are two main types of lysimeters: the drainage and the weighing types. In the first case, potential evaporation is obtained as the difference between added and drained water quantity. In the second case, changes in the total weight of the soil sample are measured, whereby the real ET during a short time period (10 min) can be estimated. Indeed, the actual ET measurements from weighing lysimeters have become one of the most accurate methodologies to study the return of water to the atmosphere by the combined processes of evaporation and transpiration (Malone et al., 2000), and are the standard method to directly measure the actual evapotranspiration (ET_a) (Payero and Irmak, 2008; Reicosky et al., 1983).
In connection with the additional measurement of deep percolation (DP) and precipitation (P), the actual ET_acan easily be derived using the surface water balance:

$$ET_a = P - DP \pm \Delta W \quad \text{(I.3)}$$

Where ΔW is the change of soil water storage measured by the lysimeter.

c. The Energy Balance Bowen Ratio (EBBR) method

The Energy Balance Bowen Ratio (EBBR) method is a relatively simple technique based on net radiation, soil heat flux, and the air temperature and vapour pressure gradients measurements (Allen et al., 2011). It is an indirect method, compared to the previous methods such as EC, which directly measures turbulent fluxes, or weighing lysimeters, which measures the mass change of an isolated volume of surface soil-vegetation. EBBR produces the 30 min estimates of the vertical fluxes of sensible and latent heat fluxes at the local surface. Many studies have investigated the use of the BR method to estimate the sensible and latent heat fluxes (Aston, 1985; Black and McNaughton, 1971; Euser et al., 2014; Jara et al., 1998; Peacock and Hess, 2004). The Bowen ratio can be determined as the ratio of the gradients of temperature and vapor pressure across two fixed heights above the surface (Bowen, 1926) or as the ratio of the sensible and latent heat flux:

$$\beta = \frac{H}{LE} = \frac{\Delta T}{\Delta e} \quad \text{(I.4)}$$

The Bowen ratio is combined with the energy balance to yield the following expressions for H and LE:

$$LE = \frac{R_n - G}{1+\beta} \quad (I.5)$$

$$H = \frac{\beta}{1+\beta}(R_n - G) \quad (I.6)$$

d. Scintillometry

A scintillometer is an optical instrument that consists of a light/radiation source (transmitter) and receiver; it is used to measure small fluctuations of the refractive index of air caused by variations in temperature, humidity, and pressure. The transmitter emits electromagnetic radiation over a separation distance (or path length), which, depends on aperture size, effective height above the surface, and atmospheric stability. The receiver detects and evaluates the intensity fluctuations of the transmitted signal, called scintillation. Scintillometer provides continuous measurements of sensible heat fluxes over path lengths from 100 m up to few kilometres. Several investigations have demonstrated the potential of using scintillometer to measure reliable averaged sensible heat fluxes over path lengths which are similar to satellite pixel scale (Artogensis, 1997; De Bruin et al., 1995; Ezzahar et al., 2007; Kohsiek, 1985; Lagouarde et al., 1996). The scintillometer method is based on the measure of the structure parameter of refractive index (C_n^2), which characterises the turbulence intensity within the atmosphere (Ezzahar et al., 2007; Ochs and Wilson, 1993). By using the Monin-Obukhov Similarity Theory (MOST) and complementary parameters (meteorological conditions and site features such as vegetation height), C_n^2 can be directly related to sensible heat flux. For more details on this method, the readeris invited to refer to Ezzahar et al. (2007).

I.3. Modeling approaches of Evapotranspiration

In-situ measurements are able to give only localized estimates of ET over relatively homogeneous areas. In addition, they cannot be extended at large scales due to the heterogeneity of the landscape and the complexity of hydrologic processes. In fact, the factors that conditioning the soil-vegetation-atmosphere exchanges (land surface temperature, wind, soil characteristics, type of crop..) are highly variable in space and time and are specific for each field. Therefore, none of the approaches mentioned before can adequately account for these variabilities. The spatial modelling has become a dominant means to estimate ET fluxes

over regional and continental areas (Anderson et al., 2007; Fisher et al., 2017). Different methods have been developed to use remote sensing data in surface flux estimation schemes. It is always difficult to classify these methods, since their complexity depends on the balance between the empirical and physically based modules used.

An overview of existing ET modeling approaches is discussed below.

I.3.1. Empirical models

The empirical models are the most used approaches for spatializing ET through remote sensing. In this context, the empirical relationship between land surface temperature and air temperature observationswas used. This simplified method for estimating ET was firstly derived by Jackson et al. (1977) at two different times of day at field scale and later modified by Seguin and Itier, (1983) for mapping daily ET over large scales from LST measurements (Courault et al., 2005; Lagouarde and Brunet, 1991). This approach assumes that the daily ET is related to the instantaneous $(LST - T_a)$ measurements obtained around mid-day:

$$ET_d = R_{n_d} - B(LST - T_a)^n \quad (I.7)$$

Where B and n are the regression adjusted constants which depend respectively on surface roughness and atmospheric stability. LST can be obtained by observed in-situ or by thermal infrared remote sensing images.

This method assumes that the ratio H/R_n is constant during the day, and that the daily variation of the heat flux in the soil is negligible (G = 0).

The main advantage of this empirical regression method is its simplicity and relatively high accuracy (1 mm / day) when calibrated in-situ dataset. However, the adjusted constants are site-specific (climate, vegetation, soil…), which may limit the application of this approach to other sites and heterogeneous surfaces (Carlson et al., 1995).

I.3.2. Mechanistic models

Estimation of ET can be based on more detailed and complex models such as Soil-Vegetation-Atmosphere transfer models (SVAT), which include a coupled energy balance and water balance model. Many SVAT models have been developed in the last 20 years for meteorological needs which explains their more detailed description of physical processes. This approach gives access to simulate continuously the temporal evolution of surface states

(LST, soil moisture, etc…) (Deardorff, 1978; Dickinson et al., 1986; Sellers et al., 1996), variables required in the partition of the surface into soil and vegetation energy balance. In addition, most of the transfer mechanisms at ground and/or vegetation coverlevelandsome physiological processesare based on the scale of the energy balance and the parameterization of different processesindependently of remote sensing data:

- Radiative transfers are modeled in general following a simple Beer-Lambert law of by using radiative transfer schemes within the plant cover (Olioso, 1992).
- Turbulent transfersaregenerally based on the resistive schemes (Choudhury, 1989; Deardorff, 1978).
- Heat and water transfers in the soil; in most models, a system with two soil reservoirs is used, one representing the root zone and the other one representing the first centimeters of the soil which are directly concerned by soil evaporation (Carlson et al., 1990; Deardorff, 1978).
- Water transfers from the soil to the atmosphere, through the plants, based on an adequate description of stomatal regulation and water extraction by the roots (Braud et al., 1995; Taconet et al., 1986).

- Photosynthesis in relation with water transfers, through stomatal regulation or water status of leaves (Zur and Jones, 1981).

SVAT models are typically complex and highly parameterized, which can make their spatialization tricky when surfaces are poorly characterized. On the other hand, this approach is not dependent on remote sensing data, and relies solely on knowledge of radiative forcing, weather forcing, crop canopy architecture and physiology, and water supplies (rainfall and irrigation). The LST is not used as a forcing data, but is simulated by the model, as the resultant of energy balance, and can therefore possibly be corrected by assimilation methods (Castelli et al., 1999; Coudert and Ottlé, 2007; Crow, 2003; Hain et al., 2011; Olioso et al., 1999).

Among SVAT models, it may be mentioned Suivi de l'Etat Hydrique des Surfaces (SEtHyS) (Coudert et al., 2006), Soil Biosphere-Atmosphere Interaction (ISBA) (Noilhan and Mahfouf, 1996) and Interactive CAnopy Radiation Exchange (ICARE) (Gentine et al., 2007), Simple Biosphere Model (SiB) (Sellers et al., 1996) and Simple Soil-Plant-Atmosphere Transfer (SiSPAT) (Braud et al., 1995).

SVAT models provide access to detailed plant cover and soil functioning, and not just to a limited number of variables such as ET, as it is the case for empirical or residual approaches.

However, a major disadvantage of these models is that they require the adjustment of many parameters related to the properties of the observed surfaces (soil textures, type of cover observed). They also rely on atmospheric (e.g. precipitation) and anthropogenic (e.g. irrigation) forcing. If such calibrations are possible at the plot scale, where the soils and varieties grown are known and can be considered homogeneous, they become particularly difficult to perform overareas with a certain spatial extent.

I.3.3. Surface Energy Balance (SEB) models

Surface Energy Balance (SEB) models are designed to be forced by the LST and focus on solving the SEB instantaneously. SEB can be represented, at any scale (Brutsaert, 1982; Mcnaughton and Spriggs, 1989) by:

$$H + LE = R_n - G \quad (I.8)$$

where H is the sensible heat flux, LE is the latent heat flux, R_n is the net radiation absorbed by the earth's surface, and G is the heat flux into the soil. All components are usually in units W/m^2. Additional energy flux components that could also be included are photosynthesis (Stewart and Gay, 1989) and vegetation canopy storage (Shuttleworth and Wallace, 1985), but for short-term measurements, or for non-forested regions, these terms are negligible (Brutsaert, 1982; Stewart and Thom, 1973). The difference $R_n - G$ is the surface available energy, generally consumed by H and LE. G is classically expressed as a fraction of net radiation, (as an exemple, $0.05*R_n$ for fully developed plant cover, and $0.5*R_n$ for bare soil) (Kustas and Norman, 1996) or as a variable fraction depending on different parameters such as canopy fraction and soil characteristics (Bastiaanssen et al., 1998; Kustas et al., 1993; Su, 2002).

The methods of resolution of SEB thus differ mainly on the partition of the available energy between the turbulent fluxes. In the review of ET estimation methods, several authors classified two categories of approach to describe the surface and its resistance network (Kalma et al., 2008; Overgaard et al., 2006):

- The "single-pixel" methods for which the fluxes are calculated independently for each pixel. Among these models, we can distinguish three models (i) Methods considering the surface as a homogeneous mixture of soil and vegetation without distinction between soil evaporation and transpiration of vegetation (Monteith, 1965; Penman, 1948): (ii) Models taking into account vegetation and bare soil as two separate sources

for energy transfers (Shuttleworth and Wallace, 1985); (iii) multi-source models, which are essentially extensions of the dual-source model.

- Contextual models based on the contrasts between hot and cold pixelswithin a given image, these models link surface temperature and other satellite data (reflectance, vegetation indices) to evapotranspiration by semi-empirical laws.

a. Single-source models

Single source models treat the land surface as one homogeneous surface, so that they cannot distinguish between soil evaporation and planttranspiration. Their simplicity and yet physically sound basis has made the mono-source models widely used. Although, single-source energy balance models may provide reliable estimates of turbulent heat fluxes. They often need field calibration and hence may be unable to be applied over a diverse range of surface conditions. Kustas et al. (1990) have shown that single source model is not suitable for ET estimation over partially vegetated surfaces. Single-source energy balance models include Surface Energy Balance Algorithm for Land (SEBAL; Bastiaanssen et al., 1998), Simplified Surface Energy Balance Index (S-SEBI; Roerink et al., 2000), Surface Energy Balance System (SEBS; Su, 2002), Mapping ET at High Resolution with Internalized Calibration (METRIC; Allen et al., 2007), and Operational Simplified Surface Energy Balance (SSEBop; Senay et al., 2013, 2001).

b. Double-source models

Over homogeneous areas, single source models can evaluate ET with relatively high accuracy. However, there is a strong need to develop a dual-source modeling to separate the heat and water exchange and interaction between soil and atmosphere and between vegetation and atmosphere, over partially vegetated areas. Considering contributions of energy fluxes from soil and vegetation components, dual source models have been proposed to more precisely depict water and heat transfers from sparse or heterogeneous canopies. Among the dual-source approaches, two typical configurations can be distinguished (Boulet, 1991; Lhomme and Chehbouni, 1999). One is the ‘layer’ (or coupled) approach in which each source of water and heat fluxes is superimposed and coupled. It has a more complicated model structure and performs better over homogeneous vegetated surfaces. The layer approach cannot distinguish the difference between evaporation from the soil under and between vegetation canopies, which may lead to significant errors when applied to surfaces with large heterogeneity in soil wetness. The other one is the patch (uncoupled) approach,

which represents the soil and the canopy as two springs side by side, where water and heat fluxes from each source interact independently with the above atmosphere. This latter approach may be more appropriate for more clumped vegetation, when vegetation is agglomerated and surrounded by large areas of bare soil (Blyth and Harding, 1995; William P. Kustas and Norman, 1997; Norman et al., 1995). It assumes that each component receives full radiation loading but neglects evaporation from under-canopy soil surfaces. Several models have been developed based on this approach, including the Two Source Energy Balance Model "TSEB" (Norman et al., 1995), Mapping Evapotranspiration with Internalized Calibration "METRIC" (Allen et al., 2007), and the Two-source Trapezoid Model for Evapotranspiration "TTME" (Long and Singh, 2012).

c. Multi-source models

For surfaces with multiple types of vegetation, neither the single nor the dual source model can capture energy fluxes from the surface due to the different canopy resistances and structures among different vegetation types. The energy transfers within these areas are often represented by multi-source models. The first models of this kind were designed for sparse canopies to take into accountseparately the vegetation and soil contributions (Shuttleworth and Wallace, 1985; Shuttleworth and Gurney, 1990). Afterward, more complex representations were proposed to take into account the heterogeneous canopies with diverse components (main vegetation, herbaceous substrate, bare soil) (Dolman, 1993; Huntingford et al., 1995). The multi-source models are generally represented by resistance networks, which combine surface and air resistances within the canopy. If vegetation or bare soil surfaces are large enough to allow different aerodynamic resistances to be defined for each patch, a patch (uncoupled) representation should be chosen. In the opposite case, if the different sources are close to each other and do not allow the definition of separate aerodynamic resistances, a layer approach should be preferred. To estimate ET, based on the layer model, Dolman. (1993) distinguished the vegetation layer into upper-canopy and understory layers and estimated energy fluxes from each layer respectively. In addition, (Williams and Flanagan, 1996) separated the vegetation canopy into different horizontal, and the total flux from the entire canopy was calculated as the sum through the layers. More specifically, this model should also be considered as a multiple-source model, as vegetation layers at different heights receive different radiation laoding and have different canopy resistances.

d. Contextual models

Unlike the models described above, where the energy balance equation is explicitly solved for each pixel independently of the others, other approaches are based on the use of the spatial variability captured by satellite imagery (reflectance, vegetation indices) to derive the ET at the local and regional scales (Gowda et al., 2008). These methods, known as contextual methods, are based on the simultaneous presence of hot and cold pixels due to the existence of wet and dry pixels on the same satellite image (Chirouze et al., 2014). Roughly, the intermediate water status of a given temperature pixel is scaled between the hottest points considered the driest and the coldest points considered the wettest. The physical borderlines of LST corresponding to fully dry and fully wet conditions for both soil and vegetation are determined in the space defined by LST and NDVI (Jiang and Islam, 2001, 1999) and/or the space defined by LST and albedo (Merlin et al., 2013; Roerink et al., 2000). There are various models based on this method, such as SEBI (Surface Energy Balance Index, Menenti et al., 1989), S-SEBI (Simpli_ed Surface Energy Balance Index, Roerink et al., 2000), SEB-1S (Monosource Surface Energy Balance model, Merlin et al., 2013). More details about the contextual approach can be found in Kalma et al. (2008) and Li et al. (2009), who offer a summary of various existing contextual models.

I.4. Remote sensing of Evapotranspiration

Regarding the data availability over extended areas, remote sensing is the only viable technique that can provide very relevant information to feed ET models. It has shown a great potential for characterizing land surfaces (land use, vegetation coverage, soil moisture, water stress, etc.). Amongst the variety of remotely sensed variables, there are three in particular that are pertinent to the estimation of ET: vegetation cover index, land surface temperature and surface soil moisture. The approaches based on each variable are described below.

I.4.1. Models based on vegetation index

Vegetation indices (VI) have been available since the launch of the first satellites used for vegetation monitoring in the early 1970s (Bannari et al., 1995; Bausch and Neale, 1990; Huete et al., 2011; Rouse et al., 1974). Nevertheless, the Normalized Difference Vegetation Index (NDVI) is the most common VI (Tucker, 1979). NDVI computed from red and near infrared bands of the satellite can be considered as a useful indicator to study vegetation characteristics and consequently ET rates (Nouri et al., 2012). Over the last two decades, several authors have confirmed the linear relationship between remote sensed vegetation indices and the vegetation photosynthesis by vegetation canopy (Glenn et al., 2008), between

ET and NDVI (Rossato et al., 2005) and between NDVI and basal crop coefficient for irrigated agricultural fields (Duchemin et al., 2006). Unlike complex and physically based models, FAO-56 is one of the simplest ET estimation approaches based on correlation of crop ET and NDVI (Allen et al., 2000; Er-Raki et al., 2010, 2007; Hunsaker et al., 2003). It requires fewer input data, and provides acceptable ET estimates (Allen et al., 2000; Er-Raki et al., 2007; Rafi et al., 2019). FAO-56 is based on the concepts of reference evapotranspiration ET_0 and crop coefficientsK_c, which is a direct representation of actual crop growth conditions in the field. It has been introduced to separate the climatic demand from the plant response (Allen et al., 1998). This approach is mostly used for annual crops where VI dynamic defines well the phenological stages (Glenn et al., 2011; Senay et al., 2011). However, in complex areas (trees, herbaceous, degraded shrubs, etc…) the model must be adjusted with additional meteorological data (Maselli et al., 2014) as the K_c varies in space and time for a number of reasons including the land use pattern, irrigation management, natural variability of soil properties, vegetation amount and atmospheric boundary conditions (temperature, wind notably). No common relationship was found between ET and VI for different sites and climatic conditions.

I.4.2. Models based on Land Surface Temperature

The spatial modeling has become a dominant means to estimate ET fluxes over regional and continental areas (Anderson et al., 2007; Fisher et al., 2017). One of the most widely used ET spatial models is the temperature-based approach as the land surface temperature (LST) is potentially a signature of both ET and the soil water availability via the surface energy balance. In recent decade, many efforts have been devoted to extract the LST from remote sensing data. Thermal sensors, on board satellites and aircrafts in the spectral range of the thermal infrared (between 8 and 14 μm) offer the possibility of obtaining spatially distributed LST data. ASTER (Advanced Space borne Thermal Emission), Landsat-8 and MODIS (Moderate-Resolution Imaging Spectroradiometer) provide images ranging from 90 m to 100 m and 1 km for applications in the Earth's surface processes (Zhou et al., 2014). Despite their low resolution, MODIS data are the most widely used because they cover the entire surface of the Earth every 1–2 days, whereas the revisit period for ASTER and Landsat is 16 days.

A variety of temperature-driven models with empirical and stronger physical basis have been described above (Section I.3). Among well-known temperature-driven energy flux models, the TSEB model proposed by Norman et al. (1995) has been showing high robustness for a

wide range of landscapes (Colaizzi et al., 2012). This model has two key input variables, which can be derived from remote sensing data. The first one is the LST as it is used to estimate the sensible heat flux. The second is vegetation cover fraction (f_c) as it controls the partitioning of the energy between soil and vegetation. The TSEB model adopts an iterative procedure, in which an initial estimate of the plant transpiration is given by the Priestly-Taylor (PT) formulation (Priestley et al., 1972). This assumption is relatively simple, requires few input data and has proven to be remarkably accurate and robust for estimating potential ET in a wide range of conditions (Fisher et al., 2008). Recently, Boulet et al. (2015) have developed the Soil-Plant-Atmosphere and Remote Sensing Evapotranspiration (SPARSE) model similar to the basic assumption of TSEB model. Nevertheless, SPARSE is solved in two modes: the prescribed and the retrieval mode to constrain the output fluxes. The former first generates equilibrium LST from the evaporationand the transpiration efficiencies estimates by assuming that their values are equal to 1. Then, LST is implemented in the SPARSE retrieval mode to circumscribe the output fluxes by both limiting cases (namely the fully stressed and potential conditions). In spite of the good retrieval performances of ET by this model, significant uncertainties are observed during the quasi-senescent vegetation period (Boulet et al., 2015).

I.4.3. Models based on Surface soil moisture

Over the past 50 years, several studies have documented that soil moisture (SM) status may be derived indirectly from thermal infrared data. Nemani et al. (1993) found a strong negative relationship between LST and NDVI across biomes with a distinct change in the slope between dry and wet days. In studies dedicated to SM the estimation Carlson et al. (1995) and Gillies and Carlson, (1995) have proved the previous idea, they developed a universal triangular method to explore relationships between SM, LST and NDVI. However, the atmospheric effects, the cloud cover as well as the effect of the vegetation have limited the development of these approaches.

While many bands in the electromagnetic spectrum are sensitive to changes in SM, the microwave domain is recognized as the most promising tool due to its independence to atmospheric conditions and is strongly related to water content in the first centimeters of soil (Schmugge et al., 2002). Microwave sensors can be classified as either active (radars) or passive (radiometers). The radars have proved to be the most useful platforms for monitoring surface moisture at high spatial resolution (Balenzano et al., 2011). However, the impact of vegetation cover, its structure and soil roughness on the backscatter signal remains extremely

difficult to model at high spatial resolution over large areas (Satalino et al., 2014). Therefore, global SM products are generally derived from the radiometers such as the C-band Advanced Microwave Scanning Radiometer (AMSR-E) (Njoku et al., 2003) on the Earth Observing System (EOS) Aqua satellite launched on May 2002. The AMSR-E instrument provides the SM at approximately 60 km resolution (4-8 GHz). The first L-band mission dedicated to SM monitoring is the Soil Moisture and Ocean Salinity (SMOS) mission (Kerr et al., 2010) launched in November 2009 that provides global maps of SM every three days at 40 km resolution (1.4 GHz). One difficulty is that microwave radiometry requires a large antenna to detect the signals emitted by the surface with sufficient sensitivity, which limits the resolution of the data to a few tens of km. The use of such coarse spatial resolution data is generally unsuitable or even incompatible with many hydrological and agricultural applications. To overcome the limitations linked to radars (higher spatial resolution and lower accuracy) and radiometers (higher accuracy and lower spatial resolution), the Soil Moisture Active and Passive (SMAP) mission (Entekhabi et al., 2010) was expected to provide SM at a spatial resolution of 9 km at 3 days repeat intervals, by combining radar and radiometer measurements. However, the radar on broad SMAP stopped transmitting on July 2015 due to anomaly that involved the radar's high power amplifier, and since then SMAP has continued to work with data from radiometer only.

The brightness temperature from the radiometers and the backscattering coefficient from radars have a great potential for the SM estimation. Therefore, combining these two sensor observations can provide complementary information included in the land surface microwave signature. Several studies have attempted to combine passive and active microwave remote sensing observations for the SM estimation (Njoku et al., 2003; Zhong et al., 2012). Neverthless, satellite observations are provided at different overpass times which can be lead to some differences on land surface parameters especially SM (Li et al., 2011). Other studies seek to estimate SM without the complementary information provided by active observations. One such approach was to employ optical/thermal remote sensing data that provide finer resolution information to downscale passive microwave SM estimations (Chauhan et al., 2003; Merlin et al., 2010; Piles et al., 2011). The relationship between SM, LST and vegetation coverhas been commonly represented as a triangle (Carlson et al., 1994) or trapezoidal pattern relationship (Moran et al., 1994). For instance, Piles et al. (2011) applied a new polynomial-fitting method based on the results of Chauhan et al. (2003), by linking coarse resolution SM from SMOS and MODIS products to provide SM data at 10km and 1km resolution. Another potential approach to estimate SM through the semi-empirical

relationship between SM and soil evaporative efficiency (SEE, defined as a ratio of actual to potential soil evaporation) has been applied by several authors (Fang and Lakshmi, 2014; Merlin et al., 2012b, 2008). These authors used finer resolution MODIS VI, LST and surface albedo to compute SEE based on the triangle approach to generate a disaggregated SMOS SM product up to 1 km resolution. Merlin et al. (2012a) improved the evaporation-based method developed in Merlin et al. (2008). DisPATCh (DISaggregation based on Physical And Theoretical scale CHange) includes the effect of vegetation water stress (Moran et al., 1994) within a trapezoid-based approach by using a 1st order Taylor series expansion of a SEE model. Merlin et al. (2013) implemented a simple correction for elevation effects. Multiple recent studies have used the SEE-based algorithm for validation of downscaled SM product from coarse-scale satellite (AMSR-E, SMOS and SMAP) (Chan et al., 2016; Colliander et al., 2017; Djamai et al., 2015; Malbéteau et al., 2016; Molero et al., 2016).

Alternatively to the use of LST as a proxy for ET, numerous studies have stressed that the SM plays a critical role in the partitioning of available energy into latent and sensible heat fluxes and is the prominent controlling factor of actual ET (Boulet et al., 2015; Gokmen et al., 2012; Kustas et al., 1999; Kustas et al., 1998; Li et al., 2006). Several authors have revised the well-known LST-based TSEB model and replaced the LST with microwave-derived SM to estimate daily ET (Bindlish et al., 2001; Kustas et al., 1998; Kustas et al., 1999; Li et al., 2006). Bindlish et al. (2001) found that the impact of SM on surface fluxes is strongly related to the vegetation cover. The impact is high for low fraction cover, and relatively weak for high cover fraction. Moreover, the soil evaporation is constrained by the SM through soil-texture dependent coefficients reported in Sellers et al. (1992). In the sameway, Li et al. (2006) indicated that the model performance is sensitive to these two coefficients, and thus they proposed to average the output of LST-based TSEB and SM-based TSEB models, in order to provide more consistent results over a wide range of conditions. More recently, Yao et al. (2017) evaluated three satellite-based PT algorithms (ATI-PT, VPD-PT and SM-PT for apparent thermal inertia-, vapour pressure deficit- and SM-based formulations of the PT coefficients, respectively) to estimate terrestrial water flux in different biomes. Their finding showed that the SM-PT algorithm had relatively better results compared to those of ATI-PT and VPD-PT. However, all three models underestimated ET in irrigated crops, reflecting that these algorithms may not capture well the soil evaporation, notably through its (site-specific) parameterization with SM. In the same vein, Purdy et al. (2018) updated the PT Jet Propulsion Laboratory (PT-JPL) and incorporated the SM data derived from SMAP (Soil

Moisture Active and Passive, Entekhabi et al., 2010) to constrain both evaporation and transpiration, separately. The model showed high improvements compared to the original PT-JPL, especially in dry conditions. However, the model relied on evaporation and transpiration reduction parameters, whose values were set a priori.

I.5. Objectives

Several studies agree with the view that combining both LST and SM information at a time would enhance the robustness and accuracy of ET estimates in various biomes and climates (Gokmen et al., 2012; Kustas et al., 2003, 1998; Li et al., 2006). Nevertheless, few studies have simultaneously combined both observations in a unique energy balance model. One difficulty lies in developing a consistent representation of the soil evaporation (as constrained by SM, Chanzy and Bruckler, 1993), the total ET (as constrained by LST, Norman et al., 1995) and the plant transpiration (as indirectly constrained by both LST and SM, Ait Hssaine et al., 2018a).

In this context, the objective of this thesis is to improve the estimation of ET by combining multi-resolution optical / microwave remote sensing and surface-atmosphere exchange modeling. The proposed strategy consists ini) disaggregating the microwave SM data ii) estimating soil evaporation, and iii) partitioning the ET between soil evaporation and plant transpiration. To realise these objectives:

1-We rely on the DisPATCh remote sensing algorithm (Merlin et al., 2012a) that combines the coarse scale microwave-retrieved SM with high-resolution optical/ thermal data within a downscaling relationship to produce SM at 1km resolution. The method is based on the spatial relationship between microwave SM data and the soil evaporative efficiency (SEE) derived from optical data (including thermal) at higher spatial resolution. DisPATCh converts the high-resolution optical-derived SEE fields into high- resolution SM fields given a semi-empirical SEE model and a first-order Taylor series expansion around the SMOS observation. As part of this thesis, the C4DIS processor has been applied to the MODIS tile in Morocco to generate the moisture product over the 2014-2018 period. The DisPATCh SM are then evaluated by the in-situ measurements of intensive sites of the Tensift Observatory (http://trema.ucam.ac.ma).

2- DisPATCh SM data are used as input to a soil evaporation model. Several methods for estimating evaporation from SM observations at the surface have been proposed by Cahill et al. (1999), Dekić et al. (1995), Lee and Pielke, (1992), and Mahfouf (1991). Although many

formulations have been proposed since the 1960s, there is still no consensus on a better way of modeling soil evaporation over large areas (Desborough et al., 1996; Sakaguchi and Zeng, 2009). Nevertheless, the bibliographic review of these models allows to draw the following conclusions: 1) the existing formulations differ in four aspects: the low and high limit values of SM, the non-linearity of the relation between evaporation and SM, need of input data other than SM and depth of SM measurements (Merlin et al., 2011), 2) Simple empirical expressions may be more accurate and robust than other physically based models (Dekić et al., 1995; Mihailović et al., 1995), and 3) none of these formulations are evaluated under different types of soil and variable atmospheric conditions. Based on these findings, a new model of evaporation developed by Merlin et al. (2016) have been used to estimate soil evaporation.

3- A new energy balance model for evaporation /transpiration partitioning is developed to simultaneously integrate remote sensing LST and SM data. To build this model from a state-of-the-art ET model, the following characteristics are taken into account: i) modeling based on LST data, ii) using dual source representation, allowing an explicit separation of soil evaporation and plant transpiration, and iii) parameterizing the surface fluxes with a network of resistances, more directly related to SM than models with evaporative efficiency. The TSEB model (Norman et al., 1995) is selected because it satisfices these three criteria. The transpiration in TSEB model is estimated based on Priestley Taylor (PT) approach. Indeed, the PT assumption that empirically relates ET to net radiation (Priestley and Taylor, 1972) has shown a growing interest (Anderson et al., 2007; Kustas and Norman, 1999; Norman et al., 1995). PT coefficient noted α_{PT} directly relates latent heat flux to the energy available at the surface. By neglecting the aerodynamic resistance term included in the full Penman-Monteith equation (Monteith, 1965), the PT formulation is relatively simple, requires less input data and has proven to be remarkably accurate and robust for estimating potential ET in a wide range of conditions (Fisher et al., 2008). It is therefore well suited for operational (McAneney and Itier, 1996) and large scale (Anderson et al., 2008) applications. In addition, recent studies based on in-situ global data sets have reported a good robustness of the PT modelingapproach over a variety of biomes (Ershadi et al., 2014). Nevertheless, severalstudies (Ait Hssaine et al., 2018a; Fisher et al., 2008; Jin et al., 2011; Yang et al., 2015) have stressed that the PT coefficient varies under different types of surface and according to various atmospheric conditions in the range 0.5-2.0 with an average value estimated around 1.3 (above references). Other studies (Gonzalez-dugo et al., 2009; Long and

Singh, 2012 and Morillas et al., 2014) reported that the PT approach may overestimate the canopy ET, especially for low soil wetness, and/or sparse vegetation cover, because it does not include a reasonable reduction of the initial canopy ET under stress conditions. For this purpose, the modification of the PT-based TSEB formalism (Kustas et al., 1999; Norman et al., 1995) was investigated by integrating LST and SM data simultaneously (the modified version is named TSEB-SM). An innovative calibration procedure was also implemented to retrieve the main parameters of soil evaporation (soil resistance) and plant transpiration (α_{PT}).

The following text of this manuscript is structured in seven chapters:

- Chapter 2 presents a detailed description of the study sites, as well as the acquisition devices of field /remote sensing data necessary to extract the surface biophysical characteristics and climatic variables.
- Chapter 3 describes the used modeling approaches.
- Chapter 4 presents the validation results of TSEB model over sparse and heterogeneous vegetation in Sahel region (Niger).
- Chapter 5 discusses the improviement made on TSEB model by integrating SM data (TSEB-SM): a feasibility study using in-situ data over 3 sites in Morocco was investigated.
- Chapter 6: presents an application of TSEB-SM in real life using readily available satellite thermal and microwave data for estimationg ET at 1 km resolution.
- Chapter 7 offers general conclusions and future perspectives

Chapter.II. Modeling approaches : Description and implementation

Chapter.II. Modeling approaches : Description and implementation 24
II.1. Introduction 25
II.2. TSEB Model Description and Implementation 25
II.2.1. Algorithm for solving the energy balance and the equation system 28
II.2.2. Calibration procedure 29
II.3. TSEB-SM Model Description and Implementation 30
II.3.1. Algorithm for solving the energy balance and the equation system 30
II.3.2. Calibration procedure 32
II.4. Aggregation scheme 35
II.5. Disaggregation model of SM data 37
II.6. Conclusion 39

II.1. Introduction

This chapter describes the main equations of both the original version of TSEB model (Norman et al., 1995) and those of the new TSEB-SM model (Ait Hssaine et al., 2018b) are fully described. Note that the main difference between the two models concerns the treatment of soil evaporation, which is either estimated as a residual term in TSEB and explicitly represented through a soil resistance term in TSEB-SM. After that, the equations for calculating SM from DisPTACh algorithm and turbulent fluxes at large scale from flux aggregationmodelare briefly reproduced.

II.2. TSEB Model Description and Implementation

The TSEB model was presented and described by Norman et al., (Norman et al., 1995). It solves two separate energy balances for the soil and vegetation and estimates evaporation as residual terms of the energy balance. This model adopts the Priestley-Taylor (PT) parameterization and an iteration procedure estimate the energy partitioning. Two main input variables of TSEB model are: i) the first is land surface temperature (LST), used for estimating the sensible heat flux and ii) the vegetation cover fraction (f_c), which controls partitioning of the surface energy between vegetation and underlying soil. These key variables (LST and f_c) are usually derived from remote sensing sensors.

In TSEB, the directional radiometric temperature ($T_{rad}(\theta)$) is divided into its soil and vegetation cover fractions as seen by the radiometer, and is expressed as follows:

$$T_{rad}(\theta) = [f(\theta) * T_{veg}^4 + (1 - f(\theta)) * T_{soil}^4]^{1/4} \quad \text{(II.1)}$$

Where T_{veg} and $T_{soil}$are the vegetation and soil temperatures (K). The fraction of the field of view of the infrared radiometer occupied by canopy, $f(\theta)$, can be calculated by combining the view zenith angle $\theta$and the vegetation cover fraction f_c considering vegetation with a spherical distribution of leaf angles (Kustas and Norman, 1997) :

$$f(\theta) = 1 - \exp\left(\frac{-0.5*LAI}{\cos(\theta)}\right) \quad \text{(II.2)}$$

And f_c is simply $f(\theta = 0)$, namely:

$$f_c = 1 - \exp(-0.5 * LAI) \quad \text{(II.3)}$$

The LAI estimates were then used to derive the canopy height by the empirical equation:

$$h_c = \left(\frac{LAI - LAI_{min}}{LAI_{max} - LAI_{min}}\right) \quad \text{(II.4)}$$

Net radiation, R_n, is the sum of incoming and outgoing short and long wave radiation fluxes:

$$R_n = (1 - \alpha)SW + \varepsilon_s LW - (\varepsilon_{veg} f_c \sigma T_{veg}^4 + \varepsilon_{soil}(1 - f_c)\sigma T_{sol}^4)) \quad \text{(II.5)}$$

Where α is the surface albedo, SW is the incoming solar radiation and LW is the incoming long wave radiation (atmospheric radiation), ε_s, ε_{veg} and ε_{soil} are the surface, soil and leaf emissivity, respectively.In this study, the soil emissivity and leaf emissivity were taken as constant values from the literature (0.95 and 0.97, respectively).σ is the Stefan-Boltzman constant (σ=5.6698 10-8 $W.m^{-2}.K^{-4}$).

The double source energy balance corresponds to the simple source balance shared between the soil and vegetation components:

$$R_{n,soil} = H_{soil} + LE_{soil} + G \quad \text{(II.6)}$$

$$R_{n,veg} = H_{veg} + LE_{veg} \quad \text{(II.7)}$$

With $R_{n,soil}$ being the soil net radiation, H_{soil} the soil sensible heat flux, LE_{soil} the soil latent heat flux, $R_{n,veg}$ the vegetation net radiation, H_{veg} the vegetation sensible heat flux and LE_{veg} the vegetation latent heat flux.

The surface sensible heat flux (H) is partitioned between the vegetated canopy and soil using the following relations:

$$H_{soil} = \rho c_p \frac{T_{soil} - T_a}{r_s + r_{ah}} \quad \text{(II.8)}$$

$$H_{veg} = \rho c_p \frac{T_{veg} - T_a}{r_{ah}} \quad \text{(II.9)}$$

where ρ ($kg.m^{-3}$) is the density of air, c_p ($W.s^{-1}. kg^{-1}K^{-1}$) the specific heat capacity of air,T_a the air temperature,T_{veg} and T_{soil} respectively the canopy and soil temperatures, r_{ah} the aerodynamic resistance to heat transfer across the canopy–surface layer interface, and r_s the resistance to heat flux in the boundary layer immediately above the soil surface.

The r_{ah} is calculated from the adiabatically corrected log temperature profile equation (Brutsaert, 1982) expressed as:

$$r_{ah} = \frac{\left(\frac{\ln(z_u - d)}{z_m} - \Psi_m\right)\left(\frac{\ln(z_h - d)}{z_m} - \Psi_h\right)}{v_{kar}^2 * U_a} \quad \text{(II.10)}$$

wherez_u and $z_T$are the height of wind speed measurement U_a and air temperature measurement T_a, respectively.dis the displacement of reference plan (d = 2/3*h_c), z_m is the roughness length for momentum (z_m = $h_c/8$) , V_{kar} is the von Karman constant taken to be 0.4, and Ψ_m and Ψ_H are the adiabatic correction factors for momentum and heat, respectively (Brutsaert, 1982).

Although r_s is rather complex as it depends on many factors, Sauer et al.(1995) provided a reasonable approximation:

$$r_s = \frac{1}{a+b*U_s} \tag{II.11}$$

where a=0.004 m.s^{-1}, b=0.012, and U_s is the wind speed at a height above the ground where the effect of soil roughness is minimal (typically between 0.05 and 0.2 m). Using the empirical relations from Campbell and Norman(1998):

$$U_s = U_h \exp\left[a_{sc}\left(\frac{z}{h_c} - 1\right)\right] \tag{II.12}$$

With a_{sc} being the leaf size expressed as:

$$a_{sc} = 0.28 LAI^{2/3} h_c^{1/3} s^{-1/3} \tag{II.13}$$

And U_h the wind speed at the top of vegetation canopy given by:

$$U_h = \left[\frac{\ln\left(\frac{h_c - d}{z_m}\right)}{\ln\left(\frac{z_u - d}{z_m}\right) - \Psi_m}\right] \tag{II.14}$$

The surface soil heat flux is estimated as a fraction of $R_{n,soil}$:

$$G = c_G R_{n,soil} \tag{II.15}$$

where $c_G \sim 0.35$ (Choudhury et al., 1987).

The latent heat flux from the vegetated canopy is derived from the PT formula:

$$LE_{veg} = \alpha_{PT} f_g \frac{\Delta}{\Delta+\gamma} R_{n,veg} \tag{II.16}$$

where γ is the psychometric constant (≈67 Pa K^{-1}), f_g the fraction of leaf area index (LAI) that is green, Δ the slope of the saturation vapor pressure versus temperature curve, and $\alpha_{PT} \sim 1.26$ for TSEB model (Priestley and Taylor, 1972).

II.2.1. Algorithm for solving the energy balance and the equation system

The algorithmfor solving the energy balance and the equation systemis presented in the schematic diagramin figure II.1.

In order to solve the system that includes more unknowns than equations, an iterative process is used that closes on the Obukhov length (LMO). The algorithm starts by calculating the wind and turbulence variables (LMO,U_*,U_s, and r_{ah}expressed by the above equations).

The available energy and heat fluxes are then determined by calculating the net radiation (R_n) and its partition between the vegetation ($R_{n,veg}$) and the soil ($R_{n,soil}$), as well as the conduction flux in the soil (G). The plant transpiration (LE_{veg}) is estimated by the PT equation, which allows the residual calculation of the vegetation sensitive heat flux (H_{veg}) as well as the vegetation temperature (T_{veg}). The soil temperature (T_{soil}) is estimated by radiometric temperature and canopy fraction, and is then used to estimate thesoil heat flux (H_{soil}). An energy balance on the soil is used to calculate soil evaporation (LE_{soil})

The estimated components of latent heat flux (LE_{veg} and LE_{soil}) are assumed to be positive, meaning that there is no condensation. If LE_{soil} is negative, then its value is set to zero and a new value of LE_{veg} is calculated as a residual term of the vegetation energy balance. If LE_{veg} is negative, then transpiration is reduced iteratively by decreasing the value of the PT coefficient until the LE_{veg} value becomes positive or zero.

The heat fluxes then allow the recalculation of LMO. The iterative process is repeated until stability of LMO between two iterations with a numerical error (approximately 10^{-3}).

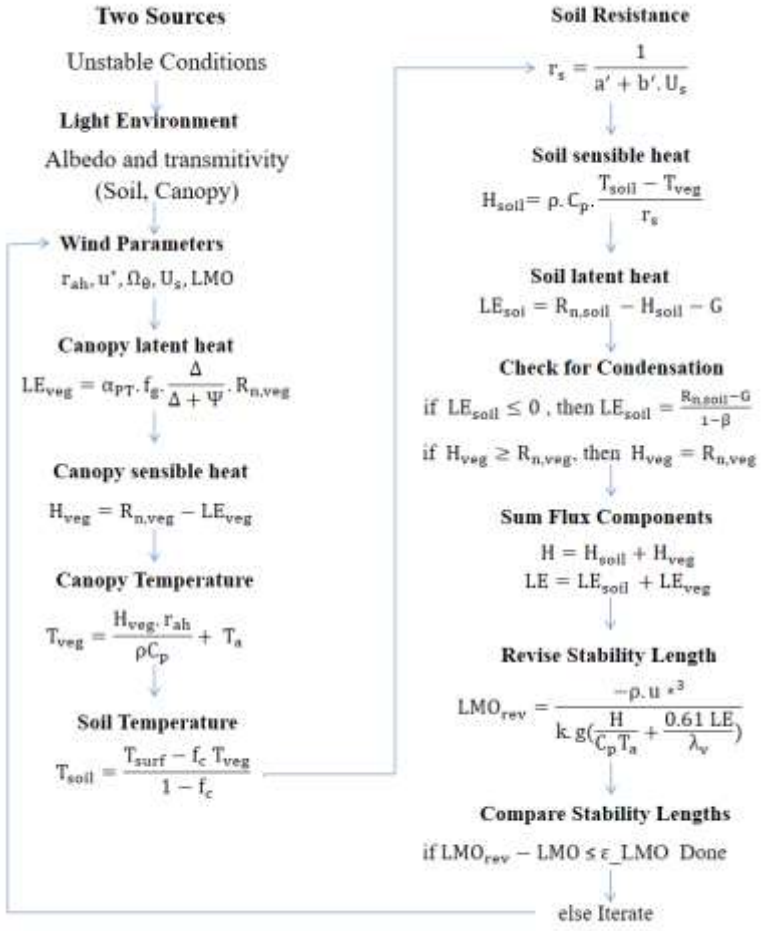

Figure II. 1. *Schematic diagram of TSEB model*

II.2.2. Calibration procedure

The PT coefficient (α_{PT}) is one of the most sensitive parameters of TSEB, because it drives the vegetation latent heat flux. Most studies conducted with TSEB have used its generic value around 1.3 (Anderson et al., 2007; Bindlish et al., 2001; Colaizzi et al., 2014; Kustas and Norman, 1999; Norman et al., 1995). Other studies have identified different values of α_{PT} depending on the vegetation fraction cover and particular forcing conditions. Notably, the PT coefficient was found to be smaller for dry surfaces and higher for humid conditions (Eichinger et al., 1996). Nevertheless, the relative stability of α_{PT} in many conditions has led to set α_{PT} constant. Consistent with this assumption, $\alpha_{PT}$is set to 1.26 in TSEB (Priestley and Taylor, 1972). Moreover, as an auxiliary parameter in Equation (2.16), f_g also needs to be calibrated. Kustas and Norman (1997) assumed that f_g was generally equal to 1, by considering that vegetation keeps being fully green during the growing stage, which represents most of the agricultural season. Note that green vegetation indices such as NDVI

(Normalized Difference Vegetation Index) can provide a strong constraint on f_g. However, it may be difficult to separate between senescent vegetation and soil from green vegetation indices only. In this context, Merlin et al. (2014) combined NDVI and surface albedo to estimate the fractions of both senescent and green vegetation. For the purpose of the comparison between TSEB and TSEB-SM using in-situ data sets, and consistent with most studies using TSEB, herein f_g is set to 1 all along the agricultural season.

II.3. TSEB-SM Model Description and Implementation

The TSEB formalism is modified to integrate SM as an additional constraint on modeled ET. In practice, the energy balance for vegetation and soil in TSEB-SM is the same as in TSEB, but the soil evaporation is now explicitly represented as a function of SM via a soil resistance term. Note that Song et al. (2016) have recently introduced SM in TSEB using a formulation of soil evaporative efficiency. While there is partial equivalence between both formulations, the soil resistance formulation is preferred herein as its parameters can be calibrated either from soil texture information (Merlin et al., 2016) or from a combination of LST and SM data under bare soil conditions (Merlin et al., 2018).

The soil latent heat flux is estimated as:

$$LE_{soil} = \frac{\rho c_p}{\gamma} \frac{(e_s - e_a)}{r_{ah} + r_s + r_{ss}} \quad \text{(II.17)}$$

Where e_s is the saturated vapor pressure at the soil surface, e_a is the air vapor pressure, and r_{ss} is the resistance to vapor diffusion in the soil. r_{ss} is expressed as follows (Silans, 1986):

$$r_{ss} = \exp\left(a_{rss} - b_{rss} * \frac{SM}{SM_{sat}}\right) \quad \text{(II.18)}$$

with SM being the soil moisture in the 0-5 cm soil layer, a_{rss} and b_{rss} are two empirical parameters and SM_{sat} the soil moisture at saturation expressed as:

$$SM_{sat} = 0.1 * (-108 * f_{sand} + 49.305) \quad \text{(II.19)}$$

withf_{sand} is the percentage of sand in the soil.

II.3.1. Algorithm for solving the energy balance and the equation system

The flowchart of Figure II.2 summarizes the different steps followed to resolve the energy balance in TSEB-SM model. The algorithm is based on an iterative procedure that loops on the Monin-Obukhov length (LMO), which is a scale parameter that characterizes the degree

of instability or stability of the boundary layer. LMO is approximately the height at which aerodynamic shear, or mechanical energy, is equal to the buoyancy energy. In practice, LMO is used as correction factor to determine the aerodynamic resistance r_{ah}. First, the algorithm starts by initializing the soil and vegetation temperatures, as well as sensible and latent heat fluxes. Then it calculates the available energy for the soil-vegetation-atmosphere interface by estimating the surface net radiation (R_n) and its partition between the vegetation and the soil, as well as the soil heat flux. The way soil and vegetation temperatures are estimated is in fact a specificity of the new model, which is based on the explicit resolution of the energy balance for soil and vegetation respectively. Component temperatures are obtained by minimizing cost functions F_{soil} and F_{veg}:

$$F_{soil,k} = \left(R_{n,soil,k} - H_{soil,k} - LE_{soil,k} - G_k\right)^2 \quad \text{(II.20)}$$

with k being a loop index. By using the Newton method formula:

$$F_{veg,k} = \left(R_{n,veg,k} - H_{veg,k} - LE_{veg,k}\right)^2 \quad \text{(II.21)}$$

$$T_{soil,k+1} = T_{soil,k} - \frac{F_{soil,k}}{dF_{soil,k}} \quad \text{(II.22)}$$

$$T_{veg,k+1} = T_{veg,k} - \frac{F_{veg,k}}{dF_{veg,k}} \quad \text{(II.23)}$$

wheredF_{soil} and dF_{veg} are the first derivative of the cost function for soil and vegetation, respectively.

At the end of each iteration, the simulated LST (noted $T_{surf,sim}$ in Figure II.2) and heat fluxes are used to recalculate the LMO iteratively. The iterative procedure is repeated until LMO (and H) converges, meaning that the difference between two successive values is smaller than a given threshold (numerical uncertainty).

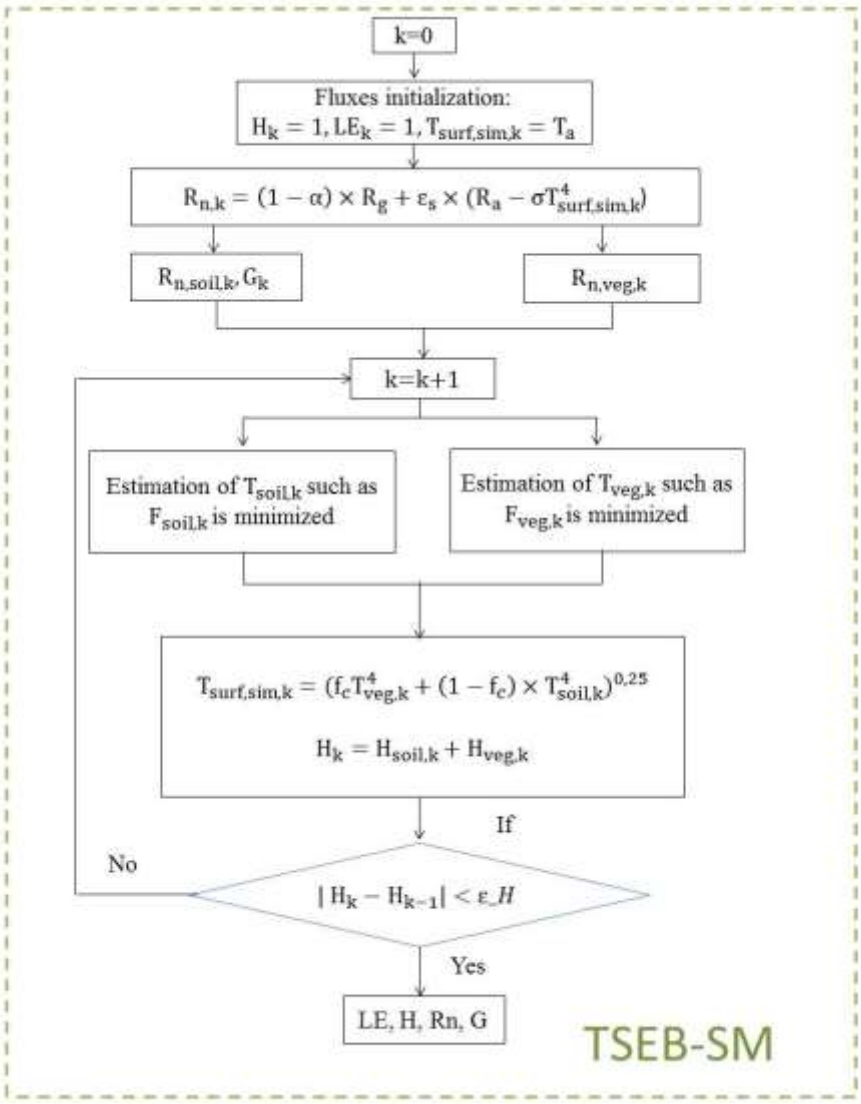

Figure II. 2. *Schematic diagram of TSEB-SM model*

II.3.2. Calibration procedure

The calibration procedure of TSEB-SM is presented in the schematic diagram of Figure II.3. It is done in two steps: the first aims to provide first guess estimates of a_{rss} and b_{rss} (named $a_{rss,FG}$ and $b_{rss,FG}$) as input to the second step that aims to provide the final values of (a_{rss}, b_{rss}) and α_{PT} at the seasonal and daily time scales, respectively.

Given that soil evaporation and plant transpiration may compensate each other to result in similar total ET values, it is important to ensure that the calibration procedure is well defined, meaning that a unique triplet (a_{rss}, b_{rss}, α_{PT}) is systematically obtained at the desired time scale. In order to do so, the calibration data set is divided into two regions with specific

behaviors: i) data with $f_c \leq f_{c,thres}$ for which ET is mainly controlled by soil evaporation and ii) data with $f_c > f_{c,thres}$($f_{c,thres}$ is taken =0.5) for which ET is dominated by plant transpiration. In both data sets, soil evaporation and plant transpiration may occur simultaneously but the LST over the mixed surface is expected to be more sensitive to soil evaporation and plant transpiration for $f_c \leq 0.5$ and $f_c > 0.5$, respectively (Merlin et al., 2012a; Moran et al., 1994).

The first calibration step initializes α_{PT} =1.26 and inverts r_{ss} at each time (30-min) step for data with $f_c \leq 0.5$. The r_{ss} is first adjusted to minimize the following cost function:

$$F_{inst} = \left(T_{surf,sim} - T_{surf,mes}\right)^2 \quad \text{(II.24)}$$

using the Newton method:

$$r_{ss,k+1} = r_{ss,k} - \frac{F_{inst,k}}{dF_{inst,k}} \quad \text{(II.25)}$$

Where $T_{surf,sim}$ and $T_{surf,mes}$ are the LST simulated by TSEB-SM model and observed over the crop field at the 30-min time step, respectively. The inverted r_{ss} is then correlated to the observed SM to estimate a_{rss} and b_{rss}. In practice, a_{rss} and $-b_{rss}/SM_{sat}$ are the intercept and the slope of the linear regression of the $\ln(r_{ss})$ versus SM relationship (see Equation 2.18). As the retrieved pair (a_{rss}, b_{rss}) depends on the α_{PT} value, an iterative loop is run on a_{rss}, b_{rss} and α_{PT} until convergence of a_{rss} and b_{rss} is achieved. At each iteration, the inverted a_{rss} and b_{rsss} are used as input to invert α_{PT} for data with $f_c > 0.5$. The PT Taylor coefficient is adjusted, at the daily time scale, to minimize the following cost function:

$$F_{daily} = \sum_{i=1}^{N}\left(T_{surf,sim,i} - T_{surf,mes,i}\right)^2 \quad \text{(II.26)}$$

with N being the number of 30min LST measurements available for a given day. To keep a (time) scale consistency between all three retrieved parameters in calibration step 1, the daily inverted α_{PT} is averaged at the seasonal time scale before being used as input to the following (next iteration) inversion of a_{rss} and b_{rss}. Note that a sensitivity study was undertaken (results not shown) to verify that initialization values for a_{rss}, b_{rss} and α_{PT} do not impact on simulation results and retrieved parameters. The second calibration step refines the estimation of α_{PT} at the daily scale. The first guess $a_{rss,FG}$and $b_{rss,FG}$obtained in step 1 are first used as input to the retrieval procedure of daily α_{PT} for data with $f_c > 0.5$ (minimization of F_{daily}). Next, the daily retrieved $\alpha_{PT}$is smoothed to remove outliers as well as to reduce random

uncertainties in daily retrieved α_{PT}. Then, the smoothed α_{PT} is normalized between its minimum and maximum values reached during the agricultural season. Especially, the minimum value of smoothed α_{PT} is forced to 0 at harvest so that transpiration is zero at the end of the agricultural season:

$$\alpha_{PT,cal,daily} = \frac{\alpha_{PT,daily_{smooth}} - \min\left(\alpha_{PT,daily_{smooth}}\right)}{\max\left(\alpha_{PT,daily_{smooth}}\right) - \min\left(\alpha_{PT,daily_{smooth}}\right)} * \max\left(\alpha_{PT,daily_{smooth}}\right) \quad \text{(II.27)}$$

Note that the minimum value of smoothed α_{PT} could be different from zero due to errors in the a priori parameterization of resistances (notably r_{ss}) in TSEB-SM model. Finally r_{ss} is calibrated a last time to ensure consistency between daily calibrated $\alpha_{PT,cal,daily}$and final $a_{rss,cal}$and $b_{rss,cal}$ (see Figure II.3).

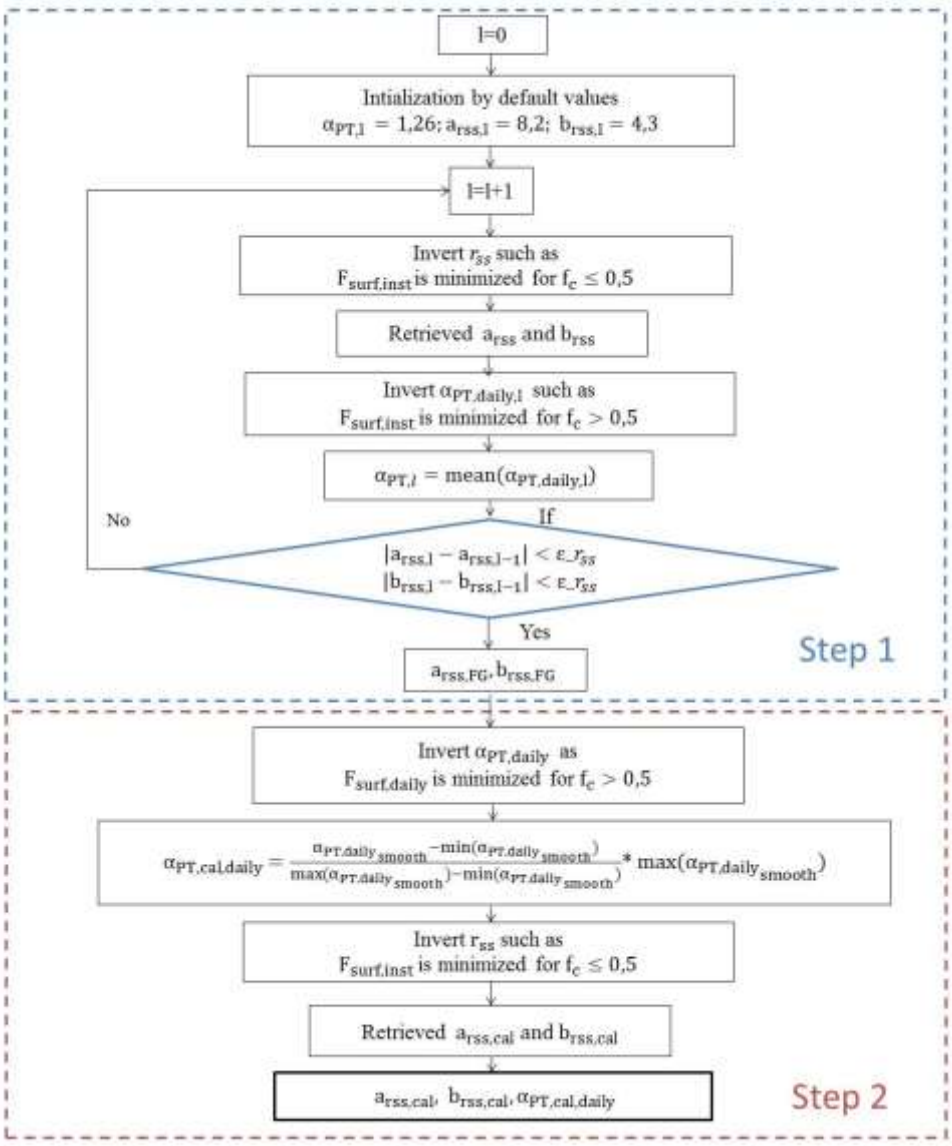

Figure II. 3. *Schematic diagram of the two-step calibration strategy of TSEB-SM model.*

II.4. Aggregation scheme

The spatial aggregation is a method to bridge the model parameters controlling surface exchange at a patch scale with the areal average value of equivalent model parameters applicable at a larger scale in order to estimate grid scale surface fluxes using the same equations that govern the patch scale behaviour (Chehbouni et al., 2000). In general, aggregation can be applied either to the input forcing of the evapotranspiration models, or to the fluxes derived from fine resolution input fields (Ershadi et al., 2013). Here the first assumption is used to link between local and effective values of land surface parameters (Chehbouni et al., 2000, 1995; Ezzahar et al., 2009b; Lhomme et al., 1994). The chosen averaging approach is directly related to the considered variable. For albedo (α) and

displacement height$d$, a simple arithmetic average is used:

$$\langle \alpha \rangle = \sum_i f_i \alpha_i \quad \text{(II.28)}$$

$$\langle d \rangle = \sum_i f_i d_i \quad \text{(II.29)}$$

From the Stefan-Boltzmann law, the aggregated value of the land surface temperature LST can be obtained from:

$$\langle LST \rangle = \left[\frac{\sum_i f_i \varepsilon_i LST_i^4}{\langle \varepsilon \rangle} \right]^{0.25} \quad \text{(II.30)}$$

Where f_i is the fraction of the surface covered by the patch i (with $\sum_i f_i = 1$). Finally, the aggregation of the roughness length is obtained from a logarithmic average as follows:

$$\ln\langle z_0 \rangle = \sum_i f_i \ln(z_0) \quad \text{(II.31)}$$

Because of the absence of a soil occupation map for the Wankama study site, the aggregation schemeusing in-situ measurementsis done by weighted average of the estimated variables from the data of the threeEC stations. Following (Ezzahar et al., 2009b), the local values obtained by each EC system are assumed to be representative for the sites where those systems are installed along the basin. Sites millet, fallow, and degraded shrubs represented about 54%, 26%, and 20% of the Wankama catchment.

Three different aggregation methods are implemented to calculate the inputs of TSEB model from the MODIS products. They differ in the way the pixel scale inputs are used to derive the grid scale ones. The first scheme consists in averaging the MODIS products at their nominative resolution scale on a geographic windows of 10*8pixels around the scintillometer transect (i.e. independently of the scintillometer footprint; cf. figure II.4). The second scheme averages the MODIS products over the scintillometertransect without taking into account the representativity of the corresponding pixels with regards to the footprint (i.e. each pixel belonging to the footprint have the same contribution to the aggregated value). Finally, a weighted average aggregation scheme is implemented. It consists in weighting the MODIS pixel according to their proportion occupied in the footprint. The aggregated values of MODIS products are then used as inputs of the TSEB model at Terra-MODIS and Aqua-MODISoverpass time.

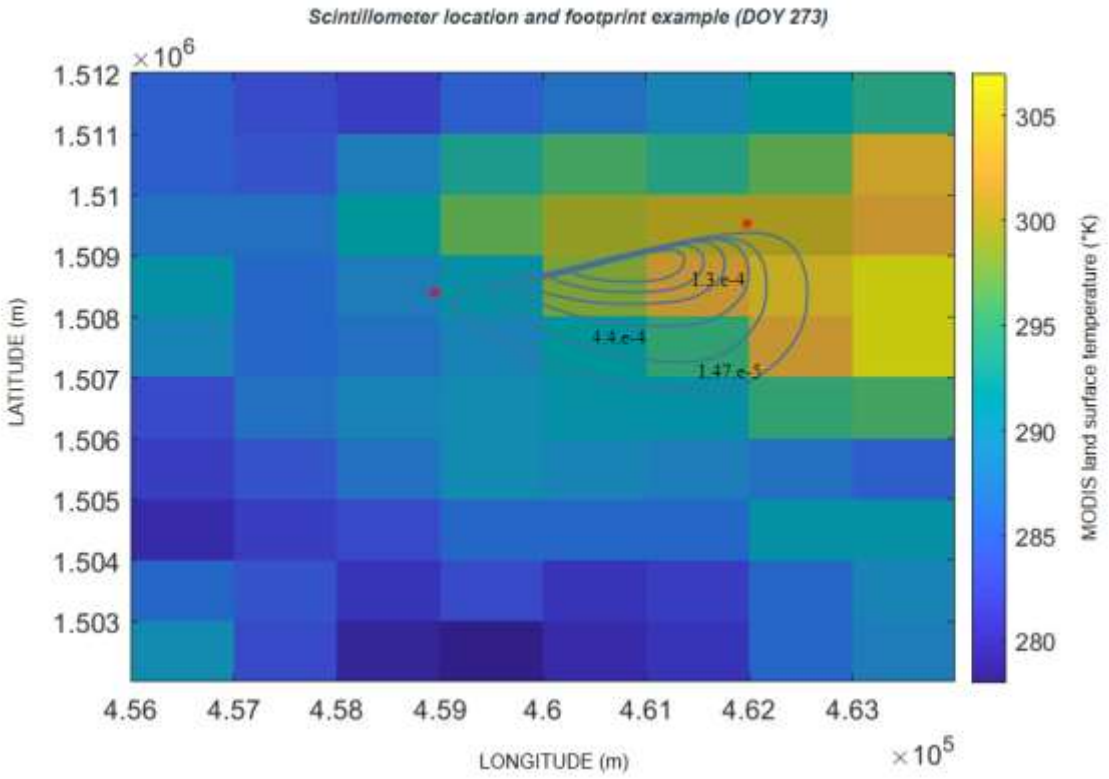

Figure II. 4. *Footprint of the LAS, calculated using the footprint model of Horst and Weil, superposed with a LST/MODIS image on DOY 273.*

II.5. Disaggregation model of SM data

The DisPATCh remote sensing algorithm combines the coarse scale microwave-retrieved SM with high-resolution optical/thermal data within a downscaling relationship to produce SM at higher spatial resolution. A detailed description of the algorithm can be found in Merlin et al. (2012) and Malbéteau et al. (2016).

Briefly, the soil evaporation from the 0–5 cm soil layer and the vegetation transpiration from the root-zone soil layer are first decoupled by separating LST into its soil and vegetation components (Merlin et al., 2012). The optical-derived soil temperature is then used to estimate the soil evaporative efficiency (SEE, ratio of actual to potential soil evaporation), which is known to be relatively constant during the day on clear sky conditions.

Finally, DisPATCh converts the high-resolution optical-derived SEE fields into high-resolution SM fields given a semi-empirical SEE model and a first-order Taylor series expansion around the SMOS observation.

The downscaling relationship is expressed as:

$$SM_{HR} = SM_{LR} + \frac{\partial SM_{mod}}{\partial SEE} SEE_{LR}(SEE_{HR} - SEE_{LR}) \quad \text{(II.32)}$$

WhereSM_{HR} represents the 1 km disaggregated SM, SM_{LR} the SMOS observation,$\frac{\partial SM_{mod}}{\partial SEE}$ the partial derivative of SM relative to SEE at LR, SEE_{HR} the MODIS-derived SEE, and SEE_{HR}its average within the SMOS pixel.

The HR SEE is estimated as:

$$SEE_{HR} = \frac{T_{s,max} - T_{s,HR}}{T_{s,max} - T_{s,min}} \quad \text{(II.33)}$$

$T_{s,max}$ and $T_{s,min}$ are end-members temperatures estimated from the polygons obtained by plotting MODIS surface temperature against MODIS NDVI datasets as in Merlin et al. (2012a).

Soil temperature is based on a linear decomposition of the surface temperature into its soil and vegetation components. Itis expressed as:

$$T_{s,HR} = \frac{T_{MODIS} - f_{c,HR} T_{v,HR}}{1 - f_{c,HR}} \quad \text{(II.34)}$$

WithT_{MODIS}being the 1 km resolution MODIS land surface temperature, f_c the MODIS-derived vegetation cover fraction, and $T_{v,HR}$ the vegetation temperature. In this study, vegetation temperature is estimated using the approach proposed by Carlson et al. (1994). The vegetation cover fractionis written as:

$$f_{c,HR} = \frac{NDVI_{MODIS} - NDVI_s}{NDVI_v - NDVI_s} \quad \text{(II.35)}$$

with$NDVI_{MODIS}$ being the 1 km resolution MODIS NDVI, $NDVI_s$ the NDVI corresponding to bare soil, and$NDVI_v$ the NDVI corresponding to full-cover vegetation. Minimum and maximum NDVI values are set to 0.15 and 0.90, respectively.

In our application, we applied DisPATCh to 40 km resolution SMOS level-3 SM and 1 km resolution MODIS optical/thermal data to produce SM at a 1 km resolution (Molero et al., 2016). The input dataset is generated by taking into account different combinations of SMOS SM (ascending 6 am and descending 6 pm) and MODIS (Terra overpass 10:30 am and Aqua 1:30 pm from one day before until one day after the SMOS overpass), as well as the GTOPO

Digital Elevation Model (DEM) used to correct LST for topographic effects (Malbéteau et al., 2016; Merlin et al., 2013). The characteristics of these data are described in Table II.1.

Table II. 1. Input data of DisPATCh chain

Product	Variable	Resolution	Projection	Format
SMOS CLF31A/CLF31D	SM	25 km/ 3 days	EASE grid	NetCDF
	LST_day_Q			
MODIS MOD11A1/MYD11A2	C	1 km/ 1 day	USGS Sinusoidal	HDF
MODIS MOD13A2	NDVI,QC	1 km/ 16 days	USGS Sinusoidal	HDF
GTOP030	MNT	0.01°	WGS84	GeoTIFF

II.6. Conclusion

TSEB and TSEB-SM models described above are used to estimate the ET within different cultures. For this purpose, different data have been used as input to feed these two models. In particular, the two key inputs, LST and f_c are used to force the TSEB model. While SM is used as an additional constrain of soil evaporation in TSEB-SM model. The three products (LST, f_c and SM) are either measured at the field scale using in-situ measurements or extracted from thermal/microwave remote sensing images. In addition, the meteorological data including air temperature, solar radiation, relative humidity, and wind speed are also used to force TSEB and TSEB-SM. To achieve these objectives, the experiments carried out and the data collected (field and spatial) are presented in the following chapter.

Chapter.III. Sites and data used

Chapter.III. Sites and data used 40
III.1. Introduction 41
III.2. Sites and in-situ data description 41
III.2.1. Watershed of Tensift el Haouz 41
III.2.2. Wankama basin (Niger) 48
III.2.3. Spatial data 52
III.3. Conclusion 54

III.1. Introduction

The first part presents the study sites and the description of the in-situ experimental. Indeed, six sites; including 2 irrigated and 1 rainfed wheat in the Haouz plain of the Tensift watershed (centre of Morocco), and three rainfed fields (Millet, fallow, and degraded shrubs) in the Wankama basin (Niger), have been chosen to calibrate and test the modeling approaches developed in the previous chapter. While, the second section is devoted to the presentation of remote sensing data (Optic, thermal and microwave) used to feed the models.

III.2. Sites and in-situ data description

III.2.1. Watershed of Tensift el Haouz

The Tensift catchment, located around Marrakech city, is one of the most important Moroccan watersheds (Figure III.1). It is characterized by a very contrasting relief and altitudes; between 0 and 4167 m. The catchment is surrounded by the the High Atlas Mountains on its south side, the small mountains called "Jbilet" on the north, by the watershed line on the east and the Atlantic Ocean on the west where the outlet is located. This Tensift watershed covers an area of about 20450 km². It consists of three main areas:

- **Jbilet** form a massif located north of the Tensift on a width of 20 to 30 km from north to south. Natural vegetation represents only a small area because of an intensive exploitation by overgrazing and deforestation for firewood and significant expansion of cultivated areas. The predominant agricultural activity in Jbilet zone is the rainfed cereal crop (wheat and barley), called Bour
- **The High Atlas** is a large mountain range that limiting the Haouz plain on the south (800 km long and 70 km wide). It is the "water tower" of the region. It is the main source of water for crop irrigation in the plain. The water is transported to the plain either directly by hydraulic systems (dams and both modern and traditional canals) or indirectly by contributing to the aquifers recharge (Abourida et al., 2005; Boudhar et al., 2007; Chaponnière et al., 2005).
- **The Haouz plain**, which is the main area of our study, covers about 6000 km^2 of almost surface. The plain is crossed from the South to the North by several wadis draining the reliefs of the High Atlas and join the Wadi Tensift (main collector of the superficial waters of the basin). The relief of the Haouz plain is very little, marked with slopes not exceeding 5%. The altitude is about 900 m at the foothills of the Atlas

mountain and gradually decreases towards the North, reaching about 300 m at the Wadi Tensift. The climate in the region is semiarid, with an average yearly precipitation of about 250 mm, of which approximately 75% falls during the winter and spring (November- April). The average air humidity is 50% and the reference evapotranspiration ET_0 is estimated as 1600 mm/year (Allen et al., 1998; Jarlan et al., 2015), which is greatly exceeding the annual rainfall.

In the Haouz plain, three sites; including 2 irrigated and 1 rainfed wheat are selected to test our model. In the following, several inputs (including LST, SM and f_c) are used to force the TSEB-SM. Turbulent fluxes from the EC system used to validate the model estimates are also described below.

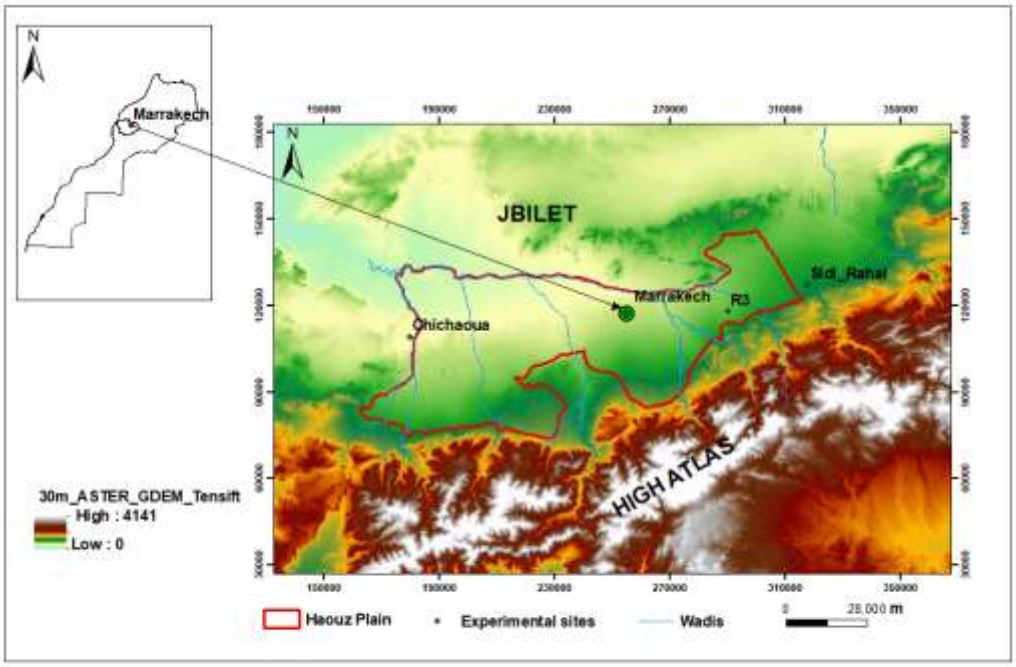

Figure III. 1. *Geographical situation of the Tensift watershed, its hydrographic network as well as the limit of the Haouz plain.*

III.2.1.1. R3 zone

The R3 area is an irrigated zone located 40 km eastern Marrakech city (Figure III.1). The study area covers 2800 ha and is mainly used for cereal production. The soil type is clay-loam. Approximately 85 % of available water is used for agriculture, with flood irrigation being the most widely used method (Belaqziz et al., 2014, 2013). The irrigation is managing by regional agricultural office (Office Régional de Mise en Valeur Agricole du Haouz or

ORMVAH) through a network of concrete channels directly connected to a dam. The irrigation scheduling is defined before the beginning of the cropping season according to the dam water level and is negotiated with the farmer's associations.

In the frame work of this PhD Thesis, the experimentation in R3 zone was carried out in wheat crop field of about 4 ha (Figure III.2), to monitor the energy and water balance as well as the soil and vegetation characteristics and conditions during the entire wheat growing cycle. The data set was collected from December 2002 to May 2003.

III.2.1.2. Chichaoua area

The Chichaoua study site is located 70 km western Marrakech city. Data sets are collected during wheat season, from November 2016 to May 2017 over two wheat crops of about 1.5 ha each (Figure III.2). The plots are supplied by drip irrigation method. During the 2016‑17 experiment, one plot (called the reference field) was irrigated according to the crop water needs estimated by the FAO-56 method. For the other field, so called (controlled field), the wheat was stressed in some periods (Rafi et al., 2019). The seasonal water irrigation was 374 and 504 mm for the controlled, and reference fields, respectively.

III.2.1.3. Sidi Rahal area (Bour field)

This study site is located about 60 km eastern Marrakech city (see Figure III.2). The experiment was set up in a 1 ha rainfed wheat ("Bour") field in 2013 (Ali Eweys et al., 2017; Amazirh et al., 2018; Merlin et al., 2018). The field was seeded during 3 wheat seasons (September 2014-Juin 2015 (S1), September 2016-Juin 2017 (S2), and October 2017-May 2018 (S3)), while it was not ploughed (remained as bare soil) during the 2015-2016 (B1) agricultural season due to strange lack of precipitation in autumn-winter 2015 (Merlin et al., 2018).

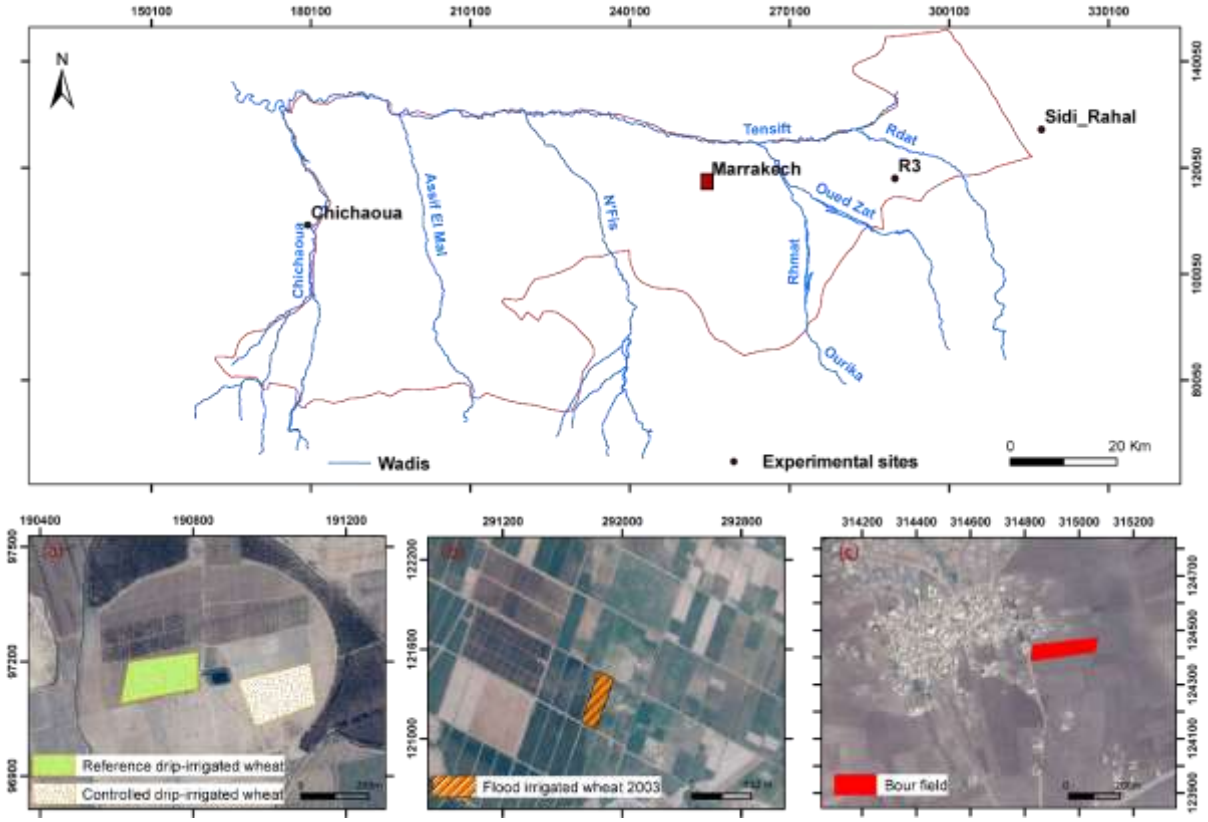

Figure III. 2. *Location of the four study sites: (a) flood-irrigated wheat crop in the R3 zone (east of Marrakech), (b) rainfed wheat crop in Bour site (east of Marrakech) and (c) two (controlled and reference) drip-irrigated wheat crops near Chichaoua city (west of Marrakech) in the Tensift basin, central Morocco. (Flat area).*

III.2.1.4. Experimental setup

III.2.1.4.1. Climatic data

For each experiment, an automatic weather station was set up, near the three studied wheat fields (R3, Chichaoua and Sidi Rahal). This station is equipped with instruments to measure solar radiation, wind speed and direction, air temperature and air humidity and rainfall. These climate forcing data, available at a half-hourly time step, are either sent in real time by remote transmission to the LMI-TREMA server (at the Faculty of Semlalia Sciences) or stored on a central data logger, before to be processed and analysed.

III.2.1.4.2. Turbulent heat flux measurements

To quantify the exchanges between the canopy and the atmosphere, the three studied field were equipped by an eddy covariance (EC) tower to measure the latent (LE) heat and sensible (H) heat fluxes. EC systems included a CSAT3 3D sonic anemometer (Campbell scientific

Ltd, Logan USA) which measures the fluctuations in the wind velocity components and temperature, a LICOR-7500 open-path infrared gas analyzer (Campbell scientific Ltd, Logan USA) installed over the R3 site and a Krypton hygrometer (KH20, Campbell Scientific Ltd, Logan USA) installed over both Chichaoua sites and Bour filed to measure the concentration of water vapour. The half-hourly fluxes were calculated off-line using the EC processing software 'ECpack', after performing all required corrections for planar fit correction, humidity and oxygen (KH20), frequency response for slow apparatus, and path length integration (Dijk et al., 2004). EC towers were also equipped with Kipp and Zonen CNR radiometers to measure net radiation (R_n) and heat flux plates (Campbell Scientific Ltd, Logan USA) to measure the soil heat flux (G). Analysis of the energy balance closure showed that the sum of latent and sensible heat flux measured independently by the EC systems was often lower than the available energy (R_n-G). The relative closure was satisfied by about 88%, 64%, and 70% (of available energy) for the R3, controlled and reference sites, respectively and about 68%, 79%, 76%, and 79% for S1, B1, S2 and S3, respectively in the Bour field . This problem could not be explained neither by the mismatch in the spatial extent of flux measurements, nor by the uncertainties associated with the measurements of soil heat flux and net radiation (Ezzahar et al., 2009b; Hoedjes et al., 2007; Twine et al., 2000). Correction was hence performed using the approach suggested by Twine et al. (2000). Indeed, the daily (computed using 30-minute estimates between 9 am and 5 pm) Bowen ratio (called β =H/LE) and the 30-minute flux estimates are combined to derive the corrected 30-minute turbulent fluxes ($LE = \frac{(R_n - G)}{(1+\beta)}$ and $H = \frac{\beta}{(1+\beta)}(R_n - G)$)

III.2.1.4.3. Land surface temperature

Land surface temperature is measured at the EC station by using two Apogee IRTS-P infrared radiometers, oriented downward and measuring the surface leaving radiance between 8 to 14 µm, set up at a 2-m height above ground. An estimate of LST is obtained by averaging both measurements.

III.2.1.4.4. Vegetation data

a. Leaf area index (LAI)

LAI is a dimensionless quantity that characterizes plant canopies. It is defined as the one-sided green leaf area per unit ground surface area; it is an important structural property of vegetation. Because leaf surfaces are the primary border of energy and mass exchange,

important processes such as canopy interception, evapotranspiration, and gross photosynthesis are directly proportional to LAI. The most commonly method used for measuring LAI is 'The hemispheric photography technique', which relies on the acquisition and processing of hemispheric photographs (Becker et al., 1989). It consists on taking photos with a camera equipped with a FC_E8 Fish-eye lens (180° wide-angle lens). Several photos are taken in order to have a representative LAI value of the parcel (about 10 photos). The photos are taken under optimal lighting conditions to avoid the effects of shadow and overexposure phenomena that make the classification more delicate. The photos are then digitally processed to extract the value of the LAI. The principle treatment is as follows: 1) The photo is decomposed into a matrix, and a binary classification (soil / vegetation) is carried out based on thresholds in the green and red bands (Khabba et al., 2009). 2) The useful part of the matrix is extracted by masking the strong angles, which are outside the studied system. 3) Extraction of vegetation cover rate on concentric rings associated with fixed viewing angles 4) Calculating the average directional LAI on photos taken in each parcel.

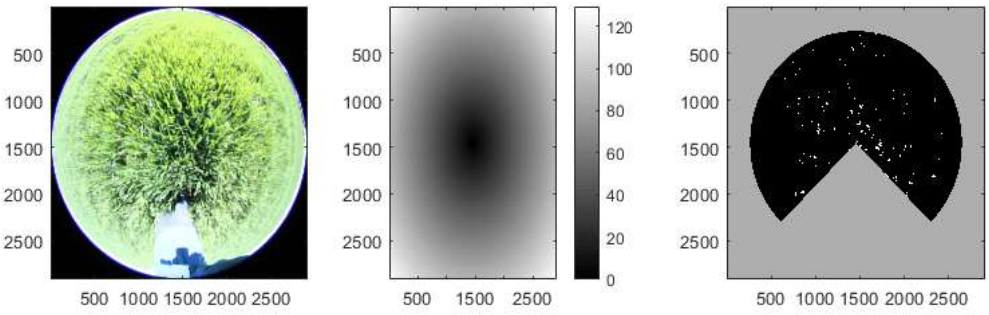

Figure III. 3. *Example of the digital processing procedure for photos taken in rainfed wheat field*

b. Vegetation cover fraction

The vegetation cover fraction (f_c) defined as the vegetated surface area projected on the ground at nadir, per soil surface area unit. It is dimensionless and varies between zero and one. In-situ methods of measuring the fraction of the canopy are very varied but the most widely used approach is the digital photography-based method. This is the same procedure as for the LAI. The vegetation cover fraction is then the ratio between the number of pixels of vegetation and the total number of pixels. Based on a comparison of the various techniques used to obtain field measurements of the f_c, White et al. (2000) have argued that hemispheric photography is the simplest and most reliable technique.

In our work, the f_c is considered as a variable which controls the energy partitioning between surface vegetation and soil.

c. Surface soil moisture

Among many existing methods for measuring in-situ soil moisture, we find:

The gravimetric method, which is a direct method. The soil moisture content may be expressed by weight as the ratio of the mass of water present to the dry to the dry weight of the soil sample, or by volume as ratio of volume of water to the total volume of the soil sample. To determine any of these ratios for a particular soil sample, the water mass must be determined by drying the soil to constant weight and measuring the soil sample mass after and before drying. The water mass (or weight) is the difference between the weights of the wet and oven dry samples. The limits of this method are the destructive nature of the approach, the need to have a laboratory operator to perform the measurements and their low representativity, which is about only few centimeters. However, this method has the advantage of being simple and inexpensive.

The electromagnetic method, which is an indirect approach that measure an electric field in the ground. The idea is to use the quasi-linear relationship between the measured electric field and the soil moisture. However, this relationship depends on the type of soil. It is therefore necessary to calibrate, from the gravimetric measurements, the measurements for each type of soil in order to match the measurement (in mV) and the soil moisture. This approach has the advantage of being able to obtain measurements of soil moisture over a long period of time with a high temporal resolution and automatically, thanks to the data acquisition units. In addition, these electromagnetic techniques are non-destructive, non-radioactive and the sensors are not costly.

Two types of measuring devices are used in our study fields; the theta-probe devices that provide spatially point measurements and Time Domain Reflectometry (TDR) probes (model CS615, CS655) which are installed in a soil pit near the EC towers to measure soil water content at different soil depths of 5, 10, 20, 30, 50, 100 cm and 5, 15, 25, 35, 50, 80 cm and 5, 15, 30, 50, 80 cm and 5,10, 20, 30, 50, 70 cm for the flood-, controlled drip- and reference drip-irrigated wheat and Bour field, respectively.



Figure III. 4. *Photograph of (a) TDR (Time Domain Reflectometry) and (b) Theta Probe instruments*

III.2.2. Wankama basin (Niger)

The data needed to test the TSEB model (presented in Chapter 2) were collected in the Wankama basin on three contrasting crops (millet, fallow and degraded shrubs). The LST and LAI observations, as well as the H and LE fluxes (from EC and scintillometer devices) to validate the estimation of TSEB at patch and grid scale, are collected during this study.

III.2.2.1. Site description

The region of interest is part of the Wankama catchment, which is located 70 km eastern the Niamey city, Niger (Figure III.5). It is situated between an upland at an altitude of 255 m and a pond at 200 m (Boulain et al., 2008). This semi-arid site belongs to the AMMA-CATCH-Niger observatory (Cappelaere et al., 2007), one of three meso-sites along the West African latitudinal transect (Lebel et al., 2009). The climate is typically Sahelian with a short rainy season from June to September with an annual mean of 560 mm for the years 1905–2004, and very strong year-to-year and spatial variability. The site is characterized with high temperatures throughout the year with a daily average which ranges from 24°C to 35°C. Additionally, the potential evapotranspiration is about 2500 mm/year (Massuel et al., 2011), greatly exceeding the annual rainfall. The soil is sandy (>90% sand) and poor in nutrients (Rockström and Valentin, 1997). The study area is covered by: (1) Millet fields cover 58% of the catchment's surface area. This rainfed crop is cultivated traditionally with little chemical fertilizer and no pesticides, being by far the main crop grown. (2) Fallow savannah fields represent 23% of the total surface area and they are no more than five years old and typical of the Niamey region. (3) Degraded shrubs occupy the remaining area (Ramier et al., 2009).

Vegetation usually emerges after the first rainfall events occurring in June or early July, peaks around the end of the rainy season in early September and then dries out during the senescence phase.

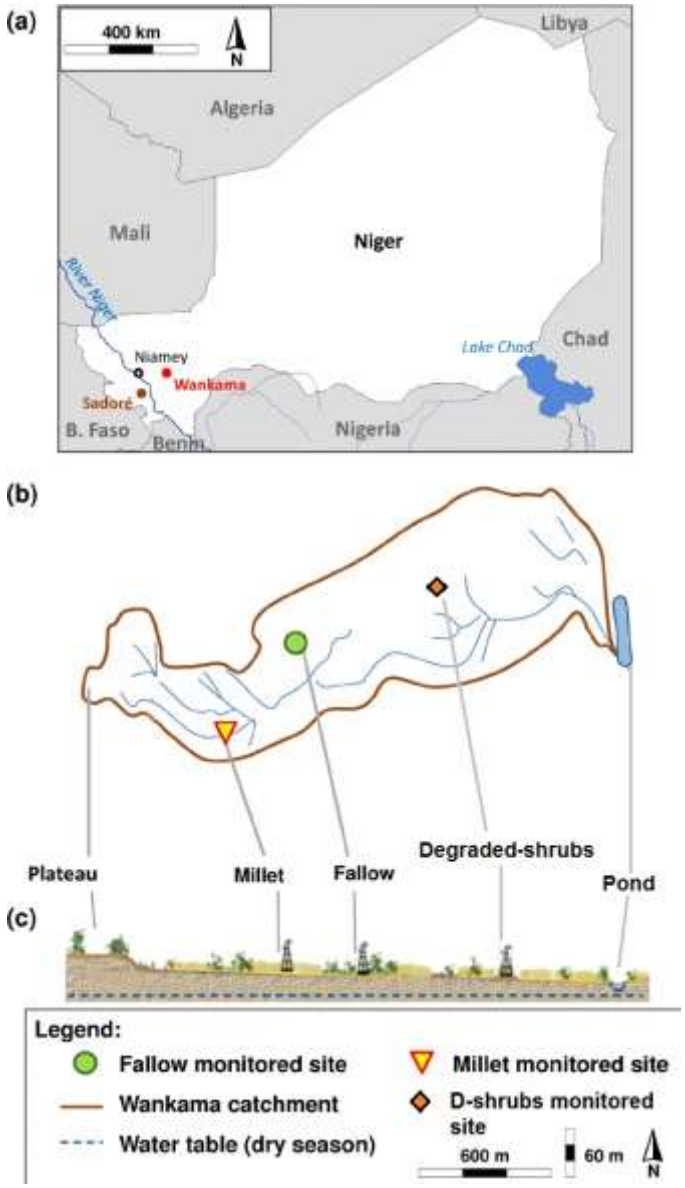

Figure III. 5. *(a) Map of the Wankama basin; (b) location of the three study sites (millet, fallow and (c) basin toposequence*

III.2.2.2. Experimental setup

a. Patch scale

The experiment was conducted between 23 July and 23 October 2006. The site was instrumented by different instruments summarized in table III.1.

Table III. 1. Characteristics of the instruments equipping EC station.

Site	Instrument	Measurements	Height or depth
Millet and Fallow	**Fluxes MAST**		
	Campbell CSAT3 sonic anemometer	Wind direction and speed	5,1m (Millet) et 4,95m (Fallow)
	Li-Cor7500 IRGA	CO2 and H2O concentration	4,8m(Millet) et 4,65m (Fallow)
	CNR1 Kipp & Zonen radiometer	Shortwave and longwave incoming and outcoming radiation	2,5m(Millet) et 3,4m(Fallow)
	Vaisala HMP45	Air temperature and relative humidity	2m
	Soil measurements		
	Campbell CS616 water content reflectometer (x6)	Soil volumetric water content	-.1, -.5, -1, -1.5, -2 and -2.5 m
	Campbell T108 temperature probe (X6)	Soil temperature	-.1, -.5, -1, -1.5, -2 and -2.5 m
	Hukseflux HFP01SC heat flux plates (x3)	Surface soil heat flux	-.05 m
Degraded shrubs	**Flux MAST**		
	Solent R3-50 sonic anemometer	Wind direction and speed	5 m
	Kipp & Zonen CNR1 radiometer	Shortwave and longwave incoming and outcoming radiation	2 m
	Vaisala WXT510 weather transmitter	Air temperature, relative humidity, atmospheric pressure, wind speed, wind direction	2 m
	RIMCO tipping bucket raingauge	Rainfall amount, duration and intensity	0 m
	Soil measurements		
	Campbell CS616 water content reflectometer (x2)	Soil volumetric water content	-.1, -.5 m
	Campbell T107 temperature probe (X2)	Soil temperature	-.1, -.5 m

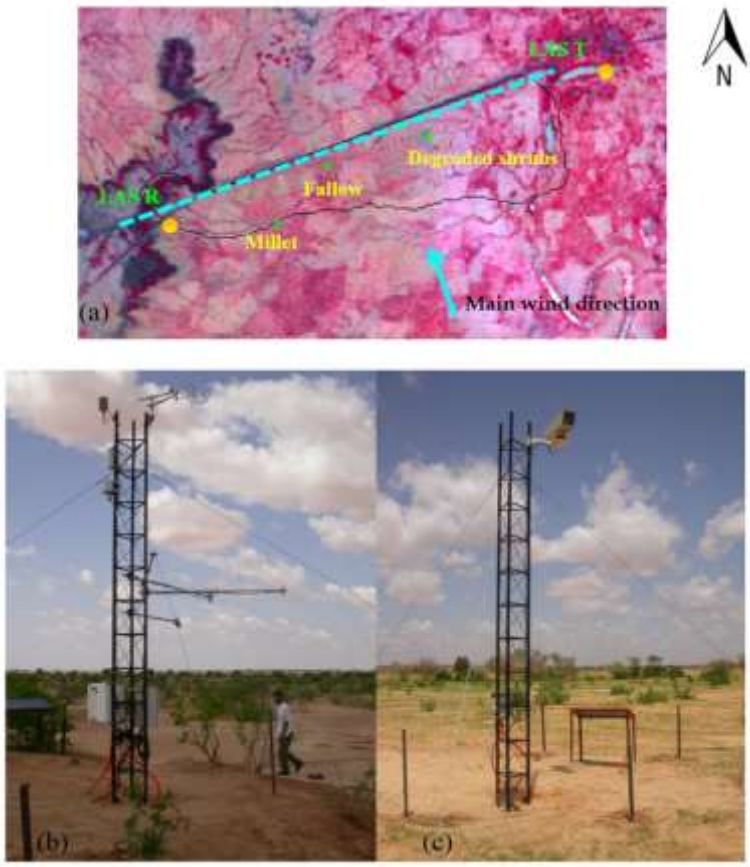

Figure III. 6. *(a) An overview of theWankama basin and the experimental setup, locations of LAS (T and R stand for transmitter and receiver, respectively) and three EC systems are shown (millet, fallow and degraded shrubs sites). Photos (EC system (b) and scintillometer (**c**)) were taken by J. Ezzahar as part of the ACN project.*

b. Grid scale

A Large Aperture Scintillometer (LAS) was set up over a 3.2 km transect spanning the three ecosystem types, i.e., millet and fallow fields and the degraded shrubs. The LAS used in this study was developed and built by the Meteorology and Air Quality Group from the Wageningen University (Netherlands). This instrument was constructed according to the basic design described in Ochs and Wilson (Ochs and Wilson, 1993). It has an aperture size of 0.15 m and the transmitter operates at a wavelength of 0.94 µm. At the receiver, C_n^2 is sampled at 1 Hz and averaged over 1 min intervals by a CR510 datalogger (Meijninger et al., 2005). The transmitter and the receiver were installed on 10 m towers with an altitude difference of approximately 46 m. The receiver was installed at the highest part of the basin (upland) whilst the transmitter was installed at the lowest part of the basin (Figure III.5). The direction of the

LAS path was 250° from the north. At the receiver tower, a 2D anemometer (Wp200, R.M. Young Company, Traverse City, MI, USA) to measure wind speed and direction at 10 m was also installed. Additionally, the air temperature and humidity were measured using Vaisala HMP45C probe.

III.2.3. Spatial data

III.2.3.1. MODIS and MSG data

a. MODIS products

The MODIS instrument operates on both Terra and Aqua spacecraft. It has a viewing swath width of 2330 km and views the entire surface of the Earth every 1–2 days. Its detectors measure 36 spectral bands between 0.405 and 14.385 μm, and it acquires data at three spatial resolutions: 250 m, 500 m, and 1000 m. The MOD15A2 LAI is a 1 km global data product updated once every 8 days derived from the MODIS sensor on board TERRA. The MODIS LAI algorithms were developed jointly by personnel at Boston University, the University of Montana SCF and NASA GSFC. The algorithm consists of a main procedure based on the inversion of a 3D radiative transfer model thanks to a look-up-table. This algorithm exploits the spectral information content of MODIS surface reflectances at up to seven spectral bands. Should this main algorithm fail, a back-up algorithm is triggered to estimate LAI empirical relationships with vegetation indices. The LAI products in the collection version 5 are available from 2001 to present. The MCD43B3 α product is upscaled from MCD43A3 and provides both the white-sky-albedo (α) and the black-sky- α at 1-km resolution every 16 days. Both Terra and Aqua data are used in the generation of this product. We were interested in a single integrated value over the entire solar emission spectrum (0.3–5.0 μm) called shortwave broadband α. The black-sky- α (directional hemispherical reflectance) is a directional α corresponding to 100% of direct light; it depends on the solar zenithal angle unlike the white-sky- α (bihemispherical reflectance) which corresponds to a completely diffuse light. The "blue sky" α used in this study is a weighted average between these two extreme values. The weighting depends essentially on the aerosol content of the atmosphere (Lewis and Barnsley, 1994). In our case, we considered that we have 85% direct light and 15% diffuse, and the final α value is calculated as follows (Lewis and Barnsley, 1994):

$$\alpha = 0.85 * \alpha_{\text{black-sky}} + 0.15 * \alpha_{\text{white-sky}} \quad \text{(III.1)}$$

The MOD11A1 and MYD11A1 at 1 km spatial resolution under clear-sky conditions are the daily land surface temperature (LST) products, derived from Terra and Aqua, respectively. LST is derived from the brightness temperature using bands 31 and 32 through a generalized split-window algorithm. The daily level 3 MODIS LST (collection 5) were used in this study.

The MOD11A1 and MYD11A1 at 1 km spatial resolution under clear-sky conditions are the daily land surface temperature (LST) products, derived from Terra and Aqua, respectively. LST is derived from the brightness temperature using bands 31 and 32 through a generalized split-window algorithm.
The MOD13A2 provides spatio-temporal coverage of vegetation conditions via several indices at 1 km resolution as a gridded level-3 product in the Sinusoidal projection. One particular vegetation index of interest in this study is the normalized vegetation index (NDVI), available at 16 day temporal intervals. This product is derived from band 1 and 2 of the MODIS Terra satellite.

All MODIS products were downloaded from the website (https://search.earthdata.nasa.gov/search).

b. SEVIRI Land Surface Temperature

The Spinning Enhanced Visible and InfraRed Imager (SEVIRI) aboard Meteosat Second Generation (MSG) is a multi-spectral sensor, imaging across the visible and near-IR, which provides data with a high temporal and spectral resolution every 15 min in 12 wavebands, and image spatial sampling scales of 3 km for nadir view. The land surface temperature is estimated from top of atmosphere (TOA) brightness temperatures of SEVIRI split-window channels, centered on 10.8 and 12.0 μm, using a generalized split-window (GSW) algorithm (Wan and Dozier, 1996) with the adoption of SEVIRI data (Trigo et al., 2008). IR radiance is absorbed and scattered even by thin clouds and aerosols. Therefore, the retrieval of LST works only for completely cloud-free pixels and the quality of this product is automatically assessed by means of the accuracy of the parameters used in the LST algorithm. LST products used in this study are distributed by EUMETSAT through the Satellite Application Facility on Land Surface Analysis (LSA SAF).

III.2.3.2. SMOS data

The SMOS mission measures the natural (passive) microwave radiation around the frequency of 1.4 GHz (L-band). It aims to monitor SM at a depth of about 3–5 cm with a spatial

resolution of about 40 km and an accuracy better than 0.04 m^3/m^3 (Kerr et al., 2012). The revisiting time at the equator is every 3 days for both ascending and descending passes, which are sun synchronous at 6 am and 6 pm respectively. The SMOS level-3 1-day global SM product (MIR CLF31A\D, version 2.72 in reprocessing mode RE02) posted on the ~25 km Equal Area Scalable Earth (EASE) version 1.0 grid is used as input to DisPATCh algorithm.

III.3. Conclusion

Two different study sites, along with the remote sensing and meteorological data are described in this chapter. Thereafter, the Wankama Niger site will be used to validate the TSEB model (which provide estimates of evapotranspiration) over heterogeneous field. While, Haouz plain sites (including irriagated fields (Chichaoua and R3) and rainfed field (Bour)) will be used to test the robustness of the new version of TSEB model (named TSEB-SM) which integrates LST, SM and f_c simultaneously to retrieve the main parameters of soil evaporation (soil resistance) and plant transpiration (α_{PT}). Then, DISPATCh SM and MODIS data will be integrated within the TSEB-SM to provide large-scale estimates of evapotranspiration.

Chapter.IV. Validation of TSEB model over sparse and heterogeneous vegetation in Sahel region (Niger)

Chapter.IV. Validation of TSEB model over sparse and heterogeneous vegetation in Sahel region (Niger) 55

IV.1. Introduction 56

IV.2. Results and discussion 57

IV.2.1. Experimental data analysis 57

IV.2.2. Results of multi-Scale surfaces fluxes 61

IV.3. Summury and Conclusions 72

IV.1. Introduction

Estimates of turbulent fluxes (i.e., sensible and latent heat fluxes H and LE) over heterogeneous surfaces is not an easy task. The heterogeneity caused by the contrast in vegetation, hydric and soil conditions can generate a large spatial variability in terms of surface–atmosphere interactions.

SEB model driven by MODIS (Moderate resolution Imaging Spectroradiometer) and MSG (Meteosat Second Generation) observations in conjunction with an aggregation scheme are used to derive area-averaged H and LE over a heterogeneous watershed in Niamey, Niger (Wankama catchment) (Allies et al., 2017; Boulain et al., 2009; Ezzahar et al., 2009b; Ramier et al., 2009; Velluet et al., 2014). A spatial aggregation approach is conceived as a method which seeks to link the model parameters that control surface exchange (LST, α, d, z_0, LAI, h_c) on a patch scale with the area-average value of equivalent model parameters applicable on a larger scale or grid-scale, assuming that the same equations are used to describe surface fluxes at both scales (Ershadi et al., 2013; Ezzahar et al., 2009b, 2009a; Liu et al., 2016; Long et al., 2011). In general, aggregation scheme can be applied on the input requirements (Ezzahar et al., 2009b) or directly to predicted fluxes (Saadi et al., 2018). Nevertheless, the efficiency of this approach lies on the evaluation of their outputs/performances against field observations, which requires the development of a measurement network at the local scale such as Eddy covariance systems (Baldocchi, 2014; Baldocchi et al., 2018, 2016, 2001). Such a system is very costly, and man-power demanding with a competent staff for data processing and maintenance, as well as an important energy supply for operation. To overcome these difficulties, Large Aperture Scintillometer (LAS) is one of the alternative techniques employed to validate the satellite remote sensing H and LE estimates due to the comparable spatial resolutions. It has already been used in various contexts over complex topography and heterogeneous vegetation cover (Brunsell et al., 2011; Ezzahar et al., 2009b; Liu et al., 2013). Consequently, LAS is becoming popular in hydro-meteorological studies because it is relatively cheap, robust, and easy to operate and maintain. Additionally, the LAS can be potentially used to improve the representation of surface heterogeneity in land-surface-atmosphere models operating at large scales.

In this chapter, the thermal-based two-source energy balance (TSEB; (Norman et al., 1995)) has been chosen as it has been evaluated with success in different contexts including sparse canopy in semi-arid areas (Diarra et al., 2017; Kustas and Norman, 1999). TSEB algorithm is described in detail in chapter 3. As far as we know, the TSEB model has never been tested over a heterogeneous Sahelian agro-ecosystem. Therefore, a validation at patch scale was firstly investigated using in-situ measurements from three eddy-covariance stations sampling the dominating canopy (millet, fallow and degraded shrubs) of the studied area. TSEB predictions of the convective fluxes are then evaluated at the scintillometer fooprint scale by aggregating the station scale predictions fed by the in-situ observations of albedo, LST and Leaf area index (LAI). In a second step, remote sensing products are used. A first evaluation is directly conducted at the scale of the scintillometer measurements by using 3 km LST observations from the MSG SEVIRI instrument. Finally, three aggregation schemes of MODIS products are tested to assess if a better representation of heterogeneity based on the 1-km products improves our large-scale estimates. Data collected in the context of the African Monsoon Multidisciplinary Analysis (AMMA) program

IV.2. Results and discussion

As a preliminary step, the quality of experimental data including EC and scintillometer surface fluxes and satellite products are assessed. In a second step, the TSEB predictions are evaluated at the station scale. Finally, the TSEB predictions of the convective fluxes are evaluated at the scale of the scintillometer fooprint: (1) by aggregating the station scale predictions using the in- situ observations of albedo, LST and LAI. This constitutes the ideal case (2) by using 3 km LST observations from the MSG SEVIRI instrument directly at the scale of the scintillometer measurements; and (3) by testing three aggregation schemes of MODIS products in order to assess if a better representation of heterogeneity based the 1-km products improves our large-scale estimates

IV.2.1. Experimental data analysis

IV.2.1.1. In-situ surface fluxes

The quality of EC measurements is usually assessed by assuming that the energy balance is closed. The comparison of the (R_n-G) and the sum of the latent and sensible heat fluxes ($LE_{EC} + H_{EC}$), measured independently by the EC systems (data not shown here), showed an underestimation of the turbulent fluxes by about 8%, 17%, and 20% for the millet, fallow and

degraded shrubs, respectively. Several practical reasons preclude perfect closure (Foken et al., 2006), e.g. spatial scale discrepancies between measurements of energy balance components, and spatial heterogeneities; storage between measurement levels (canopy and superficial soil); so-called eddy flux losses (not measured here); difficulties with ground flux estimation (Guyot et al., 2009; Heusinkveld et al., 2004). Results reported in other experimental studies have shown that balance shortfalls commonly stand between 10% and 40 % of the available energy (Foken et al., 2006; Mauder and Foken, 2006). As a conclusion, closure is quite satisfactory for our experiment, especially at the millet site which was more homogenous than fallow and degraded shrubs sites.

Figure IV.1 plots the time series of the average between 9 am and 5 pm of H_{LAS}, and LE_{LAS} during the entire study period. Note that the scintillometer only calculates H, and LE is derived as a residual term of the energy balance ($LE_{LAS} = R_n - G - H_{LAS}$). In this case, the available energy has been aggregated using the values measured at each instrumented field ($< R_n - G >_{agg} = \sum_1^3 f_i (R_n - G)_i$). Stages 1, 2 and 3 present respectively the beginning of season (June 1st –mid July), the growing stage which took place over two months (mid July-to mid-September) and the senescence stage (from mid-September). Preliminary to the scintillometer data analysis, a comparison between H_{LAS} against weighted EC fluxes was done for the wind direction interval 70° to 250°, because the footprint of the LAS covers the monitored sites where the EC systems were installed. The statistical results show a good agreement between the LAS sensible heat fluxes and those derived from the EC systems with a relative error of about 20% (Ezzahar et al., 2009b). The H_{LAS} and LE_{LAS} dynamics are almost stable throughout the season and LE_{LAS} does largely dominate H_{LAS} through the growing stage. Rainfall is rather regular between mid-July and mid-September, which ensured enough soil moisture to keep millet growing until mid-September. It can be seen that every rainfall event caused an immediate response with a significant energy shift between H and LE. LE_{LAS} is around 200 W/m^2 and increases after each rain event, and peaks at the end of August with 315 W/m^2, which corresponds to the LAI peak for Millet crop (Boulain et al., 2009). In the same period, soil moisture was high and reached its maximum. Some points with very low LE_{LAS} values were recorded during the growing stage which can be explained by the very dry conditions or by a considerable amount of bare soil. A sharp increase of LE_{LAS} was shown after the 40-mm rain event of 20nd September. However, LE_{LAS} decreases systematically from the end of September to the end of October, while H_{LAS} reaches its maximum (265 W/ m^2).

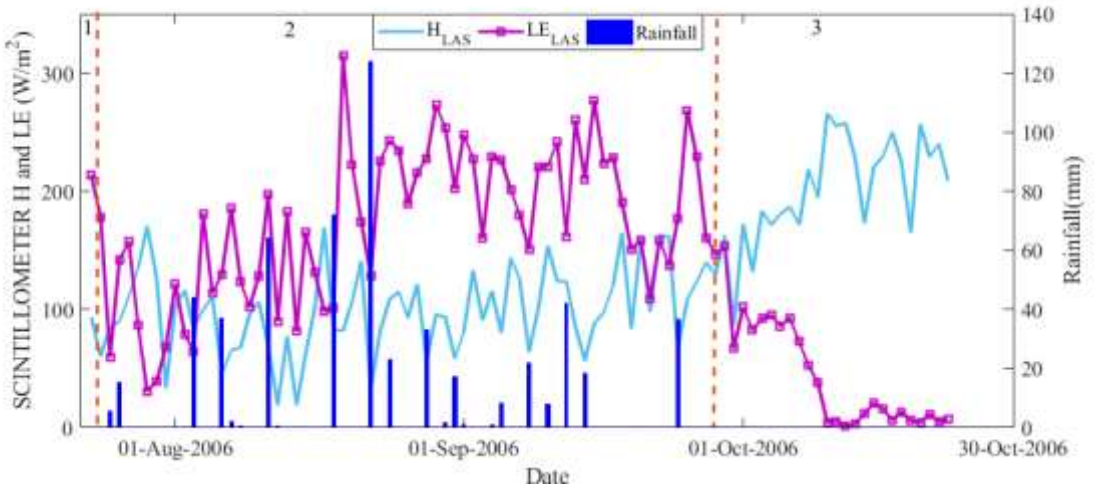

Figure IV. 1. *Time series of LAS latent and sensible heat fluxes (daily average between 9am and 5pm)*

IV.2.1.2. Remote sensing products

First, an evaluation of the agreement between MODIS albedo and LST products and in-situ measurements is required because of their great influence on the predicted fluxes. This comparison is carried out only for clear sky days when MODIS images are available. Figure IV.2 displays the scatter plots of MODIS derived LST and albedo against in-situ measurements, for millet and fallow sites as only one month of measurements were available for the degraded shrub site. The agreement between MODIS and measured albedo is relatively poor (RMSE=0.05, R=0.45). This may be attributed to the lack of representativity of the sites covered by relatively dense vegetation with regards to the north from the LAS path mainly composed of bare soil. This lack of representativity is particularly prominent in the Sahel as soils are very clear, especially at the beginning (July) of the season. The dry spell produced a short period of albedo increase. During the rain events, albedo follows a very markedly decreasing general trend, with large fluctuations due to alternating dry and wet spells (Ramier et al., 2009). This assumption is supported by the observed positive bias of 0.03. The LST comparison shows a reasonable correlation of R=0.77 with an RMSE=3.8 K, and an underestimation of LST MODIS by -1.8 K on average. The RMSE is on the upper limit of the values reported in the literature that usually range between 2 and 4 K (Yu et al., 2014). The observed scattering may also stem from the fact that the in-situ LST is not representative for the satellite LST. A finer look at the results highlights also a very contrasted bias between the two sites: over Millet that dominates the Wankama land use with 58% of the area, the bias is logically low (MBE=-0.5 K) while it reaches more than -4 K over the denser and thus colder vegetation of the fallow site.

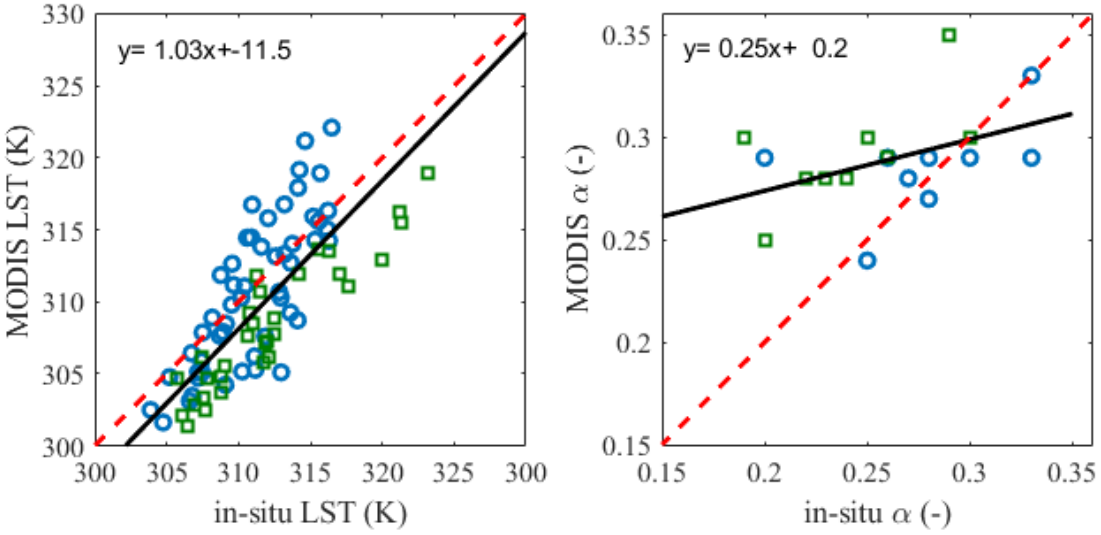

Figure IV. 2. *Scatterplot of MODIS Ts (a), and α (b) versus in-situ data (only Millet and Fallow sites are considered)*

Finally, Figure IV.3 shows an intercomparison of MSG SEVIRI and MODIS LST averaged over a 3 x 3 pixel windows to match the MSG resolution at time of Terra and Aqua MODIS overpasses. The overestimation of MSG SEVIRI LST with regards to MODIS LST is prominent along the whole LST range. This could be linked to the view zenith angle differences between MSG SEVIRI and MODIS satellites. The impact of changes in viewing angle is enhanced with surface heterogeneities. In addition, LST was retrieved using one MSG SEVIRI window channel (10.8 µm), while the MODIS algorithm is based on two windows channel (11.03 µm and 12.02 µm). These dissimilarities related to the spectral characteristics of the two instruments can induce the observed differences in retrieved LST. Finally, the positioning error of MSG that has been found to reach up to 8 pixels i.e. ~30 km (Aksakal et al., 2013) could also explain this over-estimation, in particular if the pixel is shifted to the north of the area characterized by bare and hot soils.

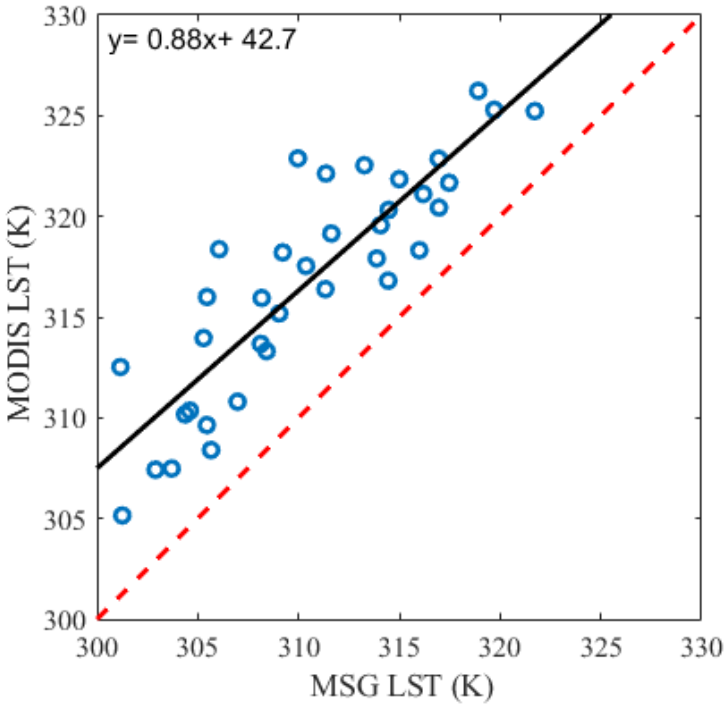

Figure IV. 3. *Scatterplot of MODIS versus MSG SEVIRI LST*

IV.2.2. Results of multi-Scale surfaces fluxes

The TSEB predictions are evaluated at the station scale both using in-situ and MODIS derived products. Focus is then put on the evaluation of TSEB at the grid scale using in-situ, MODIS and MSG products.

IV.2.2.1. Station scale

a. Using in-situ data

The available energy and turbulent fluxes predicted by the TSEB model are compared to those measured over the three eddy covariance stations at half-hourly time step. Table IV.1 summarizes the statistical results including the number of observations (n), the correlation coefficient (R), the root mean square error (RMSE), and the mean bias error (MBE). It can be seen that the TSEB model estimates correctly the available energy (R_n-G) with RMSE of 52, 49, 57 W/m² for millet, fallow and degraded shrubs (see figures IV.4.a, IV.4.b and IV.4.c), respectively. A first remarkable feature is the slight underestimation (-23 W/m^2) for the millet site. The second remarkable feature is a stronger dispersion for the degraded shrubs area. This dispersion is mainly related to the estimation of the soil heat flux, with RMSE=38 W/m^2, Mean Bias Error MBE=23 W/m^2 and RMSE=60 W/m^2, MBE=54 W/m^2 for the millet and

degraded shrubs sites, respectively. Indeed, affected by the complexity of the physical processes that occur in the soil as well as the vegetation cover, soil heat flux is the most difficult parameter to estimate with great precision. Several studies have pointed out this difficulty in estimating G especially on sparse vegetation (Ezzahar et al., 2009b, 2009a, 2007). In addition, measuring this parameter at 5 cm and in sparse vegetation represents a major challenge to get representative measurement. The installation of heat flux plates in the soil must take into account several criteria: the plates must be totally covered to ensure that it is not directly exposed to the sunlight especially when the soil is very sandy as in the Wankama catchment where sand represents 80 to 90% (Verhoef et al., 2012). Additionally, heavy rainfall within a few hours, which is relatively common in the Sahel region, can uncover the plates and thus lead to exposing them to sunlight. Moreover, the use of the Brutsaert formula (developed for clear sky days by Brutsaert (Brutsaert, 1975) for the incoming longwave radiation (that replaced the measurements when they were not available for this station, to estimate R_n) can create a significant dispersion for low radiation values in cloudy conditions (Ezzahar et al., 2007).

The agreement between the measured and predicted turbulent fluxes is obviously lower than for the estimated available energy (see figures, IV.4.d, IV.4.e and IV.4.f for H and IV.4.g, IV.4.h and IV.4.i for LE)but, despite a significant dispersion, correlation coefficients and RMSEs are encouraging (Table IV.1). The observed dispersion can be related to the footprint effect, as the footprint of the EC system is considerably larger than the representativity scale of the measured input variables (mainly α, LST and LAI). In addition, other parameters such as roughness length (z_{0m}) and displacement height (d) were estimated as a fraction of the vegetation height using classical rules of thumb (Shaw and Pereira, 1982; Thom, 1971). These equations have been established for homogeneous and dense covers while the study sites are heterogeneous and sparse. A further step to minimize dispersions would be to estimate these variables using EC data following Hoedjes et al. (2007) and Lagouarde et al. (2006). Finally, several empirical and constant model parameters have been used in the TSEB model, which require calibration according to the specific conditions of the study area. Among them, the Priestley-Taylor parameter (α_{PT}) directly relates latent heat flux to the available energy at the surface. Most studies driven by TSEB model have used its theoretical value of 1.26 (Bindlish et al., 2001; Colaizzi et al., 2014; Kustas and Norman, 1999; Norman et al., 1995). Other studies have identified that it is variable under different surface and atmospheric conditions (varies in the range 0.5-2). In particular, the α_{PT} was found to be smaller for dry surfaces and higher for humid conditions (Eichinger et al., 1996). In the same context, (Ait Hssaine et al.,

2018b) demonstrated, using a new TSEB-based evapotranspiration model (called TSEB-SM), that α_{PT} cannot be considered as a constant because it varies in time according to several factors including LAI, green vetation cover fraction and soil water availability. In particular, it can take extreme values under dry, water deficit and advective conditions. Interestingly enough, the partition between latent and sensible heat fluxes is correctly reproduced for the degraded shrub site (mean biases lower than 0.92 W/m² and 11 W/m^2 for respectively, H and LE). Indeed the results of sensible heat flux over the millet crop matches perfectly with the results found by Lhomme et al. (1994) (RMSE=43 W/m^2) who used a two layer model to estimate H from LST. Lhomme et al. (1994) used an empirical relationship between LST and Ta ($\delta T = a(LST - Ta)^m$), m and a being statistically determined by adjusting the modelled to the H observed by the Bowen ratio method.

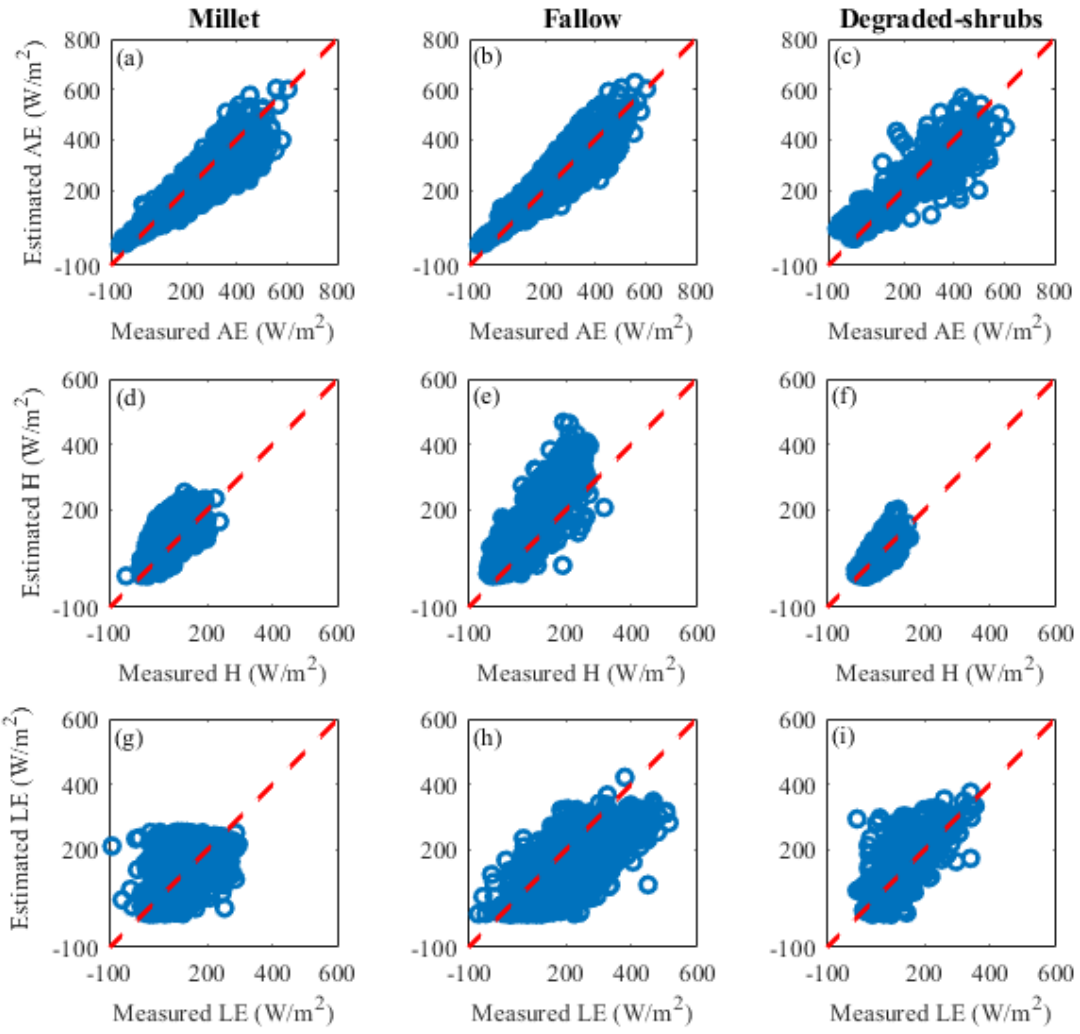

Figure IV. 4. *Scatterplot of simulated versus observed AE,H and LE for the (left) Millet, (middle) Fallow and (right) Degraded shrubs, respectively, using in-situ data.*

Table IV. 1. Statistical metrics of the comparison between measured and estimated values of available energy and turbulent fluxes (H and LE) at patch and grid scale

		Fluxes	n	R	MBE	RMSE
			(-)	(-)	(W/m^2)	(W/m^2)
Patch-scale (using in-situ data)	Millet	H	1442	0.81	26	43
		LE	1442	0.69	-17	66
		R_n-G	1442	0.92	-23	52
	Fallow	H	1905	0.89	-21	40
		LE	1905	0.88	0.38	65
		R_n-G	1905	0.98	-37	49
	Degraded-shrubs	H	486	0.82	0.92	24
		LE	486	0.71	11	65
		R_n-G	486	0.95	-42	57
Patch-scale (using MODIS data)	Millet	H	52	0.45	13	31
		LE	52	0.58	58	94
		R_n-G	52	0.67	4	50
	Fallow	H	52	0.73	25	54
		LE	52	0.71	32	93
		R_n-G	52	0.79	23	69
	Degraded-shrubs	H	-	-	-	-
		LE	-	-	-	-
		R_n-G	-	-	-	
Grid-scale (using *in-situ* data)		H	370	0.87	-21	37
		LE	186	0.72	39	75
Grid-scale using MSG SEVIRI data		H	51	0.39	-19	65
		LE	51	0.2	32	75
Grid-scale (using MODIS data)	Scheme 1	H	20	0.71	-48	73
		LE		0.85	73	102
	Scheme 2	H	20	0.7	-30	65
		LE		0.82	49	91
	Scheme 3	H	20	0.71	-23	63
		LE		0.82	45	88

b. Using MODIS

An intercomparison between (R_n-G) and turbulent fluxes measured by each station and the fluxes estimated by TSEB model using MODIS data is done and the error statistics are reported in Table IV.1. Overall, the discrepancies between the available energy estimated from TSEB model and measured one, for both sites (millet and fallow) is likely due to greater scatter between MODIS and measured α, and to the difference between MODIS and in-situ LST. In all cases, LE does largely dominate H through the growing season (July-September), in particular for the fallow field. For the Millet site, the late start of the rainy season had significant adverse effects and the crop was not able to take advantage of the abundant rainfall because of insufficient plant development (Boulain et al., 2006). For both sites, an overestimation of simulated LE compared to measured ones is recorded at the end of the season. Indeed, the saturation of TSEB in the higher range of LE is due to the fixed maximum value for α_{PT} (equal to 1.26) (Ait Hssaine et al., 2018b). The structure of the model cannot accommodate large evaporative demand conditions and strong advective conditions (Song et al., 2016b). Moreover, the change in wind direction in monsoon periods strengthens advection effects. As conclusion, TSEB prediction although slightly biased at the end of the season reproduces quite well the observations: RMSE/ MBE are relatively low for both Millet and Fallow sites.

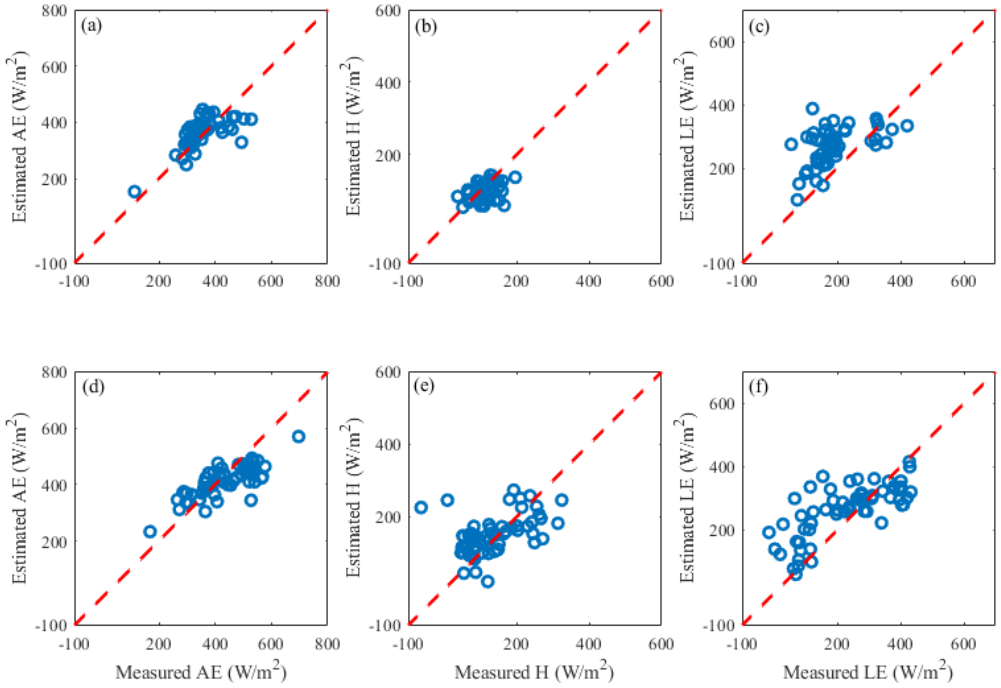

Figure IV. 5. *Scatterplot of simulated versus observed AE,H and LE for the (left) Millet, (middle) Fallow and (right) Degraded shrubs, respectively, using MODIS data.*

IV.2.2.2. Grid scale

a. Using in-situ data

Figure IV.6 displays the comparison between three sites-averaged turbulent fluxes values derived from TSEB model using weighted input data (LST, α, d, z_0, LAI, h_c) compared against the turbulent fluxes measured by the scintillometer. The corresponding statistics are shown in Table IV.1. TSEB provides satisfying results for the sensible heat flux with a relative error of about 24% (R=0.87, RMSE=37 W/m^2, MBE=-21 W/m^2). Indeed, the scintillometer path is very heterogeneous. This can generate a difference in flux even between two adjacent plots. Therefore, the dispersion observed can be related to the differences in the footprint of LAS, as well as to the uncertainties of the similarity stability functions. The surface temperature is a key parameter for turbulent fluxes and for monitoring the energy balance. Weighted LST over heterogeneous surface using locally measured values can lead to errors in the partition of temperature between soil and vegetation, and consequently to estimate sensible heat flux. A visual assessment of scatter plots in 4.6.b and the statistics (Table IV.1) clearly indicates that TSEB overestimates LE fluxes with MBE=39 W/m^2, especially at the end of the season. LE measured by the LAS never exceeds 300 W/m^2 while

simulations reach 400 W/m^2, which could be related to the fixed value of α_{PT} to 1.26. Note also that any error in the available induces the LE_{LAS} errors.

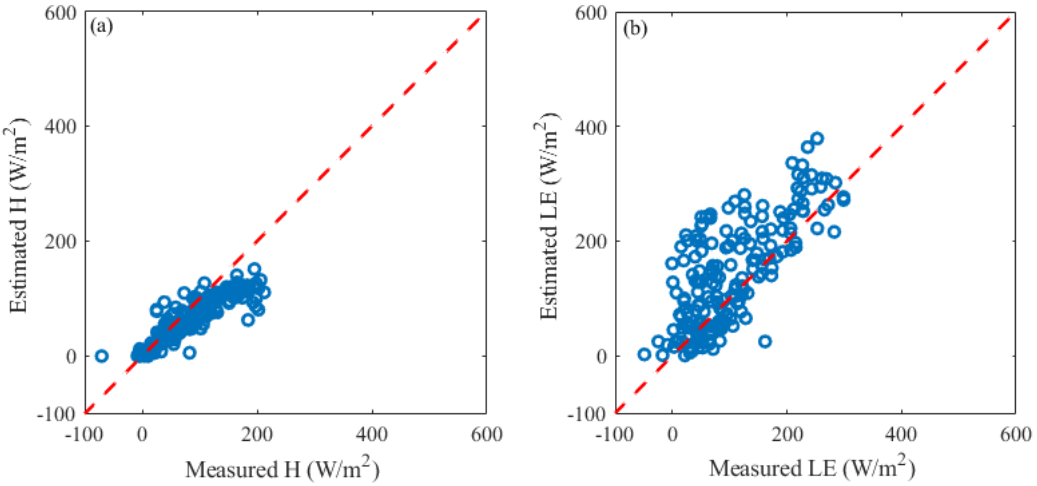

Figure IV. 6. *Sensible (a) and latent (b) heat fluxes scatterplots between LAS measurements and TSEB prediction feeded by aggregated in-situ data (at 30min time).*

b. Using 3km MSG SEVIRI LST

Here, MSG SEVIRI LST is used to simulate H and LE by TSEB directly at the scale of the scintillometer path (3 km) spanning the three vegetation types (only the interval 70° to 250° is considered). Those data were used in conjunction with an average of a 3 x 3 pixel MODIS area for α and LAI. TSEB estimates are compared to H_{LAS} and LE_{LAS}. According to precipitated amounts during the growing season, the LE is noticeably higher at the fallow site compared to millet site (Patch scale). Note that the MSG SEVIRI pixel covers diverse land cover (millet, fallow, degraded shrubs and bare soil), which can explain the discrepancies obtained between MSG SEVIRI-based and measured LE (Figure IV.7.b). By contrast, the overestimation of H at the end of the season is linked meanly to the higher surface temperatures measured by MSG SEVIRI. It is reminded that the scintillometer fetch doesn't exceed a hundred meters, while the MSG SEVIRI resolution at the study site is about 3 km.

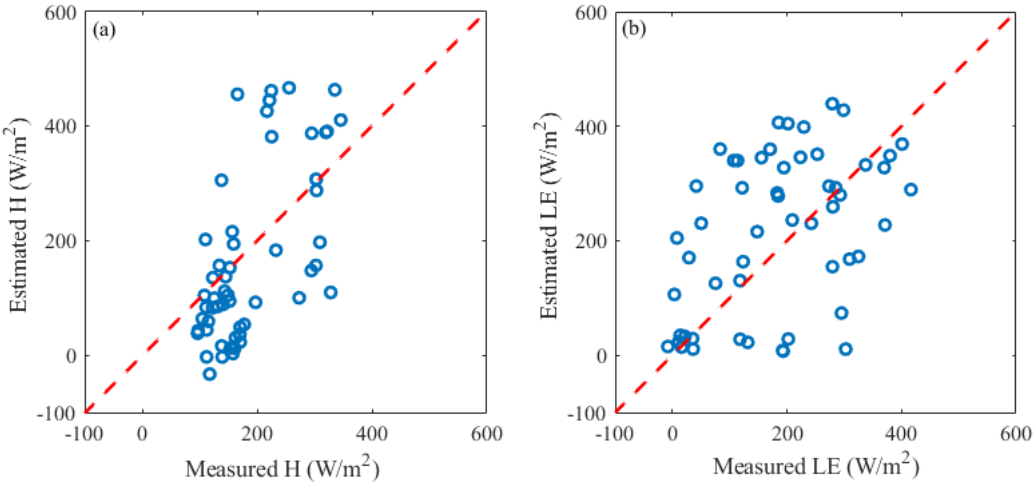

Figure IV. 7. *Sensible and latent heat fluxes scatterplots of the comparison between the LAS grid scale measurements and TSEB predictions based on MSG SEVIRI products (at MSG-SEVIRI overpass time).*

c. Using MODIS products

In this section, the effect of land cover heterogeneity on the estimated turbulent fluxes has been studied by combining TSEB model driven by Terra and Aqua remotely sensed data and an aggregation scheme, at Terra-MODIS and Aqua-MODIS overpass time. Figure IV.8 displays results for three different aggregation schemes (the simple averaging at the MODIS resolution scale (scheme1 (IV.8.a, IV.8.d)), the simple averaging over the footprint extent (scheme2 (IV.8.b, IV.8.e)), and a weighted average of the footprint extent (scheme 3 (IV.8.c, IV.8.f). Statistical metrics are reported in Table IV.1.

The simple averaging method using MODIS resolution data in Figure IV.8.a underestimates H with a relative error of about 21% (RMSE =73 W/m^2, R=0.71, MBE=-48 W/m^2). The correspondence between simulated and measured fluxes for scheme 2 is good compared to scheme 1 (figure IV.8.b). The relative error was about 13%, the RMSE value was 65W/m^2, and the linear regression forced through the origin yielded an R of 0.70 and the mean bias error was reduced to -30 W/m^2 instead of -48 W/m^2 for the first scheme. H simulated by using scheme 3 in figure IV.8.c is closer to the 1:1 line, providing a quite significant improvement with regards to the second scheme. The RMSE and the mean bias error between the simulated and measured values were 63 and -23 W/m^2, respectively. The relative error of 10% indicates that the scheme 3 is very reliable in providing area-averaged sensible heat flux over heterogeneous surfaces.

In a subsequent step, simulated LE was compared to the observed one using the three schemes described before. As shown in figure IV.8.d, the Scheme 1 overestimates LE with a relative error of about 58% (RMSE= 102 W/m^2, R=0.85, MBE=73 W/m^2). That can be explained by the fact that LE is a residual term affected by errors in both available energy and sensible heat flux. Figures IV.8.e and IV.8.f plot simulated versus observed LE for the simple scheme 2 and scheme 3. TSEB provides satisfying results with a RMSE of 65 W/m^2 and 63 W/m^2, and relative error of 39% and 35% for the second and third schemes, respectively. Based on the above results, the first scheme could not achieve satisfactorily the upscaling of turbulent fluxes over heterogeneous land surfaces. In fact, the method considers that all pixels belonging to the footprint of LAS contributes 100% of the pixel value, even for pixels of low contribution. This will obviously lead to large differences in LST, which is a key feature for determining the turbulent fluxes.

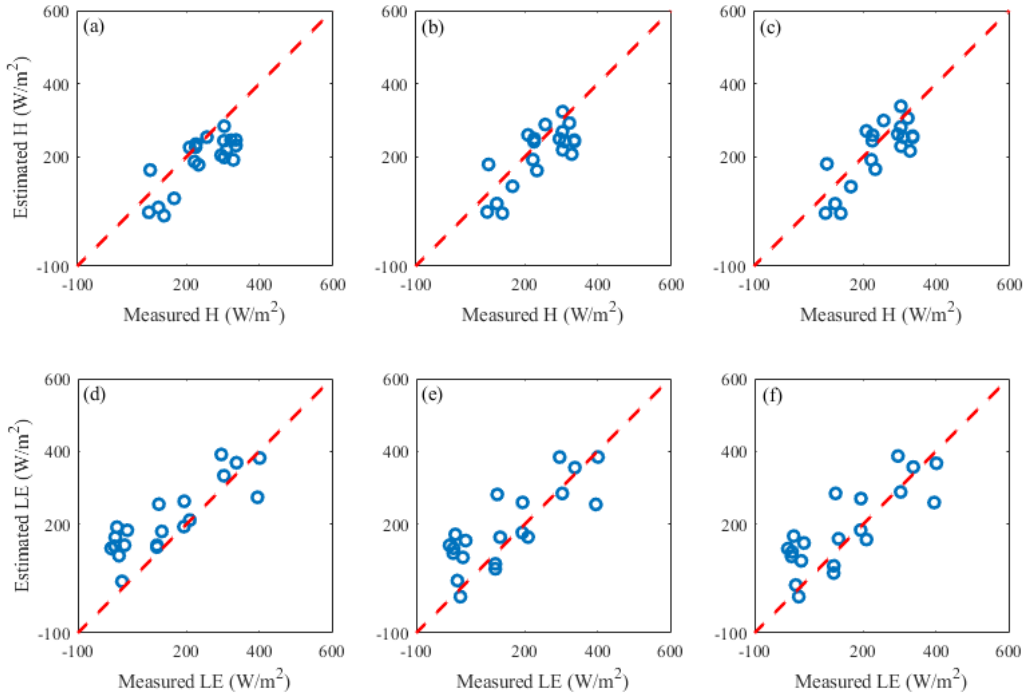

Figure IV. 8. *Sensible and latent heat fluxes scatterplots of the comparison between the LAS grid scale measurements and TSEB predictions based on MODIS products for a simple averaging (a,d), area weighted method (b,e) and footprint weighted method (c,f) (at MODIS overpass time).*

To go further into the comparison, the Figure IV.9 shows the time series of the convective fluxes observed by the LAS (H_{LAS} and LE_{LAS}) at the time of the satellite overpass and simulated by TSEB based on MODIS products for the footprint weighted method (H_{sim} and LE_{sim}). According to the availability of MODIS images, and considering the wind direction

interval 70° to 250°, only LAS data from mid-August to the end of the experiment on 22 October were available. Despite a significant scattering, both observed and simulated fluxes depict a similar behavior with a gradual switching of available energy from latent to sensible heat following the last rainfall around mid-September. An interesting feature is the underestimation of H by TSEB during the senescence while LE is overestimated for the same period. This could be attributed to the constant value of α_{PT} equal to 1.26 used in this study. Indeed, this value is usually accepted for semi-arid to sub-humid agricultural areas under irrigation regime (Anderson et al., 2007; Diarra et al., 2017; Norman et al., 1995) while it has been shown that lower α_{PT} are obtained for dry areas such as in our region of study after the end of the rainy season. Finally, the obtained significant scattering, in particular after the last rainfall could also be related to the radiative properties of vegetation that are not well represented for dry vegetation.

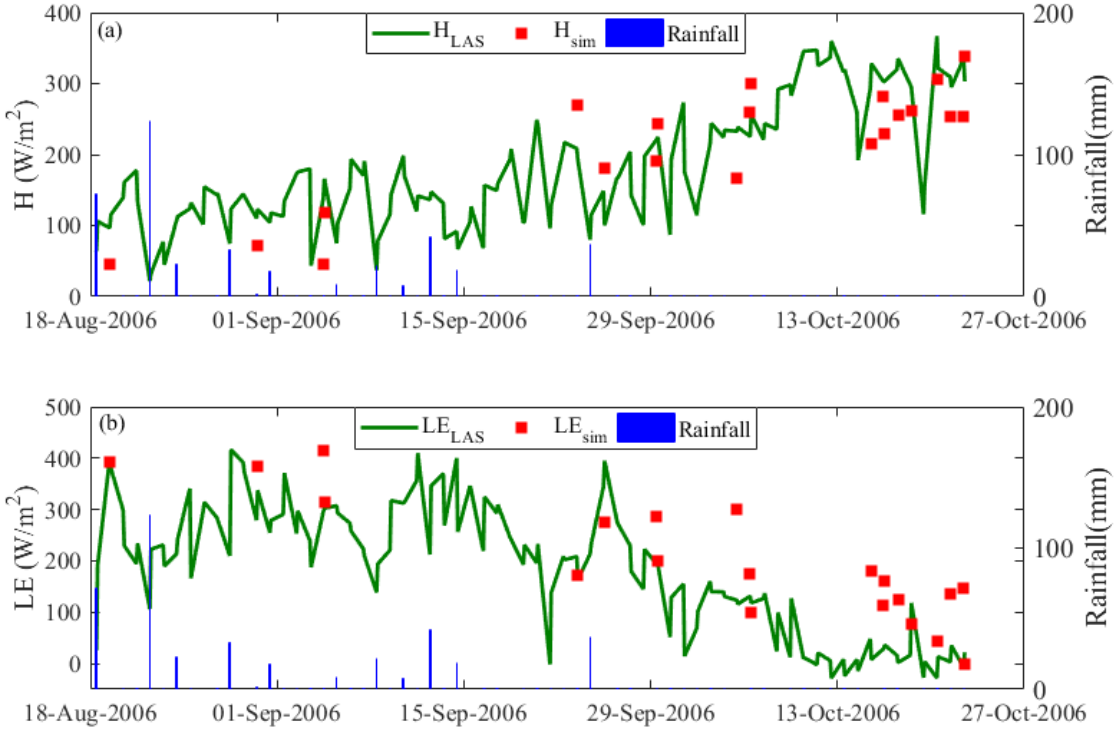

Figure IV. 9. *Time series of the comparison between the LAS grid scale measurements ($H_{LAS}$and LE_{LAS}) and TSEB predictions based on MODIS products (H_{sim} and LE_{sim}) for footprint weighted method (at MODIS overpass time).*

IV.3. Summury and Conclusions

The main objective of this chapter is to estimate the turbulent fluxes over a path covering the three dominant crops (millet, fallow and degraded shrubs) in the Wankama basin by combining TSEB model, an aggregation method and satellite data (MODIS and MSG SEVIRI). The data used to validate this approach were collected within the framework of the AMMA project. Each site was equipped with meteorological stations and Eddy Covariance systems for monitoring the energy and water balance as well as the soil and vegetation characteristics. In addition, a large aperture scintillometer was installed over a transect of about 3.2 km spanning the three dominant vegetation types (with contrasted energy balances and different fluxes behaviours) to derive the integrated H and LE values over this heterogeneous landscape. Our approach was organized into three steps. The experimental data including in-situ surface fluxes and remote sensing products were evaluated. The TSEB model was then evaluated at the station scale for the three study sites (millet, fallow and degraded shrubs) instrumented with EC systems. Finally, the TSEB prediction of surface

fluxes were evaluated at the grid-scale based on in-situ data (at the 30 min time), MODIS (at Terra and Aqua overpass time), and MSG products (at MDG-SEVIRI overpass time) and aggregation schemes.

The results obtained at the station scale for H and LE are relevant, especially when using in-situ data given the complexity of the study sites and in the range of what has been reported in the literature in terms of RMSE and correlation coefficient. Some scatter was noted, which is mainly related to the difference in footprints of the measuring instruments (about 100 m for EC systems with regard to less than 10 m for inputs variables such as LAI, albedo and LST), as well as to the fixed maximum value for α_{PT} (equal to 1.26) during the entire season. Despite this dispersion and as already underlined by several authors, TSEB provides with good performances for H and LE prediction at the station scale by using in-situ measured inputs or, to a lesser extent, MODIS derived inputs.

TSEB was then evaluated at the (1 km and 3 km) grid-scale along the scintillometer transect spanning a heterogeneous landscape. To this end, in-situ data were first aggregated to estimate the mean turbulent fluxes. In this ideal case where the major inputs are well known thanks to in-situ measurements on the dominant vegetation type, the predicted fluxes obviously showed a good agreement with the scintillometer observations with statistical metrics on the same order of values as those of the comparison at the station scale (RMSE=37 W/m^2 and 75 W/m^2 for H et LE, respectively) although some dispersions were observed. The latter were explained by the difference in the footprints of the measuring instruments as well as because LE_{LAS} was calculated as a residual term of the energy balance using the average available energy values derived from measurements at each site. In a second step, TSEB is validated at the grid-scale but with remotely-sensed inputs. To this objective, MSG SEVIRI and MODIS sensors only offers a revisit time able to sample the high inter- and intra-daily variability of the SEB in semi-arid areas. The first assessment was performed by using the MSG SEVIRI LST at 3 km without explicit representation of the sub-pixel heterogeneity. The agreement between H and LE simulated by TSEB model and scintillometer observations is very poor, in particular in terms of temporal dynamic (R=0.39 and 0.2 for H and LE, respectively). This dispersion could be attributed to the large bias on MSG SEVIRI LST linked to the heterogeneity of land cover. In addition, this highlights the need to represent the sub-pixel heterogeneity. This was tested in a final step by using 1-km MODIS products as input of the TSEB model and 3 aggregation schemes. If the results with the simplest aggregation scheme consisting in averaging MODIS inputs independently of the footprint

provides poor results (RMSE of 73 W/m^2 and $102W/m^2$ for H and LE, respectively), the statistical metrics based on the two other aggregation schemes are encouraging. In particular, the scheme 2 considering the MODIS pixel included in the scintillometer footprint only but without weighting the values based on the footprint contribution as in the scheme 3, represents a good trade-off between accuracy and ease of implementation to map evapotranspiration over complex landscape.

In this chapter, LST has been extensively used to retrieve ET at a wide range of spatial resolutions. To improve these models to take into account the water stress conditions, TSEB formalism is modified (in the next chapter), to a new model named TSEB-SM, by using, in addition to LST and f_c data, the near-surface soil moisture (SM) as an extra constraint on soil evaporation. An innovative calibration procedure of TSEB-SM is proposed to retrieve the main parameters of soil evaporation (soil resistance) and plant transpiration (α_{PT}).

Chapter.V. Improving TSEB model by integrating sm data (TSEB-SM): a feasibility study using in-situ data (LST, $f_c$and SM)

Chapter.V. Improving TSEB model by integrating sm data (TSEB-SM): a feasibility study using in-situ data (LST, fcand SM)..... 75

V.1. Introduction 76

V.2. TSEB-SM Model Description and Implementation 77

V.3. Retrieving (a_{rss}, b_{rss}) and α_{PT} parameters 77

V.3.1. Calibration first step 77

V.3.2. Calibration 2nd step 78

V.3.3. Calibration 3th step 80

V.4. Results 82

V.4.1. Interpretation of α_{PT} variabilities 82

V.4.2. Surface fluxes 84

V.5. Summary and Conclusions 88

V.1. Introduction

Data available from space can help in implementing the PT approach from three distinct perspectives: i) applying a constraint on vegetation transpiration using an a priori value for α_{PT} (Anderson et al., 2008; Kustas et al., 1999; Norman et al., 1995), ii) applying a constraint on soil evaporation using SM data (Bindlish et al., 2001; Yao et al., 2017), or iii) retrieving the PT coefficient from vegetation indices (Fisher et al., 2008; Jin et al., 2011; Yao et al., 2017) or from an interpretation of the LST-vegetation index feature space (Jiang and Islam, 2001; Pérez et al., 2017; Wang et al., 2006). While LST, vegetation indices and SM are alternatively used by satellite-based PT approaches, few studies have combined all three data types. In fact, most studies have compared LST-based versus SM-based ET models separately (Gokmen et al., 2012; Kustas et al., 2003, 1998; Li et al., 2006). Given that SM controls the soil temperature (via the soil evaporation) and that LST integrates both soil and vegetation temperatures, the main issue to integrate simultaneously SM and LST into an unique model is to ensure a robust convergence of soil/vegetation temperatures (Kustas et al., 2003; Li et al., 2006) and associated evaporation/transpiration fluxes. The recent studies of Li et al. (2015) and Song et al. (2016b) combined LST and SM to better constrain ET but both approaches relied on a priori reduction coefficients of potential ET. Reduction coefficients of potential ET are equivalent to the soil evaporative efficiency (defined as the ratio of actual to potential evaporation, e.g. Merlin et al., 2016) and to the vegetation stress functions (defined as the ratio of actual to potential transpiration, e.g. Hain et al., 2009) for the soil and vegetation component, respectively. The point is there is no universal parameterization of both soil evaporation efficiency and vegetation stress functions. Alternatively, Sun et al. (2012) proposed an innovative assimilation method to calibrate the parameters of a SVAT (Soil Vegetation Atmosphere Transfer) model from available remote sensing variables including LST and SM. Assimilation results improved ET estimates but the retrieved parameters were mostly conceptual due to the simplicity of the surface model used.

First of all, the modification of the PT-based TSEB formalism (Norman et al., 1995) to integrate LST and SM data simultaneously (the modified version is named TSEB-SM), as well as the calibration procedure of TSEB-SM to retrieve the main parameters of soil evaporation (soil resistance) and plant transpiration (α_{PT}) are described in chapter 3. In the present chapter, the approach is tested over three irrigated wheat crops in the Tensift basin, by using in-situ data, central Morocco. In each case, the calibration procedure is tested and the

TSEB-SM latent and sensible heat fluxes are evaluated and compared against the original TSEB simulations.

V.2. TSEB-SM Model Description and Implementation

The TSEB-SM is the modified version of TSEB model, by using in addition to LST and f_c data, the near-surface soil moisture (SM) as an extra constraint on soil evaporation. A calibration procedure is proposed to retrieve three key parameters: α_{PT} and the pair parameters (a_{rss},b_{rss}) of a soil resistance formulation. Specifically, a_{rss}, and b_{rss} are retrieved at the seasonal time scale from SM and LST data with $f_c \leq f_{c,thres}$, while α_{PT} is retrieved at the daily time scale from SM and LST data for $f_c > f_{c,thres}$. The TSEB-SM is tested over 1 flood- and 2 drip-irrigated wheat fields using in-situ data collected during two field experiments in 2002-2003 and 2016-2017.

V.3. Retrieving (a_{rss}, b_{rss}) and α_{PT} parameters

V.3.1. Calibration first step

Figure V.1 plots the iterative values of a_{rss}, b_{rss} and mean α_{PT} during calibration step 1. Iteration 0 corresponds to default values. The convergence of all three parameters is very fast, requiring only 2 or 3 iterations for achieving a relative error better than 1%. This result confirms the appropriateness of separating the calibration range in f_c intervals where one parameter has significantly more weight on simulation results (i.e. simulated LST and associated fluxes) than the others. The calibrated pair (a_{rss}, b_{rss}) is (5.67, 1.40), (6.51, 3.82) and (9.47, 6.87) for the flood-, controlled drip- and reference drip-irrigated field, respectively. The mean retrieved values (7.2, 4.0) are relatively close to those estimated in Sellers et al. (1992) (8.2, 4.3). The variability of a_{rss} and b_{rss} can be explained by numerous factors such as soil texture (Merlin et al., 2016) and meteorological conditions (Merlin et al., 2011). Nevertheless, retrieved parameters are significantly different for both drip sites whereas they i) are located about 200 m apart only and ii) have similar soil texture and meteorological conditions. In fact, retrieved a_{rss} is an increasing function of retrieved b_{rss} due to compensation effects between a_{rss} and b_{rss} for a given SM and LST observation pair and regardless of soil properties and meteorological conditions. Such compensation reveals the empirical nature of the r_{ss} formulation in Sellers et al. (1992).

The mean value of α_{PT} at the semi-hourly time scale (see Figure V.2) is 0.81, 0.88 and 1.24 for the flood-, controlled drip- and reference drip-irrigated wheat fields, respectively. Note that the mean value is very close to the theoretical α_{PT} value for the reference drip-irrigated field case. It is suggested that f_g generally equals 1 at the maximum of α_{PT} (peak of ET), so that the maximum α_{PT} value is directly comparable to its default value (1.26) corresponding to fully unstressed conditions (Priestley and Taylor, 1972). Nonetheless, the mean α_{PT} is significantly smaller than the default value for the flood- and controlled drip-irrigated cases. Lower values can be associated with stress conditions that may have occurred during the crop development.

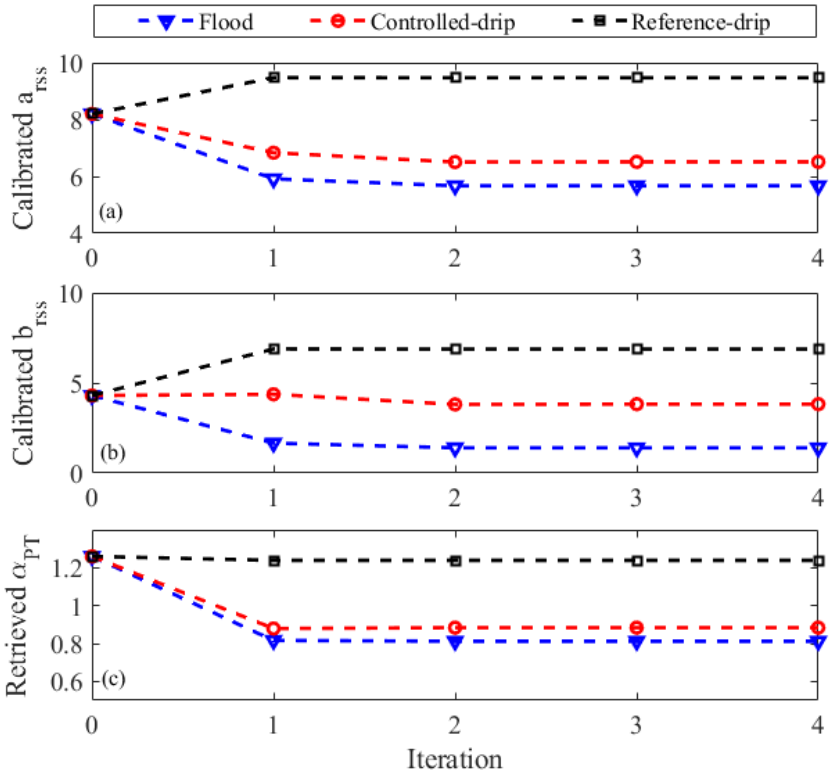

Figure V. 1. *Iterative values of a_{rss},(a), b_{rss} (b) and mean value of retrieved α_{PT} (c) for the flood-, controlled drip- and reference drip-irrigated wheat fields separately (calibration step 1).*

V.3.2. Calibration 2nd step

Figure V.2 plots the time series of daily retrieved α_{PT} for each site separately. It can be seen that the maximum value of daily α_{PT} varies from field to field. It is estimated as 1.8, 2.10 and 2.82 for the flood-, controlled drip- and reference drip-irrigated fields, respectively. It is clearly observed that the values related to drip irrigation are significantly greater than the values related to flood irrigation. This could be explained by the difference in agricultural

practices of each field (sowing date, irrigation events, rainfall and fertilization) as well as uncertainties in retrieved α_{PT}. Two effects are likely to explain the highly variable and excessively high retrieved α_{PT} values over the drip irrigated site for the first few daily retrievals. First, it is reminded that α_{PT} is retrieved for $f_c > 0.5$. When f_c is slightly larger than 0.5 (that is on the first few retrieval days of the season), large uncertainties in retrieved α_{PT} are expected because the soil surface still plays a significant role in the observed LST. Little response is shown for the first two months over the flood irrigation field, because the flux measurements over this site started when wheat was already well developed (f_c significantly larger than 0.5). Second, the R3 site is surrounded by homogeneous irrigated wheat fields while the drip irrigated fields are surrounded by dryland, which potentially reinforces advection effects, leading to enhanced retrieved α_{PT}. Note that the retrieved α_{PT} values above 2 and near 0 are due to the uncertainties in LST-derived daily estimates, especially during the periods when wheat is partially covering the soil.

As explained above, a smoothing function is applied to reduce uncertainties in daily α_{PT}. The smoothing length (it is one parameter of the smoothing function) is set to 10% of the total time series, that is about 10-20 days. Such a smoothing procedure is justified by the fact that both biomass and root-zone soil moisture commonly change across the agricultural season with a characteristic time of 1 to 2 weeks (Albergel, 2008). Furthermore, Figure V.2 clearly shows that the smoothing function removes all outliers while capturing significant patterns at the quasi daily scale. The smoothed α_{PT} ranges from 0.03 to 1.22, 0.17 to 1.26 and 0.61 to 1.38 for the flood-, controlled drip- and reference drip-irrigated wheat, respectively.

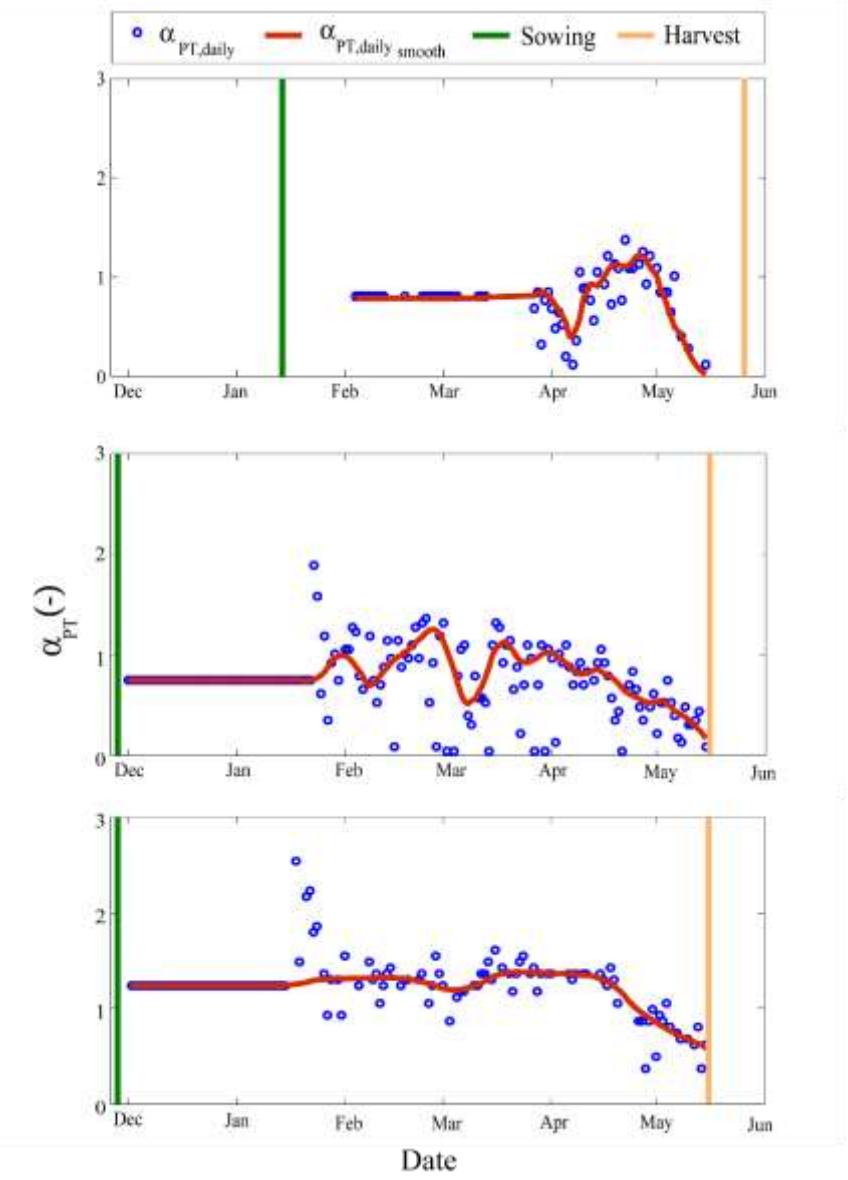

Figure V. 2. *Time series of daily retrieved and smoothed α_{PT} for the (a) flood-, (b) controlled drip- and (c) reference drip-irrigated wheat fields, separately (calibration step 2).*

V.3.3. Calibration 3th step

The normalization in Equation (3.27) of smoothed α_{PT} between its assumed minimum value (0) and smoothed maximum value makes the calibrated daily α_{PT} range from 0 to 1.22, 0 to 1.26 and 0 to 1.38 for the flood-, controlled drip- and reference drip-irrigated fields, respectively. Time series of calibrated daily α_{PT} are presented in Figure V.3 superimposed with f_c for comparison purposes. The maximum calibrated daily α_{PT} is close to the theoretical value of 1.26 in each case. However, its temporal variability is found to be significant even during the growing stage of wheat. Calibrated daily α_{PT} is more stable for the reference drip field than for both flood and controlled drip fields, with a relative change during the growing

period of 8.08% compared to 26.94% and 22.66% for the other two fields, respectively. This result is consistent with the fact that the reference drip field had been irrigated according to the water needs estimated by the FAO-56 method while the other two fields (flood and controlled drip) had been under water deficit conditions for one or several periods during the growing stage. Note that the controlled-drip field has a special feature in terms of α_{PT} daily dynamics. The maximum value is reached by the beginning of March, which is much earlier than the α_{PT} peak observed at the reference drip (around late April) and flood (beginning of May) fields, although wheat was sowed on the same date as reference drip field. It is suggested that the controlled drip-irrigated wheat did not recover well from the first (relatively long) stress period from 22/02/2017 to 06/03/2017. The irrigation water supplied after mid-March was probably not sufficient for the wheat of controlled drip field to catch up with the reference drip-irrigated wheat, even if the amount of water used for irrigation after this period was approximately the same (about 166 mm).

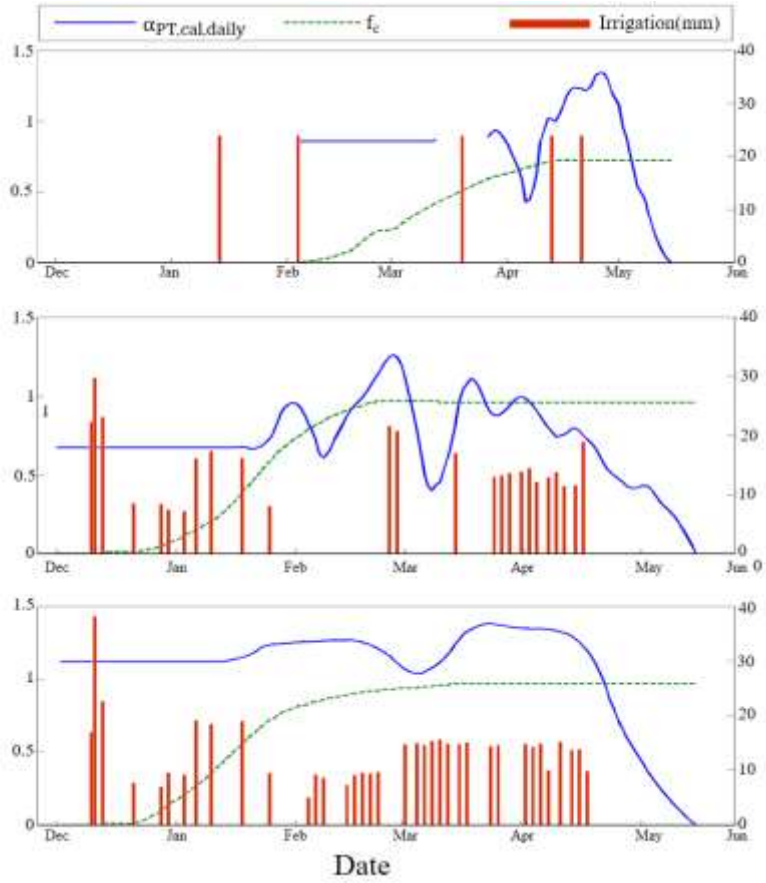

Figure V. 3. *Time series of calibrated daily α_{PT}, superimposed with fc for the (a) flood-, (b) controlled drip- and (c) reference drip-irrigated wheat fields, separately. The red segments represent irrigations during the season.*

V.4. Results

V.4.1. Interpretation of α_{PT} variabilities

α_{PT} is expected to vary according to several factors including LAI, green fraction cover and soil water availability. In order to verify the consistency of the variations in daily retrieved α_{PT}, Figure V.4 presents the time series of calibrated daily α_{PT} superimposed with near-surface (5-cm) soil moisture, deeper (30-cm) soil moisture and VWC for each site separately. It is reminded that VWC was available for the controlled- and reference drip-irrigated wheat fields only and that the daily α_{PT} for $f_c \leq 0.5$ is set to the mean daily α_{PT} obtained for $f_c > 0.5$(see Figure V.3). Therefore, the variability of α_{PT} should be interpreted for $f_c > 0.5$ only, that is from $f_c = 0.5$ until harvest. Figure V.4 illustrates the expected relationships between α_{PT} and both biomass (related to VWC) and the water availability in the soil column. In each case, the α_{PT} dynamics are driven by soil moisture variations and the maximum α_{PT} values clearly follows an envelope defined by the amount of green biomass. In fact, the contour line that

interpolates α_{PT} peaks generally increases up to the maximum of VWC and then decreases as the green vegetation fraction starts to decline at the onset of senescence. Note that the maximum of VWC may not necessarily coincide perfectly with the maximum of α_{PT} since α_{PT} is also affected by soil water availability. In the case of controlled drip field, the maximum of α_{PT} appears significantly sooner than the maximum of green biomass. This is explained by a lack of moisture in the soil in this crop field as depicted by the strong drop in the 30-cm soil moisture from early February. This can also be explained by the fact that fertilization (nitrogen) was provided to the plant via irrigation water. Hence, a deficit in irrigation had the dual effects of decreasing soil water availability and depleting the soil in nutrient compared to the reference drip field.

The qualitative analysis of α_{PT} variability in relation to soil water availability and the amount of green biomass thus indicates that α_{PT} cannot be considered as a constant. Large variations in this parameter are likely to occur during the agricultural season, especially under stress conditions. Water deficit may happen with flood irrigation when the frequency of water supplies (every 3 weeks on average over R3) is relatively low compared to the water demand under such semi-arid conditions. Indeed the water stress observed in the flood-irrigated wheat may be attributed to the increase in water depletion at the root zone through a removal of water by transpiration and percolation losses (Er-Raki et al., 2007). Water stress may also happen with drip when the technique is not appropriately implemented or by applying regulated deficit irrigation.

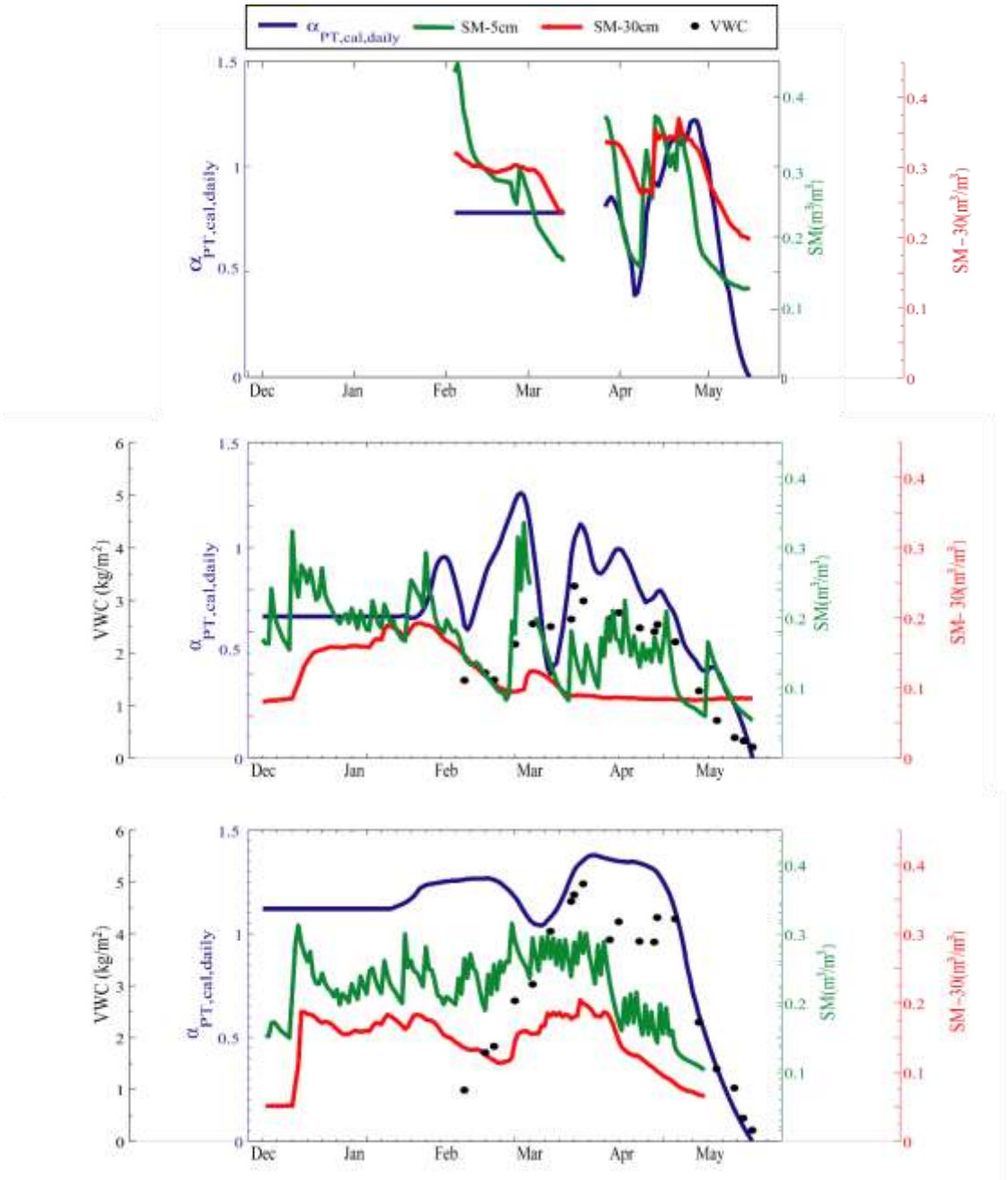

Figure V. 4. *Time series of $\alpha_{PT,cal,daily}$ superimposed with 5-cm/30-cm soil moisture (SM) and vegetation water content (VWC) for: (a) flood-, (b) controlled drip- and (c) reference drip-irrigated fields, respectively. For the flood-irrigated wheat, VWC is unavailable.*

V.4.2. Surface fluxes

The ability of TSEB and TSEB-SM for partitioning the available energy into H and LE is assessed by forcing -in each case- R_n and G to their measured values. Note that the calibration of TSEB-SM is still undertaken using observed LST, SM and fc whereas the validation of TSEB and TSEB-SM model output is undertaken using EC measurements of H and LE. The

metrics used to evaluate results comprise the determination coefficient (R^2), the root mean square error (RMSE) and the mean bias error (MBE) between simulated and observed fluxes.

Figure V.5 plots simulated versus observed LE for the three sites separately. TSEB provides satisfying results for the flood site with a RMSE of 78 W/m^2 and a relative error (estimated as RMSE divided by mean observed LE) of 27%. However, two notable features are observed for the other two (controlled and reference drip) sites: i) the LE simulated by TSEB never exceeds 500 W/m^2 over the entire growing season ($f_c > 0.5$) although observations reach 700 W/m^2 and ii) the overall MBE is about 29 W/m^2 and 66 W/m^2 for the controlled and reference drip field respectively, meaning that TSEB also overestimates LE in the lower ET range. To dig deeper, the performance of TSEB is now assessed by analyzing the metrics computed for three distinct periods of the agricultural season: the period for $f_c \leq 0.5$, for $f_c > 0.5$ and the senescence stage. Note that the senescence period is defined herein as starting after the last peak observed on the calibrated daily α_{PT} (becomes remarkable after about one week) and finishing when green fraction cover becomes zero, which corresponds to the last date of the three time series. Hence the senescence starts on 27/04/2003, 19/04/2017 and 15/04/2017 for the flood-, controlled drip- and reference drip-irrigated field, respectively. A visual assessment of scatter plots in Figure V.5 and the statistics presented in Table V.1 clearly indicate that TSEB underestimates LE fluxes at around the maximum of ET (well developed crop before senescence) while it overestimates LE fluxes during senescence until harvest. The saturation of TSEB in the higher range of ET is due to the fixed maximum value for α_{PT} (equal to 1.26). The structure of the model cannot accommodate large evaporative demand conditions and strong advective conditions (Song et al., 2016a).

Both limitations identified in the TSEB formalism seem to be partly solved by the TSEB-SM approach. In particular, the LE simulated by TSEB-SM (Figure V.5) is closer to the 1:1 line in each case ($f_c \leq 0.5$ and $f_c > 0.5$ and the senescence), providing a quite significant improvement for drip sites. The simulated LE does not saturate as it reaches 700 W/m^2 over the reference drip site. In fact, the retrieval of daily α_{PT} values larger than the theoretical maximum 1.26 significantly improves ET estimates. Moreover, the overestimation of LE during the senescence stage is much reduced for TSEB-SM. It is suggested that the decrease in calibrated daily α_{PT} integrates the drop in green vegetation fraction that takes place during senescence.

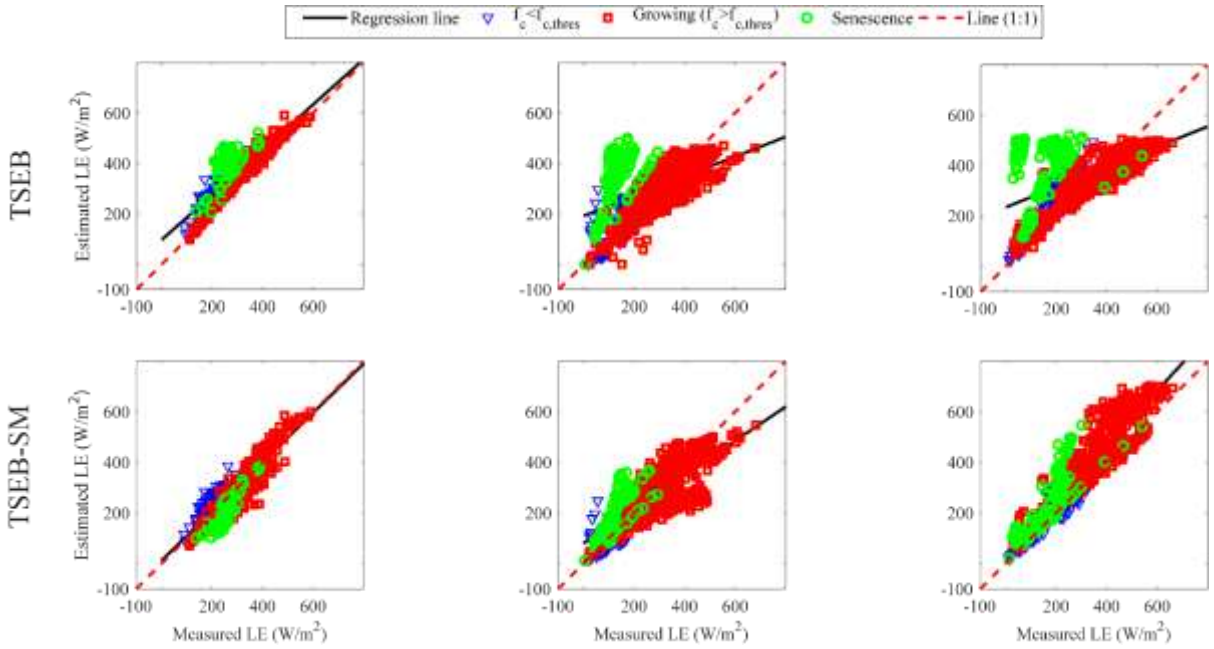

Figure V. 5. *Scatterplot of simulated versus observed LE for the (top) food-, (middle) controlled drip- and (bottom) reference drip-irrigated fields and for (left) TSEB-SM and (right) TSEB models, respectively.*

The comparison between TSEB and TSEB-SM is continued by plotting simulated versus observed H for each site in Figure V.6. Consistent with previous results obtained for LE, the calibration strategy within TSEB-SM provides in general a significantly improved RMSE compared to the original TSEB. The RMSE is 49 W/m^2 instead of 73 W/m^2, 78 W/m^2 instead of 78 W/m^2 and 119 W/m^2 instead of 128 W/m^2 for the flood-, controlled drip- and reference drip-irrigated field respectively. The determination coefficient between simulated and observed H is significantly improved from 0.61 to 0.67, from 0.37 to 0.75 and from 0.29 to 0.82, respectively when including calibrated parameters to TSEB-SM.

One can observe that the slope of the linear regression between TSEB and in-situ H is very low in all cases. The modeled H does not seem to be sensitive enough to changes in surface and atmospheric conditions during all three periods ($f_c \leq 0.5$, $f_c > 0.5$ and senescence).

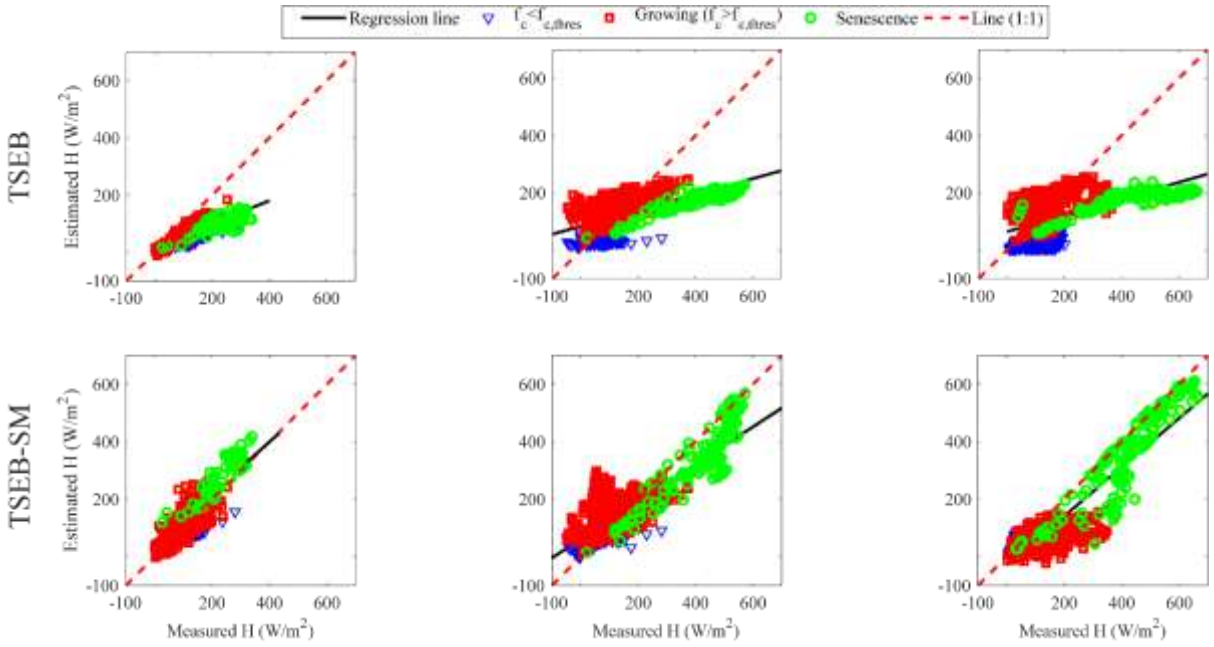

Figure V. 6. *Scatterplot of simulated versus observed H for the (top) food-, (middle) controlled drip- and (bottom) reference drip-irrigated fields and for (right) TSEB and (left) TSEB-SM model, respectively.*

Table V. 1. Error statistics (RMSE, R^2 and MBE) between modeled and measured sensible and latent heat fluxes for the flood, controlled drip- and reference drip-irrigated fields, and for TSEB and TSEB-SM model, separately (R_n and G are forced to their measured value)

		TSEB-SM			TSEB		
		RMSE (W/m^2)	R^2 (-)	MBE (W/m^2)	RMSE (W/m^2)	R^2 (-)	MBE (W/m^2)
Latent heat flux (LE)	Flood	49	0.79	-4	78	0.79	66
	Controlled drip	73	0.64	-6	119	0.22	29
	Reference drip	78	0.86	56	128	0.28	66
Sensible heat flux (H)	Flood	49	0.67	4	78	0.61	-66
	Controlled drip	73	0.75	7	119	0.37	-29
	Reference drip	78	0.82	-56	128	0.29	-66

The intercomparison between TSEB and TSEB-SM is finally undertaken by simulating the available energy, instead of forcing R_n and G to their measured values as in Table V.1. Table V.2 reports the error statistics for the four energy fluxes separately. The larger discrepancies for LE estimated from TSEB-SM model in this case is likely due to greater scatter between modeled and measured R_n, which is related to the difference between simulated and observed LST. Note also that the determination coefficient between simulated and measured G is about 0.4-0.5 for both TSEB and TSEB-SM and all three sites. This is linked in part to the relatively small magnitude and range in the observed values combined with the simplicity of the approach used to estimate G. Overall, the simulations of LE and H when modeling R_n and G are fully consistent with those obtained when forcing R_n and G to their measured values. TSEB-SM still provides superior results to TSEB in terms of RMSE, R^2 and MBE between simulated and observed fluxes. Especially the sensible heat flux is significantly improved in all cases.

Table V. 2. Error statistics (RMSE. R2 and MBE) between modeled and measured net radiation, conductive flux, and sensible and latent heat fluxes for the flood, controlled drip- and reference drip-irrigated fields, and for TSEB and TSEB-SM model, separately.

		TSEB-SM			TSEB		
		RMSE (W/m^2)	R^2 (-)	MBE (W/m^2)	RMSE (W/m^2)	R^2 (-)	MBE (W/m^2)
Net radiation (Rn)	Flood	31	0.98	-25	18	0.99	-17
	Controlled drip	27	0.98	-10	16	0.99	1
	Reference drip	50	0.95	-32	9	0.99	1
Conductif flux (G)	Flood	23	0.41	2	22	0.43	1
	Controlled drip	20	0.5	9	25	0.48	12
	Reference drip	14	0.39	14	30	0.38	26
Sensible heat flux (H)	Flood	27	0.66	34	78	0.61	-67
	Controlled drip	61	0.82	8	118	0.38	-28

V.5. Summary and Conclusions

A new evapotranspiration model named TSEB-SM is derived from the TSEB formalism by explicitly representing soil evaporation using a soil resistance. An innovative calibration

approach is also developed to retrieve the main parameters of soil evaporation and plant transpiration via the soil resistance and αPT respectively. In practice the soil resistance parameters are retrieved at the seasonal time scale from SM and LST data with $f_c \leq 0.5$. While α_{PT} is retrieved at the daily time scale from SM and LST data for $f_c > 0.5$. The performance of TSEB-SM and TSEB models is assessed in terms of LE and H partitioning using an in-situ data set collected over 1 flood- and 2 drip-irrigated wheat fields.

The convergence of the iterative calibration procedure on (a_{rss}, b_{rss}) and α_{PT} is successfully tested when all three parameters are estimated at the seasonal time scale, as well as when considering a daily variability of α_{PT}. The maximum calibrated daily α_{PT} is close to the theoretical value of 1.26 for all three sites. However, its temporal variability is found to be significant even during the growing stage of wheat. A qualitative analysis of α_{PT} variabilities in relation to soil moisture at 5 cm and 30 cm depth and to VWC indicates that α_{PT} cannot be considered as a constant in the conditions of the experiments. Large deviations about the 1.26 value are likely to occur during the agricultural season especially under dry, water deficit and advective conditions.

In terms of flux estimates, TSEB provides satisfying results for the flood site but not for the other two (controlled and reference drip) sites. The saturation of TSEB in the higher range of ET is due to the fixed maximum value for α_{PT} (equal to 1.26). Moreover, the overestimation of LE by TSEB during senescence is associated with a very low sensitivity of simulated H to any surface/atmospheric conditions. Both limitations identified in the TSEB formalism seem to be partly solved by the TSEB-SM approach with a slope of the linear regression between simulated and observed LE/H much closer to 1 in all cases. Such an evapotranspiration model simultaneously constrained by LST, f_c and SM seems to respond robustly in terms of LE/H partitioning for wheat crops under the conditions of the experiments. However, the calibrated daily α_{PT} needed to be i) smoothed to reduce random uncertainties and ii) normalized between its two extreme values since the 0 value was not necessarily reached at harvest.

In the next chapter, the microwave-derived near-surface soil moisture (SM), in addition to the thermal-derived LST and fractional vegetation cover (f_c) will be used to investigate how remote sensing data can be used to derive the main parameters (a_{rss}, b_{rss} and α_{PT}) of TSEB-SM model. In this purpose, TSEB-SM at 1 km resolution using MODIS (Moderate resolution imaging spectroradiometer) LST/ f_c data and SMOS SM data will be applied. To make the SMOS data spatially consistent with MODIS data, the SMOS SM is disaggregated at 1 km.

Chapter.VI. Remote sensing application of TSEB-SM (combining DisPATCh SM and MODIS LST data for mapping ET at 1 km resolution

Chapter.VI. Remote sensing application of TSEB-SM (combining DisPATCh SM and MODIS LST data for mapping ET at 1 km resolution 90

VI.1. Introduction 91

VI.2. TSEB-SM Model improvements 91

VI.3. Accuracy of Remote Sensing data 92

VI.4. Retrieving (a_{rss}, b_{rss}) parameters 97

VI.5. α_{PT} variablities 98

VI.5.1. Using in-situ data 98

VI.5.2. Using satellite data 99

VI.5.3. Interpretation of α_{PT} variabilities 100

VI.6. Surface fluxes 101

VI.6.1. Using in-situ data 102

VI.6.2. Using satellite data 105

VI.7. Summary and Conclusions 109

VI.1. Introduction

The TSEB-SM model was tested in the previous chapter using in-situ measurements. The model provided an important improvement in terms of latent heat flux/sensible heat flux estimates compared to the classic TSEB all along the agricultural season, especially during the crop emergence and the senescence periods. Such improvements are attributed to stronger constraints exerted on the representation of soil evaporation (via SM data and the calibrated soil parameters) and plant transpiration (via the calibrated daily PT coefficient). It is reminded that TSEB-SM is based on the original TSEB formalism, meaning that the energy balance for vegetation is the same as in TSEB using the PT formula, while the soil evaporation is explicitly represented (contrary to TSEB) as a function of SM via a soil resistance term. The use of the soil resistance formulation is justified by the fact that its main parameters (a_{rss}, b_{rss}) can be calibrated from soil texture information (Merlin et al., 2016) or a combination of SM and LST data under bare (Merlin et al., 2018) or partially covered (Ait Hssaine et al., 2018b) soil conditions.

In this part, the TSEB-SM will be applied at 1km resolution using remote sensing data including thermal-derived LST and NDVI and DisPATCh SM in order to provide surface energy fluxes over a rainfed wheat field in the Tensift basin, central Morocco during four agricultural seasons.

VI.2. TSEB-SM Model improvements

Two improvements are made on the former of TSEB-SM, First, the calibration of α_{PT} is bounded by a minimum (0) and maximum (2) acceptable physical value, in order to avoid unacceptable values of α_{PT} that can be produced due to the uncertainties in LST-derived daily estimates. Such an upper bounding is especially needed when vegetation partially covers the soil. Second, the output fluxes are normalized using the LST-derived available energy. Therefore, the new version of TSEB-SM uses both LST and SM data (in addition to vegetation cover fraction data) as forcing on a daily basis. In practice, the latent and sensible heat fluxes derived from the TSEB-SM model are re-computed using the TSEB-SM derived evaporative fraction (EF, defined as the ratio of latent heat to available energy) and the LST-derived available energy. The rationale is that numerous modelling studies have shown the regularity and constancy of EF during daylight hours in cloud-free days (Gentine et al., 2011;

Lhomme and Elguero, 1999; Shuttleworth et al., 1989) and the EF has a strong link with SM availability (Bastiaanssen and Ali, 2003), which is an important factor for estimating latent heat flux. For that purpose, the LST data collected at the Terra and Aqua-MODIS overpass times are used separately to estimate the instantaneous R_n and G. A ratio between the daily (obtained as an average value between Aqua and Terra overpass times) latent heat flux LE_{daily} and the daily available energy ($R_{n,daily}$-G_{daily}) is used to calculate an average daily EF:

$$EF = \frac{LE_{daily}}{(R_{n,daily} - G_{daily})} \quad \text{(VI.1)}$$

The daily EF and the instantaneous available energy (calculated using Terra and Aqua MODIS LST, separately) are finally used to re-calculate the instantaneous TSEB-SM output of LE and H by the following formulas:

$$LE = EF * (R_n - G) \quad \text{(VI.2)}$$

$$H = (1 - EF) * (R_n - G) \quad \text{(VI.3)}$$

VI.3. Accuracy of Remote Sensing data

The LST collected by MODIS at Terra and Aqua overpass times and the SM product derived at 1 km resolution from the DisPATCh algorithm applied to SMOS data, are used as input to TSEB and TSEB-SM models. Validation of TSEB and TSEB-SM input data prior to the evaluation of models output is an important issue, notably due to the scale mismatch existing between the spatial resolution (1 km) of MODIS/DisPATCh data and the footprint of the EC flux measurements that does not exceed 100 m (Schmid, 1994).

Several studies have demonstrated the effectiveness of DisPATCh 1km resolution SM. Malbéteau et al. (2016) compared DisPATCh SM data with the in-situ measurements of 38 stations distributed within the Murrumbidgee catchment in Southeastern Australia. Their results showed that DisPATCh improved the spatial representation of SM at 1 km resolution (compared to the original 40 km resolution SMOS SM) independently from the temporal information provided by SMOS satellite, especially in semi-arid areas. Recently, Malbéteau et al. (2018) combined the DisPATCh SM over the entire year 2014 (Sidi Rahal-Morocco) with the continuous predictions of a surface model in order to obtain a better estimate of daily SM at 1 km resolution. They found that the assimilation of DisPATCh data improved quasi systematically the dynamics of SM.

Figure VI.1 displays the scatter plots of MODIS LST (at Terra and Aqua overpass) versus in-situ measurements for the four agricultural seasons separately. The obtained R^2, RMSE, and MBE are reported in Table VI.1. The statistical comparison shows strong linear correlations ($0.76 \leq R^2 \leq 0.90$) for all years. The RMSE is around 4 K for S2 (2016-2017) and S3 (2017-2018) agricultural seasons while it reaches 6 K for S1 (2014-2015) and B1 (2015-2016), respectively. The observed scatter may stem from the fact that the localized (1 or 2 m wide) in-situ LST is not fully representative of the 1 km resolution MODIS pixel (Ait Hssaine et al., 2018b; Yu et al., 2017). For all years (S1-3, B1), it can be seen that the MBE is negative. Note that the MBE is the greatest when the temperatures are largest. Such a systematic error is probably due to the non-representativeness of the in-situ LST observations when compared to the corresponding scale of MODIS observations.

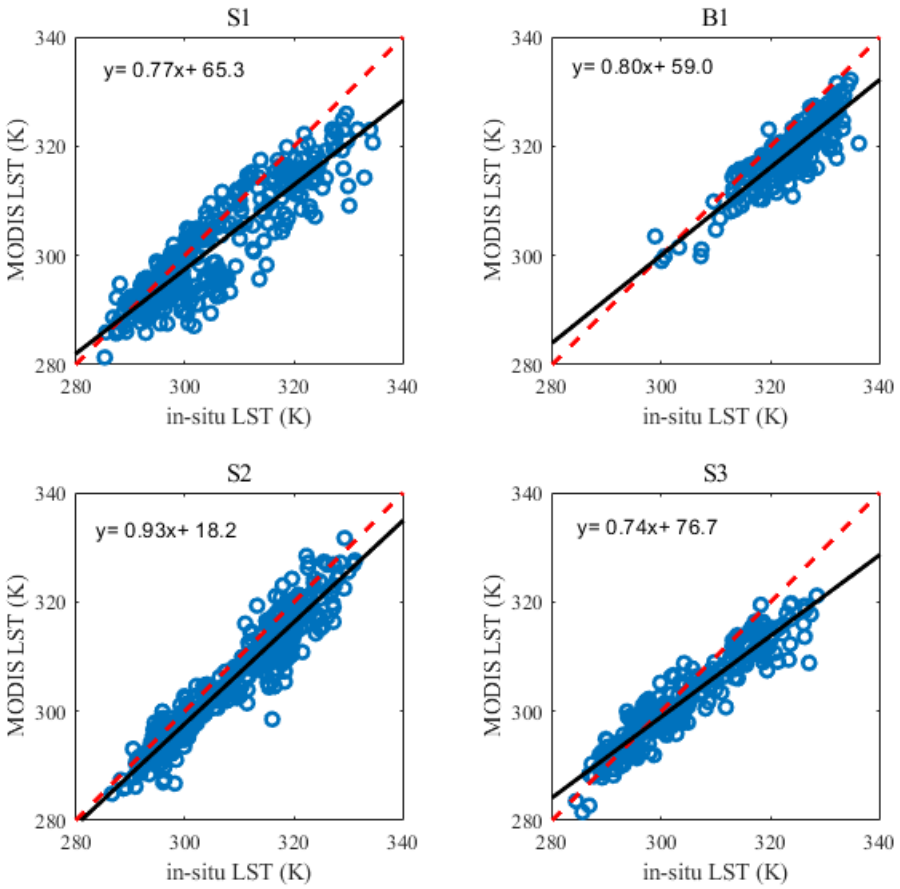

Figure VI. 1. *Scatter plots of MODIS versus in-situ LST at Sidi Rahal site for S1 (2014-2015), B1 (2015-2016), S2 (2016-2017) and S3 (2017-2018) agricultural seasons, separately, (red dashed line is the line(1:1)-black line is the regression line)*

Table VI. 1. Validation results of DisPATCh SM and MODIS LST at Sidi Rahal site.

	Period	R^2	RMSE	MBE
LST	S1	0.80	6.4 (K)	-3.7 (K)
	B1	0.76	5.6 (K)	-4.6(K)
	S2	0.91	4.3 (K)	-2.9 (K)
	S3	0.89	4 (K)	-2 (K)
SM	S1	0.55	0.07 m^3/m^3	-0.04 m^3/m^3
	B1	0.36	0.04 m^3/m^3	-0.03 m^3/m^3
	S2	0.27	0.09 m^3/m^3	-0.05 m^3/m^3
	S3	0.47	0.08 m^3/m^3	-0.03 m^3/m^3

In order to evaluate the 1 km resolution SM during the study period, Figure VI.2 shows a comparison of DisPATCh SM with in-situ measurements for the four wheat agricultural seasons (S1, B1, S2 and S3) separately. The statistical results including the coefficient of determination (R^2), the root mean square error (RMSE), and the mean bias error (MBE) are reported in Table VI.1. The R^2 ranges from 0.27 to 0.55, the RMSE from 0.04 to 0.09 m^3/m^3 and the MBE from -0.05 to -0.03 m^3/m^3. These results are encouraging considering the heterogeneous land use composed of rainfed wheat, bare soil, fallow and farm building (see Figure VI.3). In fact the localized in-situ measurements may not be perfectly representative of the 1 km resolution satellite data. Note that the efficiency of DisPATCh is supposedly higher for low SM values (Malbéteau et al., 2016), which is clearly illustrated during B1 season, while it is lower for high SM values (after rain events). This can be explained by the constraints of atmospheric and vegetation conditions on disaggregation results, as well as the saturation of SEE in the higher SM range. Another major issue that can lead to differences between DisPATCh and in-situ SM is that the ground SM sensors are buried at a depth of 5 cm while the penetration of the L-band wave varies between 2 and 5 cm depending on soil conditions (notably SM content, texture). For S2, the SM provided by DisPATCh underestimated field measurements, especially in the higher SM range. This particular behaviour could be explained by the particularly low precipitation amount during this year. Especially, it is possible that the surrounding plots were not sown by neighbour farmers, resulting in a soil that dried quickly compared to our field, which retained the SM for a longer period of time.

Note that despite the relative heterogeneity within the 1 km pixel (characterized by rainfed wheat in addition to bare soil and fallow), the comparison between field measurements and 1 km resolution satellite data reflects acceptable accuracies.

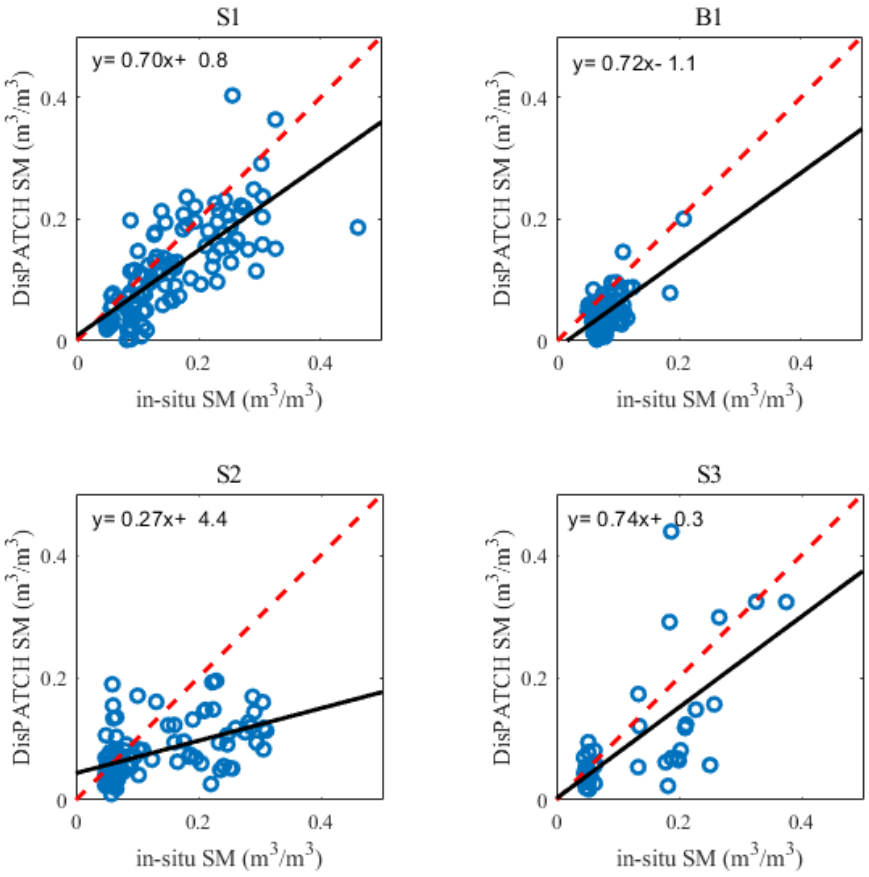

Figure VI. 2. *Scatter plots of the 1 km resolution DisPATCh versus in-situ SM at Sidi Rahal site for S1 (2014-2015), B1 (2015-2016), S2 (2016-2017) and S3 (2017-2018) agricultural seasons, separately.*

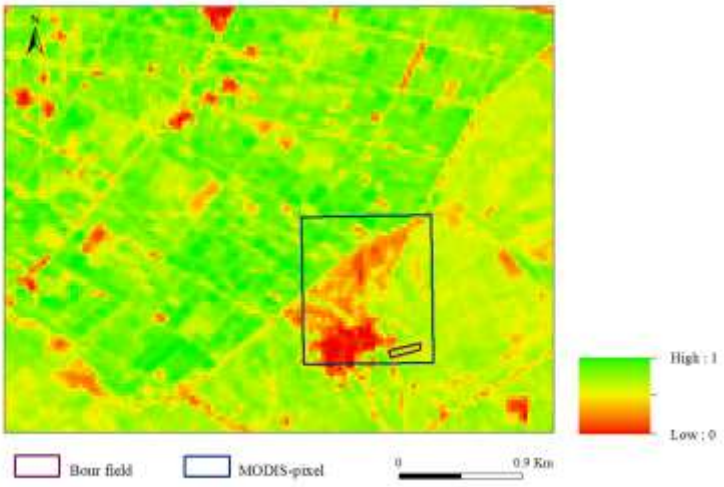

Figure VI. 3. *NDVI image derived from Landsat data acquired on 17/04/2018. The experimental field and the overlaying 1 km resolution MODIS pixel are superimposed*

VI.4. Retrieving (a_{rss}, b_{rss}) parameters

The soil resistance r_{ss} is inverted for $f_c \leq f_{c,thres}$, between 11 am and 2 pm and at Terra and Aqua overpass time step for in-situ and satellite data, respectively. The inverted r_{ss} is then correlated to the ratio SM/SM_{sat} to estimate a_{rss} and b_{rss} parameters. These latter are the intercept of the linear regression between the log (r_{ss}) and SM/SM_{sat} relationship. The calibration process is applied for each season independently. Then a pair (a_{rss}, b_{rss}) is calculated for the entire study period for in-situ and satellite data, respectively.

Figures VI.4.a and VI.4.b plot the log (r_{ss}) versus in-situ SM/SM_{sat} using in-situ and satellite data, respectively. The mean retrieved values (7.62, 2.43) and (7.32, 4.58) for in-situ and satellite data, respectively, are relatively close to the values estimated in Sellers et al. (1992) (8.2, 4.3) and in Ait Hssaine et al. (2018b) (7.2, 4). However, by comparing both figures (VI.4.a and VI.4.b), one notes that the use of in-situ data generates more scatter than with satellite data. The apparent scatter in retrieved r_{ss} could be interpreted by the impact of the daily cycle of meteorological (evaporative demand) conditions or soil properties differences (Merlin et al., 2011; 2016; 2018). The retrieved soil parameters also vary from year to year: the standard deviation is 0.39 and 1.69 for a_{rss} and b_{rss}, respectively. This can be explained by the compensation effects between a_{rss} and b_{rss} parameters which justifies the empirical nature of the r_{ss} formulation in Sellers et al. (1992). Another major issue that can lead to these differences is the depth of SM measurements (Merlin et al., 2011). In Sellers et al. (1992), the near-surface soil moisture is defined in the 0-5-cm soil layer, whereas in our field, SM measurements are made at 5-cm depth. Also, the sensing depth of SMOS observations is generally shallower than the in-situ surface measurements (Escorihuela et al., 2010). Moreover, the variability of a_{rss} and b_{rss} in Fig. 5b using remote sensing data can be linked to the scale difference between DisPATCh SM/MODIS products (1 km) and the field measurements. As shown in Figure VI.3, the field is surrounded by trees, buildings and fallows, which causes the spatial heterogeneity within the pixel of 1 km. This heterogeneity can introduce errors on the model inversion. Nevertheless, soil parameters are quite similar for in-situ and satellite data sets. Therefore, the heterogeneity issues within the 1 km pixel scale are minor in this study.

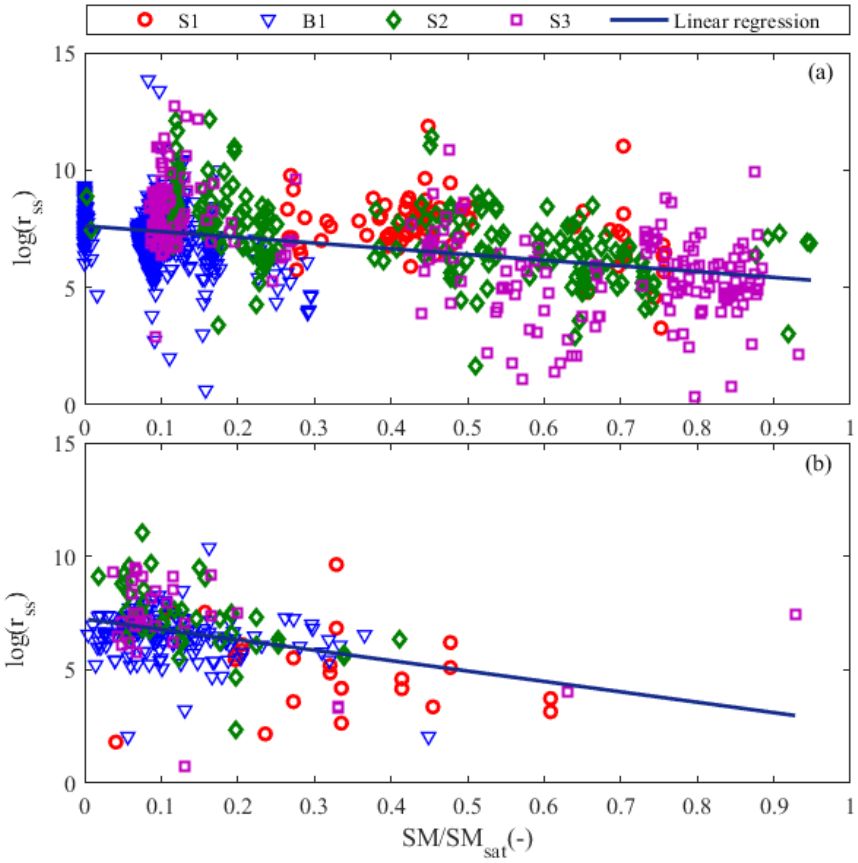

Figure VI. 4. *log(r_{ss}) versus SM/SM_{sat} (calibration step 1) using in-situ (a) and satellite (b) data.*

VI.5. α_{PT} variablities

The second calibration step consists in inverting the daily α_{PT} when vegetation is covering a significant part of soil ($f_c > f_{c,thres}$), for the three seasons of rainfed wheat (S1, S2 and S3), by using in-situ data and satellite data, separately. It is reminded that the daily α_{PT} for $f_c \leq f_{c,thres}$ is set to the mean daily α_{PT} obtained for $f_c > f_{c,thres}$ (Ait Hssaine et al., 2018b).

VI.5.1. Using in-situ data

Figure VI.5 plots the time series of daily retrieved α_{PT} for each season (S1, S2 and S3) separately, using in-situ data. The mean retrieved values of α_{PT} are 1.26, 1.12 and 1.09 for S1, S2 and S3 respectively. In all cases, the mean α_{PT} is close to the theoretical α_{PT} value (1.26). It is well observed that the retrieved α_{PT} for S1 is slightly larger compared to those obtained for both S2 and S3. This can be explained by the timing and amount of rainfall during each season. Note that unexpected low values of α_{PT} are recorded for S3 during the first few days (25 January-4 March) of the development stage. They may be associated with uncertainties in retrieved α_{PT} as the soil surface could still play a significant role in the observed LST, as well

as to a relatively low evaporative demand especially since this period coincides with cloudy days and abundant precipitations. Indeed, the coupling between transpiration (and hence retrieved α_{PT}) and LST is expected to be lower under lower atmospheric demand.

The retrieved α_{PT} is then smoothed as in Ait Hssaine et al. (2018b) to remove outliers and to reduce uncertainties at the daily time scale. The smoothed values of α_{PT} range from 0 to 1.54, 0 to 1.38 and 0.45 to 1.43 for S1, S2 and S3 respectively. The maximum of α_{PT} is close to 1.26 for S2, while it is higher for S1 and S3. This result is in accordance with the total rainfall amounts which were about 608, 214 and 421mm for S1, S2 and S3 respectively. Additionally, one can state that the stability of α_{PT} strongly depends on the rainfall distribution along the agricultural season. The daily α_{PT} is more stable for S1 than for S2 and S3. Indeed, the amount of rain during S1 is very important with two peaks of about 83 mm that occurred at the beginning of the season and during the growing stage. The second one coincides exactly with the maximum value of the retrieved α_{PT}. However, different results are obtained for S2 compared to S1 due to the lowest precipitation amount recorded over that season. As shown in Fig. 6 the amount of rain is concentrated at the beginning of the growing stage (mid December), when the α_{PT} peaks. Afterward, the smoothed α_{PT} tends to decrease because of insufficient soil water reserve in the root zone to enable wheat to continue growing. Rainfall is also significant for S3 and every rainfall event causes an immediate (daily) response of α_{PT} (after 4th March). As mentioned before, the significant error in α_{PT} retrievals for S3 between 25 January and 4 March induces strong uncertainties in the smoothing function estimates.

VI.5.2. Using satellite data

Figure VI.5 illustrates the time series of daily retrieved α_{PT} for each season separately, using satellite data. It can be seen that S1 and S2 have a very similar distribution of the retrieved α_{PT} as compared to the retrieved α_{PT} using in-situ data, respectively. For S3, only six retrieved α_{PT} values are available because of the non-availability of MODIS products during cloudy days. For this reason, no information linked to the variability of α_{PT} can be derived during this season. The retrieved values are smoothed and superimposed with the rainfall events. It is clearly shown that the smoothed α_{PT} for S1 and S2 have the same shape with a small variability, when comparing with the smoothed α_{PT} using in-situ data, with a relative error (estimated as the RMSE divided by the mean α_{PT}) of about 11 and 19 %, for S1 and S2 respectively. For S1 the maximum of smoothed α_{PT} is reached at the same time as when using the in-situ data, with a value of about 1.38, while the maximum for S2 is reached 10 days before the maximum of the α_{PT} derived from in-situ data with little response of α_{PT} to rainfall

events. These differences may be linked to uncertainties in disaggregated SMOS SM, as well as to the weaker availability of satellite data. Because of the small number of data points (retrieved α_{PT}) during S3, the smoothed α_{PT} remains at a mostly constant value (~0.7) throughout the study period, with a significant relative difference of about 34 % when comparing with the α_{PT} retrieved using in-situ data.

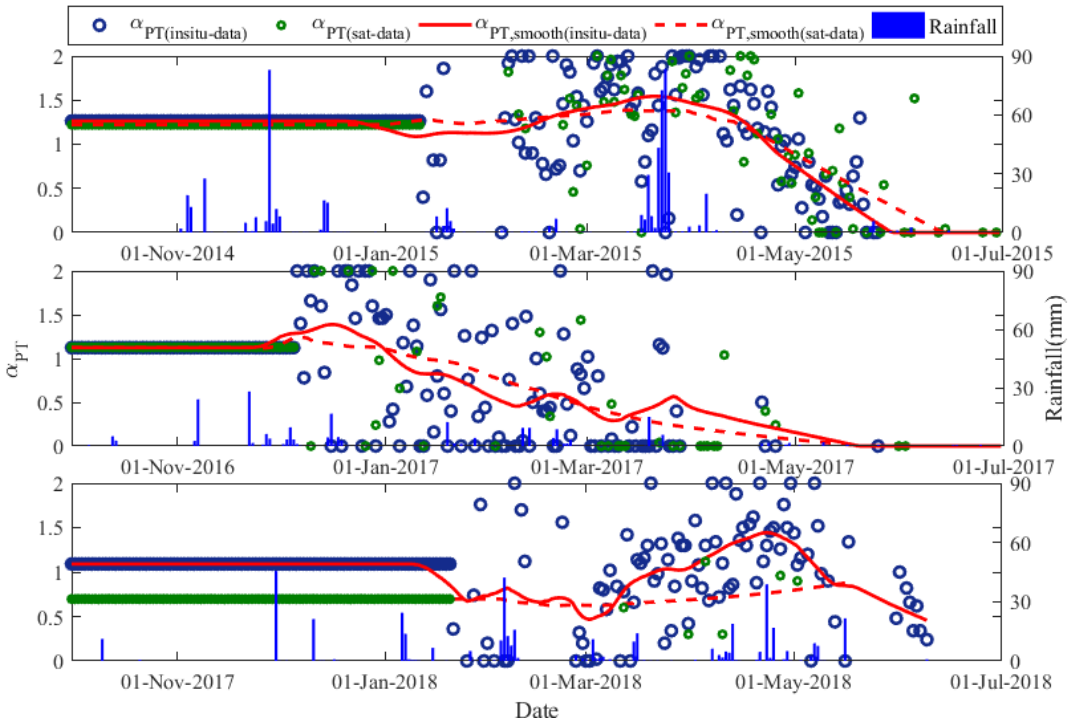

Figure VI. 5. *Time series of daily retrieved and smoothed α_{PT} (calibration step 2-using in-situ data, and satellite data) collected during S1, S2 and S3.*

VI.5.3. Interpretation of α_{PT} variabilities

Figure VI.6 plots the time series of calibrated daily α_{PT}, superimposed with NDVI and rainfall events. It is visible that the maximum value of NDVI appears sooner than the maximum value of α_{PT} for both S1 and S3. Such a delay is attributed to the high soil moisture level in the root-zone during the maturity stage. Later in the season, α_{PT} decreases as NDVI starts to decline at the onset of senescence. In contrast, the maximum value of NDVI appears later than the maximum value of α_{PT} for S2. This can be explained by the fact that rainfall at the beginning of the development phase satisfies the plant requirements, while the rainfall amount during the development stage is relatively low compared to the crop water needs (Kharrou et al., 2011). Large variations in α_{PT} occur during the agricultural season, as a result of the amount, frequency, and distribution of rainfall along the season. In general, the analysis of the α_{PT} variability using satellite data illustrates the robustness of the proposed approach, which

combines microwave and optical/thermal data to retrieve a water stress indicator at the daily time scale.

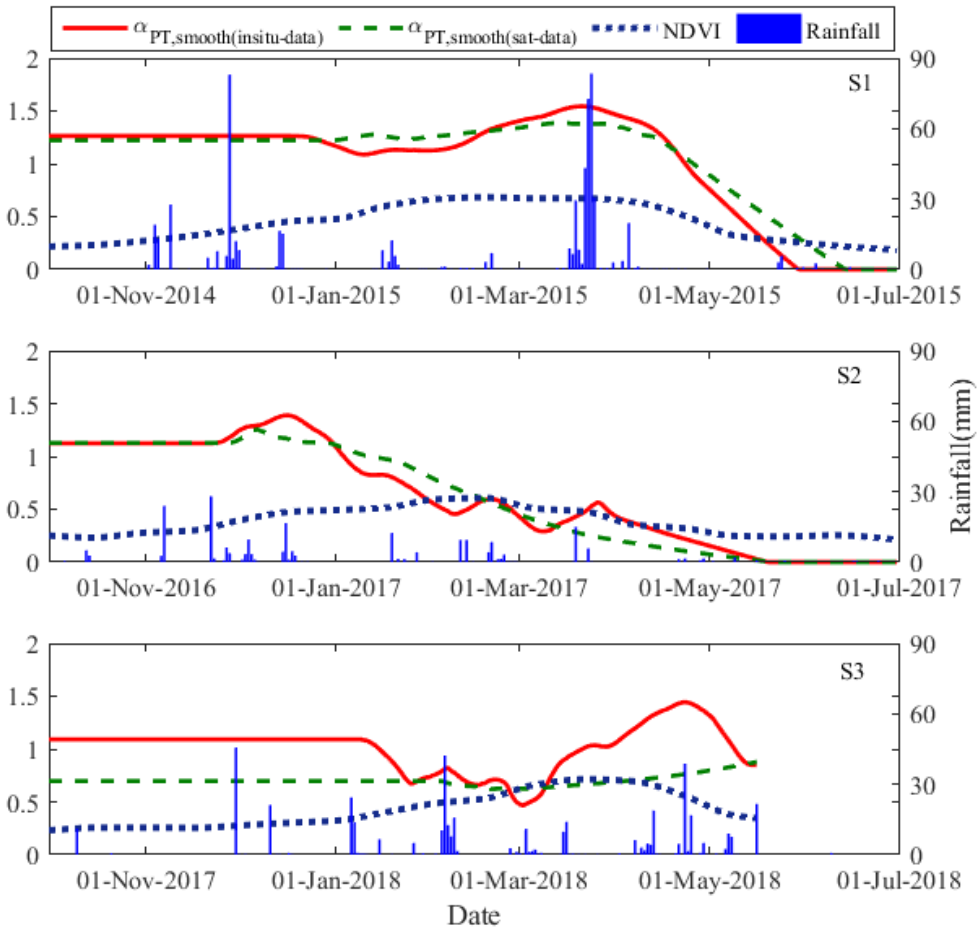

Figure VI. 6. *Time series of calibrated daily α_{PT} (red-using in-situ data, green- using satellite data) superimposed with NDVI and the rainfall events during S1, S2 and S3, separately.*

VI.6. Surface fluxes

The robustness of TSEB and TSEB-SM for partitioning (R_n-G) into H and LE is evaluated by considering several hypothesis.1) R_n and G are forced to their measured values, for each season separately. 2) The calibration process of TSEB-SM is applied using in-situ and remotely sensed LST, SM and NDVI, separately, at the Terra and Aqua MODIS overpasses. 3) The validation of TSEB and TSEB-SM model output is assessed by using EC measurements (H and LE). 4)The performance of TSEB is evaluated by analyzing the metrics computed for three distinct periods of each agricultural season: the period for $f_c \leq (f_{c,thres} = 0.5)$, for $f_c > (f_{c,thres} = 0.5)$ and the senescence stage (starting after the last peak observed on the calibrated daily α_{PT} and finishing at the end of the agricultural season), by

using the statistical results including R^2, RMSE and MBE between simulated and observed fluxes.

VI.6.1. Using in-situ data

Figure VI.7 shows an intercomparison of simulated and observed LE for the 4 seasons separately. TSEB-SM clearly provides improved results compared to the original TSEB. The obtained values of RMSE by TSEB-SM are about 68 and 72 W/m^2 for S1 and S2 respectively, which is significantly lower than those revealed by TSEB (109 and 86 W/m^2, respectively) (see Table VI.2). For B1 (season of bare soil), TSEB largely overestimates LE with a MBE of about 165 W/m^2 compared to TSEB-SM, which yields a MBE of 59 W/m^2. This overestimation of TSEB is most probably related to an inadequate value of α_{PT} (=1.26) for bare soil surfaces. In fact, 1.26 is an optimum value for the potential transpiration rate (Agam et al., 2010a; Chirouze et al., 2014). In the case of TSEB-SM, biases are reduced thanks to the calibration of the r_{ss} resistance. Additionally, according to TSEB-SM assumptions, α_{PT} for $f_c \leq 0.5$ is set to the average value of the α_{PT} retrieved for $f_c > 0.5$. During B1 season (bare soil conditions), α_{PT} was hence obtained as an average value of the mean α_{PT} retrieved for all seasons S1, S2 and S3 when $f_c > 0.5$ ($\alpha_{PT} \sim 1$). However, this value remains relatively high for a bare soil, which yields a slight overestimate of LE measurements (see B1 case in Figure VI.7).

For S3 season, the error on daily retrieved α_{PT} at the beginning of the development stage has a strong impact on LE predictions and thus yields to greater discrepancies illustrated in Figure VI.7. To overcome this error, the threshold on f_c to separate calibration steps 1 and 2 was increased to 0.63 (arbitrary value). The TSEB-SM model is then run using the new threshold. The LE simulations are improved, with a RMSE of 73 W/m^2 instead of 98 W/m^2 and a relative error (estimated as the RMSE divided by the mean observed LE) of about 42 % instead of 58 %. The increase in the threshold is intended to decrease the uncertainties in α_{PT} retrievals when vegetation is not fully covering the soil. It can be concluded that the errors in α_{PT} retrievals have a strong impact on LE estimates.

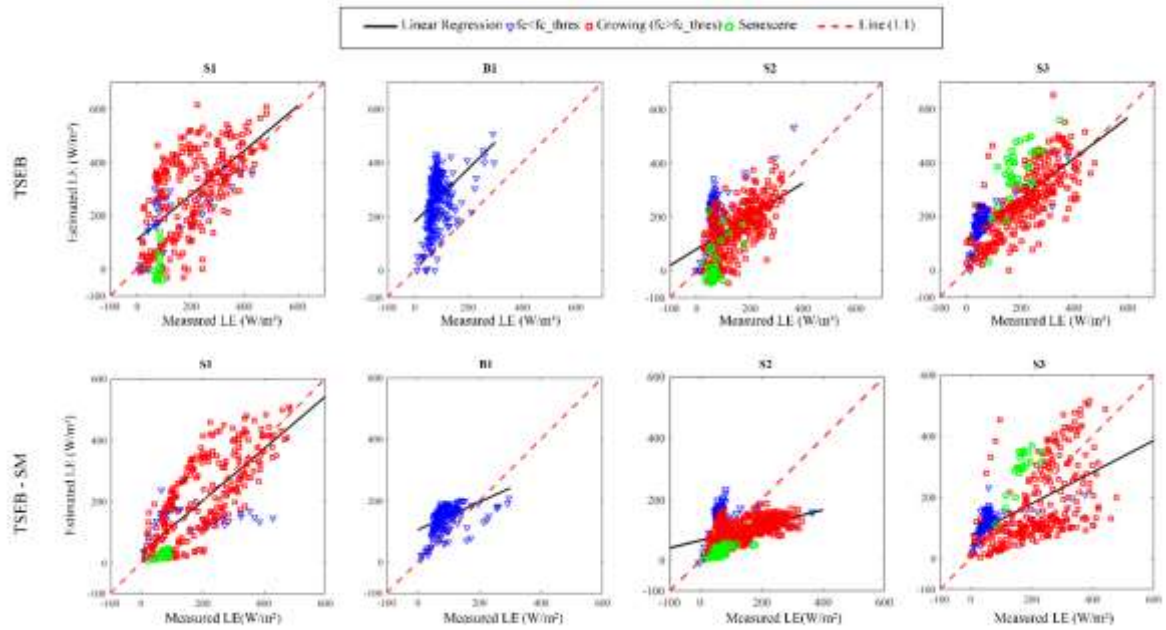

Figure VI. 7. *Scatterplot of simulated versus observed LE for (top) TSEB and (bottom) TSEB-SM models using in-situ data collected during S1, B1, S2 and S3, respectively.*

The ability of TSEB-SM to estimate the sensible heat fluxes is also investigated. Figure VI.8 displays the comparison between TSEB and TSEB-SM for each season and Table VI.2 summarized the different statistical parameters. One can notice that TSEB shows greater discrepancies in H estimation, with a RMSE of about 127, 112 and 103 W/m^2 and MBE of about -41, 1, and -71 W/m^2 for S1, S2 and S3 respectively. Both RMSE and MBE values are generally much reduced when using TSEB-SM with RMSE values of about 68, 72, and 98 W/m^2 and MBE values of about -10, 24, and 7 W/m^2, respectively. The slope of the linear regression between simulated (TSEB) and observed H is very low during B1. The simulated H does not seem to be sensitive enough to changes in surface and atmospheric conditions during all three stages ($f_c \leq 0.5$, $f_c > 0.5$ and senescence) consistent with former results obtained on a different sites of irrigated wheat (Ait Hssaine et al., 2018b). The discrepancies between TSEB-SM and in-situ H during S3 are mostly rectified by using the new threshold on f_c: the statistical results are improved, the RMSE is about 73 W/m^2 and the relative error is 39 % (instead of 52 %). It can be concluded that the uncertainty observed over the α_{PT} during the first few days of development stage (25 January-4 March) is mainly related to the impact of the soil, which is not negligible during the first weeks of the growing stage. Nevertheless, by considering the overall results obtained for the 3 seasons, the threshold of $f_{c,thres} = 0.5$ can be considered as an acceptable value to calibrate the soil resistance parameters and the Priestly Taylor coefficient.

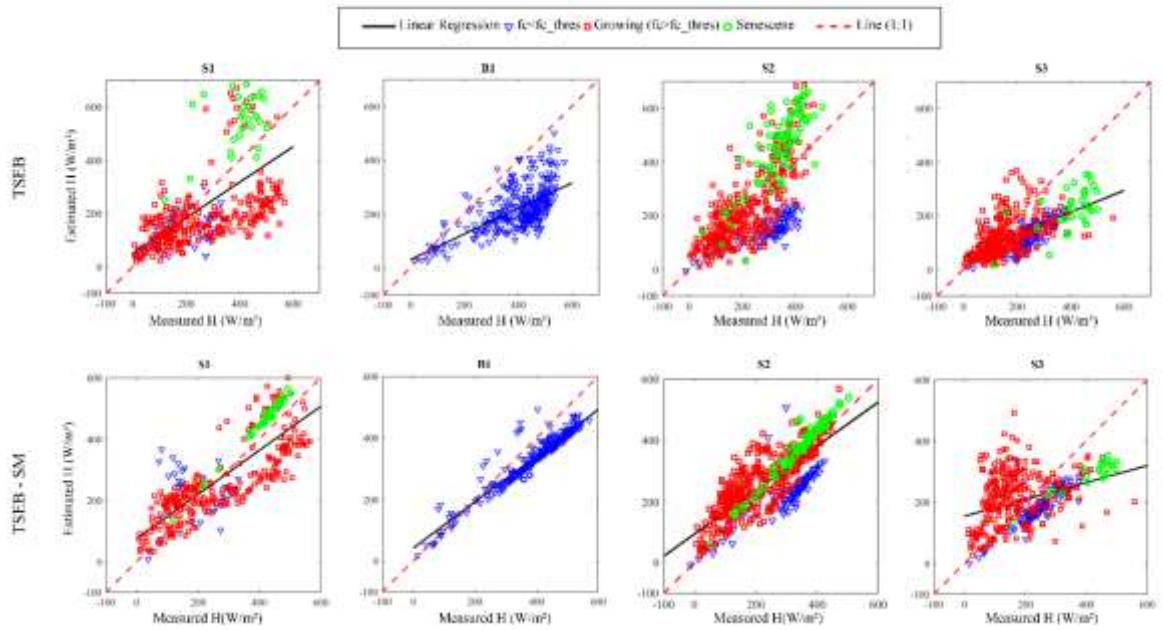

Figure VI. 8. *Same as Fig VI.7 but for H fluxes.*

Table VI. 2. Statistical results (RMSE, R^2 and MBE) between modeled and measured sensible and latent heat fluxes for S1, S2, B1 and S3, and for TSEB and TSEB-SM model, separately (R_n and G are forced to their measured value).

			TSEB			TSEB-SM		
			RMSE	R^2	MBE	RMSE	R^2	MBE
Using in-situ data	LE (W/m^2)	S1	109	0.39	76	**68**	**0.59**	**10**
		B1	136	0.15	165	**52**	**0.22**	**59**
		S2	86	**0.22**	30	72	0.16	-24
		S3	103	**0.53**	71	98	0.29	**-7**
	H (W/m^2)	S1	127	0.33	-41	**68**	**0.70**	**-10**
		B1	136	0.44	-165	**52**	**0.91**	**-59**
		S2	112	0.47	1	**72**	**0.63**	**24**
		S3	103	**0.38**	-71	98	0.14	**7**
Using satellite data	LE (W/m^2)	S1	95	0.34	119	**55**	**0.51**	**39**
		B1	66	**0.07**	181	**27**	0.01	**62**
		S2	67	0.02	94	**41**	**0.08**	**4**
		S3	56	0.55	128	**24**	**0.68**	**7**
	H (W/m^2)	S1	98	0.3	-104	**55**	**0.54**	**-39**
		B1	66	0.37	-181	**27**	**0.52**	**-62**
		S2	73	0.33	-71	**41**	**0.6**	**-4**
		S3	56	0.28	-128	**24**	**0.36**	**-7**

As a further step, the intercomparison between TSEB and TSEB-SM is assessed by predicting R_n and G fluxes instead of forcing them to their measured values. The statistical results of the comparison between simulated and observed R_n, G, H and LE are listed in Table VI.3. The simulations of LE and H when modeling R_n and G are consistent with those obtained when forcing R_n and G to their measured values. The scattering obtained when comparing turbulent flux estimations to measurements is mainly related to the uncertainty in available energy estimates, mainly related to the uncertainty in soil heat flux estimates. Indeed, as reported in Table VI.3, R_n is very well simulated for both TSEB and TSEB-SM. The R^2 between simulated and observed R_n is about 0.99 during all seasons. Meanwhile G shows a poor correlation, with an R^2 varying from 0.05 to 0.45. This is mainly linked to the simplicity of the approach used to estimate G, which requires local calibration. Kustas et al. (1998) hence indicated that the ratio $G/R_{n,soil}$ cannot be considered as a constant, because it is affected by different factors such as time of day, moisture conditions and soil texture and structure.

VI.6.2. Using satellite data

In order to gain greater insight into how TSEB and TSEB-SM models respond to different surface conditions across a landscape, an analysis of the spatial distributions and the magnitude of the turbulent fluxes using remotely sensing data produced from the two models is conducted. The comparisons between TSEB/TSEB-SM versus observed LE over the four seasons are illustrated in Figure VI.9. A visual assessment of scatter plots in Figure VI.9 and the statistical results (Table VI.2) clearly indicates that TSEB overestimates LE fluxes. The overall MBE are about 119, 181, 94 and 128 W/m^2 for S1, B1, S2 and S3 respectively. The overestimation of LE fluxes can be explained by the fact that α_{PT} is set to be 1.26 for the whole study period, including both stressed and unstressed conditions. This probably causes larger errors on the LE estimation especially during the growing stage. Indeed, the saturation of TSEB in the higher range of ET during the senescence period is precisely due to the fixed maximum value of α_{PT} to 1.26. The errors are reduced when using TSEB-SM. In fact, the constraint on plant transpiration, while retrieving daily α_{PT} values instead of using the theoretical value 1.26 significantly improves ET estimates especially for the growing stage. Moreover, the large bias of LE during the senescence stage is much reduced. It is suggested that the decrease in calibrated daily α_{PT} integrates the drop in green vegetation fraction that takes place during senescence (Ait Hssaine et al., 2018b). Additionally, the constraint on the soil evaporation via the DisPATCh SM, clearly reduces the MBE values during the

emergence period ($f_c \leq f_{c,thres}$). Finally, the constraint applied on TSEB-SM output fluxes using LST-derived available energy and TSEB-SM-derived evaporative fraction (Equation 6.1) improves the LE estimates for the whole study period. The MBE are about 39, 4, 7 and 62 W/m^2 for S1, S2, S3 and B1 respectively.

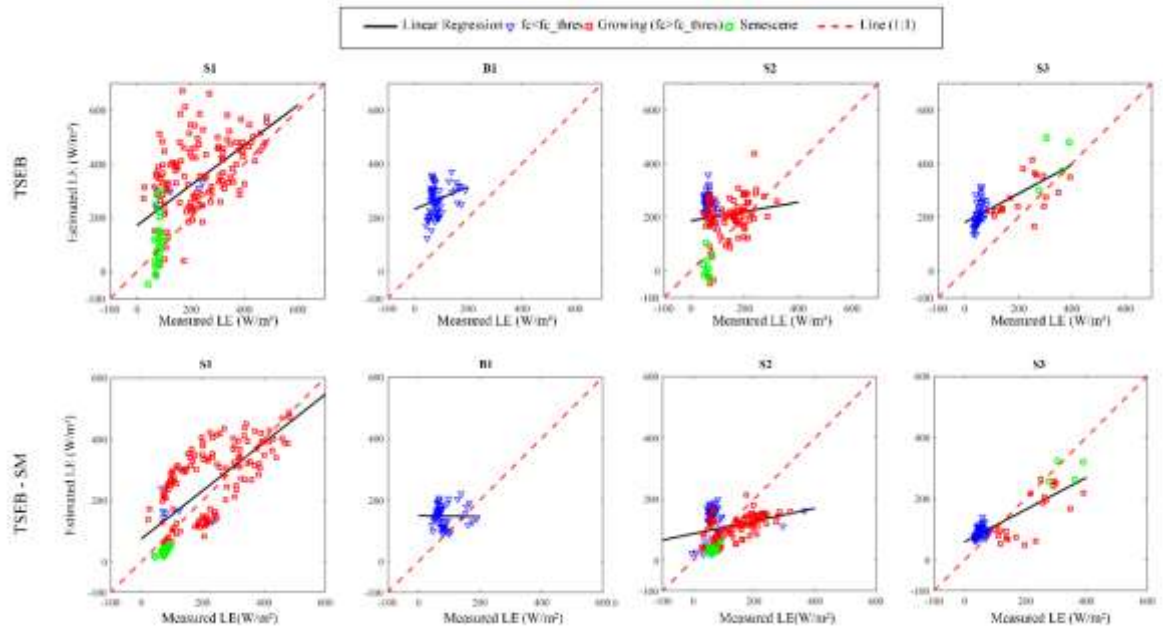

Figure VI. 9. *Same as Fig VI.7 but for satellite data.*

TSEB consistently exhibits larger errors on H estimation (see Fig. VI.10), with RMSE values up to 98, 73, 56 and 66 W/m^2 during S1, S2, S3 and B1 respectively. TSEB-SM provides in general a significantly improved RMSE compared to the original TSEB. The RMSE is 55, 41, 24 and 27 W/m^2 during S1, S2, S3 and B1 respectively.

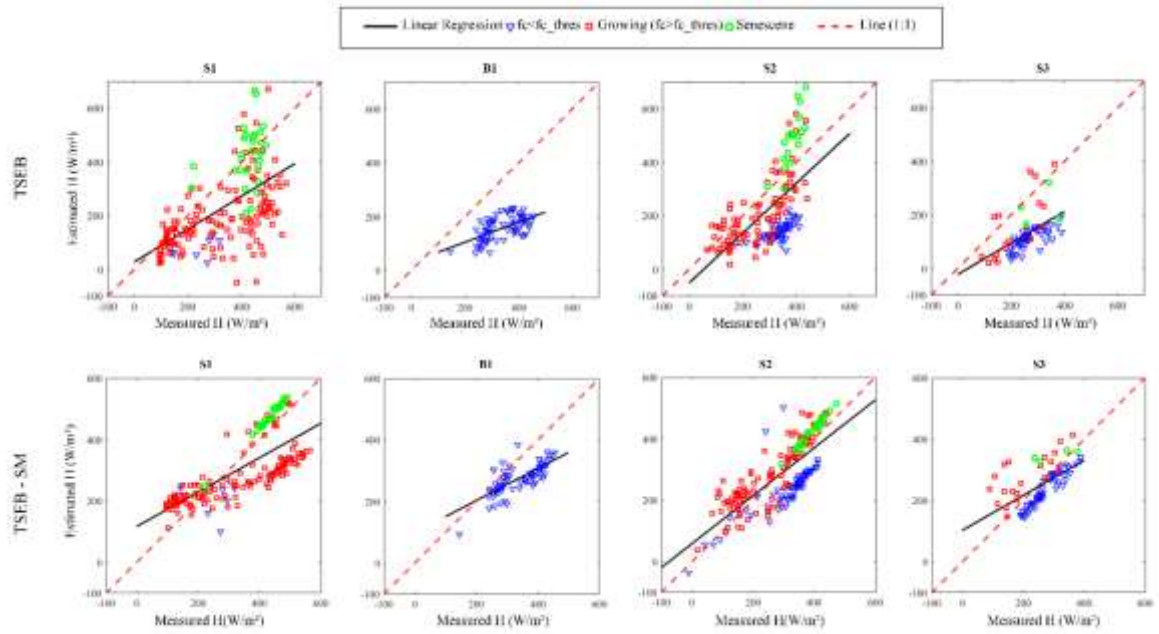

Figure VI. 10. *Same as Fig VI.8 but for H fluxes and satellite data.*

The intercomparison between TSEB and TSEB-SM is finally undertaken by simulating the available energy. The statistics listed in Table VI.3 indicate that there are similar differences between modeled versus measured R_n using either TSEB or TSEB-SM. Overall, the discrepancies between estimated and measured R_n are likely due to a greater scatter between MODIS and in-situ measured LST. Note that RMSE values up to 6 K have been noted when comparing LST MODIS with ground-based measurements. These uncertainties are likely to be explained by the huge scale mismatch between the 1 km resolution of MODIS LST and the footprint size (approximately 1 m) of ground-based radiometers. The uncertainties in key input data generate large differences in simulated R_n compared to the tower measurements. The greater scatter between modeled and measured G from the two models reflect the fact that there is a major mismatch in scale between the area sampled by the soil heat flux sensors and the 1 km resolution of model inputs. It appears that the LE estimates from TSEB-SM are generally in closer agreement with the measurements than the TSEB model outputs. The RMSE is significantly improved from 103 to 52 W/m^2, from 151 to 30 W/m^2, from 101 to 35 W/m^2 and from 83 to 24 W/m^2, during S1, B1, S2 and S3, respectively. For the sensible heat flux H, the difference between TSEB estimates and EC measurements listed in Table VI.3 indicates a fairly large underestimation, the MBE values varying between -56 W/m^2 and -240 W/m^2. However, the TSEB-SM output provides a quite significant improvement, with an absolute MBE lower than -61 W/m^2 during all seasons.

Table VI. 3. Same as Table VI.2. but for simulated R_n and G

			TSEB			TSEB-SM		
			RMSE	R^2	MBE	RMSE	R^2	MBE
Using in-situ data	R_n (W/m^2)	S1	35	0.99	-38	35	0.99	-38
		B1	14	0.99	12	14	0.99	12
		S2	20	0.99	9	20	0.99	9
		S3	**7**	0.99	-0.46	7	0.99	-0.46
	G (W/m^2)	S1	19	0.32	17	19	0.32	17
		B1	19	0.05	12	19	0.05	12
		S2	30	0.28	-13	30	0.28	-13
		S3	26	0.44	9	26	0.44	8
	LE (W/m^2)	S1	87	0.35	27	**65**	**0.58**	**-21**
		B1	141	0.12	174	**52**	**0.16**	**60**
		S2	91	**0.23**	35	**68**	0.22	**-15**
		S3	91	**0.62**	54	**84**	0.47	**22**
	H (W/m^2)	S1	127	0.33	-44	**70**	**0.73**	**34**
		B1	145	0.43	-177	**52**	**0.90**	**-60**
		S2	112	0.48	**2**	**78**	**0.68**	36
		S3	99	**0.30**	-64	**87**	0.30	**-32**
Using satellite data	R_n (W/m^2)	S1	23	0.94	8	22	0.93	8
		B1	85	0.47	32	85	0.47	32
		S2	22	0.94	12	22	0.94	12
		S3	17	0.97	2	17	0.97	2
	G (W/m^2)	S1	20	0.41	24	19	0.40	24
		B1	20	0	15	20	0	15
		S2	25	0.12	-15	25	0.12	-15
		S3	22	0.08	10	22	0.08	10
	LE (W/m^2)	S1	103	0.24	86	**52**	**0.49**	**28**
		B1	151	**0.02**	240	**30**	0.01	**65**
		S2	101	**0.07**	96	**37**	0.06	**28**
		S3	83	0.47	74	**24**	**0.69**	**14**
	H (W/m^2)	S1	112	0.34	-91	**63**	**0.44**	**-45**
		B1	150	0.16	-240	**28**	**0.49**	**-61**
		S2	97	0.4	-56	**38**	**0.52**	**-4**
		S3	85	0.12	-83	**27**	**0.28**	**-29**

VI.7. Summary and Conclusions

The microwave-derived near-surface soil moisture (SM) from SMOS and thermal-derived land surface temperature (LST) from MODIS are integrated simultaneously within a calibration procedure to retrieve the main parameters of soil evaporation (soil resistance, r_{ss}) and plant transpiration (Priestly Taylor coefficient, α_{PT}) based on a threshold on f_c. The TSEB-SM model is applied during a four-year period (2014-2018) over a rainfed wheat field in the Tensift basin, central Morocco. The first calibration step with $f_c \leq f_{c,thres}$ consists in inverting r_{ss} at Terra and Aqua overpass times. Despite the scale difference between the spatial resolution (1 km) of satellite data and the footprint size of in-situ measurements, the pair parameters (a_{rss}, b_{rss}) calculated for the entire study period using satellite data are relatively close to those derived from in-situ measurements. The second calibration step consists in estimating α_{PT} on a daily basis for $f_c > f_{c,thres}$ by using LST and SM data. The maximum of daily calibrated α_{PT} are 1.38, 1.25 and 0.87, when using satellite data, for S1, S2 and S3, respectively. Those values are in accordance with the total rainfall amounts, which were about 608, 214 and 421mm/wheat season for S1, S2 and S3 respectively. S1 and S2 have the same distribution of daily calibrated α_{PT} when comparing with the α_{PT} retrieved using in-situ data, while the retrieved α_{PT} remains at a mostly constant value (~0.7) throughout the study period S3 because of the non-availability of MODIS products during cloudy days.

An analysis of the spatial distributions and the magnitude of the turbulent fluxes using remotely sensing data produced from the two models were conducted. TSEB exhibits larger errors on H and LE estimates. These uncertainties can be linked to the theoretical value of α_{PT}, which is fixed to 1.26 for the whole study period, including both stressed and unstressed conditions, as well as to the scale mismatch between the 1 km resolution of MODIS LST and the footprint size (approximately 1 m) of the ground-based radiometer. The constraint applied on the soil evaporation represented explicitly as a function of SM via a soil resistance term reduces the errors when using TSEB-SM. In fact, the use of the SM derived from microwave data is one of the main controlling factors of the evaporative fraction, which helps to determine with more accuracy the LE/H partitioning.

Chapter.VII. Conclusion and perspectives

Improving the management of water resources in semi-arid areas requires accurate knowledge of the hydrological processes involved. ET is a critical component of the hydrologic cycle and a link between the energy, water, and carbon cycles. It strongly impacts the drought monitoring, the water resource management and climate (Littell et al., 2016; Molden et al., 2010). Furthermore, a precise estimate of ET determines the crop water requirements, which subsequently allow for optimizing water management practices and irrigation regimes (Allen et al., 1998). Three key remote sensing variables can be used to determine the spatial distribution of ET:

- microwave-derived surface (0-5 cm) soil moisture (SM), which is the main controlling factor of soil evaporation considering a given evaporative demand (e.g. Chanzy and Bruckler, 1993),
- visible/near-infratred-derived vegetation cover fraction (f_c), which provides an essential structural constraint on the evaporation/transpiration partitioning (e.g. Allen et al., 2000), and
- thermal-derived land surface temperature (LST), which is a signature of both available energy and ET rate (e.g. Norman et al., 1995).

The aim of this thesis is to consistently integrate those independent and complementary information on total ET within an energy balance model. As a state-of-the-art and commonly used model, we chose the TSEB modelling as a basis for developments.

Our initial proposal '**The validation results of TSEB model over sparse and heterogeneous vegetation in Sahel region (Niger)**' aims to test the TSEB model, which operates the ET partitioning by using the LST, f_c, and the Priestley Taylor (PT) assumption that relates transpiration to net radiation via a fixed PT coefficient (α_{PT}). This study considers the issue of using TSEB driven by MODIS (Moderate resolution imaging spectroradiometer) observations in conjunction with an aggregation scheme to derive area-averaged sensible (H) and latent (LE) heat fluxes over an heterogeneous watershed in Niamey, Niger (Wankama catchment). Data collected in the context of the African Monsoon Multidisciplinary Analysis (AMMA) program, including a scintillometry campaign, are used to test the proposed approach. The model predictions of area-averaged turbulent fluxes are compared to data acquired by a Large Aperture Scintillometer (LAS) set up over a transect about 3.2 km-long and spanning three vegetation types (millet, fallow and degraded shrubs). First, H and LE fluxes are estimated at the MSG-SEVIRI grid scale by neglecting explicitly the subpixel heterogeneity. Next, the impact of upscaling the model's inputs is investigated using in-situ input data and three aggregation schemes of increasing complexity based on MODIS products: a simple averaging

of inputs at the MODIS resolution scale, another simple averaging scheme that considers the scintillometer footprint extent, and the weighted average of inputs based on the footprint weighting function. The results obtained for H and LE are relevant. However, an overestimation of simulated fluxes is recorded at the end of the season, mainly due to the fixed maximum value for α_{PT} (equal to 1.26).

In fact, there are two main limitations of the TSEB model. The first one is when considering the most common value of the Priestley-Taylor coefficient as a constant (1.26) meaning that vegetation has access to enough water in the root zone to transpire at a potential rate. This implies that the vegetation stress conditions are not properly taken into account. Indeed, several studies found that α_{PT} is variable according to several parameters (LAI, vapour pressure deficit, and SM) (Baldocchi and Xu, 2007; Pereira, 2004), while α_{PT} can reach values up to 2 under wettest SM conditions (Baldocchi, 1997, 1994). Agam et al. (2010) reported that over partially covered surfaces, α_{PT} is more likely less than 1.26, as the soil evaporation decreases because of the drying of the top soil (Stannard, 1993). She also stressed that α_{PT} is a critical parameter for natural vegetation and sites with strong vapour pressure deficit values where the root zone moisture does not limit transpiration. The second limitation of the TSEB approach lies on the estimation of soil evaporation as a residual to the soil component energy budgets. This equation may contain biases from the net radiation, soil heat flux and sensible heat flux estimates. To overcome these limitations, data available from space can help in implementing the PT approach by applying a direct constraint on soil evaporation and plant transpiration simultaneously.

The second part of the thesis is hence dedicated to '**Improving TSEB model by integrating SM data (TSEB-SM): a feasibility study using in-situ data (the land surface temperature, vegetation cover fraction and near-surface soil moisture) data**'. For this purpose, a new ET model named TSEB-SM is derived from the TSEB formalism by explicitly representing soil evaporation using a soil resistance. To help constrain the evaporation/transpiration partition of TSEB-SM, an innovative calibration approach is also developed to retrieve the main parameters of soil evaporation (soil resistance, r_{ss}) and plant transpiration (α_{PT}). In practice, the soil resistance parameters are retrieved at the seasonal time scale from SM and LST data with $f_c \leq f_{c,thres}$ (an empirical threshold dedicated to iteratively separate the soil/vegetation parameters on ET estimates), while α_{PT} is retrieved at the daily time scale from SM and LST data for $f_c > f_{c,thres}$. TSEB-SM model is tested over 1 flood- and 2 drip-irrigated wheat fields using in-situ data collected during two field experiments in

2002-2003 and 2016-2017. The coupling of the soil resistance formulation with the TSEB formalism improves the estimation of soil evaporation, and consequently, improves the partitioning of ET. Analysis of the retrieved time series indicates that the daily α_{PT} mainly follows the phenology of winter wheat crop with a maximum value coincident with the full development of green biomass and a minimum value reached at harvest. The temporal variations of α_{PT} before senescence are attributed to the dynamics of both the root zone soil moisture and the amount of green biomass. These results encourage us to develop a parameter estimation method based on SM remote sensing.

The major limitation of the TSEB-SM model lies on the different resistances used to estimate the turbulent fluxes. Indeed, the soil resistance formulation r_{ss} is impacted by soil texture and structure. Errors on a_{rss} and b_{rss} estimations reveal the empirical nature of the r_{ss}. The soil surface resistance (r_s) is also difficult to characterize, because it depends on many factors including wind speed, roughness, and cover type (Norman et al., 1995; Sauer et al., 1995). In our work the simplified equation given by Norman et al. (1995) is used with its default coefficients (a and b) that are suitable for semi-arid regions. However, a sensitivity study of these two parameters shows their strong impact on the surface fluxes, which implies that a calibration procedure is necessary for each type of cover.

The third section '**Remote sensing application of TSEB-SM (Combining DisPATCh soil moisture and MODIS LST/f_c data for mapping ET at 1 km resolution**' aims to evaluate the performance of TSEB-SM in real-life using 1 km resolution MODIS LST and f_c data and the 1 km resolution SM data disaggregated from SMOS (Soil Moisture and Ocean Salinity) observations by using DisPATCh. The approach is applied over a rainfed wheat field in the Tensift basin, central Morocco, during a four-year period (2014-2018). The field was seeded for the 2014-2015 (S1), 2016-2017 (S2) and 2017-2018 (S3) agricultural season, while it remained under bare soil conditions during the 2015-2016 (B1) wheat seasons. Compared to eddy covariance measurements, TSEB driven only by LST and f_c data significantly overestimates latent heat fluxes for the four seasons. The overall mean bias values are 119, 94, 128 and 181 W/m^2 for S1, S2, S3 and B1 respectively. In contrast, these errors are much reduced when using TSEB-SM (SM and LST combined data) with the mean bias values estimated as 39, 4, 7 and 62 W/m^2 for S1, S2, S3 and B1 respectively. The constraint applied on the soil evaporation by using the SM derived from SMOS data is one of the main

controlling factors of the evaporative fraction, which helps to determine with more accuracy the LE/H partitioning.

There are two main limitations regarding the DisPATCh SM product used as input to TSEB-SM. The first one is linked to the temporal resolution (discussed in detail in Malbéteau et al., 2018, 2016) and the second one is linked to the spatial resolution. The temporal resolution of DisPATCh data is constrained by the number of SMOS overpasses (a global coverage every 3 days) and by the gaps in MODIS images due to cloud cover. Moreover, the spatial resolution of 1 km is still coarse for applications and validation studies at the field scale. This is the main reason why the model is applied over a rainfed parcel located within a larger area occupied mostly by rainfed wheat ('Bour'). This field was chosen to be representative at a scale of 1 km, thus enabling the comparison between 1 km resolution satellite-derived and localized in-situ measurements. Over irrigated areas however, wheat fields do not exceed 4 ha, and they are sowed and irrigated on different dates, which generate heterogeneity in SM as well as LST and NDVI fields within a 1 km resolution pixel, and result in systematic errors in the model predictions.

Overall, this thesis is based on a development of original methods exploiting optimally the synergy between different sensors. In particular, combining the microwave / optical data for the high spatial resolution estimation of root zone SM and appropriate partitioning of ET into transpiration and soil evaporation. These targeted researches respond to the needs of managing agencies by providing spatialized indicators of drought and crop water requirements. Based on the results obtained and the conclusions reached, several promising perspectives can be considered for improving this work.

Further efforts should be made to investigate the variability of α_{PT} at the daily and finer time scales and to relate its variations to variables other than biomass and soil water availability. Reciprocally, the retrieved α_{PT} could serve as a basis for deriving a proxy for root zone soil moisture and crop water needs. The aim is to evaluate the modelling approaches for partitioning the ET at regional scale, while using very different physical constraints. Besides, modelling the transpiration schemes in a more physically and realistic way, hence obviating the semi-empirical formulation of PT, can provide valuable results. Several studies incorporate the canopy conductance model into the thermal-based TSEB model under various atmospheric and SM conditions (Anderson et al., 2008, 2000; Zhan and Kustas, 2001). Recently Gan and Gao (2015) embedded a biophysical canopy conductance model (modelled as a function of the LAI, water vapor deficit, and visible radiation) into TSEB model to

replace the PT assumption, and updated the formulation of the under-canopy resistance. While optimizing the resistance networks by using the LST data, results show that the canopy conductance is successfully incorporated into the resistance network giving reasonable ET estimates. In the same way, Anderson et al. (2008) incorporated an analytical light-use efficiency (LUE, defined as the ratio between net canopy carbon assimilation rate, and the photosynthetically active radiation absorbed by the vegetative canopy) based model of canopy resistance within the TSEB model instead of using the PT based transpiration. Results show that LUE module improves the partitioning of the surface energy budget. It reflects its robustness to achieve appropriate reductions in canopy conductance in response to elevated midday vapour pressure deficits, which implicitly reduce the errors on flux predictions. These previous results are very encouraging, because they prove that the stomatal conductance can be a critical indicator for monitoring the water status/stress of crops.

Parallel to ongoing work in a more realistic representation of canopy resistance, the resistance to soil evaporation also needs some improvements. Merlin et al. (2016) proposed a pedo-transfer function to relate the main soil evaporation parameter to soil texture. To better constrain the soil evaporation using microwave / thermal data, a new formulation was developed in Merlin et al. (2018) to correct the cyclic phenomenon of drying/rewetting of the top soil during daytime/night-time.

Regarding the input data of TSEB-SM, a new method is being developed to apply DisPATCh to (Landsat-7 and Landsat-8) thermal infrared data in order to disaggregate SMOS and SMAP SM data to a spatial resolution of 100 m (Nitu Ojha's thesis). This spatial resolution of 100 m will allow the crop field size to be resolved and thus a finer and more precise estimate of SM and associated ET/water stress predictions. Alternatively, the use of active sensors recently launched, as Sentinel-1 that potentially provides the surface SM at resolutions of 20 m each 6 days. Such high spatio-temporal resolution is consistent with Sentinel-2 mission, which follows the characteristics of the canopy at resolution of 10 to 60 m with a repeat cycle of 5 days by combining both ascending and descending overpasses. The integration of these recent high-resolution products could improve the partitioning of evaporation/ transpiration and consequently provide a better estimate of ET at large scale. Recently, a new work developed in the framework of LMI/TREMA (Nadia Ouaadi thesis) demonstrates the sensitivity of the backscattering coefficient and the interferometric coherence (Sentinel-1) to SM variabilities and wheat crops growth. Nadia developed a new method to retrieve SM combining the interferometric coherence and C-band backscattering coefficient over irrigated wheat from sowing to harvest. The preliminary results are very encouraging. The proposed approach

present the advantage of applying the TSEB-SM model over extended areas. Moreover, an India-France joint high spatio-temporal resolution TRISHNA mission (Thermal infraRed Imaging Satellite for High-resolution Natural resource Assessment) will be launched at 2024-2025 horizon. It will provide the LST at resolution of 50 m, each 3 days. With its high spatial resolution and high repeatability, TRISHNA will accurately track spatio-temporal changes in different types of crops. It will help progress on the surface fluxes modelling and the crop stress detection.

In addition to SM and LST, other relevant remote sensing indicators could be used as input to the TSEB-SM approach. In particular, the Photochemical Reflectance Index (PRI) derived from narrow-band spectroradiometers is a spectral index based on the short term reversible xanthophyll pigment changes that accompany plant stress and associated photosynthetic activities. Strong relationships between PRI and LUE were shown at leaf and canopy scales and over a wide range of species (Garbulsky et al., 2011; Peñuelas et al., 2011). Suárez et al. (2008) found that PRI is well correlated to physiological indicators of water stress, such as stomatal conductance, stem water potential, and fluorescence over an olive orchard. Our challenge lies on developing a new formulation of stomatal conductance, which embed hydric stress information provided from the PRI index. In this context, the Earth Explorer - Fluorescence Explorer (FLEX) mission will be launched by 2022 to provide global maps of vegetation fluorescence, PRI, canopy temperature measurements and all the relevant variables (chlorophyll content, Leaf Area Index, etc.) needed to assess the actual physiological status of vegetation. In the same context, current work conducted in the framework of LMI/TREMA (Zoubair Rafi thesis) aims to analyse the PRI data collected over several irrigated wheat fields in Morocco by developing a new early water stress indicator that could be used in addition to LST-derived indices.

Lastly, it is important to note that TSEB-SM has not been specifically evaluated in terms of evaporation/transpiration partitioning, meaning using ground measurements separating both components simultaneously. Especially the derived evaporation/transpiration products should be validated using lysimeter and sap flow measurements instead of validating the total ET by eddy covariance system (Rafi et al. 2019). In addition, the evaluation of ET at large scale is missing. Spatialized measurements that could be collected by scintillometers installed at various points in the region would be a solution for that purpose.

References

Abourida, A., Errouane, S., Leduc, C., Chehbouni, G., 2005. Impact de la modernisation agricole sur l'évolution piézométrique de la nappe phréatique du Haouz (Maroc central) Impact de la modernisation agricole sur l'′ evolution piézométrique de la nappe phréatique du Haouz (Maroc central), in: La Modernisation de l'Agriculture Irriguée : Séminaire Euro-Méditerranéen. Rabat.

Agam, N., Kustas, W.P., Anderson, M.C., Norman, J.M., Colaizzi, P.D., Howell, T.A., Prueger, J.H., Meyers, T.P., Wilson, T.B., 2010a. Application of the Priestley–Taylor Approach in a Two-Source Surface Energy Balance Model. J. Hydrometeorol. 11, 185–198. https://doi.org/10.1175/2009JHM1124.1

Agam, N., Kustas, W.P., Anderson, M.C., Norman, J.M., Colaizzi, P.D., Howell, T.A., Prueger, J.H., Meyers, T.P., Wilson, T.B., 2010b. Application of the Priestley–Taylor Approach in a Two-Source Surface Energy Balance Model. J. Hydrometeorol. 11, 185–198. https://doi.org/10.1175/2009JHM1124.1

Ait Hssaine, B., Ezzahar, J., Jarlan, L., Merlin, O., Khabba, S., Brut, A., Er-Raki, S., Elfarkh, J., Cappelaere, B., Chehbouni, G., 2018a. Combining a Two Source Energy Balance Model Driven by MODIS and MSG-SEVIRI Products with an Aggregation Approach to Estimate Turbulent Fluxes over Sparse and Heterogeneous Vegetation in Sahel Region (Niger). Remote Sens. 10, 974. https://doi.org/10.3390/rs10060974

Ait Hssaine, B., Merlin, O., Rafi, Z., Ezzahar, J., Jarlan, L., Khabba, S., Er-Raki, S., 2018b. Calibrating an evapotranspiration model using radiometric surface temperature, vegetation cover fraction and near-surface soil moisture data. Agric. For. Meteorol. 256–257, 104–115. https://doi.org/10.1016/j.agrformet.2018.02.033

Aksakal, S., Aksakal, Kocaman, S., 2013. Geometric Accuracy Investigations of SEVIRI High Resolution Visible (HRV) Level 1.5 Imagery. Remote Sens. 5, 2475–2491. https://doi.org/10.3390/rs5052475

Albergel, J., 2008. Place des petits barrages dans la mobilisation des eaux de surface et dans la lutte contre l'érosion au Maghreb et au Moyen-Orient, in: Efficacité de La Gestion de l'eau et de La Fertilité Des Sols En Milieux Semi-Arides. Montréal, IRD, pp. 35–47.

Ali Eweys, O., José Escorihuela, M., Villar, J.M., Er-Raki, S., Amazirh, A., Olivera, L., Jarlan, L., Khabba, S., Merlin, O., 2017. remote sensing Disaggregation of SMOS Soil Moisture to 100 m Resolution Using MODIS Optical/Thermal and Sentinel-1 Radar Data: Evaluation over a Bare Soil Site in Morocco. Remote Sens. 9, 1155. https://doi.org/10.3390/rs9111155

Allen, R.G., Pereira, L.S., Howell, T.A., Jensen, M.E., 2011. Evapotranspiration information reporting: I. Factors governing measurement accuracy. Agric. Water Manag. 98, 899–920. https://doi.org/10.1016/J.AGWAT.2010.12.015

Allen, R.G., Pereira, L.S., Howell, T.A., Jensen, M.E., 2000. Evapotranspiration information reporting: I. Factors governing measurement accuracy. Agric. Water Manag. 78, 899–920. https://doi.org/10.1016/j.agwat.2010.12.015

Allen, R.G., Pereira, L.S., Raes, D., Smith, M., 1998. Crop evapotranspiration-Guidelines for computing crop water requirements-FAO Irrigation and drainage paper 56.

Allen, R.G., Tasumi, M., Morse, A., Trezza, R., Wright, J.L., Bastiaanssen, W., Kramber, W., Lorite, I., Robison, C.W., 2007. Satellite-Based Energy Balance for Mapping Evapotranspiration with Internalized Calibration (METRIC)—Applications. J. Irrig. Drain. Eng. 133, 395–406. https://doi.org/10.1061/(ASCE)0733-9437(2007)133:4(395)

Allies, A., Demarty, J., Olioso, A., Peugeot, C., Kergoat, L., Grippa, M., Boone, A., Issoufou, H.B.-A., Ma\"ınassara, I., Chazarin, J.P., O\"ı, M., Velluet, C., Bahir, M., Cappelaere, B., 2017. Estimating evapotranspiration from remote sensing in West Africa: application of S-SEBI and Ts-VI triangle methods, in: RAQRS'V - 5th International Symposium "Recent Advances in Quantitative Remote Sensing." Valencia, Spain. 2017.

Amazirh, A., Merlin, O., Er-Raki, S., Gao, Q., Rivalland, V., Malbeteau, Y., Khabba, S., Escorihuela, M.J., 2018. Retrieving surface soil moisture at high spatio-temporal resolution from a synergy between Sentinel-1 radar and Landsat thermal data: A study case over bare soil. Remote Sens. Environ. 211, 321–337. https://doi.org/10.1016/j.rse.2018.04.013

Anderson, M., 1997. A Two-Source Time-Integrated Model for Estimating Surface Fluxes Using Thermal Infrared Remote Sensing. Remote Sens. Environ. 60, 195–216. https://doi.org/10.1016/S0034-4257(96)00215-5

Anderson, M.C., Norman, J.M., Kustas, W.P., Houborg, R., Starks, P.J., Agam, N., 2008. A thermal-based remote sensing technique for routine mapping of land-surface carbon, water and energy fluxes from field to regional scales. Remote Sens. Environ. 112, 4227–4241. https://doi.org/10.1016/J.RSE.2008.07.009

Anderson, M.C., Norman, J.M., Mecikalski, J.R., Otkin, J.A., Kustas, W.P., 2007. A climatological study of evapotranspiration and moisture stress across the continental United States based on thermal remote sensing: 2. Surface moisture climatology. J. Geophys. Res. 112, D11112. https://doi.org/10.1029/2006JD007507

Anderson, M.C., Norman, J.M., Meyers, T.P., Diak, G.R., 2000. An analytical model for estimating canopy transpiration and carbon assimilation fluxes based on canopy light-use efficiency. Agric. For. Meteorol. 101, 265–289. https://doi.org/10.1016/S0168-1923(99)00170-7

Artogensis, O.K., 1997. Measuring areally-averaged sensible heat fluxes with a Large Aperture Scintillometer. Department of Meteorology Agricultural University of Wageningen the Netherlands.

Aston, A.R., 1985. Heat storage in a young eucalypt forest. Agric. For. Meteorol. 35, 281–297. https://doi.org/10.1016/0168-1923(85)90090-5

Balaghi, R., Jlibene, M., Tychon, B., Eerens, H., 2012. La prédiction agrométéorologique des rendements céréaliers au Maroc.

Baldocchi, D., 2014. Measuring fluxes of trace gases and energy between ecosystems and the atmosphere - the state and future of the eddy covariance method. Glob. Chang. Biol. 20, 3600–3609. https://doi.org/10.1111/gcb.12649

Baldocchi, D., 2003. Assessing the eddy covariance technique for evaluating carbon dioxide exchange rates of ecosystems: past, present and future. Glob. Chang. Biol. 9, 479–492.

https://doi.org/10.1046/j.1365-2486.2003.00629.x

Baldocchi, D., 1997. Measuring and modelling carbon dioxide and water vapour exchange over a temperate broad-leaved forest during the 1995 summer drought. Plant, Cell Environ. 20, 1108–1122. https://doi.org/10.1046/j.1365-3040.1997.d01-147.x

Baldocchi, D., 1994. An analytical solution for coupled leaf photosynthesis and stomatal conductance models. Tree Physiol. 14, 1069–1079.

Baldocchi, D., Chu, H., Reichstein, M., 2018. Inter-annual variability of net and gross ecosystem carbon fluxes: A review. Agric. For. Meteorol. 249, 520–533. https://doi.org/10.1016/j.agrformet.2017.05.015

Baldocchi, D., Falge, E., Gu, L., Olson, R., Hollinger, D., Running, S., Anthoni, P., Bernhofer, C., Davis, K., Evans, R., Fuentes, J., Goldstein, A., Katul, G., Law, B., Lee, X., Malhi, Y., Meyers, T., Munger, W., Oechel, W., Paw, K.T., Pilegaard, K., Schmid, H.P., Valentini, R., Verma, S., Vesala, T., Wilson, K., Wofsy, S., Baldocchi, D., Falge, E., Gu, L., Olson, R., Hollinger, D., Running, S., Anthoni, P., Bernhofer, C., Davis, K., Evans, R., Fuentes, J., Goldstein, A., Katul, G., Law, B., Lee, X., Malhi, Y., Meyers, T., Munger, W., Oechel, W., U, K.T.P., Pilegaard, K., Schmid, H.P., Valentini, R., Verma, S., Vesala, T., Wilson, K., Wofsy, S., 2001. FLUXNET: A New Tool to Study the Temporal and Spatial Variability of Ecosystem–Scale Carbon Dioxide, Water Vapor, and Energy Flux Densities. Bull. Am. Meteorol. Soc. 82, 2415–2434. https://doi.org/10.1175/1520-0477(2001)082<2415:FANTTS>2.3.CO;2

Baldocchi, D., Ryu, Y., Keenan, T., 2016. Terrestrial Carbon Cycle Variability. F1000Research 5, 2371. https://doi.org/10.12688/f1000research.8962.1

Baldocchi, D.D., Xu, L., 2007. What limits evaporation from Mediterranean oak woodlands-The supply of moisture in the soil, physiological control by plants or the demand by the atmosphere? Adv. Water Resour. 30, 2113–2122. https://doi.org/10.1016/j.advwatres.2006.06.013

Balenzano, A., Mattia, F., Satalino, G., Davidson, M.W.J., 2011. Dense Temporal Series of C- and L-band SAR Data for Soil Moisture Retrieval Over Agricultural Crops. IEEE J. Sel. Top. Appl. Earth Obs. Remote Sens. 4, 439–450. https://doi.org/10.1109/JSTARS.2010.2052916

Bannari, A., Morin, A.D., Bonn, D.F., Huete, F., 1995. A review of vegetation indices. Remote Sens. Rev. 13, 95–120. https://doi.org/10.1080/02757259509532298

Bastiaanssen, W.G.M., Ali, S., 2003. A new crop yield forecasting model based on satellite measurements applied across the Indus Basin, Pakistan. Agric. Ecosyst. Environ. 94, 321–340. https://doi.org/10.1016/S0167-8809(02)00034-8

Bastiaanssen, W.G.M., Menenti, M., Feddes, R.A., Holtslag, A.A.M., 1998. A remote sensing surface energy balance algorithm for land (SEBAL). 1. Formulation. J. Hydrol. 212–213, 198–212. https://doi.org/10.1016/S0022-1694(98)00253-4

Bausch, W.C., Neale, C.M.U., 1990. spectral Inputs Improve Corn Crop Coefficients and Irrigation Scheduling. Trans. ASAE 32, 1901. https://doi.org/10.13031/2013.31241

Becker, P., Erhart, D.., Smith, A.., 1989. Analysis of forest light environments part I. Computerized estimation of solar radiation from hemispherical canopy photographs. Agric. For. Meteorol. 44, 217–232. https://doi.org/10.1016/0168-1923(89)90018-X

Belaqziz, S., Khabba, S., Er-Raki, S., Jarlan, L., 2013. Caractérisation de la distribution des irrigations par l'utilisation de la télédétection pour les réseaux d'irrigation gravitaire "Agro-hydrology from space" project is supported by the ESA living planet program View project SAT IRR, Satellite for Irrigation scheduling View project, in: African Association of Remote Sensing of the Environment.

Belaqziz, S., Mangiarotti, S., Le Page, M., Khabba, S., Er-Raki, S., Agouti, T., Drapeau, L., Kharrou, M.H., Adnani, M. El, Jarlan, L., Le, M., El Adnani, M., 2014. Irrigation scheduling of a classical gravity network based on the Covariance Matrix Adaptation-Evolutionary Strategy algorithm. Comput. Electron. Agric. 102, 64–72. https://doi.org/10.1016/j.compag.2014.01.006

Bindlish, R., Kustas, W.P., French, A.N., Diak, G.R., Mecikalski, J.R., 2001. Influence of near-surface soil moisture on regional scale heat fluxes: Model results using microwave remote sensing data from SGP97. IEEE Trans. Geosci. Remote Sens. 39, 1719–1728. https://doi.org/10.1109/36.942550

Black, T.A., McNaughton, K.G., 1971. Psychrometric apparatus for Bowen-ratio determination over forests. Boundary-Layer Meteorol. 2, 246–254. https://doi.org/10.1007/BF00192133

Blyth, E.M., Harding, R.J., 1995. Application of aggregation models to surface heat flux from the Sahelian tiger bush. Agric. For. Meteorol. 72, 213–235. https://doi.org/10.1016/0168-1923(94)02164-F

Bolle, H.-J., 2003. Mediterranean Climate: Variability and Trends, in: Mediterranean Climate. Springer Berlin Heidelberg, Berlin, Heidelberg, pp. 5–86. https://doi.org/doi:10.1007/978-3-642-55657-9

Boswinkel, J.., 2000. International Groundwater Resources Assessment Centre (IGRAC).

Boudhar, A., Duchemin, B., Hanich, L., Chaponnière, A., Maisongrande, P., Boulet, G., Stitou, J., Chehbouni, A., Boudhar, A., Hanich, L., Chaponnière, A., Maisongrande, P., Stitou, J., 2007. Analyse de la dynamique des surfaces enneigées du Haut Atlas marocain à partir des données SPOT-VEGETATION Article scientifique Analyse de la dynamique des surfaces enneigées du Haut Atlas marocain à partir des données SPOT-VEGETATION 18, 278–288. https://doi.org/10.1684/sec.2007.0100

Boulain, N., Cappelaere, B., Ramier, D., Issoufou, H.B.A., Halilou, O., Seghieri, J., Guillemin, F., Oi, M., Gignoux, J., Timouk, F., 2008. Towards an understanding of coupled physical and biological processes in the cultivated Sahel - 2. vegetation and carbon dynamics. J. Hydrol. 375, 190–203.

Boulain, N., Cappelaere, B., Ramier, D., Issoufou, H.B.A., Halilou, O., Seghieri, J., Guillemin, F., Oï, M., Gignoux, J., Timouk, F., 2009. Towards an understanding of coupled physical and biological processes in the cultivated Sahel – 2. Vegetation and carbon dynamics. J. Hydrol. 375, 190–203. https://doi.org/10.1016/J.JHYDROL.2008.11.045

Boulain, N., Cappelaere, B., Seguis, L., Ginoux, J., Peugeot, C., 2006. Hydrologic and land use impacts on vegetation growth and NPP at the watershed scale in a semi-arid environment. Reg Env. Chang. 6, 147–156. https://doi.org/10.1007/s10113-006-0014-0

Boulet, G., 1991. Modelisation des changements d'echelle et prise en compte des heterogeneites de surface et de leur variabilite spatiale dans les interactionssol-

vegetation-atmosphere. Université Joseph Fourier– GRENOBLE I.

Boulet, G., Mougenot, B., Lhomme, J.P., Fanise, P., Lili-Chabaane, Z., Olioso, A., Bahir, M., Rivalland, V., Jarlan, L., Merlin, O., Coudert, B., Er-Raki, S., Lagouarde, J.P., 2015. The SPARSE model for the prediction of water stress and evapotranspiration components from thermal infra-red data and its evaluation over irrigated and rainfed wheat. Hydrol. Earth Syst. Sci. 19, 4653–4672. https://doi.org/10.5194/hess-19-4653-2015

Bowen, I.S., 1926. The Ratio of Heat Losses by Conduction and by Evaporation from any Water Surface. Phys. Rev. 27, 779–787. https://doi.org/10.1103/PhysRev.27.779

Braud, I., Dantas-Antonino, A.C., Vauclin, M., Thony, J.L., Ruelle, P., 1995. A simple soil-plant-atmosphere transfer model (SiSPAT) development and field verification, Journal of Hydrology ELSEVIER.

Brunsell, N.A., Ham, J.M., Arnold, K.A., 2011. Validating remotely sensed land surface fluxes in heterogeneous terrain with large aperture scintillometry. Int. J. Remote Sens. 32, 6295–6314. https://doi.org/10.1080/01431161.2010.508058

Brutsaert, W., 1982. Introduction, in: Evaporation into the Atmosphere. Springer Netherlands, Dordrecht, pp. 1–11. https://doi.org/10.1007/978-94-017-1497-6_1

Brutsaert, W., 1975. On a derivable formula for long-wave radiation from clear skies. Water Resour. Res. 11, 742–744. https://doi.org/10.1029/WR011i005p00742

Cahill, A.T., Ungaro, F., Parlange, M.B., Mata, M., Nielsen, D.R., 1999. Combined spatial and Kalman filter estimation of optimal soil hydraulic properties. Water Resour. Res. 35, 1079–1088.

Campbell, G.S., Norman, J.M., 1998. An Introduction to Environmental Biophysics, in: An Introduction to Environmental Biophysics. Springer New York, New York, NY, pp. 1–13. https://doi.org/10.1007/978-1-4612-1626-1_1

Cappelaere, B., Boulain, N., Ramier, D., Timouk, F., 2007. Un protocole expérimental pour l ' étude du couplage entre hydrologie et végétation en région centrale-sahélienne 2007, 1–9.

Carlson, T.N., Capehart, W.J., Gillies, R.R., 1995. A new look at the simplified method for remote sensing of daily evapotranspiration. Remote Sens. Environ. 54, 161–167. https://doi.org/10.1016/0034-4257(95)00139-R

Carlson, T.N., Gillies, R.R., Perry, E.M., 1994. A method to make use of thermal infrared temperature and NDVI measurements to infer surface soil water content and fractional vegetation cover. Remote Sens. Rev. 9, 161–173. https://doi.org/10.1080/02757259409532220

Carlson, T.N., Perry, E.M., Schmugge, T.J., 1990. Remote estimation of soil moisture availability and fractional vegetation cover for agricultural fields. Agric. For. Meteorol. 52, 45–69. https://doi.org/10.1016/0168-1923(90)90100-K

Castelli, F., Entekhabi, D., Caporali, E., 1999. Estimation of surface heat flux and an index of soil moisture using adjoint-state surface energy balance. Water Resour. Res. 35, 3115–3125. https://doi.org/10.1029/1999WR900140

Chan, S.K., Bindlish, R., O'Neill, P.E., Njoku, E., Jackson, T., Colliander, A., Chen, F., Burgin, M., Dunbar, S., Piepmeier, J., Yueh, S., Entekhabi, D., Cosh, M.H., Caldwell,

T., Walker, J., Wu, X., Berg, A., Rowlandson, T., Pacheco, A., McNairn, H., Thibeault, M., Martinez-Fernandez, J., Gonzalez-Zamora, A., Seyfried, M., Bosch, D., Starks, P., Goodrich, D., Prueger, J., Palecki, M., Small, E.E., Zreda, M., Calvet, J.-C., Crow, W.T., Kerr, Y., 2016. Assessment of the SMAP Passive Soil Moisture Product. IEEE Trans. Geosci. Remote Sens. 54, 4994–5007. https://doi.org/10.1109/TGRS.2016.2561938

Chanzy, A., Bruckler, L., 1993. Significance of soil surface moisture with respect to daily bare soil evaporation. Water Resour. Res. 29, 1113–1125. https://doi.org/10.1029/92WR02747

Chaponnière, A., Maisongrande, P., Duchemin, B., Hanich, L., Boulet, G., Escadafal, R., Elouaddat, S., 2005. A combined high and low spatial resolution approach for mapping snow covered areas in the Atlas mountains. Int. J. Remote Sens. 26, 2755–2777. https://doi.org/10.1080/01431160500117758

Chauhan, N.S., Miller, S., Ardanuy, P., 2003. Spaceborne soil moisture estimation at high resolution: A microwave-optical/IR synergistic approach. Int. J. Remote Sens. 24, 4599–4622. https://doi.org/10.1080/0143116031000156837

Chehbouni, A., Njoku, E.G., Lhomme, J.-P., Kerr, Y.H., 1995. American Meteorological Society Approaches for Averaging Surface Parameters and Fluxes over Heterogeneous Terrain, Source: Journal of Climate.

Chehbouni, A., Watts, C., Kerr, Y.H., Dedieu, G. et al., 2000. Methods to aggregate turbulent fluxes over heterogeneous surfaces: application to SALSA data set in Mexico. Agric. For. Meteorol. 105, 133–144. https://doi.org/10.1016/S0168-1923(00)00185-4

Chirouze, J., Boulet, G., Jarlan, L., Fieuzal, R., Rodriguez, J.C., Ezzahar, J., Bigeard, G., Merlin, O., 2014. Intercomparison of four remote-sensing-based energy balance methods to retrieve surface evapotranspiration and water stress of irrigated fields in semi-arid climate. Hydrol. Earth Syst. Sci. 18, 1165–1188. https://doi.org/10.5194/hess-18-1165-2014

Choudhury, B., Idso, S., Reginato, R., 1987. Analysis of an empirical model for soil heat flux under a growing wheat crop for estimating evaporation by an infrared-temperature based energy balance equation. Agric. For. Meteorol. 39, 283–297. https://doi.org/10.1016/0168-1923(87)90021-9

Choudhury, B.J., 1989. Estimating evaporation and carbon assimilation using infrared temperature data:vistas in modeling. Theory Appl. Opt. Remote Sens. 628–690.

Colaizzi, P.D., Kustas, W.P., Anderson, M.C., Agam, N., Tolk, J.A., Evett, S.R., Howell, T.A., Gowda, P.H., O'shaughnessy, S.A., 2012. Two-source energy balance model estimates of evapotranspiration using component and composite surface temperatures q. Adv. Water Resour. 50, 134–151. https://doi.org/10.1016/j.advwatres.2012.06.004

Colaizzi, P.D., Tolk, J.A., Evett, S.R., Howell, T.A., 2014. TWO-SOURCE ENERGY BALANCE MODEL TO CALCULATE E, T, AND ET: COMPARISON OF PRIESTLEY-TAYLOR AND PENMAN-MONTEITH FORMULATIONS AND TWO TIME SCALING METHODS. Trans. ASABE (American Soc. Agric. Biol. Eng. 57(2): 479-498. https://doi.org/10.13031/trans.57.10423

Colliander, A., Jackson, T.J., Bindlish, R., Chan, S., Das, N., Kim, S.B., Cosh, M.H., Dunbar, R.S., Dang, L., Pashaian, L., Asanuma, J., Aida, K., Berg, A., Rowlandson, T., Bosch, D., Caldwell, T., Caylor, K., Goodrich, D., al Jassar, H., Lopez-Baeza, E., Martínez-

Fernández, J., González-Zamora, A., Livingston, S., McNairn, H., Pacheco, A., Moghaddam, M., Montzka, C., Notarnicola, C., Niedrist, G., Pellarin, T., Prueger, J., Pulliainen, J., Rautiainen, K., Ramos, J., Seyfried, M., Starks, P., Su, Z., Zeng, Y., van der Velde, R., Thibeault, M., Dorigo, W., Vreugdenhil, M., Walker, J.P., Wu, X., Monerris, A., O'Neill, P.E., Entekhabi, D., Njoku, E.G., Yueh, S., 2017. Validation of SMAP surface soil moisture products with core validation sites. Remote Sens. Environ. 191, 215–231. https://doi.org/10.1016/j.rse.2017.01.021

Coudert, B., Ottlé, C., 2007. An improved SVAT model calibration strategy based on the optimisation of surface temperature temporal dynamics. Geophys. Res. Lett. 34, L04402. https://doi.org/10.1029/2006GL028778

Coudert, B., Ottlé, C., Boudevillain, B., Demarty, J., Guillevic, P., Coudert, B., Ottlé, C., Boudevillain, B., Demarty, J., Guillevic, P., 2006. Contribution of Thermal Infrared Remote Sensing Data in Multiobjective Calibration of a Dual-Source SVAT Model. J. Hydrometeorol. 7, 404–420. https://doi.org/10.1175/JHM503.1

Courault, D., Seguin, B., Olioso, A., 2005. Review on estimation of evapotranspiration from remote sensing data: From empirical to numerical modeling approaches. Irrig. Drain. Syst. 19, 223–249.

Cramer, W., Guiot, J., Fader, M., Garrabou, J., Gattuso, J.-P., Iglesias, A., Lange, M.A., Lionello, P., Llasat, M.C., Paz, S., Peñuelas, J., Snoussi, M., Toreti, A., Tsimplis, M.N., Xoplaki, E., 2018. Climate change and interconnected risks to sustainable development in the Mediterranean. Nat. Clim. Chang. 8, 972–980. https://doi.org/10.1038/s41558-018-0299-2

Crow, W.T., 2003. Multiobjective calibration of land surface model evapotranspiration predictions using streamflow observations and spaceborne surface radiometric temperature retrievals. J. Geophys. Res. 108, 4723. https://doi.org/10.1029/2002JD003292

De Bruin, H.A.R., Van Den Hurk, B.J.J.M., Kohsiek, W., 1995. The scintillation method tested over a dry vineyard area. Boundary-Layer Meteorol. 76, 25–40. https://doi.org/10.1007/BF00710889

Deardorff, J.W., 1978. Efficient prediction of ground surface temperature and moisture, with inclusion of a layer of vegetation. J. Geophys. Res. 83, 1889. https://doi.org/10.1029/JC083iC04p01889

Dekić, L., Mihailović, D.T., Rajković, B., 1995. A study of the sensitivity of bare soil evaporation schemes to soil surface wetness, using the coupled soil moisture and surface temperature prediction model, BARESOIL. Meteorol. Atmos. Phys. 55, 101–112. https://doi.org/10.1007/BF01029605

Desborough, C.E., Pitman, A.J., Iranneiad, P., 1996. Analysis of the relationship between bare soil evaporation and soil moisture simulated by 13 land surface schemes for a simple non-vegetated site. Glob. Planet. Change 13, 47–56. https://doi.org/10.1016/0921-8181(95)00036-4

Diarra, A., Jarlan, L., Er-Raki, S., Le Page, M., Aouade, G., Tavernier, A., Boulet, G., Ezzahar, J., Merlin, O., Khabba, S., 2017. Performance of the two-source energy budget (TSEB) model for the monitoring of evapotranspiration over irrigated annual crops in North Africa. Agric. Water Manag. 193, 71–88.

https://doi.org/10.1016/j.agwat.2017.08.007

Dickinson, E., Henderson-Sellers, A., Kennedy, J., Wilson, F., 1986. Biosphere-atmosphere Transfer Scheme (BATS) for the NCAR Community Climate Model. https://doi.org/10.5065/D6668B58

Dijk, A. Van, Moene, A.F., de Bruin, H.A.R., 2004. The principles of surface flux physics: theory, practice and description of the ECPACK library, Internal Report 2004/1. Intern. Report2004/1, Meteorol. Air Qual. Group, Wageningen Univ. Wageningen,the Netherlands 99.

Djamai, N., Magagi, R., Goïta, K., Hosseini, M., Cosh, M.H., Berg, A., Toth, B., 2015. Evaluation of SMOS soil moisture products over the CanEx-SM10 area. J. Hydrol. 520, 254–267. https://doi.org/10.1016/j.jhydrol.2014.11.026

Dolman, A.J., 1993. A multiple-source land surface energy balance model for use in general circulation models. Agric. For. Meteorol. 65, 21–45. https://doi.org/10.1016/0168-1923(93)90036-H

Duchemin, B., Hadria, R., Erraki, S., Boulet, G., Maisongrande, P., Chehbouni, A., Escadafal, R., Ezzahar, J., Hoedjes, J.C.B., Kharrou, M.H., Khabba, S., Mougenot, B., Olioso, A., Rodriguez, J.-C., Simonneaux, V., 2006. Monitoring wheat phenology and irrigation in Central Morocco: On the use of relationships between evapotranspiration, crops coefficients, leaf area index and remotely-sensed vegetation indices. Agric. Water Manag. 79, 1–27. https://doi.org/10.1016/J.AGWAT.2005.02.013

Eichinger, W.E., Parlange, M.B., Stricker, H., 1996. On the concept of equilibrium evaporation and the value of the Priestley-Taylor coefficient, WATER RESOURCES RESEARCH.

Entekhabi, D., Njoku, E.G., O'Neill, P.E., Kellogg, K.H., Crow, W.T., Edelstein, W.N., Entin, J.K., Goodman, S.D., Jackson, T.J., Johnson, J., Kimball, J., Piepmeier, J.R., Koster, R.D., Martin, N., McDonald, K.C., Moghaddam, M., Moran, S., Reichle, R., Shi, J.C., Spencer, M.W., Thurman, S.W., Tsang, L., Van Zyl, J., 2010. The Soil Moisture Active Passive {(SMAP)} Mission. Proc. IEEE 98, 704–716. https://doi.org/10.1117/12.795910

Er-Raki, S., Chehbouni, A., Duchemin, B., 2010. Combining Satellite Remote Sensing Data with the FAO-56 Dual Approach for Water Use Mapping In Irrigated Wheat Fields of a Semi-Arid Region. Remote Sens. 2, 375–387. https://doi.org/10.3390/rs2010375

Er-Raki, S., Chehbouni, A., Guemouria, N., Duchemin, B., Ezzahar, J., Hadria, R., 2007. Combining FAO-56 model and ground-based remote sensing to estimate water consumptions of wheat crops in a semi-arid region. Agric. Water Manag. 87, 41–54. https://doi.org/10.1016/j.agwat.2006.02.004

Ershadi, A., McCabe, M.F., Evans, J.P., Chaney, N.W., Wood, E.F., 2014. Multi-site evaluation of terrestrial evaporation models using FLUXNET data. Agric. For. Meteorol. 187, 46–61. https://doi.org/10.1016/J.AGRFORMET.2013.11.008

Ershadi, A., McCabe, M.F., Evans, J.P., Walker, J.P., 2013. Effects of spatial aggregation on the multi-scale estimation of evapotranspiration. Remote Sens. Environ. 131, 51–62. https://doi.org/10.1016/J.RSE.2012.12.007

Escorihuela, M.J., Chanzy, A., Wigneron, J.P., Kerr, Y.H., 2010. Effective soil moisture

sampling depth of L-band radiometry: A case study. Remote Sens. Environ. 114, 995–1001. https://doi.org/10.1016/J.RSE.2009.12.011

Euser, T., Luxemburg, W.M.J., Everson, C.S., Mengistu, M.G., Clulow, A.D., Bastiaanssen, W.G.M., 2014. A new method to measure Bowen ratios using high-resolution vertical dry and wet bulb temperature profiles. Hydrol. Earth Syst. Sci 18, 2021–2032. https://doi.org/10.5194/hess-18-2021-2014

Ezzahar, J., Chehbouni, A., Er-Raki, S., Hanich, L., 2009a. Combining a large aperture scintillometer and estimates of available energy to derive evapotranspiration over several agricultural fields in a semi-arid region. Plant Biosyst. 143, 209–221.

Ezzahar, J., Chehbouni, A., Hoedjes, J., Ramier, D., Boulain, N., Boubkraoui, S., Cappelaere, B., Descroix, L., Mougenot, B., Timouk, F., 2009b. Combining scintillometer measurements and an aggregation scheme to estimate area-averaged latent heat flux during the AMMA experiment. J. Hydrol. 375, 217–226. https://doi.org/10.1016/j.jhydrol.2009.01.010

Ezzahar, J., Chehbouni, A., Hoedjes, J.C.B., Chehbouni, A., 2007. On the application of scintillometry over heterogeneous grids. J. Hydrol. 334, 493–501. https://doi.org/10.1016/J.JHYDROL.2006.10.027

Fang, B., Lakshmi, V., 2014. Soil moisture at watershed scale: Remote sensing techniques. J. Hydrol. 516, 258–272. https://doi.org/10.1016/j.jhydrol.2013.12.008

FAO, 2015. La situation mondiale de l'alimentation et de l'agriculture Protection sociale et agriculture: Briser le cercle vicieux de la pauvreté rurale.

FAO, 2011. La situation mondiale de l'alimentation et de l'agriculture le rôle des femmes dans l'agriculture combler le fossé entre les hommes et les femmes pour soutenir le développement.

Federer, C.A., Vorosmarty, C., Fekete, B., 2003. Sensitivity of Annual Evaporation to Soil and Root Properties in Two Models of Contrasting Complexity. J. Hydrometeorol. 4.

Fensholt, R., Sandholt, I., Rasmussen, M.S., 2004. Evaluation of MODIS LAI, fAPAR and the relation between fAPAR and NDVI in a semi-arid environment using in situ measurements. Remote Sens. Environ. 91, 490–507. https://doi.org/10.1016/J.RSE.2004.04.009

Fisher, J.B., Melton, F., Middleton, E., Hain, C., Anderson, M., Allen, R., Mccabe, M.F., Hook, S., Baldocchi, D., Townsend, P.A., Kilic, A., Tu, K., Miralles, D.D., Perret, J., Lagouarde, J.-P., Waliser, D., Purdy, A.J., French, A., Schimel, D., Famiglietti, J.S., Stephens, G., Wood, E.F., 2017. The future of evapotranspiration: Global requirements for ecosystem functioning, carbon and climate feedbacks, agricultural management, and water resources. Water Resour. Res. 53, 2618–2626. https://doi.org/10.1002/2016WR020175

Fisher, J.B., Tu, K.P., Baldocchi, D.D., 2008. Global estimates of the land-atmosphere water flux based on monthly AVHRR and ISLSCP-II data, validated at 16 FLUXNET sites. Remote Sens. Environ. 112, 901–919. https://doi.org/10.1016/j.rse.2007.06.025

Foken, T., Wimmer, F., Mauder, M., Thomas, C., Liebethal, C., 2006. Some aspects of the energy balance closure problem. Atmos. Chem. Phys. 6, 4395–4402. https://doi.org/10.5194/acp-6-4395-2006

Gan, G., Gao, Y., 2015. Estimating time series of land surface energy fluxes using optimized two source energy balance schemes : Model formulation , calibration , and validation. Agric. For. Meteorol. 208, 62–75. https://doi.org/10.1016/j.agrformet.2015.04.007

Garbulsky, M.F., Peñuelas, J., Gamon, J., Inoue, Y., Filella, I., 2011. The photochemical reflectance index (PRI) and the remote sensing of leaf, canopy and ecosystem radiation use efficiencies: A review and meta-analysis. Remote Sens. Environ. 115, 281–297. https://doi.org/10.1016/J.RSE.2010.08.023

Gentine, P., Entekhabi, D., Chehbouni, A., Boulet, G., Duchemin, B., 2007. Analysis of evaporative fraction diurnal behaviour. Agric. For. Meteorol. 143, 13–29. https://doi.org/10.1016/j.agrformet.2006.11.002

Gentine, P., Entekhabi, D., Polcher, J., Gentine, P., Entekhabi, D., Polcher, J., 2011. The Diurnal Behavior of Evaporative Fraction in the Soil–Vegetation–Atmospheric Boundary Layer Continuum. J. Hydrometeorol. 12, 1530–1546. https://doi.org/10.1175/2011JHM1261.1

Gharsallah, O., Facchi, A., Gandolfi, C., 2013. Comparison of six evapotranspiration models for a surface irrigated maize agro-ecosystem in Northern Italy. Agric. Water Manag. 130, 119–130.

Gillies, R.R., Carlson, T.N., 1995. Thermal Remote Sensing of Surface Soil Water Content with Partial Vegetation Cover for Incorporation into Climate Models. J. Appl. Meteorol. 34, 745–756. https://doi.org/10.1175/1520-0450(1995)034<0745:TRSOSS>2.0.CO;2

Giorgi, F., 2006. Climate change hot-spots. Geophys. Res. Lett 33, 8707. https://doi.org/10.1029/2006GL025734

Glenn, E.P., Doody, T.M., Guerschman, J.P., Huete, A.R., King, E.A., McVicar, T.R., Van Dijk, A.I.J.M., Van Niel, T.G., Yebra, M., Zhang, Y., 2011. Actual evapotranspiration estimation by ground and remote sensing methods: the Australian experience. Hydrol. Process. 25, 4103–4116. https://doi.org/10.1002/hyp.8391

Glenn, E.P., Huete, A.R., Nagler, P.L., Nelson, S.G., 2008. Relationship Between Remotely-sensed Vegetation Indices, Canopy Attributes and Plant Physiological Processes: What Vegetation Indices Can and Cannot Tell Us About the Landscape. Sensors (Basel). 8, 2136–2160. https://doi.org/10.3390/s8042136

Gokmen, M., Vekerdy, Z., Verhoef, A., Verhoef, W., Batelaan, O., Tol, C. Van Der, 2012. Remote Sensing of Environment Integration of soil moisture in SEBS for improving evapotranspiration estimation under water stress conditions. Remote Sens. Environ. 121, 261–274. https://doi.org/10.1016/j.rse.2012.02.003

Gonzalez-dugo, M.P., Neale, C.M.U., Mateos, L., Kustas, W.P., Prueger, J.H., Anderson, M.C., Li, F., 2009. Agricultural and Forest Meteorology A comparison of operational remote sensing-based models for estimating crop evapotranspiration. Agric. For. Meteorol. 149, 1843–1853. https://doi.org/10.1016/j.agrformet.2009.06.012

Gowda, P.H., Chavez, J.L., Colaizzi, P.D., Evett, S.R., Howell, T.A., Gowda, P.H.;, Chavez, J.L.;, Colaizzi, P.D.;, Evett, S.R.;, Howell, T.A.;, Tolk, J.A., 2008. ET mapping for agricultural water management: present status and challenges. Irrig. Sci. J. 26, 223–237. https://doi.org/10.1007/s00271-007-0088-6

Guyot, A., Cohard, J.-M., Anquetin, S., Galle, S., Lloyd, C.R., 2009. Combined analysis of

energy and water balances to estimate latent heat flux of a sudanian small catchment. J. Hydrol. 375, 227–240. https://doi.org/10.1016/j.jhydrol.2008.12.027

Hain, C.R., Crow, W.T., Mecikalski, J.R., Anderson, M.C., Holmes, T., 2011. An intercomparison of available soil moisture estimates from thermal infrared and passive microwave remote sensing and land surface modeling. J. Geophys. Res. 116, D15107. https://doi.org/10.1029/2011JD015633

Hain, C.R., Mecikalski, J.R., Anderson, M.C., 2009. Retrieval of an Available Water-Based Soil Moisture Proxy from Thermal Infrared Remote Sensing. Part I: Methodology and Validation. Am. Meteorol. Soc. 10, 665–683. https://doi.org/10.1175/2008JHM1024.1

Heusinkveld, B.., Jacobs, A.F.., Holtslag, A.A.., Berkowicz, S.., 2004. Surface energy balance closure in an arid region: role of soil heat flux. Agric. For. Meteorol. 122, 21–37. https://doi.org/10.1016/j.agrformet.2003.09.005

Hoedjes, J.C.B., Chehbouni, A., Ezzahar, J., Escadafal, R., De Bruin, H.A.R., Hoedjes, J.C.B., Chehbouni, A., Ezzahar, J., Escadafal, R., Bruin, H.A.R. De, 2007. Comparison of Large Aperture Scintillometer and Eddy Covariance Measurements: Can Thermal Infrared Data Be Used to Capture Footprint-Induced Differences? J. Hydrometeorol. 8, 144–159. https://doi.org/10.1175/JHM561.1

Hou, A.Y., Kakar, R.K., Neeck, S., Azarbarzin, A.A., Kummerow, C.D., Kojima, M., Oki, R., Nakamura, K., Iguchi, T., Hou, A.Y., Kakar, R.K., Neeck, S., Azarbarzin, A.A., Kummerow, C.D., Kojima, M., Oki, R., Nakamura, K., Iguchi, T., 2014. The Global Precipitation Measurement Mission. Bull. Am. Meteorol. Soc. 95, 701–722. https://doi.org/10.1175/BAMS-D-13-00164.1

Howell, T.A., Schneider, A.D., Jensen, M.E., 1991. History of Lysimeter Design and Use for Evapotranspiration Measurements, in: Lysimeters for Evapotranspiration and Environmental Measurements. ASCE, Hawaii, pp. 1–9.

Huete, A., Didan, K., van Leeuwen, W., Miura, T., Glenn, E., 2011. MODIS Vegetation Indices, in: Land Remote Sensing and Environmental Change. Springer International Publishing, pp. 579–602. https://doi.org/10.1007/978-1-4419-6749-7_26

Huffman, G.J., Bolvin, D.T., Nelkin, E.J., Wolff, D.B., Adler, R.F., Gu, G., Hong, Y., Bowman, K.P., Stocker, E.F., Huffman, G.J., Bolvin, D.T., Nelkin, E.J., Wolff, D.B., Adler, R.F., Gu, G., Hong, Y., Bowman, K.P., Stocker, E.F., 2007. The TRMM Multisatellite Precipitation Analysis (TMPA): Quasi-Global, Multiyear, Combined-Sensor Precipitation Estimates at Fine Scales. J. Hydrometeorol. 8, 38–55. https://doi.org/10.1175/JHM560.1

Hunsaker, J.D., Pinter, P.J., Barnes, E.M., Kimball, A.., 2003. Estimating cotton evapotranspiration crop coefficients with a multispectral vegetation index. Irrig. Sci. J. 22, 95–104. https://doi.org/10.1007/s00271-003-0074-6

Huntingford, C., Allen, S.J., Harding, R.J., 1995. An intercomparison of single and dual-source vegetation-atmosphere transfer models applied to transpiration from sahelian savannah. Boundary-Layer Meteorol. 74, 397–418. https://doi.org/10.1007/BF00712380

IPCC, 2014. Climate Change 2014: Synthesis Report. Contribution of Working Groups I, II and III to the Fifth Assessment Report of the Intergovernmental Panel on Climate Change [Core Writing Team, R.K. Pachauri and L.A. Meyer (eds.)]. https://www.ipcc.ch/.

IPCC, 2013. Climate Change 2013: The Physical Science Basis. Contribution of Working Group I to the Fifth Assessment Report of the Intergovernmental Panel on Climate Change [Stocker, T.F., D. Qin, G.-K. Plattner, M. Tignor, S.K. Allen, J. Boschung, A. Nauels, Y. Xia,.

Jackson, R.D., Reginato, R.J., Idso, S.B., 1977. Wheat canopy temperature: A practical tool for evaluating water requirements. Water Resour. Manag. 13, 651–656. https://doi.org/10.1029/WR013i003p00651

Jara, J., Stockle, C.O., Kjelgaard, J., 1998. Measurement of evapotranspiration and its components in a corn (Zea Mays L.) field. Agric. For. Meteorol. 92, 131–145. https://doi.org/10.1016/S0168-1923(98)00083-5

Jarlan, L., Khabba, S., Er-Raki, S., Le Page, M., Hanich, L., Fakir, Y., Merlin, O., Mangiarotti, S., Gascoin, S., Ezzahar, J., Kharrou, M.H., Berjamy, B., Saaïdi, A., Boudhar, A., Benkaddour, A., Laftouhi, N., Abaoui, J., Tavernier, A., Boulet, G., Simonneaux, V., Driouech, F., El Adnani, M., El Fazziki, A., Amenzou, N., Raibi, F., El Mandour, A., Ibouh, H., Le Dantec, V., Habets, F., Tramblay, Y., Mougenot, B., Leblanc, M., El Faïz, M., Drapeau, L., Coudert, B., Hagolle, O., Filali, N., Belaqziz, S., Marchane, A., Szczypta, C., Toumi, J., Diarra, A., Aouade, G., Hajhouji, Y., Nassah, H., Bigeard, G., Chirouze, J., Boukhari, K., Abourida, A., Richard, B., Fanise, P., Kasbani, M., Chakir, A., Zribi, M., Marah, H., Naimi, A., Mokssit, A., Kerr, Y., Escadafal, R., 2015. Remote Sensing of Water Resources in Semi-Arid Mediterranean Areas: the joint international laboratory TREMA. Int. J. Remote Sens. 36, 4879–4917. https://doi.org/10.1080/01431161.2015.1093198

Jiang, L., Islam, S., 2001. Estimation of surface evaporation map over southern Great Plains using remote sensing data. Water Resour. Res. 37, 329–340. https://doi.org/10.1109/ICCRD.2011.5763991

Jiang, L., Islam, S., 1999. A methodology for estimation of surface evapotranspiration over large areas using remote sensing observations. Geophys. Res. Lett. 26, 2773–2776. https://doi.org/10.1029/1999GL006049

Jin, Y., Randerson, J.T., Goulden, M.L., 2011. Continental-scale net radiation and evapotranspiration estimated using MODIS satellite observations. Remote Sens. Environ. 115, 2302–2319. https://doi.org/10.1016/j.rse.2011.04.031

Kalma, J.D., McVicar, T.R., McCabe, M.F., 2008. Estimating land surface evaporation: A review of methods using remotely sensed surface temperature data. Surv. Geophys. 29, 421–469. https://doi.org/10.1007/s10712-008-9037-z

Kashyap, P.S., Panda, R.K., 2001. Evaluation of evapotranspiration estimation methods and development of crop-coefficients for potato crop in a sub-humid region. Agric. Water Manag. 50, 9–25.

Kerr, Y.H., Member, S., Waldteufel, P., Richaume, P., Pierre Wigneron, J., Ferrazzoli, P., Mahmoodi, A., Al Bitar, A., Cabot, F., Gruhier, C., Enache Juglea, S., Leroux, D., Mialon, A., Delwart, S., Kerr, Y.H., Richaume, P., Al Bitar, A., Cabot, F., Gruhier, C., Juglea, S.E., Leroux, D., Mialon, A., Wigneron, J.P., 2012. The SMOS Soil Moisture Retrieval Algorithm. IEEE Trans. Geosci. Remote Sens. 50. https://doi.org/10.1109/TGRS.2012.2184548

Kerr, Y.H., Waldteufel, P., Wigneron, J.-P., Delwart, S., Cabot, F., Boutin, J., Escorihuela,

M.-J., Font, J., Reul, N., Gruhier, C., Juglea, S.E., Drinkwater, M.R., Hahne, A., Martín-Neira, M., Mecklenburg, S., Kerr, Y.H., Cabot, F., Gruhier, C., Juglea, S.E., Wigneron, J.-P., Delwart, S., Drinkwater, M.R., Hahne, A., Martín, M., 2010. The SMOS Mission: New Tool for Monitoring Key Elements of the Global Water Cycle. Proc. IEEE | 98. https://doi.org/10.1109/JPROC.2010.2043032

Khabba, S., Duchemin, B., Hadria, R., Er-Raki, S., Ezzahar, J., Chehbouni, A., Lahrouni, A., Hanich, L., 2009. Evaluation of Digital Hemispherical Photography and Plant Canopy Analyzer for Measuring Vegetation Area Index of Orange Orchards. J. Agron. 8, 67–72. https://doi.org/10.3923/ja.2009.67.72

Kharrou, M.H., Er-Raki, S., Chehbouni, A., Duchemin, B., Simonneaux, V., Lepage, M., Ouzine, L., Jarlan, L., 2011. Water use efficiency and yield of winter wheat under different irrigation regimes in a semi-arid region. Agric. Sci. 2, 273–282. https://doi.org/10.4236/as.2011.23036

Kohsiek, W., 1985. A Comparison between Line-Averaged Observation of Cn2 from Scintillation of a CO2 Laser Beam and Time-Averaged in situ Observations. J. Clim. Appl. Meteorol. 24, 1099–1103. https://doi.org/10.1175/1520-0450(1985)024<1099:ACBLAO>2.0.CO;2

Kustas, W.P., Anderson, M., 2009. Advances in thermal infrared remote sensing for land surface modeling. Agric. For. Meteorol. 149, 2071–2081. https://doi.org/10.1016/j.agrformet.2009.05.016

Kustas, W.P., Daughtry, C.S.T., Van Oevelen, P.J., 1993. Analytical treatment of the relationships between soil heat flux/net radiation ratio and vegetation indices. Remote Sens. Environ. 46, 319–330. https://doi.org/10.1016/0034-4257(93)90052-Y

Kustas, W.P., Moran, M.S., Jackson, R.D., Gay, L.W., Duell, L.F.W., Kunkel, K.E., Matthias, A.D., 1990. Instantaneous and Daily Values of the Surface Energy Balance over Agricultural Fields Using Remote Sensing and a Reference Field in an Arid Environment. Remote Sens. Environ. 32, 125–141.

Kustas, W.P., Norman, J.M., 1999. Evaluation of soil and vegetation heat flux predictions using a simple two-source model with radiometric temperatures for partial canopy cover. Agric. For. Meteorol. 94, 13–29. https://doi.org/10.1016/S0168-1923(99)00005-2

Kustas, W.P., Norman, J.M., 1997. A two-source approach for estimating turbulent fluxes using multiple angle thermal infrared observations. Water Resour. Res. 33, 1495–1508. https://doi.org/10.1029/97WR00704

Kustas, W.P., Norman, J.M., 1997. A two-source approach for estimating turbulent fluxes using multiple angle thermal infrared observations. Water Resour. Res. 33, 1495–1508. https://doi.org/10.1029/97WR00704

Kustas, W.P., Norman, J.M., 1996. Use of remote sensing for evapotranspiration monitoring over land surfaces. Hydrol. Sci. J. 41, 495–516. https://doi.org/10.1080/02626669609491522

Kustas, W.P., Norman, J.M., Anderson, M.C., French, A.N., 2003. Estimating subpixel surface temperatures and energy fluxes from the vegetation index-radiometric temperature relationship. Remote Sens. Environ. 85, 429–440. https://doi.org/10.1016/S0034-4257(03)00036-1

Kustas, W.P., Zhan, X., Jackson, T.J., 1999. Mapping surface energy flux partitioning at large scales with optical and microwave remote sensing data from Washita '92, WATER RESOURCES RESEARCH. https://doi.org/10.1029/98WR02094

Kustas, W.P., Zhan, X., Schmugge, T.J., 1998. Combining optical and microwave remote sensing for mapping energy fluxes in a semiarid watershed. Remote Sens. Environ. 64, 116–131. https://doi.org/10.1016/S0034-4257(97)00176-4

Lagouarde, J.-P., Irvine, M., Bonnefond, J.-M., Grimmond, C.S.B., Long, N., Oke, T.R., Salmond, J.A., Offerle, B., 2006. Monitoring the Sensible Heat Flux over Urban Areas using Large Aperture Scintillometry: Case Study of Marseille City During the Escompte Experiment. Boundary-Layer Meteorol. 118, 449–476. https://doi.org/10.1007/s10546-005-9001-0

Lagouarde, J.P., Brunet, Y., 1991. Suivi de l'evapotranspiration reelle journaliere a partir des donnees NOAA-AVHRR lors de la campagne Hapex-Mobilhy, in: Mesures Physiques et Signatures En TeledetectionPresented at 5. Colloque International, Courchevel, FRA (1991-01-14 - 1991-01-18). Paris, p. 2(569-572).

Lagouarde, J.P., McAneney, K.J., Green, A.E., 1996. Scintillation measurements of sensible heat flux over heterogeneous surfaces, in: In: J.B. Stewart, E.T. Engman, R.A.F. and Y., Kerr (Eds.), Scaling up in Hydrology Using Remote Sensing. . Wiley, Chichester, p. 147–160.

Lebel, T., Cappelaere, B., Galle, S., Hanan, N., Kergoat, L., Levis, S., Vieux, B., Descroix, L., Gosset, M., Mougin, E., Peugeot, C., Seguis, L., 2009. AMMA-CATCH studies in the Sahelian region of West-Africa: An overview. J. Hydrol. 375, 3–13. https://doi.org/10.1016/j.jhydrol.2009.03.020

Lee, T.J., Pielke, R.A., 1992. Estimating the Soil Surface Specific Humidity. J. Appl. Meteorol. https://doi.org/10.2307/26186471

Lewis, P., Barnsley, M.J., 1994. Influence of the sky radiance distribution on various formulations of the earth surface albedo. Remote Sens. Unit 707–715.

Lhomme, J.-P., Elguero, E., 1999. Examination of evaporative fraction diurnal behaviour using a soil-vegetation model coupled with a mixed-layer model. Hydrol. Earth Syst. Sci. 3, 259–270. https://doi.org/10.5194/hess-3-259-1999

Lhomme, J.-P., Monteny, B., Amadou, M., 1994. Estimating sensible heat flux from radiometric temperature over sparse millet. Agric. For. Meteorol. 68, 77–91. https://doi.org/10.1016/0168-1923(94)90070-1

Lhomme, J.P., Chehbouni, A., 1999. Comments on dual-source vegetation-atmosphere transfer models. Agric. For. Meteorol. 94, 269–273. https://doi.org/10.1016/S0168-1923(98)00109-9

Li, F., Kustas, W.P., Anderson, M.C., Jackson, T.J., Bindlish, R., Prueger, J.H., 2006. Comparing the utility of microwave and thermal remote-sensing constraints in two-source energy balance modeling over an agricultural landscape. Remote Sens. Environ. 101, 315–328. https://doi.org/10.1016/j.rse.2006.01.001

Li, Q., Zhong, R., Huang, J., Gong, H., 2011. Comparison of two retrieval methods with combined passive and active microwave remote sensing observations for soil moisture. Math. Comput. Model. 54, 1181–1193. https://doi.org/10.1016/J.MCM.2010.11.052

Li, X., Li, X., Li, Z., Ma, M., Wang, J., Xiao, Q., Liu, Q., Che, T., Chen, E., Yan, G., Hu, Z., Zhang, L., Chu, R., Su, P., Liu, Q., Liu, S., Wang, J., Niu, Z., Chen, Y., Jin, R., Wang, W., Ran, Y., Xin, X., Ren, H., 2009. Watershed allied telemetry experimental research. J. Geophys. Res. Atmos. 114. https://doi.org/10.1029/2008JD011590

Li, Y., Zhou, J., Wang, H., Li, D., Jin, R., Zhou, Y., Zhou, Q., 2015. Integrating soil moisture retrieved from L-band microwave radiation into an energy balance model to improve evapotranspiration estimation on the irrigated oases of arid regions in northwest China. Agric. For. Meteorol. 214–215, 306–318. https://doi.org/10.1016/j.agrformet.2015.08.260

Littell, J.S., Peterson, D.L., Riley, K.L., Liu, Y., Luce, C.H., 2016. A review of the relationships between drought and forest fire in the United States. Glob. Chang. Biol. 22, 2353–2369. https://doi.org/10.1111/gcb.13275

Liu, S., Xu, Z., Song, L., Zhao, Q., Ge, Y., Xu, T., Ma, Y., Zhu, Z., Jia, Z., Zhang, F., 2016. Upscaling evapotranspiration measurements from multi-site to the satellite pixel scale over heterogeneous land surfaces. Agric. For. Meteorol. 230–231, 97–113. https://doi.org/10.1016/j.agrformet.2016.04.008

Liu, S.M., Xu, Z.W., Zhu, Z.L., Jia, Z.Z., Zhu, M.J., 2013. Measurements of evapotranspiration from eddy-covariance systems and large aperture scintillometers in the Hai River Basin, China. J. Hydrol. 487, 24–38. https://doi.org/10.1016/j.jhydrol.2013.02.025

Long, D., Singh, V.P., 2012. A Two-source Trapezoid Model for Evapotranspiration (TTME) from satellite imagery. Remote Sens. Environ. 121, 370–388. https://doi.org/10.1016/j.rse.2012.02.015

Long, D., Singh, V.P., Li, Z.-L., 2011. How sensitive is SEBAL to changes in input variables, domain size and satellite sensor? J. Geophys. Res 116, 21107. https://doi.org/10.1029/2011JD016542

Loudyi, D., Chagdali, M., Belmatrik, S., El Kadi, A., 2018. Reservoirs silting in Morocco. Hydrolink. https://doi.org/10.3390/w10070927k

Mahfouf, J.-F., 1991. Analysis of Soil Moisture from Near-Surface Parameters: A Feasibility Study. J. Appl. Meteorol. 30, 1534–1547. https://doi.org/10.1175/1520-0450(1991)030<1534:AOSMFN>2.0.CO;2

Malbéteau, Y., Merlin, O., Balsamo, G., Er-Raki, S., Khabba, S., Walker, J.P., Jarlan, L., Malbéteau, Y., Merlin, O., Balsamo, G., Er-Raki, S., Khabba, S., Walker, J.P., Jarlan, L., 2018. Toward a Surface Soil Moisture Product at High Spatiotemporal Resolution: Temporally Interpolated, Spatially Disaggregated SMOS Data. J. Hydrometeorol. 19, 183–200. https://doi.org/10.1175/JHM-D-16-0280.1

Malbéteau, Y., Merlin, O., Molero, B., Rüdiger, C., Bacon, S., 2016. DisPATCh as a tool to evaluate coarse-scale remotely sensed soil moisture using localized in situ measurements: Application to SMOS and AMSR-E data in Southeastern Australia. Int. J. Appl. Earth Obs. Geoinf. 45, 221–234. https://doi.org/10.1016/j.jag.2015.10.002

Malone, R.W., Bonta, J. V., Stewardson, D.J., Nelsen, T., 2000. Error analysis and quality improvement of the coshocton weighing lysimeters. Trans. ASAE 43, 271–280. https://doi.org/10.13031/2013.2702

Maselli, F., Papale, D., Chiesi, M., Matteucci, G., Angeli, L., Raschi, A., Seufert, G., 2014. Operational monitoring of daily evapotranspiration by the combination of MODIS NDVI and ground meteorological data: Application and evaluation in Central Italy. Remote Sens. Environ. 152, 279–290. https://doi.org/10.1016/J.RSE.2014.06.021

Massuel, S., Cappelaere, B., Favreau, G., Leduc, C., Lebel, T., Vischel, T., 2011. Integrated surface water–groundwater modelling in the context of increasing water reserves of a regional Sahelian aquifer. Hydrol. Sci. J. 56, 1242–1264. https://doi.org/10.1080/02626667.2011.609171

Mauder, M., Foken, T., 2006. Impact of post-field data processing on eddy covariance flux estimates and energy balance closure. Meteorol. Zeitschrift 15, 597–609. https://doi.org/10.1127/0941-2948/2006/0167

McAneney, K.J., Itier, B., 1996. Operational limits to the Priestley-Taylor formula. Irrig. Sci. 17, 37–43. https://doi.org/10.1007/s002710050020

Mcnaughton, K.G., Spriggs, T.W., 1989. An evaluation of the Priestley and Taylor equation and the complementary relationship using results from a mixed-layer model of the convective boundary layer, in: Estimation of Areal Evapotranspiration. IAHS Publ, Canada, p. 89.

Meijninger, W.M.L., Beyrich, F., Udi, A.L. ¨, Kohsiek, W., De Bruin, H.A.R., 2005. SCINTILLOMETER-BASED TURBULENT FLUXES OF SENSIBLE AND LATENT HEAT OVER A HETEROGENEOUS LAND SURFACE-A CONTRIBUTION TO LITFASS-2003. Boundary-Layer Meteorol. https://doi.org/10.1007/s10546-005-9022-8

Menenti, M., Bastiaanssen, W., van Eick, D., Abd el Karim, M.A., 1989. Linear relationships between surface reflectance and temperature and their application to map actual evaporation of groundwater. Adv. Sp. Res. 9, 165–176. https://doi.org/10.1016/0273-1177(89)90482-1

Merlin, O., Al Bitar, A., Rivalland, V., Béziat, P., Ceschia, E., Dedieu, G., 2011. An analytical model of evaporation efficiency for unsaturated soil surfaces with an arbitrary thickness. J. Appl. Meteorol. Climatol. 50, 457–471. https://doi.org/10.1175/2010JAMC2418.1

Merlin, O., Al Bitar, A., Walker, J.P., Kerr, Y., 2010. An improved algorithm for disaggregating microwave-derived soil moisture based on red, near-infrared and thermal-infrared data. Remote Sens. Environ. 114, 2305–2316. https://doi.org/10.1016/j.rse.2010.05.007

Merlin, O., Chirouze, J., Olioso, A., Jarlan, L., Chehbouni, G., Boulet, G., 2014. An image-based four-source surface energy balance model to estimate crop evapotranspiration from solar reflectance / thermal emission data (SEB-4S). Agric. For. Meteorol. 184, 188–203. https://doi.org/10.1016/j.agrformet.2013.10.002

Merlin, O., Escorihuela, M.J., Mayoral, M.A., Hagolle, O., Al Bitar, A., Kerr, Y., 2013. Self-calibrated evaporation-based disaggregation of SMOS soil moisture: An evaluation study at 3km and 100m resolution in Catalunya, Spain. Remote Sens. Environ. 130, 25–38. https://doi.org/10.1016/j.rse.2012.11.008

Merlin, O., Jacob, F., Wigneron, J.P., Walker, J., Chehbouni, G., 2012a. Multidimensional disaggregation of land surface temperature using high-resolution red, near-infrared, shortwave-infrared, and microwave-L bands. IEEE Trans. Geosci. Remote Sens. 50,

1864–1880. https://doi.org/10.1109/TGRS.2011.2169802

Merlin, O., Olivera-Guerra, L., Aït Hssaine, B., Amazirh, A., Rafi, Z., Ezzahar, J., Gentine, P., Khabba, S., Gascoin, S., Er-Raki, S., 2018. A phenomenological model of soil evaporative efficiency using surface soil moisture and temperature data. Agric. For. Meteorol. 256–257, 501–515. https://doi.org/10.1016/J.AGRFORMET.2018.04.010

Merlin, O., Rüdiger, C., Al Bitar, A., Richaume, P., Walker, J.P., Kerr, Y.H., 2012b. Disaggregation of SMOS soil moisture in Southeastern Australia. IEEE Trans. Geosci. Remote Sens. 50, 1556–1571. https://doi.org/10.1109/TGRS.2011.2175000

Merlin, O., Stefan, V.G., Amazirh, A., Chanzy, A., Ceschia, E., Tallec, T., Beringer, J., Gentine, P., Er-Raki, S., Bircher, S., Khabba, S., 2016. Modeling soil evaporation efficiency in a range of soil and atmospheric conditions: A downward approach based on multi-site data. Submitt. to Water Resour. Res. 3663–3684. https://doi.org/10.1002/2015WR018233.Received

Merlin, O., Walker, J.P., Chehbouni, A., Kerr, Y., 2008. Towards deterministic downscaling of SMOS soil moisture using MODIS derived soil evaporative efficiency. Remote Sens. Environ. 112, 3935–3946. https://doi.org/10.1016/j.rse.2008.06.012

Mihailović, D.T., Rajković, B., Dekić, L., Pielke, R.A., Lee, T.J., Ye, Z., 1995. The validation of various schemes for parameterizing evaporation from bare soil for use in meteorological models: A numerical study using in situ data. Boundary-Layer Meteorol. 76, 259–289. https://doi.org/10.1007/BF00709354

Molden, D., Oweis, T., Steduto, P., Bindraban, P., Hanjra, M.A., Kijne, J., 2010. Improving agricultural water productivity: Between optimism and caution. Agric. Water Manag. 97, 528–535. https://doi.org/10.1016/J.AGWAT.2009.03.023

Molero, B., Merlin, O., Malbéteau, Y., Al Bitar, A., Cabot, F., Stefan, V., Kerr, Y., Bacon, S., Cosh, M.H., Bindlish, R., Jackson, T.J., 2016. SMOS disaggregated soil moisture product at 1 km resolution: Processor overview and first validation results. Remote Sens. Environ. 180, 361–376. https://doi.org/10.1016/J.RSE.2016.02.045

Monteith, J.., 1965. Evaporation and the Environment, in: 19th Symposia of the Society for Experimental Biology. pp. 205–235. https://doi.org/10.4236/ns.2010.212173

Moran, M.S., Clarke, T.R., Inoue, Y., Vidal, A., 1994. Estimating Crop Water Deficit Using the Relation between Surface-Air Temperature and Spectral Vegetation Index. Remote Sens. Environ. 49, 246–263.

Morillas, L., Villagarcía, L., Domingo, F., Nieto, H., Uclés, O., García, M., 2014. Environmental factors affecting the accuracy of surface fluxes from a two-source model in Mediterranean drylands: Upscaling instantaneous to daytime estimates. Agric. For. Meteorol. 189–190, 140–158. https://doi.org/10.1016/j.agrformet.2014.01.018

Nemani, R., Pierce, L.E., Running, S.W., Goward, S., 1993. Developing Satellite-derived Estimates of Surface Moisture Status. J. Appl. Meteor 32, 548–557. https://doi.org/10.1175/1520-0450(1993)032<0548:DSDEOS>2.0.CO;2

Njoku, E.G., Jackson, T.J., Lakshmi, V., Member, S., Chan, T.K., Nghiem, S. V, 2003. Soil Moisture Retrieval From AMSR-E. IEEE Trans. Geosci. Remote Sens. 41. https://doi.org/10.1109/TGRS.2002.808243

Noilhan, J., Mahfouf, J.-F., 1996. The ISBA land surface parameterisation scheme, Global

and Planetary Change.

Norman, J.M., Kustas, W.P., Humes, K.S., 1995. Source approach for estimating soil and vegetation energy fluxes in observations of directional radiometric surface temperature. Agric. For. Meteorol. 77, 263–293. https://doi.org/10.1016/0168-1923(95)02265-Y

Nouri, H., Beecham, S., Kazemi, F., Hassanli, A.M., 2012. A review of ET measurement techniques for estimating the water requirements of urban landscape vegetation. Urban Water J. 10, 247–259. https://doi.org/10.1080/1573062X.2012.726360

Ochs, G., Wilson, J.J., 1993. A second-generation large-aperature scintillometer. Second. Large-aperture Scintill.

Olioso, A., 1992. Simulation des échanges d'énergie et de masse d'un couvert végétal, dans le but de relier la transpiration et la photosynthèse aux mesures de réflectance et de température de surface. http://www.theses.fr. Montpellier 2.

Olioso, A., Chauki, H., Courault, D., Wigneron, J.-P., 1999. Seguin and Itier. Remote Sens. Environ. 68, 341–356.

Olivera-Guerra, L., Mattar, C., Galleguillos, M., 2014. Estimation of real evapotranspiration and its variation in Mediterranean landscapes of central-southern Chile. Int. J. Appl. Earth Obs. Geoinf. 28, 160–169. https://doi.org/10.1016/j.jag.2013.11.012

Oudin, L., 2004. Recherche d'un modèle d'évapotranspiration potentielle pertinent comme entrée d'un modèle pluie-débit global. l'Ecole Nationale du Génie Rural, des Eaux et Forêts.

Overgaard, J., Rosbjerg, D., Butts, M.B., 2006. Land-surface modelling in hydrological perspective-a review, Biogeosciences.

Parlange, M.B., Katul, G.G., 1992. Estimation of the diurnal variation of potential evaporation from a wet bare soil surface, Journal of Hydrology.

Payero, J.O., Irmak, S., 2008. Construction, installation, and performance of two repacked weighing lysimeters. Irrig. Sci. 26, 191–202. https://doi.org/10.1007/s00271-007-0085-9

Peacock, C.E., Hess, T.M., 2004. Estimating evapotranspiration from a reed bed using the Bowen ratio energy balance method. Hydrol. Process. 18, 247–260. https://doi.org/10.1002/hyp.1373

Penman, H.., 1948. Natural evaporation from open water, bare soil and grass. Proc. R. Soc. London. Ser. A. Math. Phys. Sci. 193, 120–145. https://doi.org/10.1098/rspa.1948.0037

Peñuelas, J., Garbulsky, M.F., Filella, I., 2011. Photochemical reflectance index (PRI) and remote sensing of plant CO2 uptake. New Phytol. 191, 596–599. https://doi.org/10.1111/j.1469-8137.2011.03791.x

Pereira, A.R., 2004. The Priestley-Taylor parameter and the decoupling factor for estimating reference evapotranspiration. Agric. For. Meteorol. 125, 305–313. https://doi.org/10.1016/j.agrformet.2004.04.002

Pereira, L.S., Allen, R.G., Smith, M., Raes, D., 2015. Crop evapotranspiration estimation with FAO56: Past and future. Agric. Water Manag. 147, 4–20. https://doi.org/10.1016/j.agwat.2014.07.031

Pérez, J.Á.M., García-Galiano, S.G., Martin-Gorriz, B., Baille, A., 2017. Satellite-based

method for estimating the spatial distribution of crop evapotranspiration: Sensitivity to the priestley-taylor coefficient. Remote Sens. 9. https://doi.org/10.3390/rs9060611

Piles, M., Camps, A., Vall-Llossera, M., Panciera, R., Rüdiger, C., Kerr, Y.H., Walker, J., 2011. Downscaling SMOS-Derived Soil Moisture Using MODIS Visible/Infrared Data. IEEE Trans. Geosci. Remote Sens. 49. https://doi.org/10.1109/TGRS.2011.2120615

Plan Bleu, 2009. Etat de l'environnement et du développement en méditerranée. Centre d'activités régionales PNUD/PAM.

Price, J.C., 1990. Using spatial context in satellite data to infer regional scale evapotranspiration. IEEE Trans. Geosci. Remote Sens. 28, 940–948. https://doi.org/10.1109/36.58983

Priestley, C.H.B., Taylor, R.J., 1972. On the Assessment of Surface Heat Flux and Evaporation Using Large-Scale Parameters. Mon. Weather Rev. 100, 81–92. https://doi.org/10.1175/1520-0493(1972)100<0081:OTAOSH>2.3.CO;2

Prueger, J.H., Hatfield, J.L., Kristian Aase, J., Pikul, J.L., 1997. Bowen-Ratio Comparisons with Lysimeter Evapotranspiration. Agron. J. 89, 730–736.

Purdy, A.J., Fisher, J.B., Goulden, M.L., Colliander, A., Halverson, G., Tu, K., Famiglietti, J.S., 2018. Remote Sensing of Environment SMAP soil moisture improves global evapotranspiration. Remote Sens. Environ. 219, 1–14. https://doi.org/10.1016/j.rse.2018.09.023

Rafi, Z., Merlin, O., Le Dantec, V., Khabba, S., Mordelet, P., Er-Raki, S., Amazirh, A., Olivera-Guerra, L., Ait Hssaine, B., Simonneaux, V., Ezzahar, J., Ferrer, F., 2019. Partitioning evapotranspiration of a drip-irrigated wheat crop: Inter-comparing eddy covariance-, sap flow-, lysimeter- and FAO-based methods. Agric. For. Meteorol. 265, 310–326. https://doi.org/10.1016/J.AGRFORMET.2018.11.031

Ramier, D., Boulain, N., Cappelaere, B., Timouk, F., Rabanit, M., Lloyd, C.R., Boubkraoui, S., Métayer, F., Descroix, L., Wawrzyniak, V., 2009. Towards an understanding of coupled physical and biological processes in the cultivated Sahel - 1. Energy and water. J. Hydrol. 375, 204–216. https://doi.org/10.1016/j.jhydrol.2008.12.002

Reicosky, D.C., Sharratt, B.S., Ljungkull, J.E., Baker, D.G., 1983. Comparison of alfalfa evapotranspiration measured by a weighing lysimeter and a portable chamber. Agric. Meteorol. 28, 205–211. https://doi.org/10.1016/0002-1571(83)90026-2

Rockström, J., Valentin, C., 1997. Hillslope dynamics of on-farm generation of surface water flows: The case of rain-fed cultivation of pearl millet on sandy soil in the Sahel. Agric. Water Manag. 33, 183–210. https://doi.org/10.1016/S0378-3774(96)01282-6

Roerink, G.., Su, Z., Menenti, M., 2000. S-SEBI: A simple remote sensing algorithm to estimate the surface energy balance. Phys. Chem. Earth, Part B Hydrol. Ocean. Atmos. 25, 147–157. https://doi.org/10.1016/S1464-1909(99)00128-8

Rossato, L., Alvalá, R.C.S., Ferreira, N.J., Tomasella, J., 2005. Evapotranspiration estimation in the Brazil using NDVI data. Brugge, Belgium.

Rouse, J.W., Haas, R.H., Schell, J.A., Deering, D.W., 1974. Monitoring vegetation systems in the Great Plains with ERTS, in: NASA. Goddard Space Flight Center 3d ERTS-1 Symp. pp. 309–317.

Saadi, S., Boulet, G., Bahir, M., Brut, A., Delogu, É., Fanise, P., Mougenot, B., Simonneaux, V., Lili Chabaane, Z., 2018. Assessment of actual evapotranspiration over a semiarid heterogeneous land surface by means of coupled low-resolution remote sensing data with an energy balance model: comparison to extra-large aperture scintillometer measurements. Hydrol. Earth Syst. Sci. 22, 2187–2209. https://doi.org/10.5194/hess-22-2187-2018

Sakaguchi, K., Zeng, X., 2009. Effects of soil wetness, plant litter, and under-canopy atmospheric stability on ground evaporation in the Community Land Model (CLM3.5). J. Geophys. Res 114, 1107. https://doi.org/10.1029/2008JD010834

Satalino, G., Balenzano, A., Mattia, F., Davidson, M.W.J., 2014. C-Band SAR Data for Mapping Crops Dominated by Surface or Volume Scattering. IEEE Geosci. Remote Sens. Lett. 11, 384–388. https://doi.org/10.1109/LGRS.2013.2263034

Sauer, T.J., Norman, J.M., Tanner, C.B., Wilson, T.B., 1995. Measurement of heat and vapor transfer coefficients at the soil surface beneath a maize canopy using source plates. Agric. For. Meteorol. 75, 161–189. https://doi.org/10.1016/0168-1923(94)02209-3

Schleussner, C.-F., Lissner, T.K., Fischer, E.M., Wohland, J., Perrette, M., Golly, A., Rogelj, J., Childers, K., Schewe, J., Frieler, K., Mengel, M., Hare, W., Schaeffer, M., 2016. Differential climate impacts for policy-relevant limits to global warming: the case of 1.5 • C and 2 • C. Earth Syst. Dynam 7, 327–351. https://doi.org/10.5194/esd-7-327-2016

Schmid, H.P., 1994. Source areas for scalars and scalar fluxes. Boundary-Layer Meteorol. 67, 293–318. https://doi.org/10.1007/BF00713146

Schmugge, T.J., Kustas, W.P., Ritchie, J.C., Jackson, T.J., Rango, A., 2002. Remote sensing in hydrology. Adv. Water Resour. 25, 1367–1385. https://doi.org/10.1016/S0309-1708(02)00065-9

Schwabe, K., Albiac, J., Connor, J.D., Hassan, R.M., Meza González, L., 2013. Drought in Arid and Semi-Arid Regions. Springer Netherlands, Dordrecht. https://doi.org/10.1007/978-94-007-6636-5

Seguin, B., Itier, B., 1983. Using midday surface temperature to estimate daily evaporation from satellite thermal IR data. Int. J. Remote Sens. 4, 371–383. https://doi.org/10.1080/01431168308948554

Sellers, P.J., Heiser, M.D., Hall, F.G., 1992. Relations between surface conductance and spectral vegetation indexes at intermediate (100m2 to 15km2) length scales. J. Geophys. Res. 97, 19033–19059.

Sellers, P.J., Randall, D.A., Collatz, G.J., Berry, J.A., Field, C.B., Dazlich, D.A., Zhang, C., Collelo, G.D., Bounoua, L., Sellers, P.J., Randall, D.A., Collatz, G.J., Berry, J.A., Field, C.B., Dazlich, D.A., Zhang, C., Collelo, G.D., Bounoua, L., 1996. A Revised Land Surface Parameterization (SiB2) for Atmospheric GCMS. Part I: Model Formulation. J. Clim. 9, 676–705. https://doi.org/10.1175/1520-0442(1996)009<0676:ARLSPF>2.0.CO;2

Senay, G.B., Bohms, S., Singh, R.K., Gowda, P.H., Velpuri, N.M., Alemu, H., Verdin, J.P., 2013. Operational Evapotranspiration Mapping Using Remote Sensing and Weather Datasets : a New Parameterization for the Sseb Approach. J. Am. water Resour. Assoc. 49. https://doi.org/10.1111/jawr.12057

Senay, G.B., Budde, M., Verdin, J.P., Melesse, A.M., 2001. A Coupled Remote Sensing and Simplified Surface Energy Balance Approach to Estimate Actual Evapotranspiration from Irrigated Fields. Sensors 7, 979–1000.

Senay, G.B., Leake, S., Nagler, P.L., Artan, G., Dickinson, J., Cordova, J.T., Glenn, E.P., 2011. Estimating basin scale evapotranspiration (ET) by water balance and remote sensing methods. Hydrol. Process. 25, 4037–4049. https://doi.org/10.1002/hyp.8379

Serbin, S.P., Ahl, D.E., Gower, S.T., 2013. Spatial and temporal validation of the MODIS LAI and FPAR products across a boreal forest wildfire chronosequence. Remote Sens. Environ. 133, 71–84. https://doi.org/10.1016/j.rse.2013.01.022

Shaw, R.H., Pereira, A.., 1982. Aerodynamic roughness of a plant canopy: A numerical experiment. Agric. Meteorol. 26, 51–65. https://doi.org/10.1016/0002-1571(82)90057-7

Shuttleworth, W.. ., Wallace, J.., 1985. Evaporation from sparse crops-an energy combination theory. Q. J. R. Meteorol. Soc. 111, 839–855. https://doi.org/10.1256/smsqj.46909

Shuttleworth, W., Gurney, R., Hsu, A., Ormsby, J., 1989. FIFE: the variation in energy partition at surface flux sites. Remote Sens. Large-Scale Glob. Porc. (IAHS Publ.) 186, 67–74.

Shuttleworth, W.J., Gurney, R.J., 1990. The theoretical relationship between foliage temperature and canopy resistance in sparse crops. Q. Journal-Royal Meteorol. Soc. 497–519.

Silans, A.P. de, 1986. Transferts de masse et de chaleur dans un sol stratifié soumis à une excitation atmosphérique naturelle : comparaison : modèles-expérience. http://www.theses.fr.

Song, L., Kustas, W.P., Liu, S., Colaizzi, P.D., Nieto, H., Xu, Z., Ma, Y., Li, M., Xu, T., Agam, N., Tolk, J.A., Evett, S.R., 2016a. Applications of a thermal-based two-source energy balance model using Priestley-Taylor approach for surface temperature partitioning under advective conditions. J. Hydrol. 540, 574–587. https://doi.org/10.1016/j.jhydrol.2016.06.034

Song, L., Liu, S., Kustas, W.P., Zhou, J., Xu, Z., Xia, T., Li, M., 2016b. Application of remote sensing-based two-source energy balance model for mapping field surface fluxes with composite and component surface temperatures. Agric. For. Meteorol. 230–231, 8–19. https://doi.org/10.1016/j.agrformet.2016.01.005

Stannard, D.I., 1993. Comparison of Penman-Monteith, Shuttleworth-Wallace, and Modified Priestley-Taylor Evapotranspiration Models for wildland vegetation in semiarid rangeland. Water Resour. Res. 29, 1379–1392. https://doi.org/10.1029/93WR00333

Stewart, J.., Gay, L.., 1989. Preliminary modelling of transpiration from the fife site in Kansas. Agric. For. Meteorol. 48, 305–315. https://doi.org/10.1016/0168-1923(89)90075-0

Stewart, J.B., Thom, A.S., 1973. Energy budgets in pine forest. Q. J. R. Meteorol. Soc. 99, 154–170. https://doi.org/10.1002/qj.49709941913

Su, Z., 2002. The Surface Energy Balance System (SEBS) for estimation of turbulent heat fluxes. Hydrol. Earth Syst. Sci. 6, 85–100. https://doi.org/10.1109/VLSID.2007.18

Suárez, L., Zarco-Tejada, P.J., Sepulcre-Cantó, G., Pérez-Priego, O., Miller, J.R., Jiménez-

Muñoz, J.C., Sobrino, J., 2008. Assessing canopy PRI for water stress detection with diurnal airborne imagery. Remote Sens. Environ. 112, 560–575. https://doi.org/10.1016/j.rse.2007.05.009

Subedi, A., Chávez, J.L., 2015. Crop Evapotranspiration (ET) Estimation Models: A Review and Discussion of the Applicability and Limitations of ET Methods. J. Agric. Sci. 7, 50–68. https://doi.org/10.5539/jas.v7n6p50

Sun, X.Y., Newham, L.T.H., Croke, B.F.W., Norton, J.P., 2012. Three complementary methods for sensitivity analysis of a water quality model. Environ. Model. Softw. 37, 19–29. https://doi.org/10.1016/j.envsoft.2012.04.010

Taconet, O., Carlson, T., Bernard, R., Vidal-Madjar, D., 1986. Evaluation of a Surface/Vegetation Parameterization Using Satellite Measurements of Surface Temperature. J. Clim. Appl. Meteorol. https://doi.org/10.2307/26183504

Tanner, B.D., 1988. Use Requirements for Bowen Ratio and Eddy Correlation Determination of Evapotranspiration, in: Planning Now for Irrigation and Drainage in the 21st Century. ASCE, pp. 605–616.

Tanner, B.D., Swiatek, E., Greene, J.P., 1993. Density Fluctuations and Use of the Krypton Hygrometer in Surface Flux Measurements, in: Management of Irrigation and Drainage Systems: Integrated Perspectives. pp. 945–952.

Thom, A.S., 1971. Momentum absorption by vegetation. Q. J. R. Meteorol. Soc. 97, 414–428. https://doi.org/10.1002/qj.49709741404

Trigo, I.F., Monteiro, I.T., Olesen, F., Kabsch, E., 2008. An assessment of remotely sensed land surface temperature. J. Geophys. Res 113, 17108. https://doi.org/10.1029/2008JD010035

Tucker, C.J., 1979. Red and photographic infrared linear combinations for monitoring vegetation. Remote Sens. Environ. 8, 127–150. https://doi.org/10.1016/0034-4257(79)90013-0

Twine, T.E., Kustas, W.P., Norman, J.M., Cook, D.R., Houser, P.R., Meyers, T.P., Prueger, J.H., Starks, P.J., Wesley, M.L., Wesely, M.L., 2000. Correcting eddy-covariance flux underestimates over a grassland, Agricultural and Forest Meteorology.

UNEP, 2012. Annual report, United Nations Environment Programme. United Nations Environment Programme (UNEP).

Velluet, C., Demarty, J., Cappelaere, B., Braud, I., Issoufou, H.B.-A., Boulain, N., Ramier, D., Mainassara, I., Charvet, G., Boucher, M., Chazarin, J.-P., Oï, M., Yahou, H., Maidaji, B., Arpin-Pont, F., Benarrosh, N., Mahamane, A., Nazoumou, Y., Favreau, G., Seghieri, J., 2014. Building a field- and model-based climatology of local water and energy cycles in the cultivated Sahel – annual budgets and seasonality. Hydrol. Earth Syst. Sci. 18, 5001–5024. https://doi.org/10.5194/hess-18-5001-2014

Verhoef, A., Ottlé, C., Cappelaere, B., Murray, T., Saux-Picart, S., Zribi, M., Maignan, F., Boulain, N., Demarty, J., Ramier, D., 2012. Spatio-temporal surface soil heat flux estimates from satellite data; results for the AMMA experiment at the Fakara (Niger) supersite. Agric. For. Meteorol. 154–155, 55–66. https://doi.org/10.1016/j.agrformet.2011.08.003

Vorosmarty, C.J., Green, P., Salisbury, J., Lammers, R.B., 2000. Global Water Resources:

Vulnerability from Climate Change and Population Growth. Science (80-.). 289, 284–288. https://doi.org/10.1126/science.289.5477.284

Wan, Z., Dozier, J., 1996. A Generalized Split-Window Algorithm for Retrieving Land-Surface Temperature from Space, IEEE TRANSACTIONS ON GEOSCIENCE AND REMOTE SENSING.

Wang, K., Li, Z., Cribb, M., 2006. Estimation of evaporative fraction from a combination of day and night land surface temperatures and NDVI: A new method to determine the Priestley-Taylor parameter. Remote Sens. Environ. 102, 293–305. https://doi.org/10.1016/j.rse.2006.02.007

White, M.A., Asner, G.P., Nemani, R.R., Privette, J.L., Running, S. V., 2000. Measuring fractional cover and leaf area index in arid ecosystems: digital camera, radiation transmittance, and laser altimetry methods. Remote Sens. Environ. 74, 45–57.

Williams, T.G., Flanagan, L.B., 1996. Effect of changes in water content on photosynthesis, transpiration and discrimination against 13CO2 and C18O16O in Pleurozium and Sphagnum. Oecologia 108, 38–46. https://doi.org/10.1007/BF00333212

Wilson, K., Goldstein, A., Falge, E., Aubinet, M., Baldocchi, D.D., 2002. Energy Balance Closure at FLUXNET Sites. Agric. For. Meteorol. 113, 223–243.

Word Bank, 2017. Managing Urban Water Scarcity in Morocco. Washington, DC 20433.

Yang, Y., Long, D., Guan, H., Liang, W., Simmons, C., Batelaan, O., 2015. Comparison of three dual-source remote sensing evapotranspiration models during the MUSOEXE-12 campaign: Revisit of model physics. Water Resour. Res. 51, 3145–3165. https://doi.org/10.1002/2014WR015619

Yao, Y., Liang, S., Yu, J., Zhao, S., Lin, Y., Jia, K., Zhang, X., Cheng, J., Xie, X., Sun, L., Wang, X., Zhang, L., 2017. Differences in estimating terrestrial water flux from three satellite-based Priestley-Taylor algorithms. Int. J. Appl. Earth Obs. Geoinf. 56, 1–12. https://doi.org/10.1016/j.jag.2016.10.009

Young, M.., Wierenga, P.., Mancino, C.., 1997. Monitoring Near-Surface Soil Water Storage in Turfgrass using Time Domain Reflectometry and Weighing Lysimetry. Soil Sci. Soc. Am. J. 61, 1138–1146. https://doi.org/10.2136/sssaj1997.03615995006100040021x

Yu, W., Ma, M., Li, Z., Tan, J., Wu, A., 2017. New scheme for validating remote-sensing land surface temperature productswith stationobservations. Remote Sens. 9, 1–24. https://doi.org/10.3390/rs9121210

Yu, W., Ma, M., Wang, X., Geng, L., Tan, J., Shi, J., Yu, W., Ma, M., Wang, X., Geng, L., Tan, J., Shi, J., 2014. Evaluation of MODIS LST Products Using Longwave Radiation Ground Measurements in the Northern Arid Region of China. Remote Sens. 6, 11494–11517. https://doi.org/10.3390/rs61111494

Zhan, X., Kustas, W.., 2001. A coupled model of land surface CO2 and energy fluxes using remote sensing data. Agric. For. Meteorol. 107, 131–152. https://doi.org/10.1016/S0168-1923(00)00229-X

Zhong, R., Huang, J., Wei, J., Li, Q., Guo, J., Su, W., 2012. Large-Scale Microwave Remote Sensing of Retrieving Surface Multi-parameters Using Active and Passive Satellite Data: In the Tibetan Plateau Region of Maqu, in: Computer and Computing Technologies in Agriculture V - 5th IFIP TC 5/SIG 5.1 . China, pp. 415–426.

https://doi.org/10.1007/978-3-642-27278-3_44

Zhou, Y., Yang, G., Wang, S., Wang, L., Wang, F., Liu, X., 2014. A new index for mapping built-up and bare land areas from Landsat-8 OLI data. Remote Sens. Lett. 5, 862–871. https://doi.org/10.1080/2150704X.2014.973996

Zur, B., Jones, J.W., 1981. A model for the water relations, photosynthesis, and expansive growth of crops. Water Resour. Res. 17, 311–320. https://doi.org/10.1029/WR017i002p00311